STUDIA UNIVERSITATIS
BABEŞ-BOLYAI

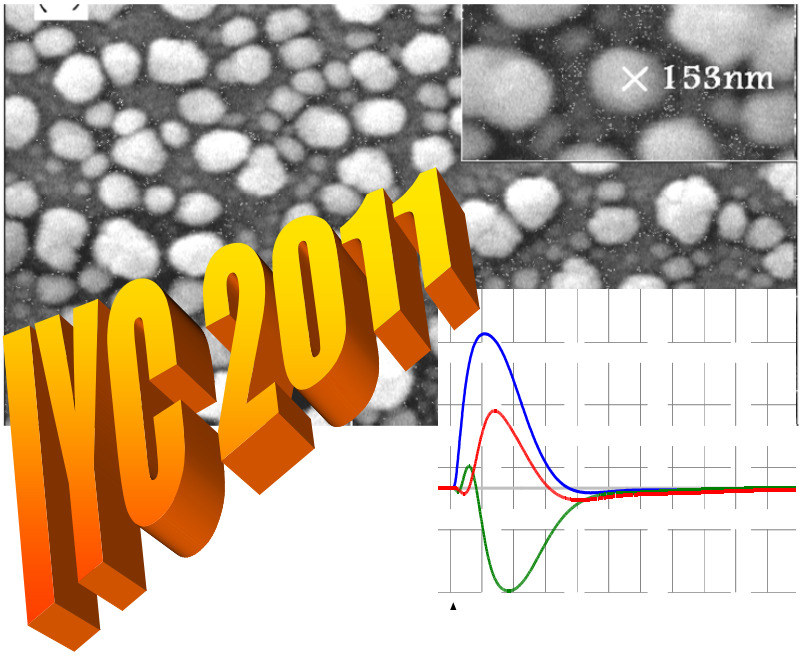

CHEMIA

2/2011

YEAR **Volume 56 (LVI) 2011**
MONTH **JUNE**
ISSUE **2**

S T U D I A

UNIVERSITATIS BABEŞ–BOLYAI

CHEMIA

2

Desktop Editing Office: 51ST B.P. Hasdeu, Cluj-Napoca, Romania, Phone + 40 264-40.53.52

CUPRINS – CONTENT – SOMMAIRE – INHALT

Studia Universitatis Babes-Bolyai Chemia has been selected for coverage in Thomson Reuters products and custom information services. Beginning with V. 53 (1) 2008, this publication is indexed and abstracted in the following:

- Science Citation Index Expanded (also known as SciSearch®)
- Chemistry Citation Index®
- Journal Citation Reports/Science Edition

STUDIA UBB CHEMIA, LVI, 2, 2011 (p. 5 - 18)

MODEL PREDICTIVE CONTROL OF A DIVIDING-WALL COLUMN

ANTON A. KISS[a], ROHIT R. REWAGAD[a, b]

ABSTRACT. This study explores an optimal model predictive control (MPC) of a dividing-wall column (DWC). Energy minimization is implicitly achieved by using an additional loop controlling the heavy component in the top of the feed side, by using the liquid split as manipulated variable. An industrial case-study is presented based on the separation of the mixture benzene-toluene-xylene (BTX) in a DWC. The results of the dynamic model simulations show that MPC leads to a significant increase in performance – lower overshooting and shorter settling times – as compared to previously reported PID controllers.

Keywords: *DWC, Petlyuk, BTX, MPC, PID, energy efficient control*

INTRODUCTION

Along with reactive distillation, dividing-wall column (DWC) is one of the best examples of process intensification, as it can bring significant reduction in both CapEx and OpEx [1-4]. Classic separations of ternary mixtures developed from direct sequences to thermally coupled columns such as Petlyuk (Figure 1), and the integrated DWC configuration [5-8]. Nonetheless, this process integration leads also to significant changes in the operating mode and ultimately in the controllability of the system [9-12].

In the past decades, the advanced process control received considerable attention in both academia and industry [13-18]. While advanced control strategies made the nonlinear process control more practical, there is still a considerable gap between the control theory and the industrial practice. It is frustrating for the control theory community that elegant and comprehensive frameworks for system analysis and design are rarely implemented in the chemical industry that still applies the well-known PID.

While a variety of controllers are used for binary distillation columns, only several control structures were studied for DWC. In most cases, PID loops within a multi-loop framework were used to steer the system to the desired steady state and reach the goals of dynamic optimization [19-25].

[a] *AkzoNobel Research, Development and Innovation, Process Technology Expert Capability Group, Zutphenseweg 10, 7418 AJ Deventer, The Netherlands, tony.kiss@akzonobel.com*
[b] *University of Twente, Faculty of Science and Technology, Enschede, The Netherlands*

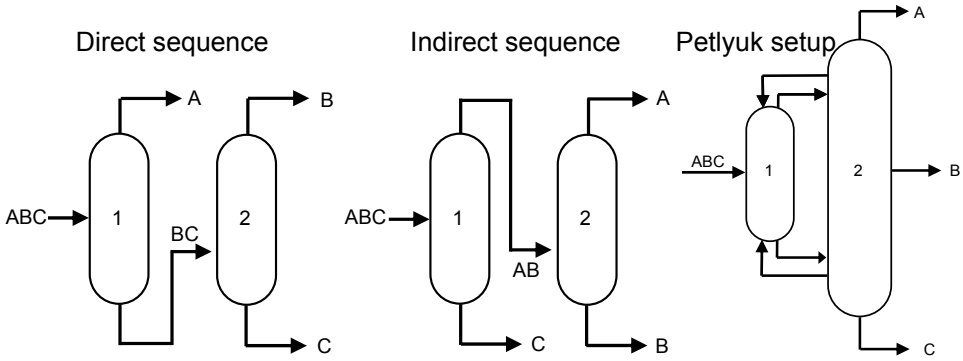

Figure 1. Separation of a ternary mixture via direct and indirect distillation sequences and Petlyuk configuration – thermodynamic equivalent of DWC.

Despite of the complex design and controllability issues, the use of advanced controllers in case of DWC is even more limited. Woinaroschy and Isopescu [26] showed the ability of iterative dynamic programming to solve time optimal control of DWC. Recently, Diggelen et al. [12] published a comparison study of various control structures based on PID loops versus more advanced controllers including LQG/LQR, GMC and high order controllers obtained by H_∞ and μ-synthesis – but no optimal energy control was used. The LQG with integral action and reference inputs was found to deliver the best control performance. When the liquid split is manipulated to achieve minimal energy requirements, the DB/LSV structure was reported as the most effective multi-loop PID control strategy [25].

In few DWC studies reported, MPC outperformed PID while taking into account simultaneously a larger number of manipulated variables [27-29]. Adrian et al. [27] used a black box approach using commercial software was applied in the identification of prediction model and development of the controller, which restricts the understanding to a larger extent.

All these studies investigate different systems and types of disturbances and hence a common conclusion to identify the best controller cannot be withdrawn. In this work we propose an advanced control strategy based on MPC. The control scheme is enhanced by adding an extra loop controlling the heavy component in the top of the feed side, by using the liquid split as manipulated variable, thus implicitly achieving energy minimization. To allow a fair comparison with previously published work, this study considers as industrial case-study the ternary separation of benzene-toluene-xylene (BTX) in a DWC. The results show that MPC leads to a significant increase in performance, as compared to conventional PID controllers within a multi-loop framework. Moreover, the dynamic optimization employed by MPC allows the operation of DWC with minimum energy requirements.

PROBLEM STATEMENT

Following the brief literature review, it is clear that due efforts are placed into developing reliable control strategies for DWC [24]. As the distillation process is a multivariable process, this leads to a multivariable control problem. Due to its very well-known benefits [14-16], Model Predictive Control is a worthwhile option to control in an optimal way a multivariate, nonlinear and constrained process such as DWC. However, up to this date and to the best of our knowledge, the control of DWC using MPC has been studied only by Adrian et al., but only to a certain degree [27]. Moreover, their results do now allow a fair comparison with other ternary separation systems previously reported in literature.

Therefore, there is a need to further investigate the applicability of MPC to DWC. In this study, we consider an industrially relevant ternary separation system (benzene-toluene-xylene, BTX) and compare the MPC performance with the best multi-loop PID control strategy reported. The internal prediction model used by the MPC in this work is derived from the linearization of the nonlinear distillation model, and not from step-response experiments. Such method is more accurate as the resulting first-principle linear model represents all the states, just as the nonlinear model, and it is not limited to the range of the identification experiments.

All the control strategies are enhanced by adding an extra loop control aimed to implicitly minimize the energy requirements by caring out the dynamic optimization. The goal is to maintain the product purities at their given set point, even in the presence of disturbances, while preserving the minimum energy requirements. It is very important for a distillation column to handle the disturbances in the feed, as its flow rate and composition depends heavily on the up-stream process. The column must also meet the required product purities in order to comply with the on-spec targets. For that reason, we based our investigation on the criteria of disturbance rejection in the feed flow rate and composition, as well as set point tracking of the product purities.

MODEL PREDICTIVE CONTROL

MPC is an optimization-based multivariable control technique using (non-)linear process models for the prediction of the process outputs. The schematic representation of MPC is best shown in Figure 2. At each sampling time the model is updated on the basis of new measurements and state variable estimates. Then the open-loop optimal manipulated variable moves are calculated over a finite prediction horizon with respect to some optimization function (e.g. cost, energy), and the manipulated variables for the subsequent prediction horizon are implemented. Then the prediction horizon into the future and the previous steps are repeated. [14-16].

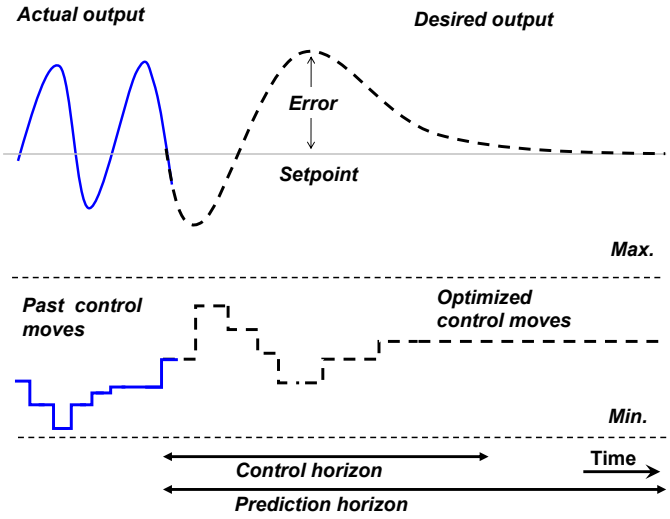

Figure 2. Schematic representation of the Model Predictive Control (MPC)

RESULTS AND DISCUSSION

The dynamic nonlinear model of the column was described in more detail in a previous study by Diggelen et al., dealing with the comparison of control strategies for DWC [12]. Due to the assumptions made, the model is relatively simple but it does capture all the essential elements required to describe and control the DWC system. The following key assumptions were used: 1. constant pressure, 2. constant relative volatility, 3. neglected energy balances, and 4. linear liquid dynamics. The full dynamic model was successfully implemented in Mathworks Matlab and Simulink® [30, 31].

Figure 3 (left) illustrates the modeled DWC, consisting of 6 sections of 8 stages each. The feed stream consisting of benzene-toluene-xylene (noted here as ABC for convenience) is fed into the prefractionator side (feed side of the DWC), between section 1 and 2. Benzene is obtained as top distillate, xylene as bottom product, while toluene is withdrawn as side stream of the column (product side of the DWC, between sections 4 and 5).

The selection of the property model is crucial in any simulation – an issue already recognized in the world of chemical processes modeling by the axiom "*garbage in, garbage out"* meaning that the simulation results have the same quality as the input data and parameters [32]. For the BTX system considered in this work, several reliable property models are available, such as NRTL or UNIQUAC. Figure 3 (right) provides the composition profile inside the DWC by means of a ternary diagram. The bottom, side and top product are close to the left, top and right corners, respectively. For meaningful dynamic responses, the steady state purity of all products is considered to be 97%.

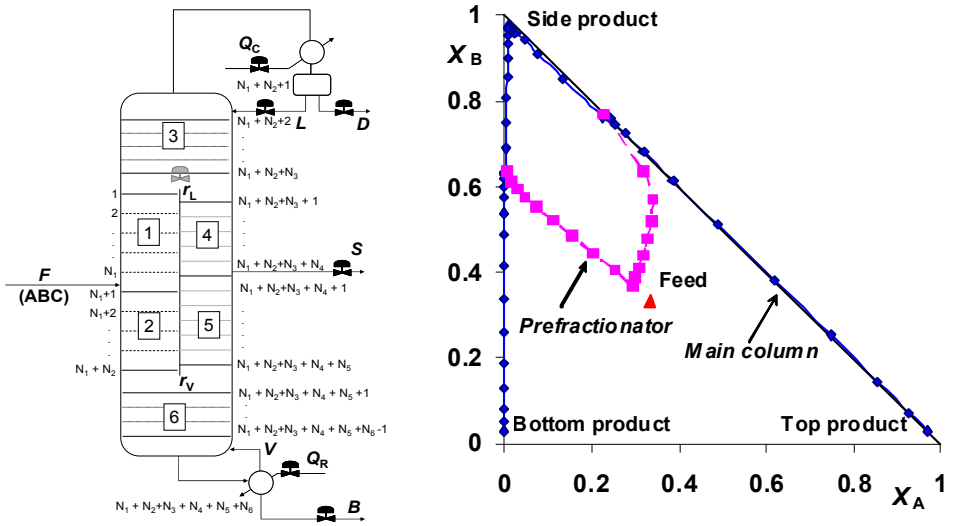

Figure 3. Schematics of the simulated DWC: 6 sections of 8 stages each (left). Composition profile inside DWC, as ternary diagram (right)

In case of DWC, two multi loops are needed to stabilize the column, and another three to maintain the set points specifying the product purities. Based on the results of previous studies [12, 25] – which showed that the DB/LSV structure performed best as compared to all other PID structures – we consider in this work only the best PID configuration as reference case. In this configuration (DB/LSV), the liquid levels in the reflux tank and reboiler are maintained by means of D (distillate) and B (bottoms flow rate) whereas the product compositions are maintained by manipulating L (liquid reflux), S (side product flowrate) and V (vapor boil-up) respectively [12].

An additional optimization loop is added to manipulate the liquid split (r_L) in order to control the heavy component composition in the top of fractionators (Y_{C_PF1}), and implicitly achieving minimization of the energy requirements. Several studies demonstrated that implicit optimization of the energy usage is achieved by controlling the heavy impurity at the top of the prefractionator [23, 25]. The MPC controller was designed to handle a 10×6 system of inputs and outputs. The inputs include the controlled variables – mole fraction of A in distillate (x_A), B in the side stream (x_B), C in the bottom product (x_C) and C in the top of the prefractionator (Y_{C_PF1}), liquid holdups in the reflux tank (H_t), reboiler (H_r) and the disturbance variables. The disturbance variables defines the feed by feed flowrate (F), compositions of benzene ($x_{F,A}$) and toluene ($x_{F,B}$) in the feed and heat quality (q_F). The outputs include the manipulated variables – D, B, L, S, V and r_L. Figure 4 shows the DB/LSV scheme and the MPC alternative proposed in this work.

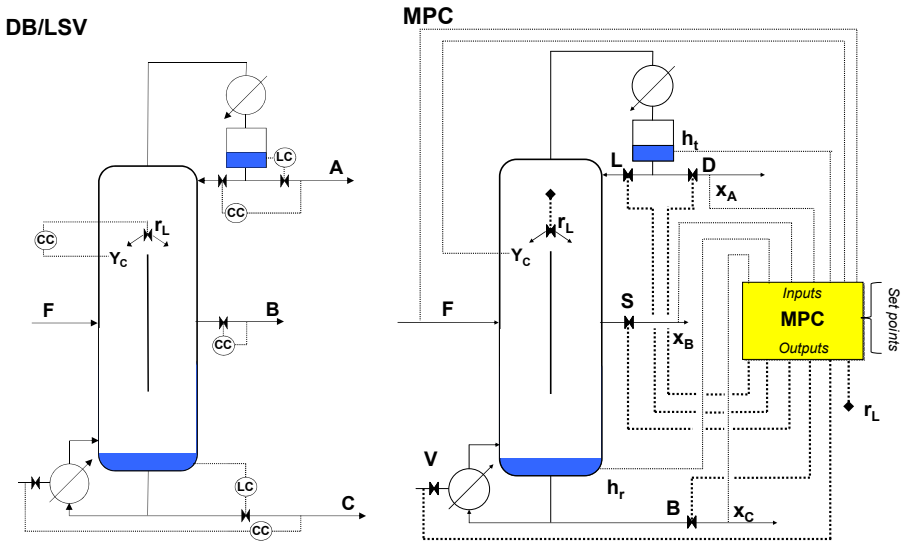

Figure 4. Control structures based on PID loops (left) and MPC (right)

The full nonlinear process model was linearized in order to obtain the continuous state space model. The resulting state space model has 156 states (96 compositions for A and B, C being calculated as the remaining difference; 8 compositions of A and B in the vapor and liquid splitters, reflux tank and reboiler; 48 liquid hold ups on trays; 4 hold ups for the vapor and liquid splitters, reflux tank and reboiler), 10 inputs and 6 outputs representing the controlled and manipulated variables chosen. Prior to the deployment of the controller, the best practices of control engineering require to check the quality of the linearization In order to avoid any mismatch between the models representing the plant and controller. Such a mismatch may cause serious instability in the operation of the plant.

Consequently, the quality of the linearization was evaluated by performing a closed loop simulations while exerting disturbances. The feed flowrate (F) was subjected to a step change of +10% compared to its nominal value, and the deviations in the product compositions were analyzed. This disturbance and the test variables were selected due to its dominant first-order time constant. Thus it serves as a worst case scenario. To validate the linearization in a closed loop, only the level controllers were used to control the inventory in the column and the rest of the multi-loops were kept open. As a result, Figure 5 confirms that a close match exist between the nonlinear and linearized model used in this study. Remarkably, only minor differences can be observed between the linear and the non-linear models.

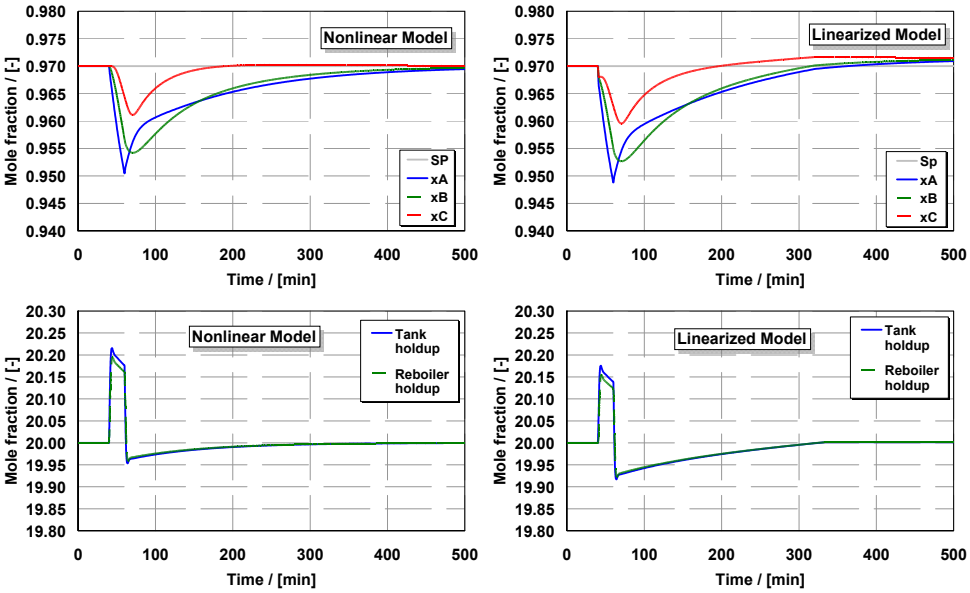

Figure 5. Comparison between nonlinear and linearized system: dynamic response after a step change of +10% in feed flowrate for 20 min.

The PID control loops were tuned by the direct synthesis method proposed by Luyben [13]. Table 1 shows the tuning parameters of the PID controller. As fairly accurate evaluations of the process time constants τ, 20, 40 and 60 min were used, respectively. For the level controllers, a larger reset time τ_i = 100 min was chosen as no tight control is required.

As no reliable design rules are available in the literature for tuning MPC controllers [14-16], heuristics combined with a trial and error method were used – dependent on a number of factors related to the controller and the process: prediction (p) & control (m) horizon, input (w_u) & ouput (w_y) weights, sampling time (Δk), operating constraints on inputs and outputs as well as the rate of change rate of inputs (Δu). Table 2 shows the tuning parameters for the MPC control structure proposed here (Figure 4, right).

Table 1. Tuning parameters of the PID controllers of the DB/LSV structure

DB/LSV	P (%/%)	I (min)	D (min)	Control direction
$x_A \rightarrow L$	3	40	0	–
$x_B \rightarrow S$	3	20	0	+
$x_C \rightarrow V$	3	40	0	–
$y_C \rightarrow r_L$	1	20	0	+
Tank level → D	1	100	0	+
Reboiler level → B	1	100	0	+

Table 2. Tuning parameters of the MPC controller

	Manipulated variables						Controlled variables						
Weights	D	B	L	S	V	r_L	x_A x_B x_C	y_{C_PF1}	h_t	h_r	F	$x_{F,A}$ $x_{F,B}$	q_F
w^y	1	0.8	0.3	0.9	0.3	0.1	–	–	–		–	–	–
w^y	–	–	–	–	–	–	1	1	0.3	0.5	1	1	0.5
$w^{\Delta u}$	0.2						0.1						
Constraints	[kmol/min]					[-]	[-]		[m]	[kmol/min]		[-]	[-]
(±)	0.2	0.2	0.3	0.2	0.3	0.15	0.02	0.005	0.1	0.1	0.1	0.02	0.5

Prediction horizon p	Control horizon m	Sampling time Δk
30	5	3 min

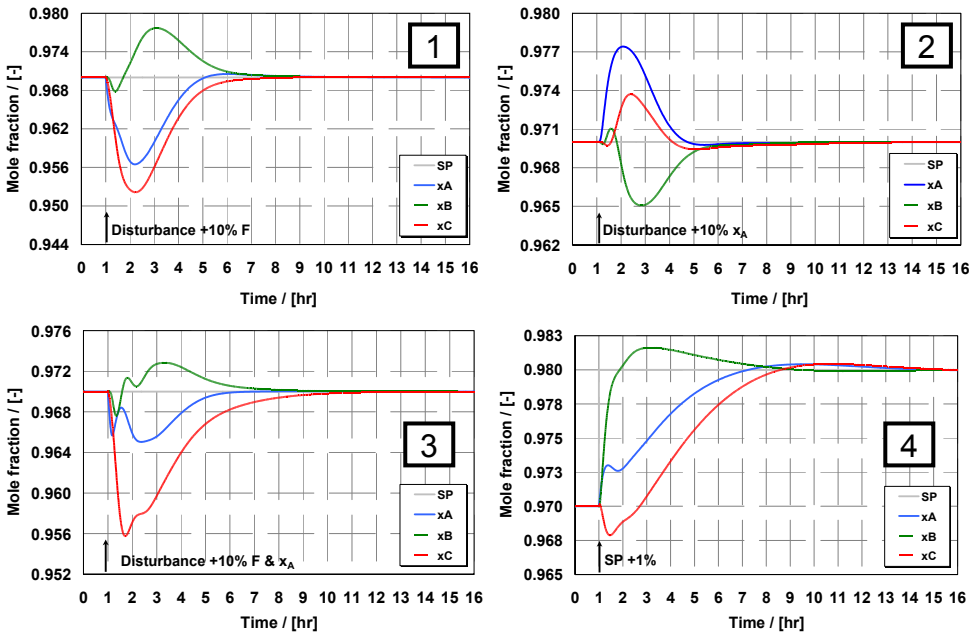

Figure 6. Dynamic response of DB/LSV PID control structure, at a persistent disturbance of +10% in the feed flow rate (1), +10% x_A in the feed composition (2), +10% in both feed flow rate and composition (3) and +1% increase of setpoint (4)

In the dynamic simulations performed in this study, the purity set points (SP) are 97% for all product specifications. Persistent disturbances of +10% in the feed flow rate (F) and +10% in the feed composition (x_A) were exerted either alone or simultaneously for the dynamic scenarios. The ability of the controllers to track the set point is also tested by changing all purity set points from 0.97 to 0.98. The chosen disturbances are either measured (MPC), or unmeasured (PID) in which case the controllers are relying only on the feedback action. Such disturbances and set point changes resemble the most common transitory regimes arising in practice, due to planned changes or unexpected disturbances in actual operation.

As illustrated by the next figures, the mole fractions of components A in the top distillate (x_A), B in the side stream (x_B) and C in the bottom product (x_C) are returning to their set point (SP) within reasonable short settling times. Figure 6 show that the control structure DV/LSB exhibits overshooting mainly in the toluene composition.

The dynamic response of the MPC controller is shown in Figure 7, being characterized by low overshooting and short settling times. The MPC steer the system to the given set points under the specified constrains unlike the PID controller that cannot be directly subjected to constrains.

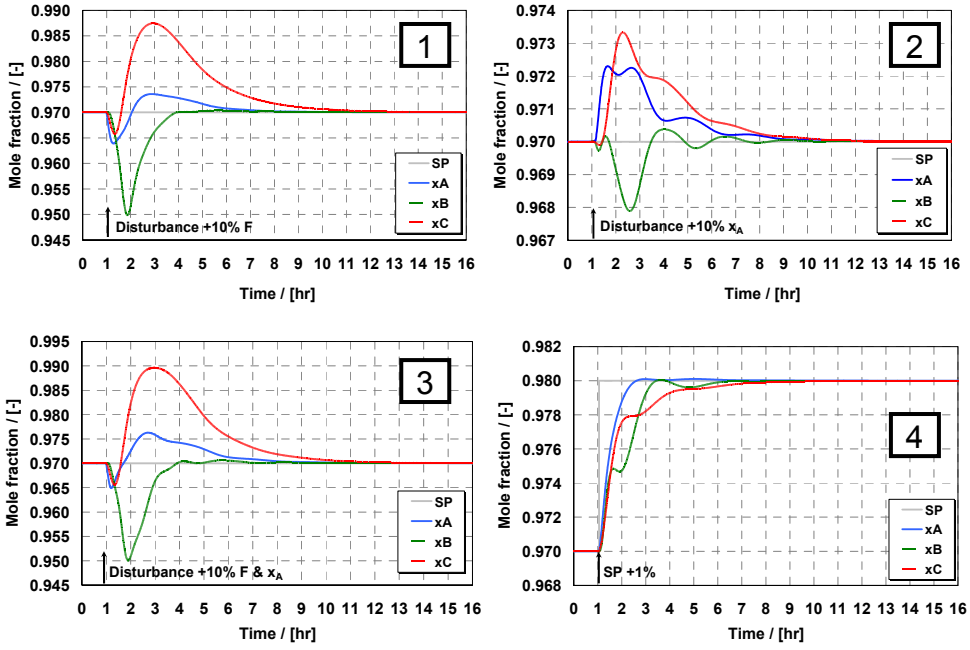

Figure 7. Dynamic response of MPC control structure, at a persistent disturbance of +10% in the feed flow rate (1), +10% x_A in the feed composition (2), +10% in both feed flow rate and composition (3) and +1% increase of setpoint (4)

In case of +10% F and +10% x_A disturbances illustrated by Figure 7, it can be observed that the composition profiles of MPC are identical in nature. However, these profiles are inverted for the PID controller in case of the same disturbances as seen in Figure 6. This demonstrates the ability of MPC to deliver a consistent performance. Such consistency would be valuable in actual plant operation to accommodate the resultant changes and their retentive effects over time. For example, in any case of the disturbances, one can expect the average value of the purity of toluene to be reduced over time if the MPC is in action.

Both PID and MPC control structures exhibit short settling time of less than 10 hours for all components. The performance of these controllers is compared in Figure 8, in terms of the integral absolute error (IAE) that conveniently accounts for both overshooting and settling times. IAE is defined here as the integral of the SP error (e) over the settling time period (t). Accordingly, MPC is the most stable control structure with low values of IAE. Moreover, the performance of MPC for set point tracking is excellent as clearly demonstrated by Figure 7.

This study proved that MPC based on linear prediction model is very well able to control the highly nonlinear DWC process. Although the application of nonlinear based controllers is appealing, only a minor improvement in the performance is expected because of the precise linearization of the nonlinear model. With today's powerful computational infrastructure and accurate linearization methods, a linearized model of the process can be updated on-line in the MPC controller's hardware. Any large changes in the operating points and capacity will require the re-linearization around the new nominal conditions in order to ensure the robustness of the controller. By approximating a nonlinear system as a family of affine systems, the analysis of the nonlinear system can be transformed into an analysis of several linear systems.

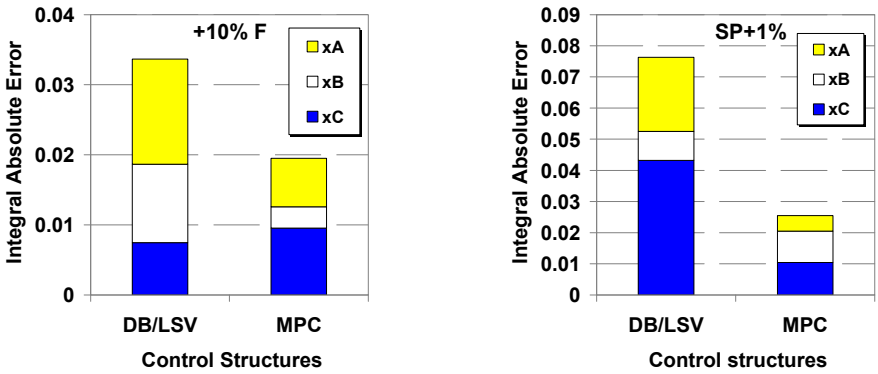

Figure 8. Comparison of controllers performance in terms of integral absolute error (IEA), at a persistent disturbance of +10% x_A in the feed composition (left), and +1% increase of the setpoint (right)

CONCLUSIONS

The full-size nonlinear model used for a DWC in this work, is truly representative of industrial applications. The quality of the linearized model used for the predictions inside MPC is derived from and tested against the full nonlinear model. The variables were selected to achieve the aim of regulatory and inventory control in the column, at the same time minimizing the energy requirements in a very simple, yet practical way. The optimal energy control is based on a simple strategy to control the heavy component composition at the top of the prefractionator side of the DWC by manipulating the liquid split. The performance of the MPC was effectively evaluated against a conventional PID control structure (DB/LSV) that was previously reported to be the best performing in DWC operation.

MPC delivers an outstanding overall performance in case of different industrially relevant disturbances and set point tracking. The integral absolute error (IEA) measured for MPC performance is the lowest. The major reason for this excellent feature of MPC is its ability to act simultaneously and consistently on all the manipulated variables when the disturbances are exerted. The consistent performance delivered by MPC can be very useful in actual plant operation to accommodate the resultant changes over time.

This study proves the ability of linear MPC to control a non-minimal phase and nonlinear process, such as DWC. The significant match in the open loop response of the linearized and nonlinear model suggests that nonlinear MPC is not expected to deliver a significantly better performance. The functionality of the proposed MPC control scheme demonstrated in this study provides an excellent platform for its easy transfer to other DWC applications, such as ternary separations.

ACKNOWLEDGMENTS

We thank Ben H. L. Betlem (University of Twente, NL) for the very constructive discussions. The financial support given by AkzoNobel to Rohit Rewagad, University of Twente, during his MSc internship is also gratefully acknowledged.

NOTATION

ABC – Ternary mixture of components A, B and C
BTX – Benzene-toluene-xylene
B – Bottoms product
D – Distillate stream
DWC – Dividing-wall column
F – Feed stream
H_T – Reflux tank level
H_R – Reboiler tank level

IEA – Integral absolute error
L – Liquid flow
MPC – Model predictive control
m – Control horizon
N_j – Tray number j
Q_C – Condenser duty
Q_R – Reboiler duty
PF – Pre-fractionator
PID – Proportional-integral-derivative controller
p – Prediction horizon
R – Reflux rate
r_L – Liquid split
r_V – Vapor split
S – Side stream
V – Vapor flow
w^v – Weight of variable *v*
x_i – Molar fraction of component *i* in liquid phase
y_i – Molar fraction of component *i* in vapor phase
Δk – Sampling time
τ – Time constant

REFERENCES

1. A. A. Kiss, H. Pragt, C. van Strien, Reactive Dividing-Wall Columns - How to get more with less resources?, *Chemical Engineering Communications*, **2009**, *196*, 1366.
2. R. Isopescu, A. Woinaroschy, L. Draghiciu, Energy reduction in a divided wall distillation column, *Revista de Chimie*, **2008**, *59*, 812.
3. L. Draghiciu, R. Isopescu, A. Woinaroschy, Capital cost reduction by the use of divided wall distillation column, *Revista de Chimie*, **2009**, *60*, 1056.
4. O. Yildirim, A. A. Kiss, E. Y. Kenig, Dividing-wall columns in chemical process industry: A review on current activities, *Separation & Purification Technology*, **2011**, *80*, 403.
5. F. B. Petlyuk, V. M. Platonov, D. M. Slavinskii, Thermodynamically optimal method for separating multicomponent mixtures, *International Chemical Engineering*, **1965**, *5*, 555.
6. G. Kaibel, Distillation columns with vertical partitions, *Chemical Engineering Technology*, **1987**, *10*, 92.
7. N. Asprion, G. Kaibel, Dividing wall columns: Fundamentals and recent advances*, Chemical Engineering & Processing*, **2010**, *49*,139.

8. I. Dejanovic, Lj. Matijasevic, Z. Olujic, Dividing wall column - A breakthrough towards sustainable distilling, *Chemical Engineering and Processing: Process Intensification*, **2010**, *49*, 559.
9. I. J. Halvorsen, S. Skogestad, Optimizing control of Petlyuk distillation: understanding the steady-state behaviour, *Computers & Chemical Engineering*, **1997**, *21*, 249.
10. I. J. Halvorsen, S. Skogestad, Optimal operation of Petlyuk distillation: understanding the steady-state behaviour, *Journal of Process Control*, **1999**, *9*, 407.
11. S. J. Wang, D. S. H. Wong, Controllability and energy efficiency of a high-purity divided wall column, *Chemical Engineering Science*, **2007**, *62*, 1010.
12. R. C. van Diggelen, A. A. Kiss, A. W. Heemink, Comparison of control strategies for dividing-wall columns, *Industrial & Engineering Chemistry Research*, **2010**, *49*, 288.
13. W. L. Luyben, M. L. Luyben, Essentials of process control, *McGraw-Hill*, **1997**.
14. M. Morari, J. H. Lee, Model predictive control: past, present and future, *Computers & Chemical Engineering*, **1999**, *23*, 667.
15. A. A. Kiss, S. P. Agachi, Model predictive control of temperature of a PVC emulsion process, *Hungarian Journal of Industrial Chemistry*, **1999**, *27*, 117.
16. E. F. Camacho, C. Bordons, Model predictive control, 2nd edition, *Springer*, **2004**.
17. S. Skogestad, I. Postlethwaite, Multivariable feedback control, Analysis and Design, 2nd Edition, John Wiley, **2005**.
18. P. S. Agachi, Z. K. Nagy, M. V. Cristea, A. Imre-Lucaci , Model based control: case studies in process engineering, *Wiley-VCH*, **2006**.
19. F. Lestak, R. Smith, The control of dividing wall column, Chemical Engineering Research & Design, **1993**, *71*, 307.
20. M. Serra, A. Espuña, L. Puigjaner, Control and optimization of the divided wall column, *Chemical Engineering and Processing*, **1999**, *38*, 549.
21. M. Serra, A. Espuña, L. Puigjaner, Study of the divided wall column controllability: influence of design and operation, *Computers & Chemical Engineering*, **2000**, *24*, 901.
22. M. Serra, M. Perrier, A. Espuña, L. Puigjaner, Analysis of different control possibilities for the divided wall column: feedback diagonal and dynamic matrix control, *Computers & Chemical Engineering*, **2001**, *25*, 859.
23. H. Ling, W. L. Luyben, New control structure for divided-wall columns, *Industrial & Engineering Chemistry Research*, **2009**, *48*, 6034.
24. A. A. Kiss, C. S. Bildea, A control perspective on process intensification in dividing-wall columns, *Chemical Engineering and Processing: Process Intensification*, **2011**, *50*, 281.
25. A. A. Kiss, R. R. Rewagad, Energy efficient control of a BTX dividing-wall column, *Computers & Chemical Engineering*, **2011**, *35*, 2896.
26. A. Woinaroschy , R. Isopescu, Time-optimal control of dividing-wall distillation columns, *Industrial & Engineering Chemistry Research*, **2010**, *49*, 9195.
27. R. Adrian, H. Schoenmakers, M. Boll, MPC of integrated unit operations: Control of a DWC, *Chemical Engineering & Processing*, **2004**, *43*, 347.

28. M. Kvernland, I. J. Halvorsen, S. Skogestad, Model Predictive Control of a Kaibel distillation column, *Proceedings of the 9th International Symposium on Dynamics and Control of Process Systems (DYCOPS)*, July **2010**, 539.
29. C. Buck, C.Hiller, G. Fieg, Applying model predictive control to dividing wall columns, *Chemical Engineering & Technology*, **2011**, *34*, 663.
30. A. Bemporad, M. Morari, N. L. Ricker, Model predictive control toolbox 3: User's guide, *The Mathworks Inc.*, **2009**.
31. R. R. Rewagad, A. A. Kiss, Dynamic optimization of a dividing-wall column using model predictive control, *Chemical Engineering Science*, **2012**, Article in press. DOI: 10.1016/j.ces.2011.09.022
32. A. A. Kiss, A. C. Dimian, P. D. Iedema, Don't gamble with physical properties of polymers, *Studia UBB Chemia*, **2009**, *54(2)*, 121.

STUDIA UBB CHEMIA, LVI, 2, 2011 (p. 19 - 27)

COMPARATIVE STUDY BETWEEN SINGLE STRENGTH JUICES AND COMMERCIAL NATURAL JUICES BY IRMS AND EPR

DANA ALINA MAGDAS[a], NICOLETA SIMONA VEDEANU[b], LAURA BOLOJAN[c], ROMULUS PUSCAS[a], GRIGORE DAMIAN[c]

ABSTRACT. Authenticity has probably always been a major concern of many consumers and it is still gaining more and more importance. In our study we used two analytical methods to characterize antioxidant activity and to evaluate the authenticity of juices; isotope ratio mass spectrometer (IRMS) and Electron Paramagnetic resonance (EPR). Isotope ratio mass spectrometry is a promising tool for origin assignation of food, thus ^{13}C, ^{18}O and ^{2}H measurements are intensively used in forensic study to prove product authenticity. This application has been particularly useful in food quality control, because it allows the detection of added sugar and water in fruit juices and in tracing the geographical origin of food. The obtained results have shown that the both commercial juices are authentic fruit juices with no exogenous water and no addition of C_4 sugar, according to those labels. Antioxidant properties of commercially-available ground and instant coffees were investigated by means of electron paramagnetic resonance (EPR) using as oxidants, 4-hydroxy-2,2,6,6-tetramethylpiperidine N-oxyl (TEMPOL)

Keywords: *Fruit juice, antioxidants, Stable isotopes, EPR spectroscopy, Tempol*

INTRODUCTION

The study of antioxidant capacity of different fruits, juice and vegetables has prompted research in the fields of food science and human health, paying an important role in reducing the risk of degenerative diseases such as cardiovascular disease, various cancers and neurological diseases. In this context, the spectroscopic and spectrometric methods for the determination of the antioxidants activity of natural sources for different types of foods and extracts are important tools in development of efficient extraction procedures.

[a] *Institutul National de Cercetare-Dezvoltare pentru Tehnologii Izotopice si Moleculare, Donath, Nr. 65-103, RO-400293 Cluj-Napoca, ROMANIA, amagdas@itim-cj.ro*

[b] *Universitatea de Medicina si Farmacie ''Iuliu Hatieganu'', Departamentul de Biofizica, Str. Pasteur Nr.6, RO-400349, Cluj-Napoca, ROMANIA*

[c] *Universitatea Babeş-Bolyai, Facultatea de Fizica, Str. Kogălniceanu, Nr. 1, RO-400084 Cluj-Napoca, ROMANIA*

At the same time, the antioxidant activity of natural source has a great importance in selecting effective antioxidant extracts to be used in foods and nutritional supplements.

On the other hand, fruit juice quality and authenticity determination is an important research subject with significant relevance for industry, food safety and consumer protection. Unscrupulous companies and traders seek substantial benefits using adulterated juices to gain market advantage by using sugars, syrups, raw materials or false label indications for consumers. Adulteration of a product consists in making it impure by fraudulent addition of a foreign or inferior substance. The result is either an alteration of the product and of its quality or a falsification. The falsification is a voluntary act with the intention of abuse. The falsification may be more or less sophisticated and its sophistication as well as its costs increases with the improvement of analytical methods [1].

In our study we used two analytical methods to characterize antioxidant activity and to evaluate the authenticity of juices; isotope ratio mass spectrometer (IRMS) and Electron Paramagnetic resonance (EPR).

The isotope ratio mass spectrometer (IRMS) allows the precise measurement of mixtures of stable isotopes, measuring isotopic variations arising from mass-dependent isotopic fractionation in natural systems

Each plant has its own unique pattern of naturally occurring stable isotopes of carbon (^{12}C, ^{13}C), hydrogen (^{1}H, ^{2}H) and oxygen (^{16}O, ^{18}O), whose distribution has been influenced by a number of physical and/or biochemical properties and geoclimatic conditions.

Determination of $\delta^{18}O$ and $\delta^{2}H$ values of water from fruit juices is today applied in routine analysis as an automated and acknowledged method in order to differentiate between directly pressed and rediluted single strength juices. The principle consists in the fact that authentic juices have elevated $\delta^{18}O$ and $\delta^{2}H$ content of water as compared to water from rediluted products made using tap water which is relatively depleted in heavy oxygen and hydrogen isotopes [2].

Photosynthetic CO_2 assimilation via the C_3, C_4 and CAM pathways is of major importance in the use of carbon stable isotope ratio analysis in food authenticity control. The detection of commercial C_4 cane or corn derived sugar syrups in C_3 agricultural products is thus facilitated by characteristic differences in $\delta^{13}C‰$ values. The technique is necessarily comparative, as it must take into account the natural variation of $\delta^{13}C$ values in authentic products due to environmental factors such as water availability and light intensity [3].

The antioxidant activities of studied juice samples were followed by means of EPR spectrometer EMX monitoring of the radical concentrations of the oxidant 4-hydroxy-2,2,6,6-tetramethylpiperidine N-oxyl (TEMPOL) after the addition of the juice drinks.

In this study two single strength juices (one apple juice and one grape juice) were compared with other two commercial fruit juices (one apple juice and one grape juice), in order to check the correct labeling of present on Romanian market, using stable isotope measurements (oxygen, hydrogen and carbon) and EPR spectroscopy.

RESULTS AND DISCUSSION

Isotope ratio mass spectrometer (IRMS)

Vacuum concentration with aroma does not affect the chemical composition of fruit juices and therefore the determination of deuterium (D) and oxygen-18 (^{18}O) content in waters is the most reliable procedure for differentiating between a natural single strength juice and a juice rediluted from concentrate. The (IRMS) technique is based on the fact that when absorbed by a plant, the rainwater or the irrigation water is fractionated by evapotranspiration [4,5], and enriched in the heavy isotopes (deuterium and oxygen-18) with respect to the light isotope (hydrogen and oxygen-16). It is known that climatic conditions affect the isotope content of rainwaters and therefore that of fruit juices waters: the warmer climate, the higher the deuterium and oxygen-18 contents of water [2]. Rainwater and tap water have nearly the same isotopic content and the water of fruit juices derived from concentrate by dilution with tap water has an isotopic content close to that of tap water. This makes it easy to distinguish diluted concentrates from the isotopically more enriched water of authentic single strength juice [2].

The variation of $\delta^{18}O$ values in water of authentic apple single strength juice from central Europe (Germany, Italy, Belgium, Poland, Austria, Hungary and the Czech Republic) for the seasons 1991-1994 obtained by Rossmann [6], have featured a relatively large range of variation, with a mean value of about -4‰. In our study we obtained for the single strength apple juice, made from apple from Transylvania, values of $\delta^{18}O$ =-5.52‰ and δD=-51.7 ‰, very close to those obtained for commercial apple juice ($\delta^{18}O$ =-5.24‰ and δD=-49.3‰), meanwhile the isotopic values obtained for lab water (tap water) were $\delta^{18}O$ = -10.78‰ and δD = -76.5‰, respectively (Table 1). From these results we can conclude that the commercial apple juice is authentic apple juice with no exogenous water, according to its label. Also, for the grape commercial juice the isotopic analysis we obtained $\delta^{18}O$ = 0.95‰ and δD = -16.5‰, have shown that this juice does not contain exogenous water. Its isotopic values are even more positive than the isotopic values that we obtained for grape single strength juice. The explanation consists in the fact that the grapes that were used in preparation of investigated juices come from different geographic regions.

Depending on their origin, sugars added are divided into two types: C_3 and C_4. Sugars naturally occurring in apples and grapes juices belong to the C_3 type, while cane sugar and sugars produced from the hydrolysis of maize starch are of the C_4 type.

Table 1. Oxygen, hydrogen and carbon stable isotope data for investigated samples

Sample number	Type of sample	$\delta^{18}O_{vs\ SMOW}$ (‰)	$\delta D_{vs\ SMOW}$ (‰)	$\delta^{13}C_{vs\ PDB}$ (‰)
1.	Apple single strength juice	-5.52	-51.7	-30.2
2.	Grape single strength juice	-0.99	-35.4	-28.8
3.	Commercial apple juice	-5.24	-49.3	-27.4
4.	Commercial grape juice	0.95	-16.5	-25.9
5.	Tap water	-10.78	-76.5	-

Generally, C_4 plants, have $^{13}C/^{12}C$ isotopic ratios, referred to as $\delta^{13}C$ values, ranging between -8 and -13‰, whereas C_3 plants, have values between -22 and -30‰. An addition of C_4 sugars in apple and grape juices would result in a higher value of $\delta^{13}C$. The results obtained by Rumel et al. [7] for approximately 150 authentic orange juices shown that the mean value $\delta^{13}C$ of investigated samples are varying between (-29‰ to -23‰). Such differences in $\delta^{13}C$ values due to environmental factors were reported by different authors for orange juices. For apple juices Doner et. al. [8] observed that the mean $\delta^{13}C$ value of juices from different varieties of apples and cultivated in different geographical locations was around -25.4‰, with no significant correlation between the variety of apple or geographical origin.

For our investigated samples, the obtained $\delta^{13}C$ value is typical for C_3 plants, with no evidence about a possible adulteration with C_4 sugars. The differences in $\delta^{13}C$ values that appear here are more probably due to environmental factors than to the apple or grape variety.

EPR spectroscopy

The nitoxide radicals are relatively stable towards oxidation but they can be easily reduced to the corresponding hydroxylamines. The standard redox-potential of piperidine nitroxide derivatives (E_0=0.2eV is high enough to oxidise biological compounds such as polyphenolics, ascorbic acid, semiquinones and superoxide radicals [9-12]. Thus, when mixing a nitroxide radical with an antioxidant-containing juice, the number of paramagnetic species decreases in time with different rates, depending on the sort of juice. Recording the EPR signal decay caused by the reaction with natural or artificial reductants

or with products of metabolic reactions, it is possible to draw conclusions about antioxidant capability. An important constituent of the antioxidant complex of apples and grapes is the ascorbic acid. This vitamin is a versatile, water-soluble, donor, antioxidant. The chemical instability of vitamin C is due to the fact that it is a strong reducing agent and can be deactivated by a wide range of oxidizing agents [13].

The intensity of the EPR signal in experimental samples was found to decrease in time and was correlated to the total content of polyphenols and vitamins (Figures 1 and 2)

The rate of reaction between antioxidant compounds and Tempol was monitored based on the normalized double integrated residual EPR signal, which is in turn correlated with number of paramagnetic species in time (Figures 3 and 4). The decrease of relative concentration of the paramagnetic species in time was fitted to an exponential function [10]: $I(t) = I_0 + a\,e^{(-k\,t)}$ where I_0 and a are parameters depending on the experimental conditions [14,15]. The antioxidant nature, expressed by kinetic reduction constant (k) is a fingerprint of authenticity of juices or antioxidant compounds.

Figure 1. EPR spectra of Tempol at different time of incubation in fresh apple juice

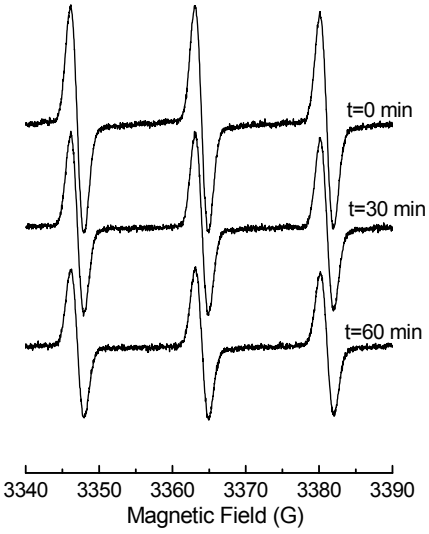

Figure 2. EPR spectra of Tempol at different time of incubation in fresh grape juice

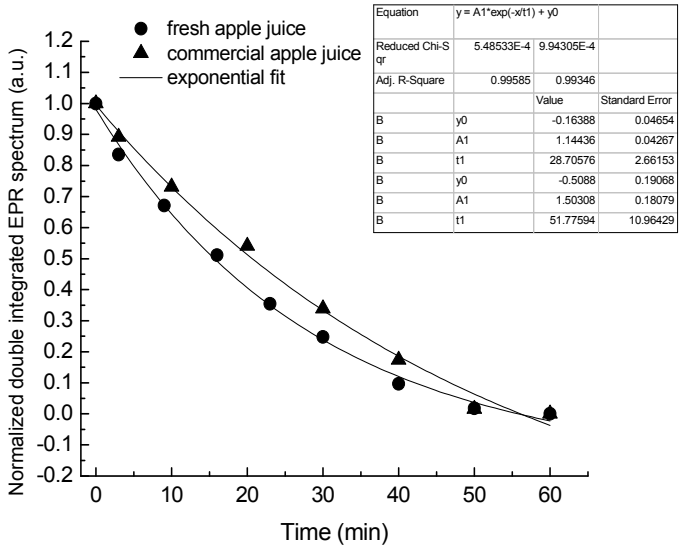

Equation	y = A1*exp(-x/t1) + y0		
Reduced Chi-Sqr	5.48533E-4	9.94305E-4	
Adj. R-Square	0.99585	0.99346	
		Value	Standard Error
B	y0	-0.16388	0.04654
B	A1	1.14436	0.04267
B	t1	28.70576	2.66153
B	y0	-0.5088	0.19068
B	A1	1.50308	0.18079
B	t1	51.77594	10.96429

Figure 3. Normalized double integrated EPR spectra for fresh and commercial apple juice in function of time

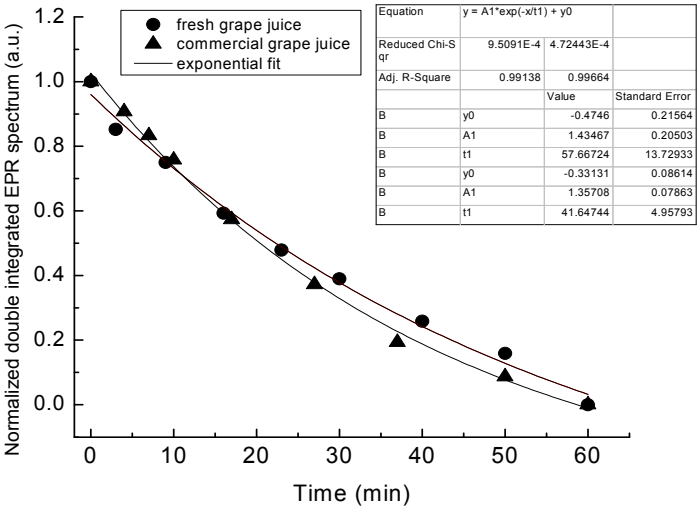

Equation	y = A1*exp(-x/t1) + y0		
Reduced Chi-Sqr	9.5091E-4	4.72443E-4	
Adj. R-Square	0.99138	0.99664	
		Value	Standard Error
B	y0	-0.4746	0.21564
B	A1	1.43467	0.20503
B	t1	57.66724	13.72933
B	y0	-0.33131	0.08614
B	A1	1.35708	0.07863
B	t1	41.64744	4.95793

Figure 4. Normalized double integrated EPR spectra for fresh and commercial apple juice in function of time

Comparing the antioxidant characteristics of fresh apple juice with the commercial apple juice we may say that fresh apple juice has the most significant antioxidant character (k_{fresh}=0.02, $k_{commercial}$=0.035). A similar situation was found in the case of grape juice;(k_{fresh}=0.017, $k_{commercial}$=0.024). In terms of antioxidant activity, it can be concluded that the studied juices have similar quality fresh juices.

Although there is a small difference in the antioxidant activity of fresh apple juice and commercial apple juice and between fresh grape juice and fresh grape juice, respectively, it can be said that EPR method together with MS suggests that the two commercial juices are authentic fruit juices.

CONCLUSIONS

In this study two single strength juices (one apple juice and one grape juice) were compared with other two juices commercial fruit juices (one apple juice and one grape juice), in order to check the correct labeling of present on Romanian market were investigated by the mean of stable isotope measurements (oxygen, hydrogen and carbon).

The obtained results have shown that the both commercial juices are authentic fruit juices with no exogenous water and no addition of C4 sugar, according to those labels.

Under antioxidant activity studied by EPR spectroscopy, it can be concluded that the studied juices have similar quality fresh juices.

EXPERIMENTAL SECTION

1. Sample preparation

For oxygen-18 determination 5 ml of raw juice (neither centrifuged nor filtered) was equilibrated with CO_2 for 15 hours according to the CEN:ENV 13141:1997 method at 25±0.1^{0}C [2]. The carbon dioxide was then extracted and purified. For the hidrogen analysis a distillation under static vacum was performed by using Rittenberg „trausers” on 2-3 ml of fruit juice, always with the quantitative recovery of the water [16].

For $\delta^{13}C$ analysis, the separation and purification of the pulp was made according to [17-18] by the separation of a sample of about 50ml of fruit juice by centrifugation (10 min at 1400 times g) from the pulp. The pulp was then re-suspended in water (50 ml), mixed thoroughly, centrifuged (10 min at 1400 times g) and the supernatant was discarded. Then, the washing process was repeated once with water and twice more with acetone and the resulted precipitate was dried under vacuum. The obtained dried solid was homogenized by mixing it with a spatula.

2. Isotope measurements

The procedure of IRMS consists in measuring the isotope ratio of an analyte converted into a simple gas, isotopically representative of the original sample, before entering the ion source of an IRMS [4]. The ^{18}O isotopic contents of the water samples were then analyzed using a stable isotope ratio mass spectrometer IRMS (Delta V Advantage, Thermo Scientific). For δ^2H the equipment used was a Liquid-Water Isotope Analyzer (DLT-100, Los Gatos Research).The results of our ^{18}O and ^{2}H analyses of the fruit juices are reported using conventional δ notation relative to the Vienna-Standard mean Ocean Water (V-SMOW) standard (i.e. δ (‰)= $[(R_x/R_S)-1]x1000$, where R_x is the $^{18}O/^{16}O$ or $^{2}H/^{1}H$ isotopic ratio of the water sample and R_S is the $^{18}O/^{16}O$ or $^{2}H/^{1}H$ isotopic ratio of the V-SMOW standard.

The measurements of $\delta^{13}C$ from pulp fruit were carried out on an Elemental Analyser (Flash EA1112 HT, Thermo Scientific), coupled with an isotope ratio mass-spectrometer IRMS (Delta V Advantage, Thermo Scientific). NBS-22 oil with a certified value of -30.03‰ vs. PDB (Pee Dee Belemnite) was used as standard. The analytical reproducibility was ±0.1‰ for $\delta^{13}C$, ±0.1‰ for $\delta^{18}O$ values and ±0.6‰ for $\delta^{2}H$ values.

3. EPR measurement

1mM water TEMPOL solution was added to 2 ml of juices. The homogenized solution was injected with a Hamilton microsyringe into a quartz capillary of about 10 cm length and an interior diameter about 1 mm. EPR measurements were performed on a Bruker EMX spectrometer operating at 9.4548 GHz with 100 kHz modulation frequency, at room temperature. The reaction mixture-containing 20 µl capillary was then positioned in the standard cavity TE102 (Bruker Instruments, ER 4102ST). The sample was scanned using the following parameters: center field, 3510 G; sweep width, 60 G; power, 2 mW; receiver gain, 1×10^3; modulation amplitude, 2 G; time of conversion, 30 ms; time constant, 61.4 ms; number of scans, 1. The spectra were recorded at different time intervals. The integral intensities of EPR spectra were obtained by evaluating their double integrals (DIEPR) using the WIN EPR program (Bruker).

ACKNOWLEDGMENTS

"This work was supported by the PN II (2007-2013) Program, Contract no.TE 120/2010."

REFERENCES

1. M. S. Murthy, B. R. Harish, K. S. Rajanadam, K. Y. Ajoy Pavan Kumar, C*hemical Engineering Science*, **1994**, *49*, 2198.
2. L. J. Jackman, "Applications of Nuclear Magnetic Resonance Spectroscopy in Organic Chemistry", Pergamon Press, Inc., New York, **1959**, chapter 4.
1. J. Yinon, “Advances in Forensic Applications of Mass spectrometry”, CRC Press, **2004**, chapter 4.
2. J. Koziet, A. Rossmann, G. J. Martin, P. Johnson, *Analytica Chimica Acta,* **1995**, *302*, 29.
3. S. D. Kelly “Using stable isotope ratio mass spectrometry in food authentication and traceability”, Woodhead Publishing, Cambridge, UK, **2003**, chapter 7.
4. M. H. O’Leary, “Stable isotopes in the biosphere” Kyoto University Press, Japan, **1995**, chapter 3.
5. J. Bricout, *Rev. Cytol. Biol., Veget.-Bot.,* **1978**,*1*,133.
6. A. Rossmann, *Food Reviews International*, **2001**,*17*(3), 347-381.
7. S. Rumel, S. Hoelzl, P. Horn, A. Rossman, C. Schlicht, *Food Chemistry,* **2010**,*18*, 4, 890.
8. L.W. Doner, H. W. Kreuger, R. H. Reesman, *Journal of Agricultural and Food Chemistry*, **1980**, *28*, 362.
9. Kocherginsky VN., Swartz H., *Nitroxide Spin Labels: Reaction in Biology and Chemistr*y, CRC Press, Boca Raton, 1995.
10. D. Petrisor, G. Damian, S. Simon, A. Hosu, V. Miclaus, *Mod. Phys. Letters B,* **2008**, *22*/27, 2689.
11. M. Victor, J. McCreath, M. Rocha, *Recent patents on Anti-Infective Drug Discovery,* **2006**, *1*, 17.
12. R. A. Larson, Naturally Occuring Antioxidants, CRC, Boca Raton, USA, **1997**.
13. A. J. Stewart, W. Mullen, A. Crozier, *Molecular Nutrition and Food Research,* **2005**, *49*, 52.
14. A. Hosu, C. Cimpoiu, V. Miclaus, G. Damian, I. Tarsiche, N. Pop, *Not. Bot. Hort. Agrobot. Cluj,* **2010**, *38*/1, 1842.
15. I. D. Postescu, C. Tatomir, G. Chereches, I. Brie, G. Damian, D. Petrisor, A-M. Hosu, V. Miclaus, A. Pop, Spectroscopic characterization of some grape extracts with potential role in tumor growth inhibition, *Journal of Optoelectronics and Advanced Materials*, **2007**, *9*(3), 564-567.
16. A. Nisselbaum, A. Lifshitz, Y. Stepak, *Lebensmittel-Wissenschaft und-Technologie,* **1974**, *7*, 152.
17. T. P. Coultate, “Food - The chemistry of its components”, Cambridge: Royal Society of Chemistry, **1990**, chapter 6.
18. R. Goyer, *American Journal of Clinical Nutrition*, **1995**, *61*, 646.

STUDIA UBB CHEMIA, LVI, 2, 2011 (p. 29 - 37)

THE ELECTROCHEMICAL BEHAVIOR OF [$Cu_2(DH)_4$ γ,γ-BIPY] BY CYCLIC AND ADSORPTIVE STRIPPING VOLTAMMETRY

TATIANA CAZAC[a], EDUARD COROPCEANU[a], ROBERT SĂNDULESCU[b], LILIA CROITOR[c]

ABSTRACT. The electrochemical behavior of the [$Cu_2(DH)_4$γ,γ-bipy], (where DH is the monoanion of α,α'-dimethylglyoxime and γ,γ-bipy represents 4,4'-dipyridyl) was investigated for the first time by cyclic voltammetry and stripping cathodic voltammetry on the mercury drop electrode. The influence of some experimental parameters (pH, scan rate, concentration and electrolytic medium) on the electrochemical behavior of the complex has been examined as well. It has been established that the electrochemical reduction of [$Cu_2(DH)_4$γ,γ-bipy] is an adsorption controlled and irreversible process. The linear dependence of cathodic peak current and the concentration of [$Cu_2(DH)_4$γ,γ-bipy] has been elucidated.

Keywords: *cooper complexes, α,α'- dimethylglyoxime, 4,4'-dipyridyl, stripping voltammetry, cyclic voltammetry*

INTRODUCTION

The highly sensitive methods which allow determining the very low substance concentrations till trace level play a distinct role in solving the problems of state and dynamics evaluation of pollution, as well as in highlighting the main pollution sources of air, natural waters, rivers and soil. Investigation of the new adsorptive accumulation agents of chemical species, especially heavy metals and elaboration on its basis of the new adsorptive voltammetric methods with cathodic stripping (AdSCV) constitute the main protocol, by which the above-mentioned results can be obtained, thus presenting both theoretical and practical interest.

[a] *Institute of Chemistry, Academy of Sciences of the Republic of Moldova, 3 Academy Street, MD-2028, Chişinău, cazac_t@yahoo.com*
[b] *"Iuliu Haţieganu" University, Faculty of Pharmacy, Analytical Chemistry Dept., 4 Pasteur Street, 400349, Cluj-Napoca, Romania*
[c] *Institute of Applied Physics, Academy of Sciences of the Republic of Moldova, 5 Academy Street, MD-2028,Chişinău*

The elaboration of analytical dosage methods for biologically active organic compounds remains one of the contemporary problems of great interest for numerous research teams in the field of environment protection. Application of the adsorptive voltammetry with cathodic stripping from the arsenal of electrochemical methods allows preconcentration of the analytes's traces and furthermore, their quantification. Dioximes were used to determine cobalt traces in the analysis of extrapure metals. α-Benzyldioxime was employed by Bobrowski and Bond [1] to determine cobalt traces in the presence of high concentrations of zinc and their results have showen that even 10^6 – 10^7 times greater zinc concentrations tolerated the cobalt determination.

High sensitivity of the method with cathodic stripping in the case of α,α'-dimethylglyoxime for nickel and cobalt determination has been used in many investigations. Using a large range of voltammetric techniques, Dragic et al. [2] showed that the reduction process of the nickel dimethylglyoximate in ammonia solutions takes place with a consumption of 16 or 18 electrons. Feng et al. [3] have studied in detail the mechanism of the same process at pH 9 and optimised the experimental conditions for determination.

Donat et al. [4] have proposed the cobalt and nickel dosage at picomolar level in the presence of 1,2-cyclohexandiondioxime by differential pulse voltammetry. The greatest sensitivity was reached when the concentration of accumulation agent was 10^{-4} M, pH 7.6 and the adsorption potential -0.60 V. The selective feature of the process permits the use of a 15 minutes period of adsorption, which ensures the determination of 6 pM and 0.45 nM concentrations for cobalt and nickel, respectively.

It is well-known that dimeric compounds at dimethylglioxime containing different ligands show interesting biological activities [5] . Thus, deepening the knowledge in this field represents a perspective direction at investigations.

The current study is dedicated to study of the electrochemical behaviour of $[Cu_2(DH)_4\gamma,\gamma$-bipy] in order to elucidate the optimal experimental conditions for its quantitative determination by cathodic stripping voltammetry.

The structure of the complex is depicted as follows:

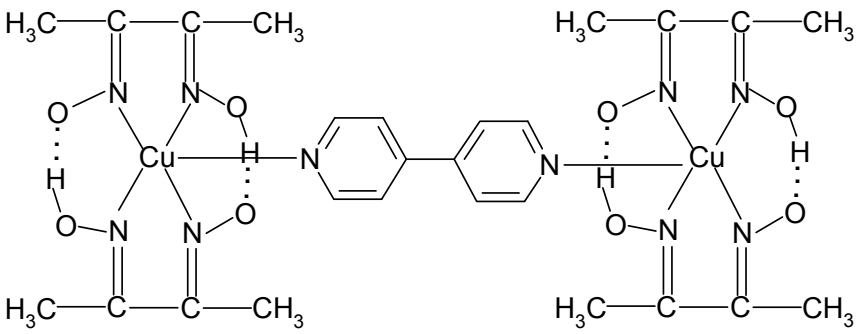

RESULTS AND DISCUSSIONS

In IR (nujol) spectrum of the complex we attributed the absorption bands of valence and deformation oscillations as follows: $\nu_{as}(CH_3)$ 2945 cm^{-1}, ν(C=N) 1563 cm^{-1}, $\delta_{as}(CH_3)$ 1424 cm^{-1}, $\delta_s(CH_3)$ 1359 cm^{-1}, ν_{as}(N-O) 1219 cm^{-1}, ν_s(N-O) 1087 cm^{-1}, γ(OH) 977 cm^{-1}, δ(CNO) 742 cm^{-1}, ν_{as}(Cu-N) 484 cm^{-1}, which proves the coordination of two dioxime radicals in trans position. The signals at 3030 and 1603 cm^{-1} were attributed to the pyridine ring of the bridge ligand.

The absorption band at 230 nm obtained in **the UV-Visible spectrum** characterizes the charge transfer from the metal to the chelate ring and corresponds to the $Cu(DH)_2$ group. The band at 275 nm indicates on the presence of coordinated 4,4'-bipyridyl.

The detailed results on elemental analysis, IR and UV-visible spectral data have been recently reported in a previous paper [7].

The voltammetric investigation of the [$Cu_2(DH)_4$γ,γ-bipy] complex illustrates its property of adsorption and reduction on mercury drop electrod surface. The voltammogram of the investigated reagent showed that the mentioned reduction takes place at -0.28 V and respectively, -1.20 V potentials (Figure 1,curve 1). It was noticed that the addition of copper ions does not increase the analytical signal. By contrary, the addition of the studied complex solution produced an increase of the reduction current, which varies proportionally with the concentration. This fact, determined us to conclude that the reduction process involved the ligand from the complex, and consists in the reduction of $[Cu(HD)_2]^0$ to $[Cu(D)_2]^{2-}{}_{ads}$ and not Cu^{2+} to Cu^0.

After the investigation of the electrochemical behaviour of [$Cu_2(DH)_4$γ,γ-bipy] by cyclic voltrammetry (Figure 2) the same well-defined reduction peak at -0.28V potential has been put into evidence. This served as a conclusive indication about the irreversible nature of the process that takes place on the electrode. It was established that after the adsorption processthe anion $[Cu_2(DH)_2]^{2-}$ is reduced on mercury drop. The cyclic voltammograms for copper dimethylglioxymate present a single reduction peak at -0.24V and γ,γ-bipy at -0.95V, respectively, the nature of the processes being dominated by diffusion. The complex formation with the two components strongly facilitates the adsorbtion of copper dimethylglioxymate on mercury drop surface.

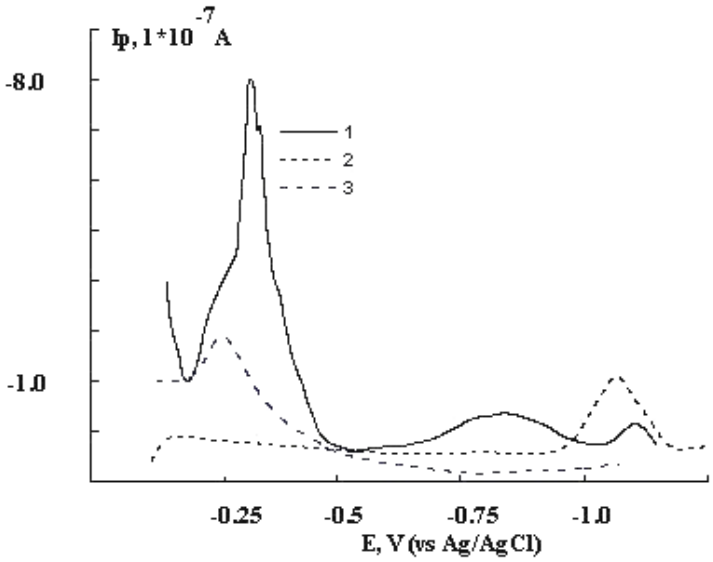

Figure 1. Square wave voltammogram of: 1- $[Cu_2(DH)_4\ \gamma,\gamma\text{-bipy}]\ 5\cdot10^{-5}$M in 0.1M KCl, 2- γ,γ-bipy $5\cdot10^{-5}$M in 0.1M KCl, 3- DMG $5\cdot10^{-5}$M in 0.1M KCl, pH 5.2 (E_{in} -100mV, E_{fin} -1260mV, $t_{el.}$ 10s, step.dur. -0.2s, step.apl. 10 mV, puls ampl. -50mV)

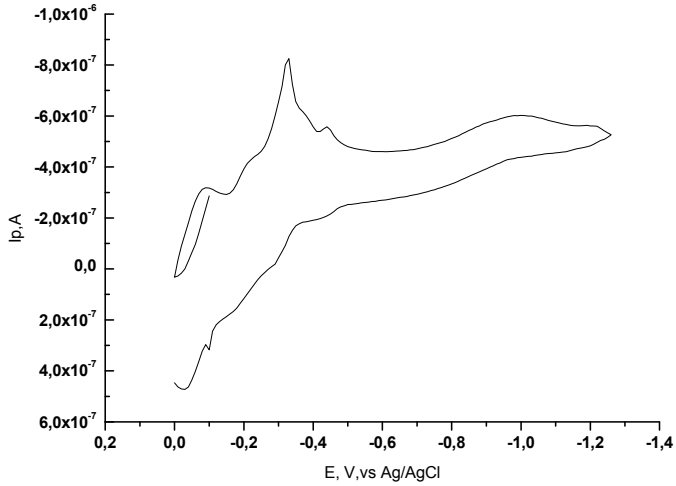

Figure 2. Cyclic voltammogram of $[Cu_2(DH)_4\gamma,\gamma\text{-bipy}]\ 5\cdot10^{-5}$ M in 0.1M KCl, pH 5.2 (WE – HMDE; RE – Ag/AgCl,(3 M KCl); AuxE Pt wire; E_{in} 0 mV, E_{fin} -1260mV, $t_{el.}$ 10s, step.dur. 0.2s, step.apl. 10 mV, puls ampl. -50mV; 20^{o} C)

The slope of the regression line, in lgI_p/lgv coordinates, determined from the investigation of the influence of the scan speed (v) on the peak current (I_p), representing the speed coefficient "X", was found to be 0.83 and 0.46 for the first and the second reduction reactions, respectively (Figure 3). The value of the experimentally obtained speed coefficient for the reduction peak at -0.28 V characterizes the electrode electrochemical processes followed by the adsorption of depolarizer on the surface of the mercury electrode (y_1), while in the case of the drop at -1.15V a diffusion process (y_2) is clearly distinguished.

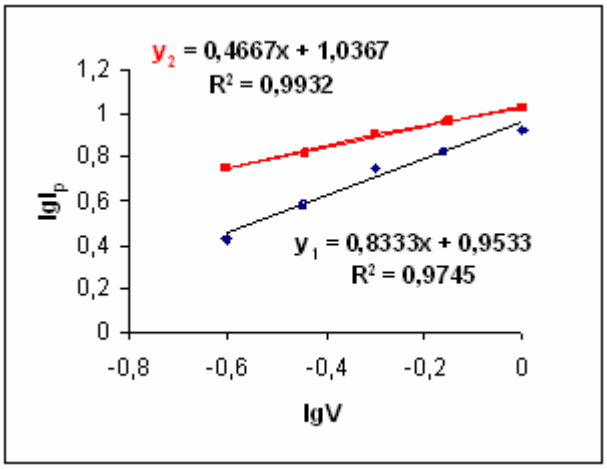

Figure 3. The slope of the regression line in lgI_p/lg V coordinates ([$Cu_2(DH)_4$ γ,γ-bipy] $5 \cdot 10^{-5}$ M in 0.1M KCl, pH 5.2; WE - DME; RE - Ag/AgCl,(3 M KCl); AuxE - Pt wire; 20° C).

The nature of the peak has been estimated from the value of the Semerano coefficient: when the slope lgI/lgV has a value close to 1, the adsorption process occurs, when it is less than 0.5, a kinetic process is involved and a value between 0.5 and 0.7 indicates on a diffusion process, accompanied by adsorption [6].

In order to demonstrate the origin of the reduction peak at -0.28 V, the voltammograms in the solutions for each separate compound of the complex were recorded. As a result, it has been concluded that this peak belongs to α,α'-dimethylglyoxime. Another points to be mentioned regard the diffusion character of the process on the surface of the mercury drop in comparison with the fact that complexation with 4,4'-bipyridyl facilitates the adsorption of α,α'-dimethylglyoxime on the drop of mercury.

An additional indication on the adsorbtive nature of the above-described process is proved by the variation curves of the current, according to the applied potential on the electrode (Figure 4). These curves demonstrate that in solution containing $[Cu_2(DH)_4\gamma,\gamma\text{-bipy}]$, the dropping time is smaller (Figure 4, curve 2) if compared to control sample of 0.1M KCl solution (curve 1).

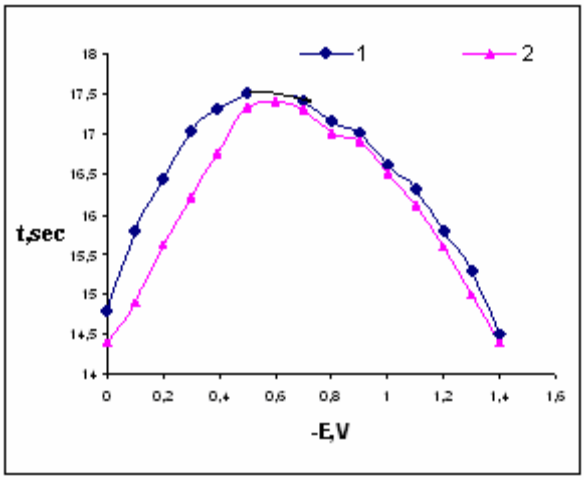

Figure 4. The variation of dropping time according to the applied potential on the electrode in solution: 1) KCl 0,1 M; 2) KCl 0,1 M + $[Cu_2(DH)_4\gamma,\gamma\text{-bipy}]$ $5\cdot10^{-5}$ M (WE - DME; RE - SCE; AuxE - Pt wire; scan rate 1 V s^{-1}; 20° C).

This phenomenon points again on the adsorption of the depolarizing compound at the surface of the mercury drop. Obviously, the ascending branch of curve 2 (Figure 4) characterizes the stronger adsorption on the mercury drop that can occur due to the presence of an electrochemically active particle of anionic nature [8-10]. This can be represented by the following equations of reactions:

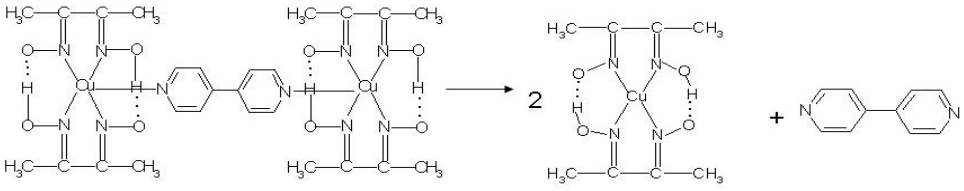

$$[Cu(HD)_2]^0 + 2H^+ + 4e \rightarrow [Cu(D)_2]^{2-}_{ads} + 2H_2$$
$$2H^+ + 2e \rightarrow H_2$$

The fact that the process on the electrode is controlled by the concentration of hydrogen ions is also certified by the investigation of the dependence of the current and the reduction potential by the pH value of the solution. In the pH area from 1.0 to 4.5 a variation of the current and the reduction potential is distinguished. At higher pH values than 4.5 the reduction potential of the reagent moves from -0.28 to -0.48 value (Figure 5).

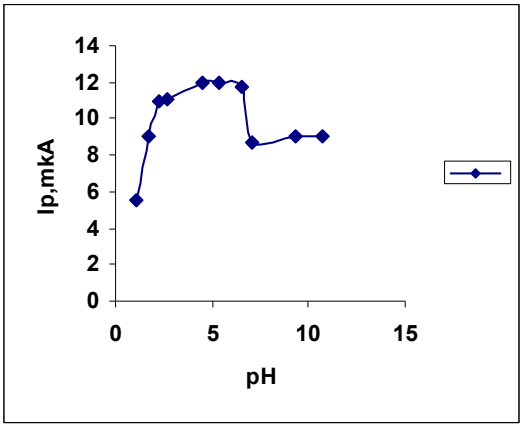

Figure 5. The dependence of the reduction current (Ip) by the pH (E_{in} -100mV, E_{fin} -1260mV, $t_{el.}$ 10s, step.dur. -0.2s, step.apl. 10 mV, puls ampl. 50mV)

The presence in solution of Zn(II), Co(II), Cr(VI), Ni(II), Mn(II), V(V), Al(III), Pb(II), Cd(II) species does not alter the value of the reduction curent of [$Cu_2(DH)_4$γ,γ-bipy] in the cases when the ratio between complex and interferent cation does not exceed 1:10. The presence of I^-, Br^-, SCN^-, CH_3COO^- anions in solution, in ratio A^- : complex of 10:1 does not influence on the value of the reduction current (Table 1).

Table 1. The influence of interferents on reduction current and potential of [$Cu_2(DH)_4$γ,γ-bipy]

Interferent	Ip, nA	E, V vs (Ag/AgCl)
[$Cu_2(DH)_4$γ,γ-bipy]	780.0	-0.28
Zn(II)	780.00	-0.30
Co(II)	783.08	-0.29
Cr(VI)	779.62	-0.28
Ni(II)	783.00	-0.28
Mn(II)	783.08	-0.28
V(V)	779.98	-0.30
Al(III)	785.56	-0.28

Interferent	Ip, nA	E, V vs (Ag/AgCl)
Pb(II)	778.32	-0.26
Cd(II)	782.34	-0.26
I^-	791.00	-0.28
Br^-	787.96	-0.28
SCN^-	783.28	-0.28
CH_3COO^-	786.65	-0.28

CONCLUSIONS

For the first time the electrochemical behavior of [$Cu_2(DH)_4$ γ,γ-bipy] by cyclic and adsorptive stripping voltammetry has been investigated. The reduction of [$Cu_2(DH)_4\gamma,\gamma$-bipy] complex on the surface of the drop mercury electrode is an irreversible, adsorbtion-controlled process. A well-defined reduction peak at -0.28V characterize this process. The influence of pH, complex concentration, accumulation time, applied potential and interferent ions has been studied in detail. Consequently, the optimal experimental conditions have been developed.

The reduction current Ip shows a linear relationship with [$Cu_2(DH)_4\gamma,\gamma$-bipy] concentration in the range 10^{-6}M - 10^{-5}M.

EXPERIMENTAL

Apparatus and materials

Elemental analyses were performed on an Elementar Analysen systeme GmbH Vario El III. The IR spectra were obtained in nujol on a FT IR Spectrum-100 Perkin Elmer spectrometer in the range 400-4000 cm^{-1}. Absorption spectra were recorded on a UV-VIS Lambda 25 Perkin Elmer spectrometer.

The voltammetric investigations were performed with a Polarograph POL 150 (France), in a cell with three electrodes, the working electrode was the hanging mercury drop electrode (HMDE), a counter electrode of platinum and Ag/AgCl as a reference electrode.

The values of pH were measured with a pH-meter CONSORT C931 (Belgium).

The stock solutions were prepared by dissolving the weighted sample of [$Cu_2(DH)_4$ γ,γ-bipy], KCl, KI, KSCN, nitrates of Zn(II), Co(II), Cr(VI), Ni(II), Mn(II), Al(III), Pb(II), Cd(II), $NaVO_3$ (SIGMA-ALDRICH, 50 mg), sodium acetate (Chimiopar), hydrochloric acid and sodium hydroxyde (PAM Corporation) in bidistilled water (Fistrum International Ltd). Working solutions were prepared by diluting the initial solutions and deaerated by nitrogen flow for 5 minutes. The accumulation of depolarizer on the electrode surface was performed in conditions of stirring the solutions.

Synthesis of [$Cu_2(DH)_4$(γ,γ-bipy)]: To a solution formed from $Cu(CH_3COO)_2 \cdot H_2O$ (Sigma-Aldrich, 200 mg, 0.001 mol) and 20 ml water α,α'-dimethylglyoxime (Sigma-Aldrich, 230 mg, 0.002 mol) dissolved in 25 ml methanol was added and 4,4'-dipyridyl (Sigma-Aldrich, 40 mg, 0,0005 mol) dissolved in 10 ml of methanol, subsequently. The reaction mixture was refluxed for 10 minutes. The dark brown solution was filtered and left for slow evaporation at room temperature. Dark brown crystals were obtained. Yield: ~30 %. Calculated for $C_{26}H_{36}Cu_2N_{10}O_8$: C, 41.97%; H, 4.88%; N, 18.83%. Found: C, 41.42%; H, 4.67%; N, 18.69%.

ACKNOWLEDGMENT

T.C. thanks the **Eugen Ionescu foundation** for granting a postdoctoral scholarship (2009-2010).

REFERENCES

1. A. Bobrowski, A.M. Bond, *Pol. Electroanalysis*, **1991**, *3(3),* 157.
2. V.V. Dragic, A.P. *Anal. Chem*., **1996**, *68*, 829.
3. Ma Feng, J. Daniel, L. Renman, *Anal. Chem.*, **1997**, *69*, 1782.
4. J.R. Donat, K.W. Bruland, *Analytical Chemistry*, **1988**, *60(3)*, 240.
5. E.B. Coropceanu, A. Deseatnic, M. Stratan, A Rija, O. Bologa, J. Tiurin, S. Labliuc, S. Clapco, I. Bulhac, *Chem. Journ. of Moldova*, **2008**, *3(2)*, 70.
6. V.I. Gorohovskaia, M. Gorohovski, "Handbook of oscilopolarography*".* High School Publ., Moskow, **1973**.
7. E.B. Coropceanu, L. Croitor, B. Wicher, M. Gdaniec, M.S. Fonari, *Inorganica Chimica Acta*, **2009**, *362*, 2151.
8. T.A. Criucova, S.I. Sineacova, T.V. Arefieva, Plarografic analysis, Moskow, **1959**.
9. F. Vydra, K. Stulic and E. Julacova. "Electrochemical Stripping Analysis". Halsted Press, New York, **1976**.
10. R. Kalvoda, *Pure Appl. Chem.,* **1987**, *59*, 715.

STUDIA UBB CHEMIA, LVI, 2, 2011 (p. 39 - 47)

URINARY STEROID PROFILES OF PATIENTS THREE WEEKS AFTER *IN VITRO* FERTILIZATION

ILDIKÓ BÍRÓ[a, b], ANITA BUFA[a, b], VIKTÓRIA POÓR[a], FERENC WILHELM[b], ZOLTÁN MÁNFAI[b], SÁRA JEGES[a], PÉTER M. GŐCZE[b], FERENC KILÁR[a]

ABSTRACT. The urinary steroid metabolite profiles were studied for patients, who failed to achieve pregnancy and for patients with ongoing pregnancy after *in vitro* fertilization (*IVF*). Ten age-matched women who failed to achieve pregnancy and twelve women with ongoing pregnancy after *IVF* were chosen. The standard "*long*" protocol was used for ovarian stimulation in *in vitro* fertilization, while intracytoplasmic sperm injection was employed for the assisted fertilization. The methoxim-silyl derivatives of twenty two steroids were determined by gas chromatography/mass spectrometry and the results were analysed by statistical evaluation. We found, that the concentrations of pregnanediol and pregnanetriol were significantly higher, and the concentration of tetrahydrocortisol was significantly lower in the pregnant patients than in women who failed to achieve pregnancy. The study concludes that the production of pregnanediol, pregnanetriol and tetrahydrocortisol is altered in early pregnancy.

Keywords: *In vitro fertilization, early pregnancy, urinary steroids, gas chromatography-mass spectrometry*

INTRODUCTION

Several studies have examined the early hormonal values and their relationship to pregnancy outcome after *in vitro* fertilization (*IVF*). Most of these studies have focused on the clinical pregnancy (>6 weeks after the last menstrual period). In most cases, however, miscarriages happen earlier, within the first 3 weeks after conception (nearly 5 weeks after the last menstrual period) (1), which is the time for the development of the structural and functional units of the placenta (2). Studies focused on clinical pregnancy miss the most critical period for pregnancy continuance.

Early pregnancy loss represents an important event in the natural and in the *IVF* cycles. Using different ultrasensitive β-hCG assays during the entire luteal phase in women who want to conceive, it has been found that

[a] *Institute of Bioanalysis, Faculty of Medicine, University of Pécs, Szigeti út 12., 7624 Pécs, Hungary, ferenc.kilar@aok.pte.hu*

[b] *Department of Obstetrics and Gynaecology, Faculty of Medicine, University of Pécs, Édesanyák útja 17., 7624 Pécs, Hungary*

the possibility of a positive pregnancy test is 22 - 57 % (3-7). At the same time, 31 - 62 % of these cycles will end in miscarriage. Interestingly, the rate of clinical abortion is between the 5 - 20 % range. However, the early pregnancy loss can be as high as 92 % of the total number of miscarriages (6). This affirms that the early events occurring in the endometrial cavity at the time of implantation are more important, than what we can detect with routine pregnancy tests or vaginal ultrasound (US) scans. Therefore any attempt to examine implantation efficiency in *IVF* should also note the chance of early pregnancy loss.

Progesterone represents a key hormone involved in endometrial receptivity. Endometrial receptivity, a term first introduced by Psychoyos (8), remains one of the major limiting factors for a successful pregnancy.

The aim of the present study was to get more information about the steroid hormone metabolite changes of early pregnancy after *IVF*.

RESULTS

The urinary steroid metabolite profiles of female patients were determined by gas-chromatography mass spectrometry analyses. The urine samples were collected 3 weeks after the embryo transfer in the *in vitro* fertilization procedure. The separation of the urinary steroid metabolites of a 34 year old woman, who failed to achieve pregnancy (member of Group 1) is shown in Figure 1.

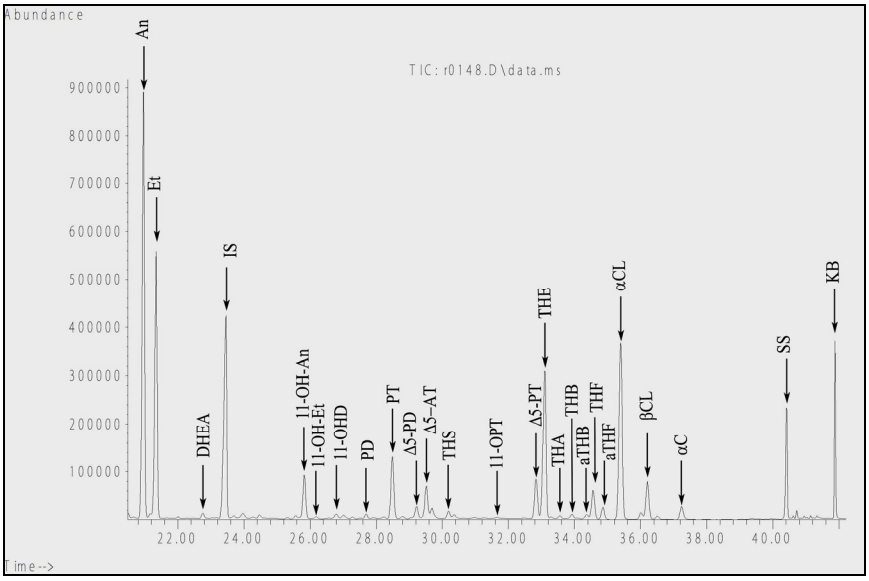

Figure 1. Separation of urinary steroid metabolites of a woman, who failed to achive pregnancy. The urine sample was collected three weeks after the embryo transfer in the *in vitro* fertilization procedure

The steroid profile of a 32 year old woman with ongoing *IVF* pregnancy (member of Group 2) is shown in Figure 2.

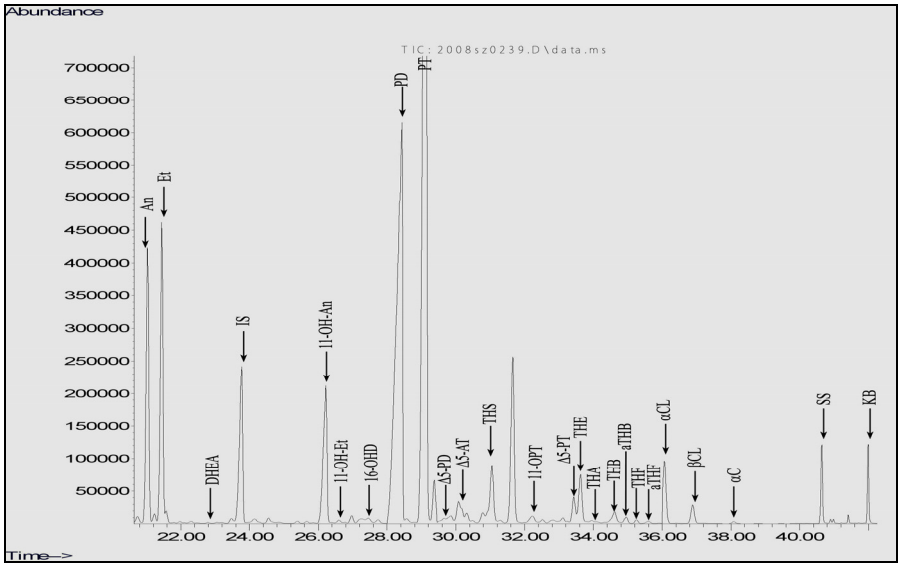

Figure 2. Separation of urinary steroid metabolites of a woman with successful pregnancy. The urine sample was collected three weeks after after the embryo transfer in the *in vitro* fertilization procedure

Altogether twenty two steroid metabolites were determined in a single run for each sample. The steroids were determined after the usual derivatization procedure, described in the Experimental.The two kinds of the profiles obtained for the two groups showed significant differences. Statistical data of the quantitative determination (nmol/24h) of the metabolites for the two groups (patients, who failed to achieve pregnancy, and patients with ungoing pregnancy) including the mean values, median (Me) and quartiles (Q1, Q2) of the amounts of the androgens, progesterone and corticoids in the “non-pregnant” group (Group 1) and in the “pregnant” group (Group 2) is summarized in Table 1.

The Mann-Whitney nonparametric test was applied to compare the concentrations of the derivatized metabolites of androgens, corticoids and progesterone in the urine of the non pregnant and pregnant patients. We found that the concentrations of pregnanediol (PD) and pregnanetriol (PT) were significantly higher (*p*-values are lower than 0.05), and the concentration of tetrahydrocortisol (THF) was significantly lower (*p*-value is lower than 0.05) in the pregnant than in the non pregnant patients.

Table 1. Statistical data of steroid metabolites of patients with successful and unavailing *in vitro* fertilization three weeks after the embryo transfer

	Group 1. (Non pregnant)					Group 2. (Pregnant)					
Derivatized steroids	Data number	Mean	Q1	Me	Q3	Data number	Mean	Q1	Me	Q3	P-values of M-W test
Androsterone (An)	10	1321	533	1017	1408	12	2961	654	1753	3250	0,262
Etiocholanolone (Et)	10	1638	669	1056	2257	12	3229	651	1832	4484	0,391
Dehydroepiandrosterone (DHEA)*	6	112	55	110	165	8	228	83	143	369	0,439
11-hydroxy-androsterone (11-OH-An)*	9	270	150	311	364	11	236	86	195	358	0,518
11-hydroxy-etiocholanolone (11-OH-Et)*	8	215	68	176	382	6	181	76	178	288	0,699
16-hydroxy-DHEA (16-OHD)*	7	432	119	542	728	12	269	137	303	337	0,398
Pregnanediol (PD)	10	7061	278	2091	5810	12	34305	17427	25399	48449	***0,001***
Pregnanetriol (PT)	10	1941	162	429	1001	12	6452	1090	5340	9424	***0,025***
Pregnenediol (Δ5-PD)*	5	261	27	145	553	8	864	334	707	1545	0,079
Androstenetriol (Δ5-AT)*	8	276	127	167	446	11	190	63	182	247	0,457
Tetrahydro-11-deoxycortisol (THS)*	5	130	55	87	227	7	277	135	304	359	0,062
11-keto-pregnanetriol (11-OPT)*	1	40	40	40	40	5	63	23	67	100	0,770
Pregnenetriol (Δ5-PT)*	7	209	114	175	312	10	306	115	213	377	0,495
Tetrahydrocortisone (THE)*	9	1150	425	1381	1531	11	685	273	408	1000	0,160
Tetrahydro-11-dehydrocorticosterone (THA)*	7	181	50	119	303	11	487	146	417	580	0,077
Tetrahydro-corticosterone (THB)*	9	259	165	182	432	10	522	245	495	736	0,072
Allo-tetrahydro-corticosterone (aTHB)*	7	249	123	196	372	10	423	144	344	596	0,283
Tetrahydrocortisol (THF)*	9	471	154	403	637	8	164	72	156	223	***0,034***
Allo-tetrahydrocortisol (aTHF)*	8	246	99	142	420	4	117	49	103	199	0,234
α-cortolone (α-CL)*	8	389	154	336	682	9	282	82	209	409	0,441
β-cortolone (β-CL)*	7	221	89	226	378	5	167	91	137	259	0,570
α-cortol (α-C)*	5	84	48	65	130	3	52	25	34	96	0,180

* The data number (number of patients) in the determination of the data for DHEA, 11-OH-An, 11-OH-Et, 16-OHD, Δ5-PD, Δ5-AT, THS, 11-OPT, Δ5-PT, THE, THA, THB, aTHB, THF, aTHF, α-CL, β-CL, α-C differ in the two groups (non pregnant and pregnant patients) since the concentration of these steroids were below the lower limit of quantification (LLOQ) in those subjects

Although higher amounts were observed in the levels of tetrahydro-11-deoxycortisol (THS), tetrahydro-11-dehydrocorticosterone (THA) and tetrahydro-11-corticosterone (THB) in Group 2 compared to Group 1, this difference could not be confirmed statistically.

DISCUSSION

The hormonal events in early pregnancy are very complex processes, and still poorly understood. We found, that the concentrations of PD and PT (progesterone metabolites) are significantly higher, and the concentration of THF (a cortisol metabolite) is significantly lower in pregnancy.

Progesterone is produced mainly by the corpus luteum up to weeks 5-6 of gestation, but after the twelfth week the placenta will be the dominant site of biosynthesis. Csapó et al. found, that the corpus luteum (CL) is needed to be maintained until the placenta takes over the production of progesterone and that luteectomy before this event induces abortion (13). However, they demonstrated that pregnancy could be supported even after removal of the CL by external administration of progesterone (14). Johnson and colleagues (15, 16) measured high concentrations of progesterone during the first trimester. Progesterone also promotes uterine musculature quiescence and local vasodilatation, by inducing nitric oxide synthesis in the decidua (endometrium of pregnancy) (17). Inadequate uterine contractility may lead to ectopic pregnancies, miscarriages, retrograde bleeding with dysmenorrhea and endometriosis (17).

The endocrine system and the immune system interact closely during maintenance of pregnancy. At the decidua, under the influence of sex steroids, there is a dramatic increase of a unique population of lymphocytes, the uterine natural killer (uNK) cells in early pregnancy. The role of these cells in human pregnancy is still not definitively established. However, they are believed to promote placental and trophoblast growth and provide immunomodulation at the maternal-fetal interface. Uterine natural killer cells are hormonally regulated by progesterone, estrogen and prolaktin (18).

In the pregnant group the lower level of THF (compared to the group failing to achieve pregnancy) is probably a maternal adaptation to the pregnancy. In the non-pregnant group the higher THF level suggests the chance of possible miscarriages (19). The increased cortisol level may decrease the production of progesterone around the time of implantation (20). The discovery of corticotrophin-releasing factor receptors on the ovary (21) is also consistent with the possible existence of a down-regulatory effect of stress on steroidogenesis (22). Furthermore, immune challenges in mice appear to promote a shift in the Th1/Th2 cytokine ratio, which has been associated with low progesterone levels and early spontaneous abortion (23, 24). It was found in rabbit cell-culture studies that glucocorticoids can cause degeneration and premature aging of the trophoblast (25, 26).

CONCLUSIONS

The aim of this study was to get information about the steroid hormone metabolite levels of early pregnancy. The significantly higher concentrations of pregnanediol (PD) and pregnanetriol (PT) – progesterone metabolites, – help to maintain pregnancy, supporting uterine musculature quiescence and local vasodilatation. The low concentration of tetrahydrocortisol (THF) in the pregnant patients compared to the non pregnant patients shows a maternal adaptation to the pregnancy.

The initiation and maintenance of pregnancy depends on complex interactions between the maternal environment and the embryo. Changes in the metabolism can be one of the lots of agents that can cause *IVF* success or failing.

This study indicates a possible correlation between *IVF* pregnancy and the level of certain steroid metabolites, showing differences between patients grouped according to the success or failure of ongoing *IVF* pregnancy, but these data does not demonstrate differences between non pregnant women in general and pregnant women in general, since non-*IVF* data are not included.

EXPERIMENTAL SECTION

Patients and sample collection

Individuals were selected from women with tubal factors, male factors and unexplained infertility. Patients with endocrine disease were not included. Exclusion criteria were an ovarian functional cyst, polycystic ovarian syndrome, ovarian endometrioma, an unilateral ovarian resection or ovariectomy. Other exclusion criterion was the body mass index above 30 kg/m^2. A written informed consent was obtained from the patients.

All patients underwent the previously described standard "*long*" protocol (9), consisting of pre-treatment with GnRH analog (GnRH-a) (0.05 mg/day), followed by stimulation with recombinant follicle-stimulating hormone (rFSH) and highly purified human menopausal gonadotropin (HMG) for controlled ovarian stimulation. 250 μg recombinant hCG was administered before 36 hours the oocyte retrieval. The luteal phase was supported by progesterone (Utrogestan, 3x600mg/day).

Age-matched individuals undergoing their first *IVF* were grouped according to the clinical outcome of *IVF*. Group 1. (n=10) were defined as patients who failed to achieve pregnancy (the mean ± S.D. ages were 34,9 ± 6,11 years). Group 2. (n=12) included patients with ongoing *IVF* pregnancy (the mean ± S.D. ages were 33,3 ± 2,74 years).

Ongoing *IVF* pregnancy was judged by hCG measurement and ultrasound.

This clinical research programme was permitted by the Regional Research Ethics Committee of the Medical Center, University of Pécs, Hungary (permission number: 2997. 28. September 2007.)

Sample preparation

The urine samples were collected over 24 h, 3 weeks after the embryo transfer and stored at -20°C until analysis. The method of the extraction and derivatization has been described in ref. 10, with some modifications described in ref. 11. Shortly, solid phase extraction, enzymatic hydrolysis and methoxime-trymethyl-silyl derivatization and extraction on Lipidex 5000 columns were carried out to obtain the sufficient derivatives for the GC-MS analyses.

Gas-chromatography-mass spectrometry

The GC/MS analysis was carried out on an Agilent 6890N gas chromatograph (Agilent, Santa Clara, USA) coupled to an Agilent 5975 mass spectrometer. The separation was performed in a HP-1-MS column with a length of 25 m, internal diameter 0.2 mm and a film thickness of 0.33 μm. The GC system was operated in constant flow mode at a flow rate of 1.5 ml/min with helium carrier gas. Splitless injection mode was employed. 2 μl of derivatized sample extract was taken into the heated injector (300°C). The GC temperature program was as follows: the initial temperature was 50°C, which was raised at 30°C/min to 190°C, and it was held for 5 min. Then the temperature was increased at 2.1°C/min to 300°C and maintained for 10 min. The transferline temperature was 300°C, and the temperature of the ion source was 200°C. The MS data were acquired at 70 eV, in selected ion-monitoring (SIM) mode.

The androgen metabolites, androsterone (An), etiocholanolone (Et), dehydroepiandrosterone (DHEA), 11-hydroxy-androsterone (11-OH-An), 11-hydroxyetiocholanolone (11-OH-Et), 16-hydroxy-DHEA (16-OHD), androstenetriol (Δ5-AT); the progesterone and intermediate metabolites, pregnanediol (PD), pregnanetriol (PT), pregnenediol (Δ5-PD), 11-keto-pregnanetriol (11-OPT), pregnenetriol (Δ5-PT); and the corticoid metabolites tetrahydro-11-deoxycortisol (THS), tetrahydrocortisone (THE), tetrahydro-11-dehydrocorticosterone (THA), tetrahydro-corticosterone (THB), allotetrahydro-corticosterone (aTHB), tetrahydro-cortisol (THF), allo-tetrahydrocortisol (aTHF), α-cortolone (α-CL), β-cortolone (β-CL), α-cortol (α-C) were quantified and identified with their characteristic mass ions, *i.e.*, the Target Ions (Tg Ion) and the Qualifier Ions (Q Ions) specific for each steroid (12).

Calculation and statistical analysis

Statistical evaluation was made by the Mann-Whitney nonparametric test, using SPSS 16.0 software (SPSS Institute Inc., Chicago, IL, USA). A *p* value of lower than 0.05 was considered to be statistically significant. The data were described by sample size (n), median (Me), and the quartiles (Q1, Q3).

ACKNOWLEDGEMENTS

The work was supported by grants GVOP-3.2.1.-2004-04-0189/3.0 and GVOP-3.2.1.-2004-04-0223/3.0, and RET 008-2005, OTKA-NKTH NI 68863. The authors thank Rita Golob for her assistance in the laboratory experiments.

REFERENCES

1. M.P. Milad, S.C. Klock, S. Moses, R. Chatterton, *Human Reproduction,* **1998**, *13*, 2296.
2. A. Malassiné, L. Cronier, *Endocrine*, **2002**, *19*, 3.
3. M.J. Zinaman, E.D. Clegg, C.C. Brown, J. O'Connor, S.G. Selevan, *Fertility and Sterility*, **1996**, *65*, 503.
4. A.J. Wilcox, C.R. Weinberg, J.F. O'Connor, D.D. Baird, J.P. Schlatterer, R.E. Canfield, E.G. Armstrong, B.C. Nisula, *The New England Journal of Medicine*, **1988**, *319*, 189.
5. J.F. Miller, E. Williamson, J. Glue, Y.B. Gordon, J.G. Grudzinskas, A. Sykes, *Lance,* **1980**, *2*, 554.
6. D.K. Edmonds, K.S. Lindsay, J.F. Miller, E. Williamson, P.J. Wood, *Fertility and Sterility*, **1982**, *38*, 447.
7. R.B. Hakim, R.H. Gray, H. Zacur, *American Journal of Obstetrics and Gynecology*, **1995**, *172*, 1510.
8. A. Psychoyos, *Journal of Reproduction and Fertility. Supplement*, **1976**, *25*, 17.
9. S.L. Tan, C. Kingsland, S. Campbell, C. Mills, J. Bradfield, N. Alexander et al, *Fertility and Sterility*, **1992**, *57*, 810.
10. C.H. Shackleton, J.W. Honour, *Clinica Chimica Acta*, **1976**, *69*, 267.
11. A. Bufa, V. Poór, A. Bálint, S. Molnár, S. Jeges, L. Pótó, P. Gőcze, F. Kilár, *Chromatographia*, **2008**, *68*, 131.
12. K. Homma, T. Hasegawa, M. Masumoto, E. Takeshita, K. Watanabe, H. Chiba et al, *Endocrine Journal*, **2003**, *50*, 783.
13. A.I. Csapó, M.O. Pulkkinen, B. Ruttner, J.C. Sauvage, W.G. Wiest, *American Journal of Obstetrics and Gynecology*, **1972**, *112*, 1061.
14. A.I. Csapó, M.O. Pulkkinen, W.G. Wiest, *American Journal of Obstetrics and Gynecology*, **1973**, *115*, 759.

15. M.R. Johnson, A.F. Riddle, J.G. Grudzinskas, V. Sharma, S. Campbell, W.P. Collins et al, *Human Reproduction*, **1993**, *8*, 316.
16. M.R. Johnson, A.A. Abbas, R. Irvine, A.F. Riddle, J.Q. Norman-Taylor, J.G. Grudzinskas et al, *Human Reproduction*, **1994**, *9*, 41.
17. C. Bulletti, D. de Ziegler, *Current Opinion in Obstetrics & Gynecology*, **2005**, *17*, 265.
18. C. Dosiou, L. C. Giudice, *Endocrine Reviews*, **2005**, *26*, 44.
19. P.A. Nepomnaschy, K.B. Welch, D.S. McConnell, B.S. Low, B.I. Strassmann, B.G. England, *Proceedings of the National Academy os Sciences of the United States of America*, **2006**, *103*, 3938.
20. P.A. Nepomnaschy, K. Welch, D. McConnell, B.I. Strassmann, B.G. England, *American Journal of Human Biology*, **2004**, *16*, 523.
21. L. Ghizzoni, G. Mastorakos, A. Vottero, A. Barreca, M. Furlini, A. Cesarone et al, *Endocrinology*, **1997**, *138*, 4806.
22. A.J. Tilbrook, A.I. Turner, I.J. Clarke, *Stress*, **2002**, *5*, 83.
23. D.A. Clark, S. Blois, J. Kandil, B. Handjiski, J. Manuel, P.C. Arck, *American Journal of Reproductive Immunology*, **2005**, *54*, 203.
24. S.M. Blois, R. Joachim, J. Kandil, R. Margni, M. Tometten, B.F. Klapp, P.C. Arck, *Journal of Immunology*, **2004**, *172*, 5893.
25. W.R. Blackburn, H.S. Kaplan, D.G. Mckay, *American Journal of Obstetrics and Gynecology*, **1965**, *92*, 234.
26. K.F. Wellmann, B.W. Volk, *Archives of Pathology*, **1972**, *94*, 147.

STUDIA UBB CHEMIA, LVI, 2, 2011 (p. 49 - 56)

INFLUENCE OF TEMPERATURE AND HEATING RATE ON BIOMASS PYROLYSIS IN A FIXED-BED REACTOR

VICTORIA GOIA[a], CĂLIN-CRISTIAN CORMOŞ[a], PAUL ŞERBAN AGACHI[a]

ABSTRACT. Biomass is one of the renewable energy resources with near zero CO_2 emissions; consequently much research has been investigated in order to replace conventional fossil fuels with biomass in energy conversion sector. Pyrolysis is a thermo-chemical conversion for the production of char, oil and gas products and it is also the initial step for other important thermo-chemical conversion processes like combustion and gasification. This paper focuses on the effects of operating parameters (pyrolysis temperature and heating rate) on pyrolysis product distribution. Therefore 178 experiments were conducted in a lab scale fixed-bed reactor at different temperatures and heating rates for differnet types of biomasses. The experiments were carried out for several types of biomass: spruce wood (SPW), corn stalks (CST), wheat straw (WST) and sawdust (SWD), meaning 58 experiments.

Keywords: *Pyrolysis, Biomass, Heating rate, Pyrolysis Temperature, Pyrolysis Yield, Thermo-chemical conversion*

INTRODUCTION

Biomass is a renewable energy source, formed from living or recently living species. The most important biomass fuel is wood, but the trees are too valuable to be burned, instead residues from woodworking industries as sawdust, could be a very valuable feedstock. Other biomass fuels are the agricultural residues such as: wheat straw, corn stalks, husks from rice, coconuts etc. Fossil fuels (e.g. oil, coal, lignite) are also derived from plant or animal species only that they have been formed during millions of years. Biomass is one of the renewable energy resources with near zero CO_2 emissions and low ash and sulphur contents. Biomass is formed absorbing CO_2 from the atmosphere, hence when is burned is not contributing to the overall carbon dioxide emissions. For this reason is considered to have nearly

[a] *Universitatea Babeş-Bolyai, Facultatea de Chimie şi Inginerie Chimică, Str. Kogălniceanu, Nr. 1, RO-400084 Cluj-Napoca,Romania, Emails: vgoia@chem.ubbcluj.ro, cormos@chem.ubbcluj.ro, sagachi@staff.ubbcluj.ro*

a zero carbon footprint. The primary products from biomass processing are: liquid, gaseous and solid, further derive the major categories of products: electricity, heat, chemicals and transportation fuels. For easier handling biomass has to be converted into liquid or gaseous products, either by biochemical or thermochemical processes [1-3].

Thermochemical processes include: gasification, combustion, hydrogenation, liquefaction and pyrolysis [4-6]:

- *Gasification* is the conversion of solid fuels (coal, biomass, coke, oil, tar, pitch) with air, oxygen and steam or a mixture of this gases at a high temperature (above 800°C) into a gaseous product containing mainly CO and H_2 (called syngas) which can be used either to produce electricity or as a raw material for the synthesis of chemicals or liquid fuels.
- *Combustion* or burning is a chain of exothermic chemical reactions between a fuel and an oxidant agent (air or oxygen) in order to produce heat which can be then converted via mechanical power into electricity. Any type of biomass can be burned only if the biomass moisture is less than 50%.
- *Hydrogenation* represents a chemical process involving reactions between a compound and hydrogen in the presence of a catalyst, which is particularly used for methane production by hydro-gasification, after the syngas is formed, the carbon monoxide reacts with hydrogen to produce methane.
- *Liquefaction* is the thermochemical conversion of a fuel into a liquid product, at low temperature and high pressure, using a catalyst. When the fuel used in liquefaction is biomass the process is called Biomass to Liquid (BtL)
- *Pyrolysis* is a thermochemical decomposition of solid fuels (e.g. biomass, fossil fuels) for the production of chemicals, heat or power, in the absence of oxygen. Pyrolysis is the initial step in all the other thermal conversions technologies, such as combustion and gasification. The process takes place at relatively low temperatures (500 - 800°C), compared with 900 - 1500°C in gasification. [2,7-9]

Depending on the heating rate, the pyrolysis process can be slow or fast, carried out in the absence of a medium. Pyrolysis can take place in the presence of a medium: H_2 – hydropyrolysis or H_2O – hydrous pyrolysis. When char production is desired, slow pyrolysis (carbonization or conventional) is used, but when the desired products are gas or liquids, fast pyrolysis (flash or ultra-rapid) is used. The main difference between slow and fast pyrolysis is the residence time of vapor in pyrolysis zone: for slow pyrolysis is in order of minutes, whereas for fast pyrolysis is in order of seconds or milliseconds. Table 1 summarizes the main characteristics of the main categories of pyrolysis [2, 8, 10].

Table 1. Characterization of main pyrolysis technologies

Pyrolysis Technology	Residence Time	Heating Rate	Final Temperature (°C)	Products
Carbonization	Days	Very low	400	Charcoal
Conventional	5-30 min	Low	600	Oil, gas, char
Fast	0.5-5 s	Very high	650	Bio-oil
Flash-liquid	<1 s	High	< 650	Bio-oil
Flash-gas	<1 s	High	< 650	Chemicals, gas
Ultra-rapid	< 0.5 s	Very high	1000	Chemicals, gas
Vacuum	2-30 s	Medium	400	Bio-oil
Hydropyrolysis	< 10 s	High	< 500	Bio-oil
Methano-pyrolysis	< 10 s	High	> 700	Chemicals

The main categories of pyrolysis products are: gas, liquid and solid, the quantity depends on the process parameters: temperature, heating rate and pressure. The gas product from pyrolysis (CO, CO_2, H_2O, C_2H_2, C_2H_6, C_2H_4 etc.) is a fuel gas with a Lower Heating Value (LHV) in the range of 11 – 20 MJ/Nm^3. The liquid yield is also known as tar or bio-oil, with a LHV in the range of 13 – 18 MJ/kg. The crude pyrolysis liquid is a black tarry fluid, with viscosity as heavy oil and it contains up to 20% water. The solid yield of pyrolysis is char and it contains about 85% carbon. The char LHV is approximately 32 MJ/kg, much more than the LHV corresponding to liquid or gas products [2, 8, 11].

RESULTS AND DISCUSSION

This paper investigates pyrolysis process for four types of biomass: spruce wood (SPW), corn stalks (CST), wheat straw (WST) and sawdust (SWD) at different temperatures and different heating rates. The main characteristics of the solid fuel are [1, 12]:

- Proximate analysis provides general informations about the fuel type and its quality. This analysis gives the amount of volatile matter, fixed carbon, moisture and ash.

- Ultimate analysis gives the elemental composition in term of percentages of carbon, hydrogen, nitrogen, sulphur, oxygen and other elements (e.g. chlorine).

- Calorific value also known as heating value, which can be Lower Heating Value (LHV) or Higher Heating Value (HHV). The heating value represents the amount of energy produced by burning a unit quantity of fuel (e.g. 1 kg).

Table 2 presents the characteristics of the four investigated sorts of biomass.

Table 2. Biomass characteristics

Parameter	SPW	CST	WST	SWD
Proximate analysis(% wt. dry)				
Fixed carbon	7.64	14.93	18.67	14.01
Volatile matter (dry)	91.55	80.90	73.17	85.65
Ash	0.81	4.16	8.16	0.33
Ultimate analysis (% wt dry)				
Carbon	45.97	46.31	45.57	50.65
Hydrogen	6.03	6.11	5.57	6.11
Nitrogen	0.18	1.07	0.63	0.23
Oxygen	46.64	42.24	39.94	42.57
Sulphur	0.37	0.11	0.13	0.11
Ash	0.81	4.16	8.16	0.33
Calorific value(MJ/kg dry)				
HHV - Gross	17.875	18.559	17.939	19.711
LHV – Net	16.560	17.225	16.724	18.378

On account of the complex mechanisms taking place during the thermochemical decomposition of biomass, pyrolysis is influenced by several parameters depending on feedstock properties and process conditions. The biomass was burned at different temperatures and different heating rates into a lab scale fixed-bed reactor to produce char, gas and oil.

Pyrolysis product composition is described above [13, 14]:

- Char contains mainly elemental carbon (~85%) and also hydrogen, oxygen and inorganic species;

- Pyrolysis gas, besides CO, CO_2 and CH_4, which are the mainly components, contains also propane, propylene, hydrogen, butane, butenes, ethane etc.;

- Bio-oil obtained through pyrolysis contains both organic (e.g. alcohols, acids, phenols, ketones, esters) and inorganic species (e.g. Fe, Si, Ca, Na, K, Al, Mg, Cr, Ni).

Pyrolysis reaction is an endothermic reaction which it can be represented as follows:

$$C_nH_mO_p \xrightarrow{Heat} \sum_{liquid} C_xH_yO_z + \sum_{gas} C_aH_bO_c + C\ (char) + H_2O$$

The relative yields of pyrolysis products can be modified by changing the heating rate, the final temperature or the residence time in the reactor.

Effect of pyrolysis temperature

Pyrolysis temperature is the maximum temperature which is achieved during pyrolysis. The composition and the product yield are affected by pyrolysis temperature. Figure 1 presents the effect of temperature on product distribution of pyrolysis of four selected biomasses at temperatures between 250ºC and 700ºC in a fixed-bed reactor.

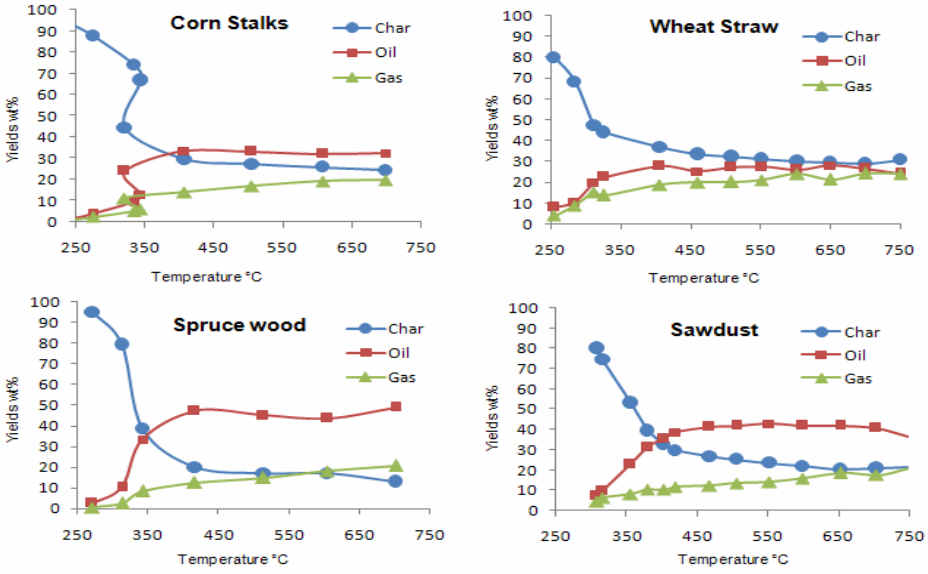

Figure 1. Temperature influence on product distribution

The results show that the amount of char significantly decreases with increasing pyrolysis temperature. This behavior could be due to greater primary decomposition of the sample at higher temperatures. Meanwhile, as expected, the oil and gas yields increases with the same temperature rising. This could be due to secondary cracking of the pyrolysis liquid, at higher temperature, into gaseous product.

Effect of heating rate

An important influence on the composition and yield of the pyrolysis product has the heating rate of biomass particles. In order to investigate the influence of heating rate on the product yields of selected biomasses, the experiments were conducted at different heating rates and keeping pyrolysis

temperature constant. Figure 2 presents the effect of heating rate (5–83 C/min) on product distribution of pyrolysis of four selected biomasses at a constant temperature in a fixed-bed reactor.

As shown in Figure 2 the heating rate has a big influence on product distribution. The oil yield is found to increase when heating rate is increased, whereas the solid yield and the gas yield decrease when rising the heating rate. If char production or gas production are desired, is recommended to use a slow heating rate of maximum 20 C/min, whiles if oil production is desired instead, is recommended to use a higher heating rate, around 60 – 80C/min.

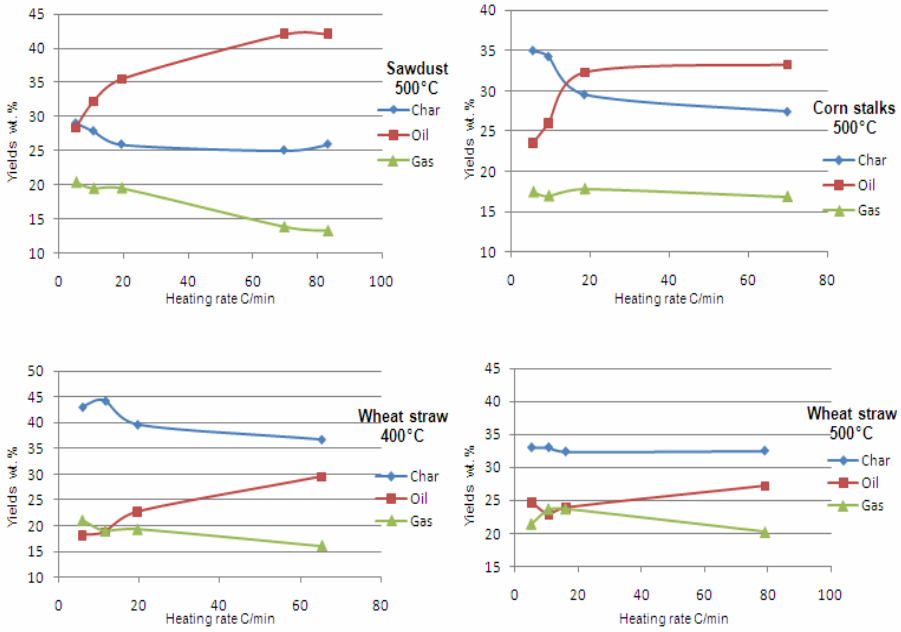

Figure 2. Heating rate influence on product distribution

CONCLUSIONS

The aim of this experimental analysis was to evaluate the effect of temperature and heating rate on pyrolysis process under various conditions. Four different biomasses were pyrolyzed in a lab scale fixed-bed reactor at different temperatures and heating rates. The results show that char yield significantly decreases with increasing pyrolysis temperature, whereas the oil and gas yields increases with the same temperature rising. When the heating rate is increased the solid yield ad the gas yield decrease and the char yield decreases. The paper shows that the operating parameters can be adjusted in order to fulfill the demand of the final product. Therefore to maximize gas production is recommended to use a slow heating rate and high

final temperature. If char production is desired instead, is recommended to use a slow heating rate and a low temperature. Whereas to maximize oil production both the temperature and heating rate are required to have higher values.

EXPERIMENTAL SECTION

The aim of this study is to determine the influence of temperature and heating rate on pyrolysis product distribution, consequently 178 experiments were made. A series of biomasses have been pyrolyzed: spruce wood (SPW), corn stalks (CST), wheat straw (WST) and sawdust (SWD), meaning 58 experiments for this study. The biomass samples are characterized by a humidity of 12%. The experiments were conducted in a lab scale fixed-bed reactor at temperatures between 250ºC and 700ºC at different heating rates. The reactor feeding with biomass was carried manually. This reactor ensures a very good repeatability and an almost complete recovery of pyrolysis products. Product composition was determined by: proximate analysis (char), ultimate analysis (char, oil) and gas chromatography (gas).

Figure 3 presents a schematic diagram of lab scale pyrolysis system.

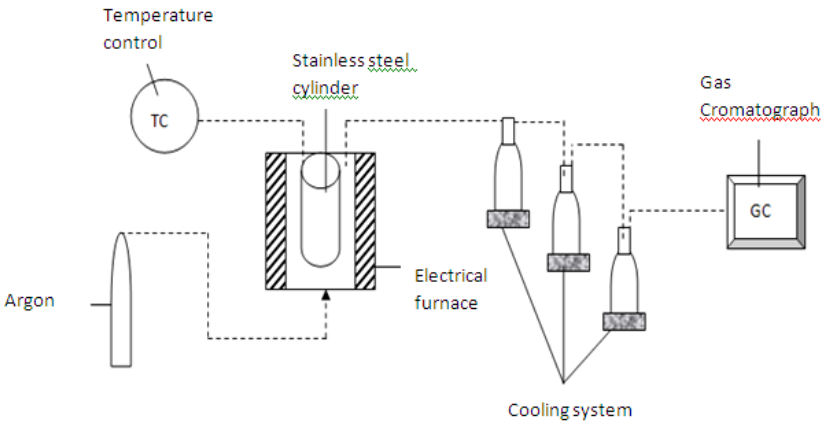

Figure 3. Schematic diagram of lab scale pyrolysis system

The pyrolysis reaction takes place into a stainless steel cylindrical container, where the biomass is introduced manually (between 0.6 – 0.7 Kg/s). The container is introduced in a small electrical furnace of which temperature is controlled by a temperature controller. The reaction takes place under inert atmosphere using Argon. The biomass is introduced in the reactor and it is heated with a heating rate between 5 – 80 C/min until the final pyrolysis temperature is reached. The volatile compounds which are formed during the pyrolysis are sent to a condensation system which is formed of three bottles

on an ice bath. The gas fraction composition, mainly hydrogen, carbon monoxide, methane, and carbon dioxide, were analyzed using a gas chromatography. The solid residue remaining in the basket and the liquid fraction were weighed after the system cooled down.

ACKNOWLEDGMENTS

The authors wish to thank for the financial support provided from programs co-financed by The Sectoral Operational Programme Human Resources Development, Contract POS DRU 6/1.5/S/3 – „Doctoral studies: through science towards society" and by Romanian National University Research Council (CNCSIS–UEFISCDI), project number PNII– IDEI code 2455/2008: "Innovative systems for poly-generation of energy vectors with carbon dioxide capture and storage based on co-gasification processes of coal and renewable energy sources (biomass) or solid waste".

REFERENCES

1. C. Higman, M. Van Der Burgt, "Gasification", Elsevier, Second edition, **2008**
2. P. Basu, "Biomass gasification and pyrolysis. Practical design and theory", Elsevier, **2010**
3. V. Maxim, C.C. Cormoş, P. Ş. Agachi, *Studia UBB Chemia*, **2010**, *1*, 51-63
4. R.C. Saxena, Diptendu Seal, Satinder Kumar, H.B. Goyal, *Renewable and Sustainable Energy Reviews*, **2008**, *12*, 1909-1927
5. H.B. Goyal, Diptendu Seal, R.C. Saxena, *Renewable and Sustainable Energy Reviews*, **2008**, *12*, 504-517
6. V. Maxim, C.C. Cormoş, A.M. Cormoş, P. Ş. Agachi, *Computer Aided Chemical Engineering*, **2010**, *28*, 697-702
7. J. Yu, C. Yao, X. Zeng, S. Geng, L. Dong, Y. Wang, S. Gao, G. Xu, *Chemical Engineering Journal*, **2011**
8. Food and Agriculure Organization of the United Nations, www.fao.org, **2011**
9. W. Lihua, W. Shurong, L. Zhongyang, *Journal of Zhejiang Univ (Eng Sci)*, **2004**, 247-252
10. Office of Scientifc and Technical Information, www.osti.gov, Integrated Pyrolysis Combined Cycle Biomass Power System Concept Definition Final Report, **2003**
11. D. Meier, O. Faix, *Bioresource Technology*, **1997**, 71-77
12. B.G. Miller, "Coal Energy Systems", Elsevier*,* **2005**
13. J.P. Diebold, *National Renewable Energy Laboratory*, report no. NREL/SP-570-27613, **1999**
14. T.A. Milne, L.C. Elam, R.C. Evans, *National Renewable Energy Laboratory*, report no. IEA/H2/TR-02/001, **1997**

STUDIA UBB CHEMIA, LVI, 2, 2011 (p. 57 - 63)

SYNTHESIS OF POLY(L-LACTIC ACID) BY DIRECT POLYCONDENSATION

OANA CADAR[a], SERGIU CADAR[a], MARIN ŞENILĂ[a], CORNELIA MAJDIK[b], CECILIA ROMAN[a]

ABSTRACT. Poy (lactic acid), a biodegradable polymer, has been extensively studied during last 15 years due to its wide range of applications. In this study, the synthesis of the poly (L-lactic) acid) with appropriate molecular weight for medical applications was investigated. Stanous(II) chloride was used as catalyst in a quantity of 0.25 wt% calculated on the monomer. Polycondensation was carried out over a period of 72 h, using xylene as solvent. The identification and purity of the obtained polymer was assessed by NMR spectroscopy. The molecular weight of PLA was measured by the intrinsic viscosity method.

Keywords: *lactic acid, catalysis, direct polycondensation.*

INTRODUCTION

Large amounts of plastics are fabricated worldwide and the removal of plastics after use is becoming a serious problem. To overcome these environmental problems, several types of biodegradable polymers have been studied: poly(butylenesuccinate), poly(3-hydroxybutyrate-co-3-hydroxyvalerate) and polycaprolactone, [1]. These polymers are degradable in soil, water or compost, but they exhibit low transparency and reduced mold resistance. Polylactic acid (PLA) has been recognized as having an excellent potential for biodegradable packaging and consumer goods because of its properties (mechanical strength, transparency, compostability and safety) [2]. Also, PLA has been used as bioadsorbable material in medical uses and has mold resistance [3]. PLA is degraded by simple hydrolysis of the ester linkage and does not necessitate enzyme to catalyze this process; the degradation rate depend on the isomer ration, the size and form of the product and the temperature of hydrolysis [4].

[a] *INCDO INOE 2000, Research Institute for Analytical Instrumentation, 67 Donath, 400293, Cluj-Napoca, Romania, oana.cadar@icia.ro*

[b] *Babes-Bolyai University Cluj-Napoca, Faculty of Chemistry and Chemical Engineering, 11 Arany Janos St., Cluj-Napoca, Romania, majdik@chem.ubbcluj.ro*

PLA is one of the few polymers in which the stereochemistry can be modified by polymerizing a mixture of L- or D-isomers in order to obtain high-molecular-weight crystalline or amorphous polymers [5].

There are two methods to produce polylactic acid from the lactic acid: direct polycondensation (PC) of lactic acid and ring-opening polymerization (ROP) of lactide monomer, which is the cyclic dimer of lactic acid [6]. During the last process water is not produced, so high-molecular-weight PLA can be obtained. However, due to the high process costs of obtaining and purifying lactide, PLA use has been limited only to some medical applications. In comparison with the catalytic ring-opening polymerization of L-lactide [7-9], attaining high-molecular-weight PLA polymers by direct dehydropolycondensation of L-lactic acid is not easy because of various factors: efficient removal of water, a water tolerant catalyst, difficult control of depolymerization and kinetic control [10-13]. The water byproduct formed by reaction induces reverse reactions that result in the hydrolysis of the ester linkages. If the temperature for reaction is too high, the rate of depolymerization becomes higher than the rate of polymerization [14, 15].

The aim of this work was to obtain poly(L-lactic) acid with appropriate-molecular weight and high-purity degree that makes it suitable for medical applications. Therefore, this study is indented to be a contribution to the study of synthesis of high-molecular-weight PLA.

RESULTS AND DISCUSSION

In this polymerization method it is extremely important to reduce efficiently the water content. For this reason, the monomer was distilled by heating at 100°C for 24 h. This process resulted in the formation of dimer and trimer of lactic acid and/or other impurities and this step has a bad effect on molecular weight of PLA. Therefore in this work, we used the monomer without the distillation step.

The removal of dimer and trimer of lactic acid and/or other impurities was performed by adding deionized water to the final solution.

Table 1 show the viscosity-average molecular weight of synthesized PLA.

Table 1. Polycondensation of lactic acid[a]

	Catalyst	Molecular sieve	Time (h)	$\overline{M_v}$
PLA-a	+	-	28+48	11900
PLA-b	-	-	72	8100
PLA-c	+	+	28+48	14400
PLA-d	-	+	72	9300

[a] All reactions were performed by azeotropic distillation technique using xylene at 135°C.

$SnCl_2 \cdot 2H_2O$ was used as catalyst in quantity of 0.25 wt% calculated according to the amount of monomer. A large amount of catalyst accelerated not only the polycondensation method but also the depolymerization [15]. The syntheses were performed with dried solvents during the process and its circulation in the closed system in order to control the equilibrium process of PLA formation: PLA-H_2O and PLA-lactide [16]. It is very important to mention that when temperatures higher than 140 ^oC were utilized, severe oxidation was occurred, which were observed by the formation of the dark brown color.

The progress of the polycondensation of L-lactic acid, in solution, was controlled by regular sampling of small amounts from the reaction mixture and determining the viscosity of the isolated PLA.

Generally, tin compounds are frequently used for the synthesis of PLA due to their high catalytic activity and good solubility in organic solvents. Due to inorganic tin compounds are less toxic than organotins and Sn(IV) compounds are less toxic than Sn(II) compounds, inorganic tin catalysts are considered a better choice as a catalyst. A possible mechanism for the catalytic activity of the stannous compounds is reported by Kim *et al.* [17].

Figure 1 shows the effect of $SnCl_2 \cdot 2H_2O$ on the viscosity-average molecular weight of PLA. $SnCl_2 \cdot 2H_2O$ has a good activity and the $\overline{M_v}$ of synthesized PLA was about 11900. This value is considerable higher than that of PLA synthesized without using $SnCl_2 \cdot 2H_2O$.

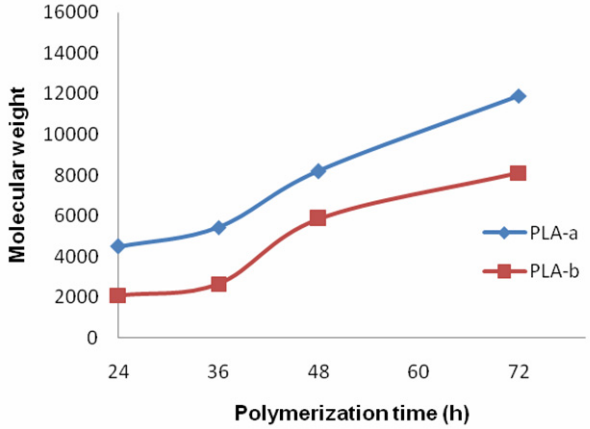

Figure 1. The effect of $SnCl_2 \cdot 2H_2O$ on the viscosity-average molecular weight of PLA synthesized by direct polycondensation method: (PLA-a) using $SnCl_2 \cdot 2H_2O$; (PLA-b) without using $SnCl_2 \cdot 2H_2O$.

No significant increase in the viscosity-average molecular weight of PLA was observed when molecular sieve were used. The molecular weight of PLA, without using molecular sieve was about 8100 and about 9300 using

molecular sieve, respectively (Figure 2). This is due to the irreversible process in which the molecular sieve are saturated as polymerization progress even though this is the most effective drying agent to reduce the dissolved water content in organic solvent.

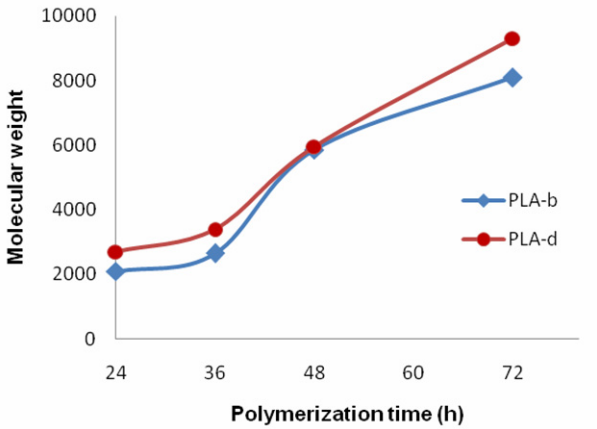

Figure 2. The effect of molecular sieve on the on the viscosity-average molecular weight of PLA synthesized by direct polycondensation method: (PLA-b) without using molecular sieve; (PLA-d) using molecular sieve.

Significant higher viscosity-average molecular weight of PLA ($\overline{M_v}$ =14400) was obtained when it was used both $SnCl_2 \cdot 2H_2O$ and molecular sieves (PLA-c).

The longer polymerization time, the higher viscosity-average molecular weight of PLA was obtained due to the high activation energy of polycondensation [15].

The IR spectra of PLA-c exhibited similar characteristic absorption peaks of ester (at 1760 and 1090 cm^{-1} for –COO- and –O-) and $–CH_2$- and $–CH_3$ groups (at 2950-3020 cm^{-1}). The characteristic absorption peaks of hydroxyl group of PLA were not observed proving that a high molecular weight PLA was obtained.

The ^1H NMR recorded spectra of the obtained crystals were similar and confirm the synthesis of PLA and demonstrate its purity. The ^1H NMR spectra of synthetized PLA were similar and exhibited the signal of methyl group at 1.68 ppm, the signal of the methyl next to alcoxy group at 3.50 ppm and the signal of methine group at 5.05 ppm. The signal of hydroxyl hydrogen of carboxyl group disappeared in the ^1H NMR spectra.

The above results were in perfect agreement with those of an authorized PLA specimen.

This kind of polymers may be useful in biomedical applications.

CONCLUSIONS

PLA was synthesized by direct polycondensation using a reactor equipped with a Dean-Stark trap in order to separate the water by-product. The highest viscosity-average molecular weight of PLA was about 14400 when $SnCl_2 \cdot 2\ H_2O$ and molecular sieve were used. Molecular sieve were used as drying agent to reduce the small amount of water in the organic solvent. These findings suggest that the method using molecular sieve could be recommended for the preparation of PLA. The molecular weight of PLA increases with the polymerization time. The temperature of the synthesis of PLA should not exceed 140 ^oC because at higher temperatures racemization can occur. The obtained PLA could be used for different medical applications.

The direct polycondensation process presented above can be applied to the synthesis of other hydroxyacids.

EXPERIMENTAL SECTION

All chemicals were purchased from Merck. All the solvent were dried over molecular sieves (3 Å) prior use. Molecular sieves were dried at 250 ^oC before use. Other chemicals were used as received. L-lactic acid was a 85-90 % (w/w) aqueous solution of monomer, 99% optically pure according to the manufacturer. Deionized water was obtained using a Milli-Q system (Millipore, Watford, Hertfordshire, UK).

The ^1H NMR spectra for the identification and purity degree of PLA were recorded on a Bruker DRX 500-MHz NMR Spectrometer; the samples were dissolved in $CDCl_3$, at room temperature. The sample concentration was about 10% by weight.

FTIR spectra were recorded using a FT-IR Spectrum BX II Perkin Elmer Spectrometer.

The molecular weight of PLA was determined by viscosimetry, using Ubbelhode capillary viscometers places in a water-bath thermostatically controlled at 30 ^oC. PLA was dissolved in chloroform (0,2 g/dl). The viscosity-average molecular weight of PLA was calculated according to the following equations [18]:

$$[\eta] = \frac{\sqrt{2(\eta_{sp} - \ln \eta_{r)}}}{C} \qquad (1)$$

where

$\eta_{sp} = \eta_r - 1$ and $\eta_r = t/t_o$, η_{sp} – the specific viscosity, η_r – the relative viscosity, C – the concentration of polymer (g/dL) and

$$[\eta] = 1.25 \times 10^{-4} \overline{M}_w^{\,0.717} \quad (2)$$

where

[η] – the intrinsic viscosity.

Synthesis of PLA by direct dehydropolycondensation

Two different polymerization methods were carried out: (a) azeotropic dehydratation at 140 °C for 72 h without using molecular sieve as dying agent and (b) azeotropic dehydratation at 140 °C for (24 + 48) h using molecular sieve as dying agent. The catalyst can be recovered after filtration and reused.

(a) Tin-catalyzed synthesis of PLA by direct dehydropolycondensation without using molecular sieve

Using a 250 mL reaction vessel equipped with a Dean-Stark trap, 20.1 g of 85-90 % L-lactic acid was azeotropically dehydrated using 100 mL xylene for 72 h at 140 ºC, in the presence of $SnCl_2$ 2 H_2O (0.2 wt.-%) as catalyst. The reaction mixture was cooled to room temperature and concentrated to about fourth-volume. 100 mL dichloromethane was slowly added and the catalyst was removed by filtration. The dissolved polymer was precipitated by addition of water and the solvent evaporation was allowed for 24 h at room temperature, maintaining the solution under stirring, thus dry solid polymer (PLA-a) was isolated.

(b) Non-catalyzed synthesis of PLA by direct dehydropolycondensation without using molecular sieve

Similar polymerization method was performed without using catalyst resulting PLA-b.

(c) Tin-catalyzed synthesis of PLA by direct dehydropolycondensation using molecular sieve

Using a 250 mL reaction vessel equipped with a Dean-Stark trap, 20.1 g of 85-90 % L-lactic acid was azeotropically dehydrated using 100 mL xylene for 24 h at 140 ºC, in the presence of $SnCl_2 \cdot 2\ H_2O$ (0.2 wt.-%) as catalyst. After the removal of water in the Dean-Stark trap, the reaction vessel was cooled to room temperature and in the place of Dean-Stark trap was mounted a tube completely packed with molecular sieve (3 Å). The refluxing solvent is returned to the vessel by way of the molecular sieves for an additional 48 h at 140 ºC. After the reaction mixture was concentrated to about fourth of the volume, the following steps were the same as for the above-mentioned polymerization methods resulting PLA-c.

(d) Non-catalyzed synthesis of PLA by direct dehydropolycondensation using molecular sieve

Similar polymerization method was performed without using catalyst to obtain PLA-d.

ACKNOWLEDGMENTS

The authors are grateful to CNMP-Romania for supporting the project PNII-72152/2008 - BIOPLAST.

REFERENCES

1. D.L. Kaplan, “Biopolymers from renewable resources”, Springer Verlag: Berlin, **1998**, 414.
2. R.M. Rasal, A.V. Janorkar, D.E. Hirt, *Progress in Polymer Science*, **2010**, *35(3)*, 338.
3. L.J. Suggs, S.A. Moore, A.G. Mikos, “Synthetic Biodegradable Polymers for Medical Applications - Physical Properties of Polymers Handbook”, Ed. James E. Mark, Springer, **2007**.
4. M.H. Hartmann - D.L. Kaplan (Ed.), “Biopolymers from Renewable Resources”, Springer-Verlag, Berlin, **1998**, 367.
5. D. Garlotta, *Journal of Polymers and the Environment*, **2001**, *9(2)*, 63.
6. T. Maharana, B. Mohantyb, Y.S. Negi, *Progress in Polymer Science*, **2009**, *34*, 99.
7. J.W. Leenslag, A.J. Pennings, *Makromol. Chem.*, **1978**, *188*, 1809.
8. F.E. Kohn, J.W.A. Van Den Berg, V.D. Ridder, J. Feijen, *Journal of Polymer Science*, **1984**, *29*, 4265.
9. H.R. Kricheldorf, S.R. Lee, *Polymer*, **1995**, *36*, 2995.
10. S. Shyamroy, B. Garnaik, S. Sivaram, *Journal of Polymer Science Part A: Polymer Chemistry*, **2005**, *43 (10)*, 2164.
11. M. Ajioka, K. Enomoto, K. Suzuki, A. Yamaguchi, *J. Environ. Polym. Deg.*, **1995**, *3*, 225.
12. H. Ohara, S. Sawa, Y. Fujii, M. Oota, “US 5880254”, Shimadzu Corporation, **1999**.
13. K. Enomoto, M. Ajioka, A. Yamaguchi, “US 5310865”, Mitsui Toatsu Chemicals Inc., **1994**.
14. Y. Doi, *Biodegradable Polymer Materials*, Kogyo Chosakai, Japan, **1990**.
15. K.W. Kim, S.I. Woo, *Macromol. Chem. Phys.*, **2002**, *203*, 2245.
16. S.I. Moon, C.W. Lee, M. Miyamoto, Y. Kimura, *Journal of Polymer Science Part A: Polymer Chemistry*, **2000**, *38*, 1673.
17. T. Yamaoka, Y. Takahashi, T. Ohta, M. Miyamoto, A. Murakami, Y. Kimura, *Journal of Polymer Science Part A: Polymer Chemistry*, **1999**, *37 (10)*, 1513.
18. C. Marega, A. Marigo, V. De Noto, R. Zannetti, *Makromol. Chem.*, **1992**, *193*, 1599.

STUDIA UBB CHEMIA, LVI, 2, 2011 (p. 65 - 74)

THE EFFECT OF CELL SURFACE TREATMENT ON LEAD(II) BIOADSORPTION BY *PHANEROCHAETE CHRYSOSPORIUM*

VIKTOR FARKAS[a], ALŽBETA HEGEDŰSOVA[b], SILVIA JAKABOVA[a,b], CORNELIA MAJDIK[c], TÍMEA PERNYESZI[a]

ABSTRACT. In this study the biosorption of Pb(II) ion from aqueous solution on non-living mycelial pellets of *Phanerochaete chrysosporium* treated with caustic, heat and ethanol was studied using batch technique with respect to initial concentration and temperature. *Phanerochaete chrysosporium* was grown in a liquid medium containing mineral and vitamin materials with a complex composition. The biomass of *P. chrysosporium* treated with ethanol revealed that it was mechanical stable and had increased adsorption capacity for Pb(II) compared to caustic, heat and untreated cells. Increasing temperature upto 32 ºC the bioadsorption capacity decreased for ethanol treated fungal cells, while it had not effect on bioadsorption by heat and untreated fungal biomass. For caustic treated fungal biomass the Pb(II) removal increased with increasing temperature.

Keywords: *bioadsorption, Pb(II), Phanerochaete chrysosporium, fungal cell surface treatment, temperature*

INTRODUCTION

Heavy metal pollution is one of the most important environmental problems today.

Heavy metals are toxic and hazardous materials and their increasing amount have been documented **[1,2]**. Various industries produce and discharge wastes containing different heavy metals into the environment such as energy and fuel production, iron and lead metallurgy, mining, smelting of metalliferous, surface finishing industry, fertilizer and pesticide industry and application, electroplating, electrolysis, electro-osmosis, leatherworking, photography, electic

[a] *Department of Analytical and Environmental Chemistry, Faculty of Science, University of Pécs, 6 Ifjúság, H-7624 Pécs, Hungary, e-mail:ptimea@ttk.pte.hu*
[b] *Department of Chemistry, Faculty of Natural Sciences, Constantine the Philosopher University, Tr. A. Hlinku 1, SK-949 01, Nitra, Slovakia*
[c] *University Babeş-Bolyai; Faculty of Chemistry and Chemical Engineering, 11 Arany J., RO-400293 Cluj-Napoca, Romania*

appliance manufacturing, metal surface treatment, aerospace and atomic energy installation etc. Metal as a kind of resource is becoming shortage and also brings about serious environmental pollution, threatening human health and ecosystem. **[1, 2]**.

Different technological methods have been developed to remove heavy metals from environment. At present, many technologies, such as sulfuration method, electrolysis, membrane and ion-exchange process, can be used for the treatment of wastewater polluted by heavy metals. However, these methods are less effective and more expensive when heavy metal concentration in the wastewater is low, and some of them can easily cause the second pollution. In recent years, applying biotechnology in controlling and removing metal pollution has been paid much attention, and gradually becomes hot topic in the field of metal pollution control because of its potential application.

Biosorption can be defined as the removal of metal or metalloid species, compounds and particulates from solution by biological material **(3).** Large quantities of metals can be accumulated by a variety of processes dependent and independent on metabolism. Both living and dead biomass as well as cellular products such as polysaccharides can be used for metal removal **(3).**

Removal of heavy metals by biosorption has many advantages, such as fast adsorption speed, removing heavy metal ions selectively under low concentration, high adsorption efficiency, wide range of pH and temperature, less investment and running cost, in addition, some heavy metals can be recovered. Biosorption, as an efficient treatment means, is gaining increasing attention.

In the concept of biosorption, several chemical processes may be involved such as adsorption, ion exchange, and covalent bonding with the biosorptive sites of the microorganisms **[6]**. Biomass cell walls, consisting mainly of polysaccharides, proteins and lipids offer many functional groups which can bind ions such as carboxylate, hydroxyl, sulphate, phosphate and amino groups.

A large quantity of materials has been investigated as biosorbents for the removal of metals or organics extensively. The tested biosorbents can be basically classified into the following categories: bacteria, fungi, yeast, algae, industrial wastes, agricultural wastes and other polysaccharide materials (2). Different kind of fungi can be used as natural biosorbent such as *Saccharomyces cerevisiae* **[2,7 - 10]**, *Aspergillus niger* **[13-14]**, *Polyporus ostreiformis* **[15]**, *Phanerochaete chrysosporium* **[16-19]**, *Trametes versicolor* **[15]**.

Phanerochaete chrysosporium is a well-known white-rot fungus and it has a strong ability to degrade various xenobiotics and exist in bleaching effluents from pulp and paper mills **[20]**. It could also be used to remove heavy metals from wastewaters by adsorbing the metals on its mycelium.

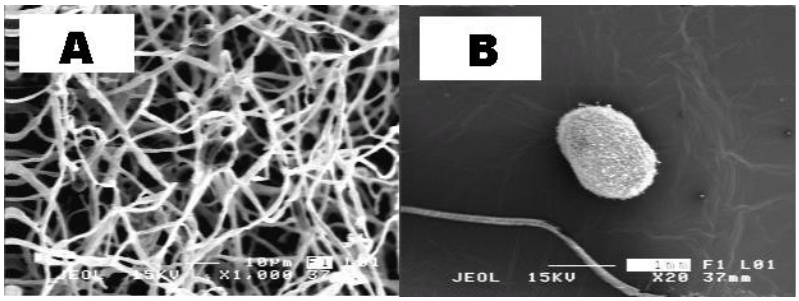

Figure 1. SEM image of *Phanerochaete chrysosporium* white-rot fungi.
A) The picture shows the mycelium of the fungi at a magnification of 1000 fold.
B) The picture shows the spherical-like fungal pellet at a magnification of 20 fold.

The treatment of native biomass improves its biosorption capacity, changes the possible binding groups **[21]**. Immobilization of these organisms improves mechanical strength, rigidity, size, porosity characteristics, and resistance to environmental restrains **[22, 23]**.

Kacar et al. (2002) have compared the biosorption capacity of alginate and immobilized live and heat inactivated *Phanerochaete chrysosporium* for Hg(II) and Cd(II) ions. The biosorption of Hg(II) and Cd(II) ions on the biosorbents depended on the experimental conditions, particularly on the pH of medium and the concentration of metals ion in the medium. Their experiment showed that the biosorption capacity decreased in order of non-living, living and immobilized cells **[15].**

Li et al (2004) studied the simultaneous biosorption of cadmium(II) and lead(II) ions by heat treated biomass of *Phanerochaete chrysosporium.* In the single-ion situation and under the optimum adsorption conditions (pH = 4.5), the maximum uptake was obtained as 15.2 mg g^{-1} at initial Cd(II) concentration of 50 mg l^{-1}, for Pb (II) ions it was 12.34 mg g^{-1}. The biomass concentration was 2 g l^{-1} in the suspension. In the binary metal solutions, both metal uptake and adsorption yield for one kind of ion decreased with increasing concentration of the other metal ion. Thus the interaction of Cd (II) and Pb (II) ions on their biosorption by *P. chrysosporium* was generally found to be antagonistic. The most logical reason for the antagonistic action was claimed to be the competition for adsorption sites of the cell surface. Pb (II) ions were found to be bound more effectively to *P. chrysosporium* than Cd (II) ions in binary metal solution **[23]**. Yetis et al. (2000) have studied the adsorption capacity of Pb(II) ion by living and non-living *P. chrysosporium* cells in aqueous solution. The resting cells of *P. chrysosporium* were able to uptake up to 80 mg Pb(II)/g dry cell at pH 5. However, live and dead cells exhibited lower capacities. The uptake capacity for Pb (II) ions of young resting fungal cells was higher than that of older fungal cells **[18].** Say, Denizli and Arica (2001) investigated the biosorption from artificial wastewaters of

Cu(II), Pb(II) and Cd(II) ions onto the dry fungal biomass of P. *Chrysosporium* fungal cells. The maximum adsorption of different heavy metal ions on the fungal biomass was obtained at pH 6.0 and the biosorption equilibrium was established after about 6 h. The experimental biosorption data for Cd(II), Pb(II) and Cu(II) ions were in good agreement with those calculated by the Langmuir model. The order of affinity for competitive conditions was as follows: Cu(II) > Pb(II) > Cd(II). This order was the same as in the non-competitive condition **[19]**.

Biosorption of heavy metals on the pretreated *P. chrysosporium* biomass has not yet been investigated completely. This paper is unique from the aspect that no one has compared the effect of different cell surface treatment of *Phanerochaete chrysosporium* on Pb(II) bioadsorption. The main objectives of the present study are the followings:

- using different pretreatment methods on *Phanerochaete chrysosporium* cells,
- comparison of the Pb(II) biosorption capacity by treated cells,
- study the effect of temperature on the bioadsoprtion process.

RESULTS AND DISCUSSION

The effect of ethanol, heat and NaOH treatment of non-living *Phanerochaete chrysosporium* mycelial pellets on Pb(II) biosorption was investigated in aqueous suspension. Figure 2a and 2b shows the effect of different treatments on Pb(II) biosoption capacity at 25 and 50 mg l^{-1} initial Pb(II) concentrations at 22^{o}C. The biomass concentration was 1 g l^{-1}. The adsorbed amounts of Pb(II) are shown in Figure 1a and the bioadsorption efficiencies (expressed in percent, %) of Pb(II) are shown in Figure 1b for different cell surface treatments in the case of both initial concentrations. The alteration of Pb(II) bioadsorption capacity on the effect of cell surface treatment was the same at both initial concentrations, although the bioadsorption capacities did not change significantly due to the morphology of mycelial fungal pellets. Non-living fungal cells were used as reference biosorbent. For untreated fungal cells at 25 mg l^{-1} Pb(II) concentration the bioadsorption capacity q_s is 16.34 mg g^{-1} (65.35 %), at 50 mg l^{-1} Pb(II) concentration q_s is 42.05 mg g^{-1} (84.11 %). The fungal cells treated with ethanol had the maximum bioadsorption capacity, at 25 mg l^{-1} initial concentration q_s is 16.91 mg g^{-1} (67.64 %), at 50 mg l^{-1} initial concentration q_s is 42.60 mg g^{-1} (85.20 %).

The caustic and heat treatment of cells slightly reduced the Pb(II) bioadsorption capacity in comparison with untreated cells. In the case of heat treated cells, at 25 mg l^{-1} Pb(II) concentration the bioadsorption capacity q_s is 15.68 mg g^{-1} (62.73 %), at 50 mg l^{-1} Pb(II) concentration q_s is 41.54 mg g^{-1} (83.07 %). In the case of caustic treated fungal cells, at 25 mg l^{-1} Pb(II) concentration the bioadsorption capacity q_s is 16.06 mg g^{-1} (64.22 %), at 50 mg l^{-1} Pb(II) concentration q_s is 41.31 mg g^{-1} (82.62 %).

The results show that increasing initial concentration of Pb(II) increased the adsorbed amount of Pb(II) and adsorption efficiency for Pb(II) by biomass. Göksungur et al. (2005) studied the biosorption of Pb(II) and Cd(II) ions from artificial aqueous solution using waste baker's yeast. The yeast cells were treated by ethanol, caustic and heat for increasing their biosorption capacity and the highest metal uptake values were obtained by ethanol treated yeast cells.**[9]**.

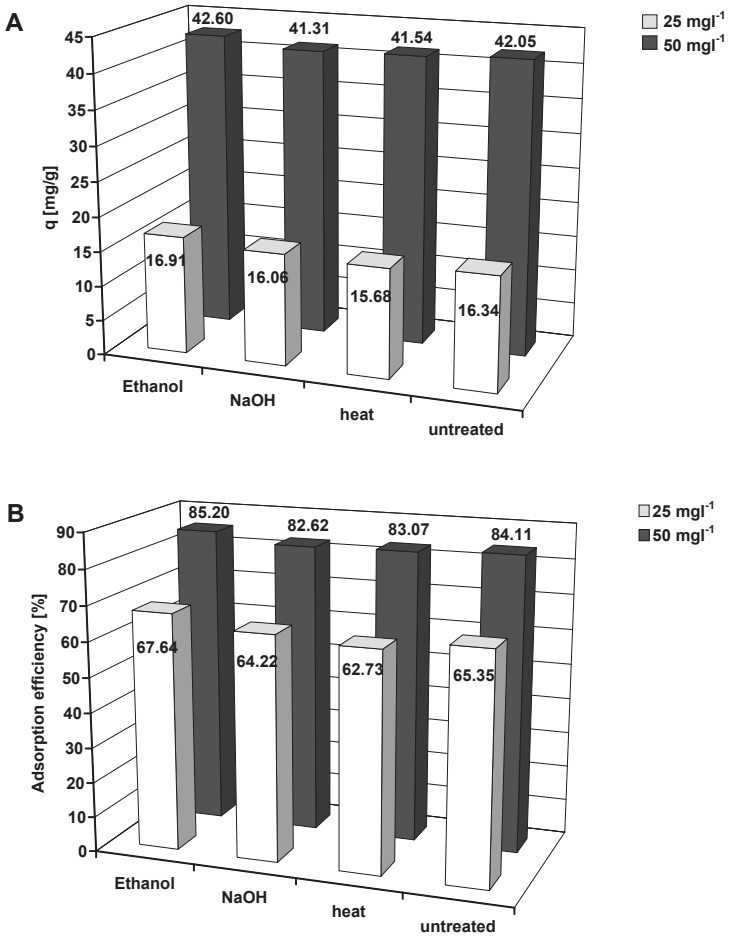

Figure 2: Effect of ethanol, heat, caustic treatment of fungal cells on Pb(II) bioadsorption process.

(a) The adsorbed amounts of Pb(II) and (b) the bioadsorption efficiencies are presented in the case of treated fungal cells.

Experimetal conditions: T = 22ºC, biomass concentration: 1 g l^{-1}, initial Pb(II) concentration: 25 and 50 mg l^{-1}, cell diameter: 0.5 – 1 mm, pH = 5.9.

The effect of temperature on Pb(II) bioadsorption by treated ***P. chrysosporium*** *biomass*

The effect of temperature on Pb(II) bioadsorption was also investigated at initial concentration of 50 mg l^{-1} at suspension concentration of 1 g l^{-1}. In Figure 3a the adsorbed amounts of Pb(II) and in Figure 3b the adsorption efficiencies for Pb(II) are presented in the case of treated fungal cells.

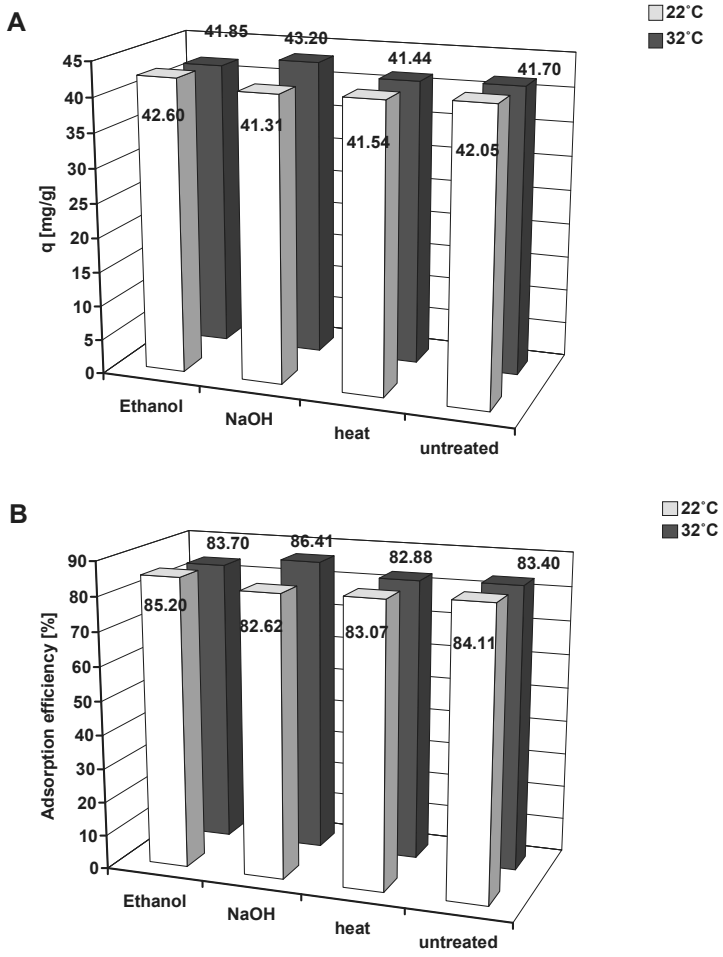

Figure 3. Effect of temperature on Pb(II) bioadsorption by ethanol, heat, caustic and untreated fungal cells. (a) The adsorbed amounts of Pb(II) and (b) the bioadsorption efficiencies are presented in the case of treated fungal cells. Experimetal conditions: T = 22.5 and 32 ºC, biomass concentration: 1 g l^{-1}, initial Pb(II) concentration: 25 and 50 mg l^{-1}, cell diameter: 0.5 – 1 mm, pH = 5.9.

The experimental results showed that increasing temperature slightly decreased the Pb(II) uptake by heat and ethanol treated fungal cells. This effect is well known and could be explained with the phenomena of ionic radius. The ionic radius of Pb (II) ion is 121 pm. A stronger physical affinity to Pb (II) ions was expected at the biosorption sites on the cells. This argument is consistent with the stronger temperature dependence of Pb (II) because physical adsorption forges a relatively loose and unstable combination that can be affected easily by thermal movement of the ions **[19]**.

For reference fungal cells at 22^{o}C the adsorption capacity q^{s} *i*s 42.05 mg g^{-1} (84.13 %), at 32^{o}C the adsorption capacity q^{s} *i*s 41.70 (83.40 %) mg g^{-1}. For heat treated fungal cells at 22^{o}C the adsorption capacity q^{s} *i*s 41.53 mg g^{-1} (83.07 %), at 32^{o}C the adsorption capacity q^{s} *i*s 41.44 mg g^{-1} (82.88 %). For ethanol treated fungal cells at 22^{o}C the adsorption capacity q^{s} *i*s 42.60 mg g^{-1} (85.2 %), at 32^{o}C the adsorption capacity q^{s} *i*s 41.85 (83.70 %) mg g^{-1}.

The heat treated biomass had the lowest adsorption capacity at 32^{o}C with 41.44 mg g^{-1}. Surprisingly the caustic treatment of fungal cells resulted a higher adsorption with 43.20 mg g^{-1} (86.41 %) at 32^{o}C in comparison with 41.31 mg g^{-1} (82.62 %) value at 22^{o}C The caustic treated biomass had the highest bioadsorption capacity for Pb(II) at 32^{o}C. This effect of caustic treatment on metal uptake was explained by the removal of protein groups of the cell wall that make non-adsorbable protein complexes with heavy metals **[25].**

CONCLUSION

In this study the effect of ethanol, heat and caustic cell surface treatment of *Phanerochaete chrysosporium* biomass on Pb(II) bioadsorption was studied at room temperature and elevated temperature (T = 32 ^{o}C). The ethanol treatment of fungal biomass resulted a higher adsorption capacity for Pb(II), while the caustic and heat treatment of cells slightly decreased the bioadsorption capacity at 22^{o}C. The experimental results showed that increasing temperature slightly decreased the Pb(II) uptake by heat and ethanol treated fungal cells, while the bioadsorption capacity of caustic treated fungal cells for Pb(II) increased in comparison with reference fungal cells. On the basis of results it can be revealed that the heat, ethanol and caustic cell surface treatment does not affect significantly the bioadsorption capacity of mycelial pellets of *Phanerochaete chrysosporium* for heavy metal due to the cell morphology. The treated and untreated *Phanerochaete chrysosporium* biomass can be used effectively as a biosorbent to remove Pb(II) from wastewaters.

EXPERIMENTAL SECTION

Chemicals

All chemicals were used in reagent grade. Stock Pb(II) solution were prepared by dissolving 0.799 g lead nitrate in 1 l of distilled water (500 mg l^{-1}). The Pb(II) concentration of the prepared solution varied between 25 and 50 mg l^{-1} for the biosorption experiments. The pH value was adjusted by using 0.1 M NaOH and HCl solutions.

Biomass cultivation

Phanerochaete chrysosporium was obtained from the Department of Environmental Microbiology, Faculty of Science, University of Pécs, Hungary was used in this study. It was cultivated as prevously described by Kirk et al **[24].** After 5 day incubation at 35^{o}C on a shaker (app. 180 rpm), the mycelial pellets were removed from the medium through filtration and inactivated in a pressure cooker at high temperature (120^{o}C) for 20 min.

Then, the mycelial pellets were washed several times with distilled water. These mycelial pellets were treated in the next step.

Preparation of treated biomass

Heat, caustic, ethanol treated *P. chrysosporium* fungal biomass were used in this study. For ethanol treatment 5 g of fungi was dissolved in 70 % (v/v) ethanol solution for 20 min. Then washed several times with distilled water 1 g of fungal cells was dissolved in 20 ml of 1 mol dm^{-3} NaOH solution for 15 min in the case of caustic treatment. For heat treatment 1g of fungi was put in 20 ml of distilled water and dried for 15 min at 120^{o}C in oven, so the heat treatment of biomass was duplicated.

Morphological study with Scanning Electron Microscope (SEM)

SEM studies were investigated in the Central Electron Microscope Laboratory, Faculty of Medicine, University of Pécs. Jeol JSM-6300 scanning electron microscope was used in this study.

Samples were only liophilized as a drying procedure before golden layer labelling. No further fixation procedure were done during the sample preparation protocol.

Study of bioadsorption

Biosorption experiments were carried out in batch mode to determine the adsorption capacity of the treated *Phanerochete chrysosporium* biomass. The biomass concentration was 1 g l^{-1}, 0.025 g dry mycelial pellets were mixed with 25 ml of solution containing a pre-determined concentration of

Pb(II) ion. Mycelial pellets and lead solution were placed in a test-tube. Tubes were agitated on a shaker at 150 rpm at constant temperature (22.5 and 32 ± 0.2°C). All experiments was performed at 22 and 32°C.

Samples were taken after 12 hours when the solution reached the equilibrium. Then they were centrifuged at 10 000 rpm for 10 min. The supernatant was used for analysis of the residual lead.

The adsorbed amount of lead(II) ion at equilibrium, q (mg/g), was obtained as follows:

$$q = \frac{(c_0 - c_e)V}{m} \quad (1)$$

where,

c_0 and c_e are the initial and equilibrium liquid phase concentrations (mg l^{-1})
V is the volume of the solution (l) and
m is the weight of the dry biomass used (g).

Analysis

Atom absorption spectrophotometer (AAS) was used to determine the equilibrium concentration of Pb(II) in the solution using standard calibration curve. Lead nitrate dissolved in nitric acid as standard solution (1000 mg/l) was from Scharlau Chemie (Germany). The Perkin Elmer AAS system was contained an Interlocked Gas Control System, and a wavelenght drive. The experiments were performed on an UV/VIS photo diode array detector at a wavelenght of 217 nm.

Standard calibration curve in the range of 1 -10 mg l^{-1} was made from lead stock solution (Scharlau, 1000 mg l^{-1}).

ACKNOWLEDGEMENT

Timea Pernyeszi and Alžbeta Hegedűsova gratefully acknowledge support for this research from the Hungarian-Slovak Intergovernmentals & Cooperation Programme (APVV SK-HU 0018-08, SK 18/2008) between University of Pécs and Constantine the Philosopher University for 2009-2011.

REFERENCES

1. P.A.S.S. Marques, M.F. Rosa, H.M. Pinheiro, *Bioprocess Engineering*, **2000**, *23*, 135.
2. J.L. Wang, C. Chen, *Biotechnology Advances*, **2006**, *24*, 427.
3. G.M. Gadd, Phytologist, **1993**, *124*, 25.

4. E. Furest, B. Volesky, *Appl. Biochem. Biotechnol*., **1997**, *67*, 215.
5. E.G. Furuya, H.T. Chang, Y. Miura, K.E. Noll, *Separation and Purification Technology,* **1997**, *11*, 69.
6. C. Quintelas, E. Sousa, F. Silva, S. Neto, T. Tavares, *Process Biochemistry*, **2006**, *41*, 2087.
7. J. Febrianto, A.N. Kosasih, J. Sunarso, Y-H. Ju, *Journal of Hazardous Materials*, **2009**, *162*, 616.
8. G-Y. Li, K-L. Huanq, Y-R. Jiang, P. Ding, *Process Biochemistry*, **2007**, *42*, 1465.
9. Y. Göksungur, S. Üren, U. Güvenc, *Bioresource Technology*, **2005**, *96*, 103.
10. A.Y. Dursun, *Biochemical Engineering Journal*, **2006**, *28*, 187.
11. A. Kapoor, T. Viraraghavan, *Bioresource Technology*, **1997**, *61*, 221.
12. S. Dey, P.R.N. Rao, B.C. Bhattacharyya, M. Bandyopadhyay, *Bioprocess Engineeering,* **1995**, *12*, 273.
13. M.Y. Arica, Ç. Arpa, A. Ergene, G. Bayramoğlu, Ö. Genç, *Carbohydrate Polymers*, **2003**, *52*, 167.
14. A. Denizli, F.Cihangir, A.Y. Rad, M. Taner, G. Alsancak, *Process Biochemistry*, **2004**, *39*, 2025.
15. Y. Kacar, C. Arpa, S. Tan, A. Denizli, Ö. Genc, M.Y. Arica, *Process Biochemistry,* **2002**, *37*, 601.
16. M.Y. Arica, Y. Kacar, Ö. Genc, *Bioresource Technology*, **2001**, *80*, 121.
17. I. García, P.R.J Pena,.B. Venceslada, A.M. Martín, M.A.M. Santos, E.R. Gómez, *Process Biochemistry*, **2002,** *35*, 751.
18. U. Yetis, A. Dolek, F.B. Dilek, G. Ozcengiz, *Wat. Res*., **2000**, *34*(16) 4990.
19. R. Say, A. Denizli, M.Y. Arica, *Bioresource Technology*, **2001**, *76*, 67.
20. A.K. Haritash, C.P. Kaushik, *Journal of Hazardous Materials*, **2009**, *169*, 1.
21. Q. Li, S. Wu, G. Liu, X. Liao, X. Deng, D. Sun, Y, Hu, Y. Huang, *Separation and Purification Technology,* **2004**, *34*, 135.
22. M. Iqbal, R.G.J. Edyvean, *Minerals Engineering*, **2004,** *17*, 217.
23. M. Íqbal, A. Saeed, *Process Biochemistry*, **2007**, *42*, 1160.
24. K.T. Kirk, E. Schultz, W.J. Connors, L.F. Lorenz, J.G. Zeikus, *Arch. Microbiol.,* **1978**, *117*, 277.
25. Y. Göksungur, S. Üren, U. Güvenc, *Tr. J. Biology*, **2003**, *27*, 23.

STUDIA UBB CHEMIA, LVI, 2, 2011 (p. 75 - 84)

A NOTE ON NULLITY OF GRAPHS

MODJTABA GHORBANI[a], MAHIN SONGHORI

ABSTRACT. The nullity of a graph is defined as the multiplicity of the eigenvalue zero in the spectrum of the adjacency matrix of the graph. In this paper we investigate the nullity of some classes of graphs.

Keywords*: Graph, Adjacency matrix, Nullity, Dendrimer.*

INTRODUCTION

Chemical graph theory is an important tool for studying molecular structures [1-3]. This theory had an important effect on the development of chemical sciences. All graphs considered in this paper are simple and connected. The vertex and edge sets of a graph G are denoted by $V(G)$ and $E(G)$, respectively. Let $G = (V, E)$ be a graph and $e \in E(G)$. Then the subgraph symbolized $G\backslash e$ is the subgraph of G obtained by removing the edge e from G. Denoted by $G \setminus \{v_1, \ldots, v_k\}$ it means a graph obtained by removing the vertices $v_1, \ldots, v_k$ from G and all edges incident to any of them.

The adjacency matrix $A(G)$ of graph G with the vertex set $V(G) = \{v_1, v_2, \ldots, v_n\}$ is the $n \times n$ symmetric matrix $[a_{ij}]$, such that $a_{ij} = 1$ if v_i and v_j are adjacent and 0, otherwise. The characteristic polynomial $\Phi(G,x)$ of graph G is defined as

$$\Phi(G,x) = \det(A(G) - xI).$$

The roots of the characteristic polynomial are the eigenvalues of the graph G and form the spectrum of this graph. The number of zero eigenvalues in the spectrum of the graph G is called its nullity and is denoted by $\eta(G)$. Denote by $r(A(G))$ the rank of $A(G)$. The nullity is calculated by formula: $\eta(G) = n - r(A(G))$, where n is the number of vertices in G.

For instance, the adjacency matrix of a path on two vertices is

$$A(P_2) = \begin{pmatrix} 0 & 1 \\ 1 & 0 \end{pmatrix}.$$

[a] *Department of Mathematics, Faculty of Science, Shahid Rajaee, Teacher Training University, Tehran, 16785-136, I. R. Iran*

So, the characteristic polynomial of a path on two vertices is $\Phi(P_2,\lambda)=\lambda^2-1$ and the eigenvalues of P_2 are ± 1. On the other hand the rank $A(P_2)$ is 2. This implies the nullity of P_2 is zero.

For the second example consider the complete graph K_3. The adjacency matrix of K_3 is

$$A(K_3)=\begin{pmatrix}0 & 1 & 1\\ 1 & 0 & 1\\ 1 & 1 & 0\end{pmatrix}.$$

Hence, $\Phi(K_3,\lambda)=\lambda^3-3\lambda-2=(\lambda-2)(\lambda+1)^2$ and then -1, -1, 2 are its eigenvalues. This matrix is of rank 3 and so, $\eta(K_3)=0$.

The goal of this paper is computing the nullity of some dendrimer infinite classes of graphs. Throughout this paper all notations are standard and mainly taken from standard book of graph theory such as [4, 5]. We also refer the readers to consult papers [6, 7].

RESULTS AND DISCUSSION

The aim of this section is the computing of nullity of some bipartite graphs. For some graphs the spectrum is known and thereby their nullity $\eta(G)$. At first we enounce the following fundamental Lemma, useful to compute the nullity of graphs:

Lemma 1 [7 - 9]. (i) Let G be a graph on n vertices. Then $\eta(G) = n$, if and only if G is a graph without edges (a non-connected graph).

(ii) Let K_n, P_n and C_n, denote a complete graph, a path and a cycle on n vertices, respectively. Then

$$\eta(K_n)=\begin{cases}1 & n=1\\ 0 & n>1\end{cases},\ \eta(P_n)=\begin{cases}0 & 2\nmid n\\ 1 & 2\mid n\end{cases}\text{ and }\eta(C_n)=\begin{cases}2 & n\equiv 0(\text{mod }4)\\ 0 & \textit{otherwise}\end{cases}.$$

(ii) Let H be an induced subgraph of G. Then $r(H) \le r(G)$.

(iv) Let $G=G_1\cup G_2\cup\cdots\cup G_r$, where G_1, G_2, …, G_r are connected components of G. Then, $r(G)=\sum_{i=1}^{r} r(G_i)$, *i.e.*, $\eta(G)=\sum_{i=1}^{r}\eta(G_i)$.

(v) Let G_1 and G_2 be bipartite graphs. If $\eta(G_1)=0$ and if the graph G is obtained by joining an arbitrary vertex of G_1 by an edge to an arbitrary vertex of G_2, then $\eta(G)=\eta(G_2)$.

(vi) If the bipartite graph G contains a pendent vertex and the induced subgraph H of G is obtained by deleting this vertex together with the vertex adjacent to it, then $\eta(G)=\eta(H)$.

Now we are ready to compute the nullity of an infinite family of dendrimers graph. To do this, consider the following examples.

Example 2. Consider the graph A depicted in Figure 1. By using Lemma 1(v), $\eta(A) = \eta(A_1)$ and by Lemma 1(vi) $\eta(A_1) = \eta(A_2)$. Hence, $\eta(A) = 0 + 0 + 0 = 0$.

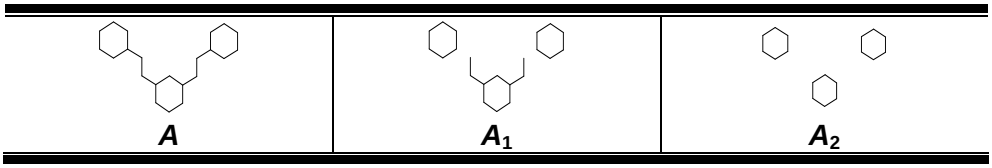

Figure 1. 2 *D* graph of *A*.

Example 3. Consider the graph B depicted in Figure 2. By using Lemma 1(v), $\eta(B) = \eta(B_1)$ and by Lemma 1(vi) $\eta(B_1) = \eta(B_2)$. Thus, according to Example 2, $\eta(B) = 0$.

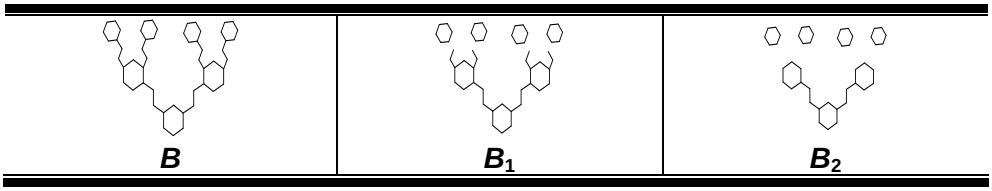

Figure 2. Computing the nullity of *B*.

Example 4. Consider the graph C depicted in Figure 3. By using Lemma 1(v), $\eta(C) = \eta(C_1)$ and by Lemma 1(vi) $\eta(C_1) = \eta(C_2)$. By continuing this method one can see that $\eta(C) = \eta(C_5) = 1$.

By using the above method we can prove the following Theorem:

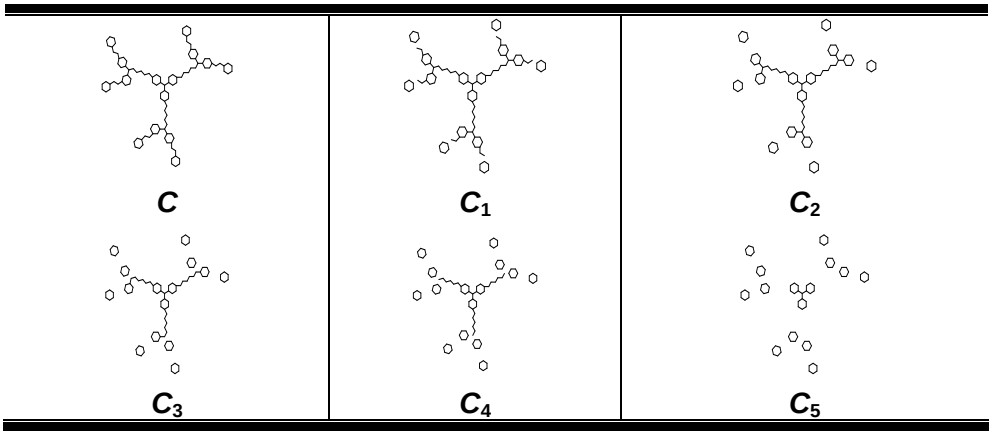

Figure 3. Computing the nullity of *C*.

Theorem 5. Consider the dendrimer graph $S[n]$ depicted in Figure 4. Then, $\eta(S[n]) = 1$.

Proof. By using Examples 2 and 3 one can see that $\eta(S[n]) = \eta(C_5)$. According to Example 4, this value is 1 and the proof is completed.

Now, we compute the nullity of the nanostar dendrimer graph $D[n]$ depicted in Figure 5. If n = 1 it is easy to see that $\eta(D[1]) = 1$. For n = 2, $\eta(D[2]) = 2$. In generally we have the following Theorem:

Theorem 6. Consider nanostar dendrimer $D[n]$, then

$$\eta(D[n]) = \begin{cases} 1 & n = 1 \\ 2 & n = 2 \\ 2^{n-1} & n \neq 1,2 \end{cases}.$$

Proof. For the cases n = 1, 2 the proof is clear. Suppose $n \geq 3$, by using Lemma 1(v), one can see that $\eta(D[n]) = \eta(D) = \eta(D_1)$. On the other hand, by Lemma 1(vi), one can deduce that $\eta(D_1) = \eta(D_2) = ... = \eta(D_{10})$. In overall, the nullity of this dendrimer is related to the number of branches of $D[n]$ and so, the proof is completed.

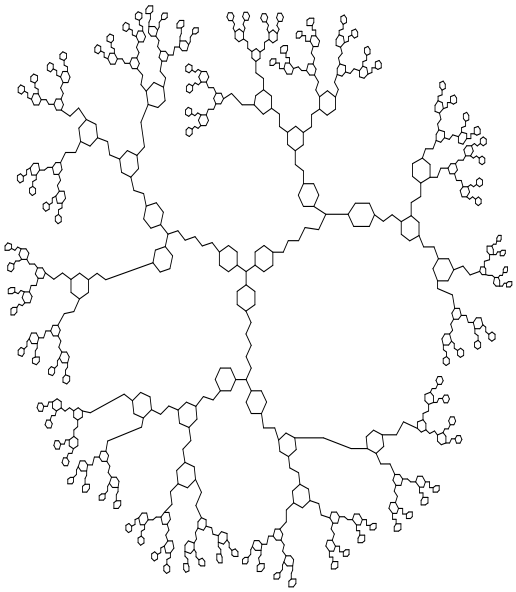

Figure 4. 2 *D* graph of $S[n]$.

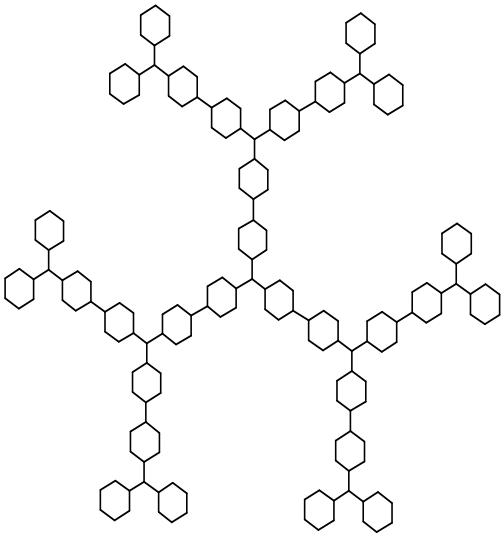

Figure 5. 2 *D* graph of *D*[*n*], for *n* = 3.

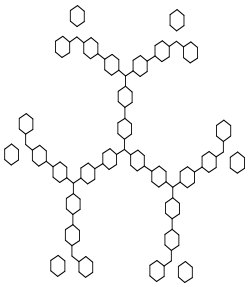	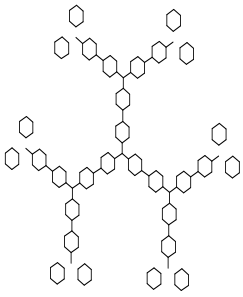	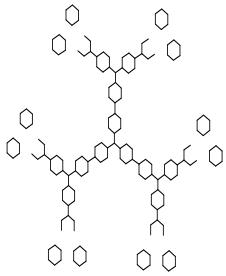
D	***D*$_1$**	***D*$_2$**
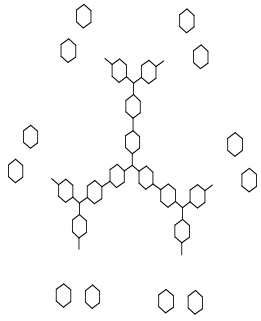	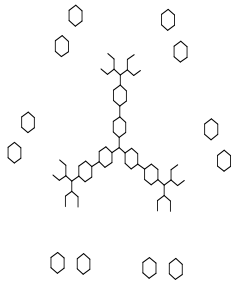	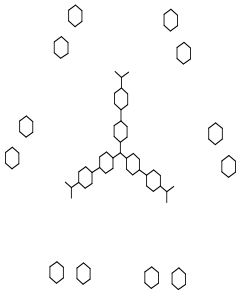
***D*$_3$**	***D*$_4$**	***D*$_5$**

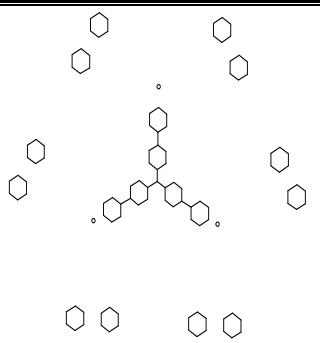	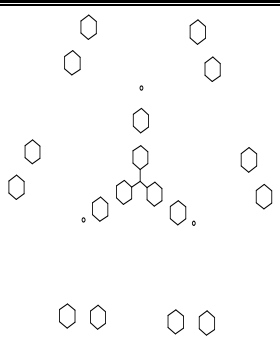	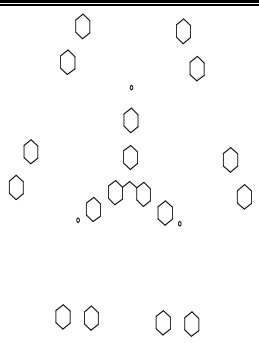
D_6	D_7	D_8
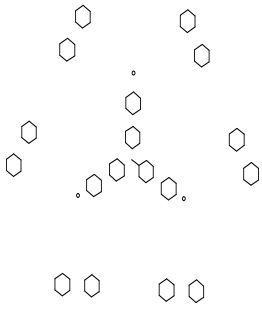	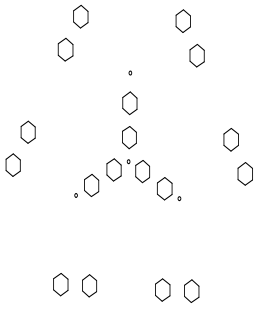	
D_9	D_{10}	

Figure 6. Computing nullity of $D[n]$, for $n = 3$.

A hypercube (Figure 7) define as follows:

The vertex set of the hypercube H_n consist of all n-tuples $b_1b_2\ldots b_n$ with $b_i \in \{0,1\}$. Two vertices are adjacent if the corresponding tuples differ in precisely one place. Clearly the hypercube H_n is isomorphic to $K_2 \times \cdots \times K_2$.

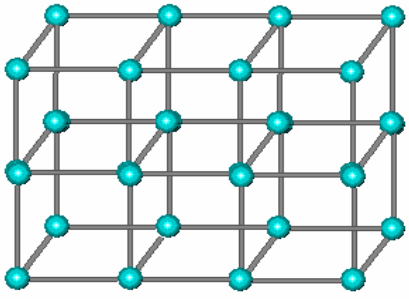

Figure 7. 3-D Graph of a Hypercube.

Theorem 7 [1]. Suppose *G* and *H* be two graph with eigenvalues λ_i $(1 \le i \le n)$ and μ_j $(1 \le j \le m)$. Then the eigenvalues of Cartesian product $/\!/ \times /\!/$ are $\lambda_i + \mu_j$.

As a corollary of Theorem 7, we compute the nullity of the hyper cube H_n. It is well – known fact the spectrum of K_n is as follows:

$$Spec(K_n) = \begin{pmatrix} -1 & n-1 \\ n-1 & 1 \end{pmatrix}.$$

So, the eigenvalues of K_2 are ± 1 with multiplicity 1. According to Theorem 7,

$$Spec(K_2 \times K_2) = \begin{pmatrix} -2 & 0 & 2 \\ 1 & 2 & 1 \end{pmatrix}.$$

By continuing this method, one can see that the spectrum of $K_2 \times \cdots \times K_2$ is:

$$Spec(K_2 \times \cdots \times K_2) = \begin{cases} \begin{pmatrix} -n & \cdots & -2 & 0 & 2 & \cdots & n \\ 1 & \cdots & \binom{n}{(n-2)/2} & \binom{n}{n/2} & \binom{n}{(n+2)/2} & \cdots & 1 \end{pmatrix} & 2 \mid n \\ \\ \begin{pmatrix} -n & 2-n & \cdots & -1 & 1 & \cdots & n-2 & n \\ 1 & \binom{n}{1} & \cdots & \binom{n}{(n-2)/2} & \binom{n}{n/2} & \cdots & \binom{n}{n-1} & 1 \end{pmatrix} & 2 \nmid n \end{cases}.$$

This implies the nullity of K_n is as follows:

$$\eta(K_n) = \begin{cases} \binom{n}{n/2} & 2 \mid n \\ 0 & 2 \nmid n \end{cases}.$$

Example 8. Consider the raph G_r, with *r* hexagons, depicted in Figure 8(a). By using Lemma 1(v) it is easy to see that $\eta(G_r) = \eta(G_{r-1})$ $(r = 1, 2, ...)$. By induction on *r* it is clear that $\eta(G_r) = 0$. Now consider graph H_r (Figure 8(b)). Since this graph has a pendent vertex, so by Lemma 1(vi), $\eta(H_r) = \eta(T_{r-1})$. Again we use Lemma 1(vi) and then we have $\eta(T_{r-1}) = \eta(H_{r-1})$. By continuing this method we see that $\eta(H_r) = \eta(H_1)$. H_1, has a pendent vertex joined to a

hexagon. Lemma 1(vi) implies that $\eta(H_1) = \eta(P_5)$. By Lemma 1(ii) it results that $\eta(H_r) = \eta(P_5) = 1$.

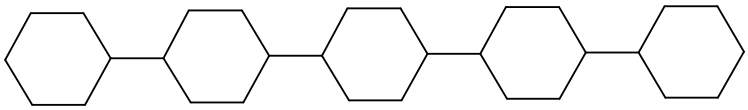

Figure 8 (*a*). Graph G_r.

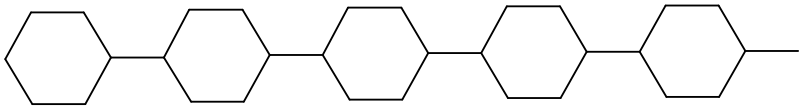

Figure 8(*b*). Graph H_r.

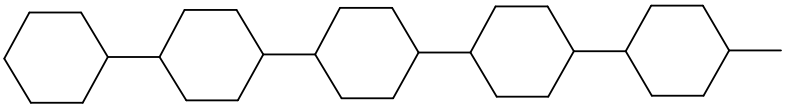

Figure 8(*c*). Graph $T_{r\text{-}1}$.

Recall that a set M of edges of G is a matching if every vertex of G is incident with at most one edge in M; it is a perfect matching if every vertex of G is incident with exactly one edge in M. Maximum matching is a matching with the maximum possible number of edges. The size of a maximum matching of G is the maximum number of independent edges of G and is denoted by $m = m(G)$.

Theorem 9 [2]. If a bipartite graph G with $n \geq 1$ vertices does not contain any cycle of length $4s$ ($s = 1, 2, \ldots$), then $\eta(G) = n - 2m$, where m is the size of its maximum matching.

In this section, by using Theorem 9, we compute the nullity of triangular benzenoid graph $G[n]$, depicted in Figure 9. The maximum matching of $G[n]$ is depicted in Figure 10. In other words, to obtain the maximum matching at first we color the boundary edges, they are exactly $3 \times n$ edges. The number of colored vertical edges in the k^{th} row is $k - 1$. Hence, the number of colored vertical edges is $1 + 2 + \ldots + n - 2 = (n - 1)(n - 2)/2$. By summation of these values one can see that the number of colored edges is $3n + (n - 1)(n - 2)/2 = (n^2 + 3n + 2)/2$ which is equal to the size of maximum matching. This graph has $n^2 + 4n + 1$ vertices, $3(n^2 + 3n)/2$ edges and, by using Theorem 9, $\eta(G[n]) = n^2 + 4n + 1 - (n^2 + 3n + 2) = n - 1$, thus we proved the following Theorem:

Theorem 10. $\eta(G[n]) = n - 1$.

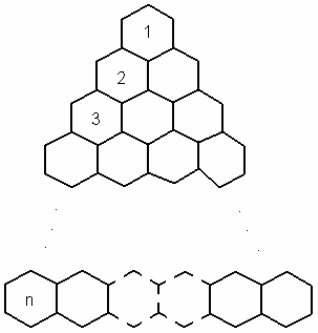

Figure 9. Graph of triangular benzenoid *G*[n].

There is an interesting result, provided by Theorem 10: the nullity of triangular benzenoid structures is very close to n, which is the value for a non-connected molecular graph. If so, this means a molecule showing such a graph cannot exist (as a bounded collection of atoms). A similar conclusion, even differently argued, was emitted by Clar [14] (see also ref. [15]).

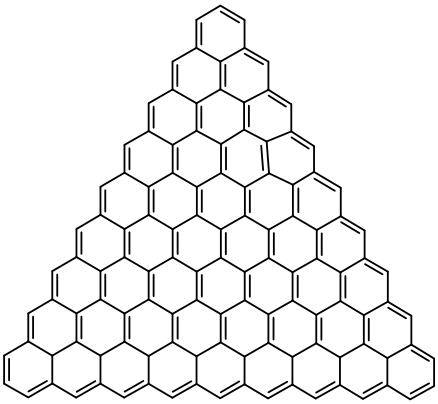

Figure 10. Graph of triangular benzenoid *G*[n].

CONCLUSION

Chemical graph theory is an important tool for studying molecular structures. This theory had an important effect on the development of the chemical sciences. In this paper we computed the nullity of some chemical graphs. This number, related to the spectral graph theory, can be informative in some extreme cases, when (quasi) non-bounded molecular graphs are predicted.

REFERENCES

1. M. V. Diudea (Ed.), “QSPR/QSAR Studies by Molecular Descriptors”, NOVA, New York, **2001**.
2. M. V. Diudea, I. Gutman, L. Jäntschi, “Molecular Topology”, NOVA, New York, **2002**.
3. M. V. Diudea, M. S. Florescu, P. V. Khadikar, “Molecular Topology and Its Applications”, EFICON, Bucharest, **2006**.
4. D.M. Cvetković, M. Doob, H. Sachs, “Spectra of Graphs”, Academic, New York, **1980**.
5. D.M. Cvetković, I. Gutman, N. Trinajstić, *Croat. Chem. Acta,* **1972**, *44*, 365.
6. S. Fiorini, I. Gutman, I. Sciriha, *Linear Algebra Appl*., **2005**, *397*, 245.
7. D. Cvetković, I. Gutman, “Application of Graph Spectra”, Matematićki institut SANU, Belgrade and Kragujevac, **2009**.
8. D.M. Cvetković, I. Gutman, *Mat. Vesnik*, **1972**, *9*, 141.
9. A. J. Schwenk, R. J. Wilson, “On the eigenvalues of a graph”, in: L. W. Beineke, R. J. Wilson, Eds., “Selected Topics in Graph Theory”, Academic Press, London, **1978**.
10. A. R. Ashrafi, M. Ghorbani, “Eccentric Connectivity Index of Fullerenes”, in: “Novel Molecular Structure Descriptors – Theory and Applications II”, 183-192.
11. A. R. Ashrafi, M. Saheli, M. Ghorbani, *Journal of Computational and Applied Mathematics*, http://dx.doi.org/10.1016/j.cam.2010.03.001.
12. M. Ghorbani, A. R. Ashrafi, M. Hemmasi, *Optoelectron*. *Adv. Mater. - Rapid Comm*., **2009**, *3*(12), 1306.
13. M. Jalali, M. Ghorbani, *Studia UBB Chemia*, **2009**, *4*(2), 145.
14. E. Clar, “The Aromatic Sextet”; J. Wiley & Sons: London, **1972**.
15. M. Randić, *Chem. Rev*., **2003**, *103*, 3449-3605 (3517).

STUDIA UBB CHEMIA, LVI, 2, 2011 (p. 85 - 93)

THE RHEOLOGICAL STUDY OF SOME SOLUTIONS BASED ON SURFACE-ACTIVE AGENTS (I)

ANDRA TĂMAŞ[a], MARTIN VINCZE[b]

ABSTRACT. The paper presents the rheological behavior study of some solutions based on surface-active agents used as auxiliaries in oil extraction technology. The influence of surfactants' structure and concentration was determined, as well as that of temperature, on the rheological behavior, by setting the dependence between the shear stress τ and the shear rate $\dot{\gamma}$. The analysis of dependence $\tau = f(\dot{\gamma})$ demonstrates that the solutions studied present non-Newtonian behavior.

Keywords: *real plastic behavior, shear rate, shear stress, surface-active agents*

INTRODUCTION

In the oil extraction process, after a certain period of operation, oil-wells depletion occurs, that means a drasting drop in productivity. The phenomenon is mostly significant in the case of the deposits whose structure is based on clays, which become hydrated in contact with water, undergoing a "swelling" process followed by the clogging of the well [1-3].

In order to increase the layer's porosity and permeability, a porous material (usually sand of a certain granulation) is introduced in the deposit through the existing cracks. The sand spreading must be done by means of a fluid carrier. The first types of fluid carriers were hydrogels (hydroxyethyl-cellulose, carboxymethylcellulose), their main disadvantage being the difficult removal from the deposit's cracks after the solid material sedimentation [3-6].

Subsequently, viscoelastic solutions were used, characterized by a very good carrying capacity for the solid material, which, in contact with crude oil, suddenly lose their viscoelastic properties (due to the change of micelar structure), leave the solid in the cracks and are then eliminated from those [5,7]. The well-known viscoelastic fluids are the solutions with cationic surfactants content [7].

[a] *Universitatea "Politehnica" din Timişoara, Facultatea de Chimie Industrială şi Ingineria Mediului, P-ţa Victoriei 2, RO-300006 Timişoara, România, andra.tamas@chim.upt.ro*
[b] *vinczemartin@hotmail.com*

Viscoelasticity may be caused by the forming process of the micelles in this case, which is different from that related to the usual ones, which are spherical [8]. Viscoelastic fluids based on surface-active agents formed very long flexible ("wormlike") cylindrical micells in solutions, which confer them useful rheological properties.

The preparation of solutions was done by dispersing water (W) under intense stirring in surfactants mixture (VA+VB and VAD+VB, respectively) at room temperature (t~25°C). The main characteristics of the surface-active agents are found in Table 1, and the compositions of the solutions obtained are presented in Table 2. The critical micellar concentration (CMC) has been determined of VA and VB aqueous solutions with different concentrations.

Table 1. The properties of the surface-active agents used

Symbol	Type	Active substance %	Molecular weight, $kg \cdot kmol^{-1}$	CMC, $mol \cdot L^{-1}$	pH of 1% aq. solution
VA	anionic	35	362	$1.5 \cdot 10^{-3}$	7÷8
VB	amphiphilic	30	355	$8.7 \cdot 10^{-4}$	7÷7.5
VAD	weakly cationic	100	488	-	-

Table 2. The composition of solutions with VA content

Symbol	Compozition, wt %	Symbol	Compozition, wt %
P_{12}	3%VA+2%VB+95%W	P_{14}	5%VA+2%VB+93%W
P_{22}	3%VA+6%VB+91%W	P_{24}	5%VA+6%VB+89%W
P_{32}	3%VA+8%VB+89%W	-	-
P_{42}	3%VA+10%VB+87%W	P_{44}	5%VA+10%VB+85%W
P_{52}	3%VA+12%VB+85%W	P_{54}	5%VA+12%VB+83%W
P_{62}	3%VA+16%VB+81%W	P_{64}	5%VA+16%VB+79%W

The rheological characterization of the solutions prepared was carried out using rotational viscometer Rheotest-2, under thermostatic conditions. It was followed the establishment of rheological relations $\tau = f(\dot{\gamma})$ where τ and $\dot{\gamma}$ are the shear stress and the shear rate, respectively, as well as the calculation of viscous flow energy E_a.

The characterization of liquids flow in ring-shaped spaces is expressed using the Taylor-Reynolds number, Ta_{Re} which depends on the geometry of the ring-shaped space (radii of the two cylinders), shear rate, liquid density and apparent viscosity [9]:

$$Ta_{\mathrm{Re}} = \frac{\dot{\gamma} \cdot (r_o - r_i)^2 \cdot \rho}{\eta_a} \quad (1)$$

RESULTS AND DISCUSSION

The influence of temperature on the rheological behavior was determined for samples P_{22}, P_{42}, P_{52} and P_{62} (with 3%VA) and for samples P_{44}, P_{54} and P_{64} (with 5% VA). In Figures 1 and 2, dependence $\tau = f(\dot{\gamma})$ is shown, at three temperature values, for solution P_{52} and P_{54}.

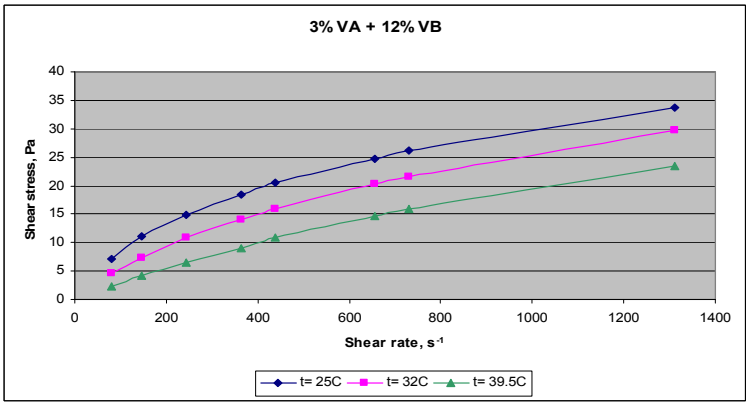

Figure 1. Dependence $\tau = f(\dot{\gamma})$ for P_{52} sample at different temperatures

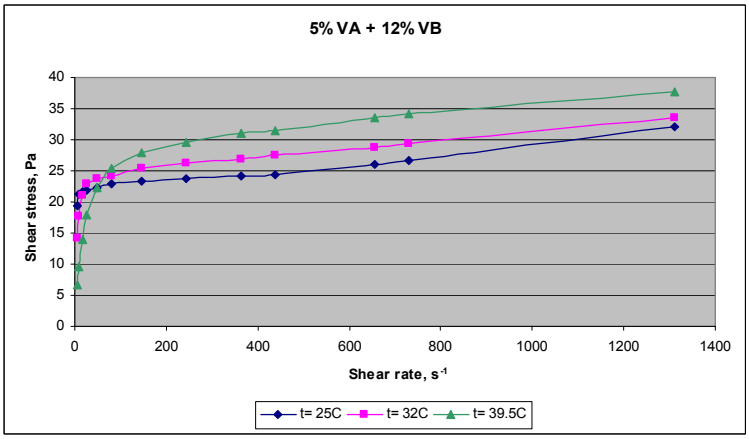

Figure 2. Dependence $\tau = f(\dot{\gamma})$ for P_{54} sample at different temperatures

The rheological equations are presented in Tables 3 and 4 for different $\dot{\gamma}$ range of values due to the change of curves inclination ($\dot{\gamma}_{ch}$ is the value of transition).

From the analysis of rheological equations for all solutions, the non-Newtonian behavior can be observed, similar to the real plastic fluids ($n<1$). Also, it was observed the decrease of coefficient K and the increase of the exponent n with the temperature increase (for P_{54} only for $\dot{\gamma}<48.6s^{-1}$), while the non-Newtonian behavior is maintained. The Ta_{Re} values increase with the temperature increase. For sample P_{54} is found that the shear stress increases as the temperature increases, as well as the change of curves slope at lower values of the shear rate.

Table 3. Rheological equations for P_{52} sample at various temperatures

Temp., °C	Equation $\tau=K\cdot\dot{\gamma}^n$	r^2	$\dot{\gamma}_{ch}$, s^{-1}	Ta_{Re}
25	$\tau=0.4\cdot\dot{\gamma}^{0.660},\ \dot{\gamma}\in(81\div243)s^{-1}$	0.9944	283.4	0.77
	$\tau=1.2\cdot\dot{\gamma}^{0.466},\ \dot{\gamma}\in(364.5\div1312)s^{-1}$	0.9979		
32	$\tau=0.14\cdot\dot{\gamma}^{0.793},\ \dot{\gamma}\in(81\div243)s^{-1}$	0.9998	281.9	1.04
	$\tau=0.46\cdot\dot{\gamma}^{0.583},\ \dot{\gamma}\in(364.5\div1312)s^{-1}$	0.9986		
39.5	$\tau=0.033\cdot\dot{\gamma}^{0.976},\ \dot{\gamma}\in(81\div243)s^{-1}$	0.9983	292.1	1.72
	$\tau=0.12\cdot\dot{\gamma}^{0.735},\ \dot{\gamma}\in(364.5\div1312)s^{-1}$	0.9964		

Table 4. Rheological equations for P_{54} sample at various temperatures

Temp., °C	Equation $\tau=K\cdot\dot{\gamma}^n$	r^2	$\dot{\gamma}_{ch}$, s^{-1}	Ta_{Re}
25	$\tau=19.7\cdot\dot{\gamma}^{0.032},\ \dot{\gamma}\in(9\div48.6)s^{-1}$	0.9985	10.1	0.00077
	$\tau=11.3\cdot\dot{\gamma}^{0.116},\ \dot{\gamma}\in(81\div1312)s^{-1}$	0.9632		
32	$\tau=10.7\cdot\dot{\gamma}^{0.234},\ \dot{\gamma}\in(9\div48.6)s^{-1}$	0.9798	23.9	0.0041
	$\tau=6.8\cdot\dot{\gamma}^{0.218},\ \dot{\gamma}\in(81\div1312)s^{-1}$	0.9936		
39.5	$\tau=3.4\cdot\dot{\gamma}^{0.496},\ \dot{\gamma}\in(9\div48.6)s^{-1}$	0.9830	70.6	0.032
	$\tau=14.2\cdot\dot{\gamma}^{0.133},\ \dot{\gamma}\in(81\div1312)s^{-1}$	0.9849		

The dependence $\tau=f(\dot{\gamma})$ for the samples with 3% VA and various percentages of VB, at 39.5˚C, is expressed in Figure 3 and the rheological equations are presented in Table 5.

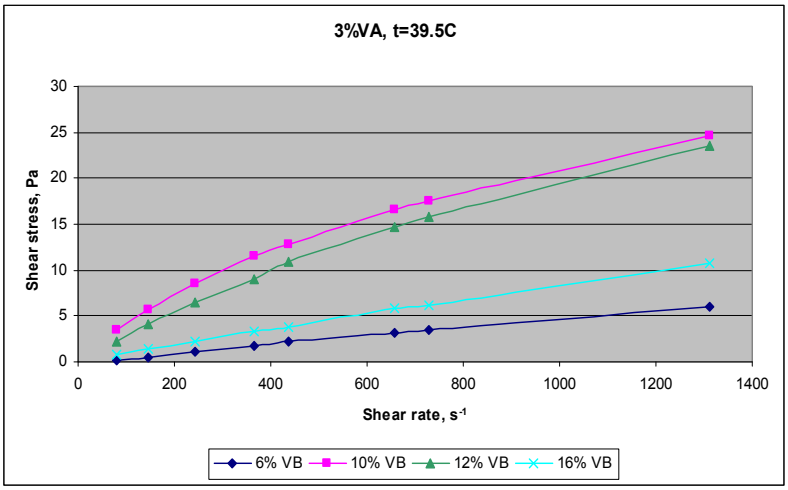

Figure 3. $\tau = f(\dot{\gamma})$ dependence for P_{22}, P_{42}, P_{52} and P_{62} samples

From Figure 3, for P_{22} and P_{62} samples it is observed that the $\tau = f(\dot{\gamma})$ dependence can be considered linear.

Table 5. Rheological equations for samples with 3% VA at 39.5˚C

Symbol	VB content, wt %	Equation	r^2
P_{22}	6	$\tau = 0.00475 \cdot \dot{\gamma}$	0.9952
P_{42}	10	$\tau = 0.17 \cdot \dot{\gamma}^{0.70}$	0.9925
P_{52}	12	$\tau = 0.06 \cdot \dot{\gamma}^{0.84}$	0.9942
P_{62}	16	$\tau = 0.0081 \cdot \dot{\gamma}$	0.9988

From the graphical representation of $\tau / \dot{\gamma}$ evolution as a function of shear rate for solutions with 3%VA (Figure 4) it is observed that the ratio decreases with the increase of $\dot{\gamma}$ (for samples with 10% and 12%VB). The apparent viscosity of the sample with 6%VB is significantly smaller than the other samples and decreases with the shear rate increase only at $\dot{\gamma} > 437.4 s^{-1}$. For samples containing 5%VA, in the same conditions, the apparent viscosity is significantly higher than 3%VA samples and decreases with the shear rate increase (Figure 5).

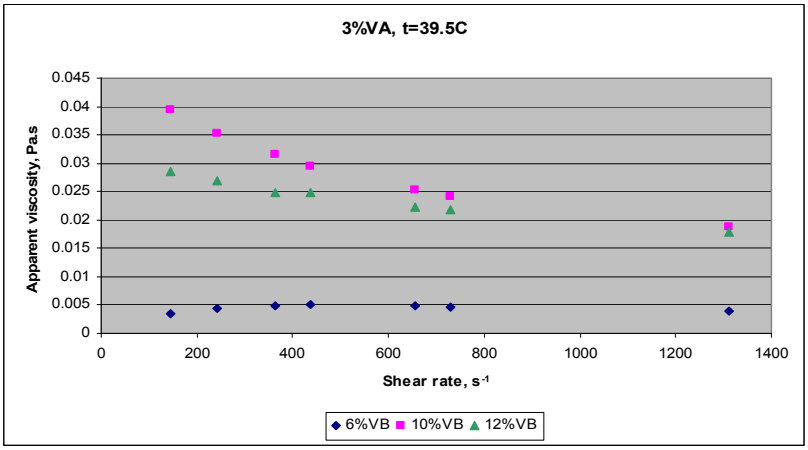

Figure 4. $\tau / \dot{\gamma} = f(\dot{\gamma})$ dependence for P_{22}, P_{42}, and P_{52} samples

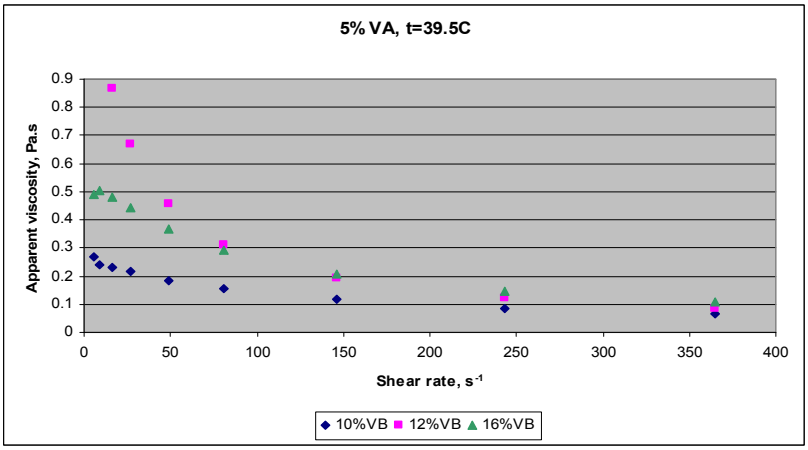

Figure 5. $\tau / \dot{\gamma} = f(\dot{\gamma})$ dependence for P_{44}, P_{54}, and P_{64} samples

The temperature increase leads to microdrops mobility intensification which influences the activation energy of the system. The phenomenon can be explained by Arhenius type equation applied to the cumulative effect described by the shear stress (eq. 2):

$$\tau = A^{'} \cdot e^{\frac{E_a}{R \cdot T}} \tag{2}$$

where: $A^{'}$ - preexponential coefficient having the dimension of shear stress; E_a - activation energy; R - general gas constant; T - absolute temperature.

The study of the influence of temperature on the activation energy of the system was done for all the analyzed solutions. Dependence $\ln\tau = f(1/T)$ was graphically represented, as obtained from the logarithmic form of equation (2), for shear stress values corresponding to the three chosen values of the shear rate.

Particular expressions of equation (2) for solutions with 3%VA are presented in Table 6.

Table 6. Particular expression of eq. (2) for samples P_{22}, P_{52} and P_{62}

$\dot{\gamma}\ s^{-1}$	**Equation** $\tau = A^{'} \cdot \exp(E_a/R \cdot T)$		
	P_{22}	**P_{52}**	**P_{62}**
145.8	$\tau = 5.6 \cdot 10^{-17} \cdot \exp(11.5/T)$	$\tau = 7.6 \cdot 10^{-9} \cdot \exp(3.0/T)$	$\tau = 1.9 \cdot 10^{-5} \cdot \exp(3.5/T)$
243	$\tau = 9.8 \cdot 10^{-14} \cdot \exp(9.4/T)$	$\tau = 3.6 \cdot 10^{-7} \cdot \exp(5.2/T)$	$\tau = 6.8 \cdot 10^{-6} \cdot \exp(3.9/T)$
729	$\tau = 2.4 \cdot 10^{-10} \cdot \exp(7.3/T)$	$\tau = 5.3 \cdot 10^{-4} \cdot \exp(3.2/T)$	$\tau = 6.0 \cdot 10^{-5} \cdot \exp(3.6/T)$

In Figure 6 the activation energy change is shown as related to the VB content for solutions with 3% VA.

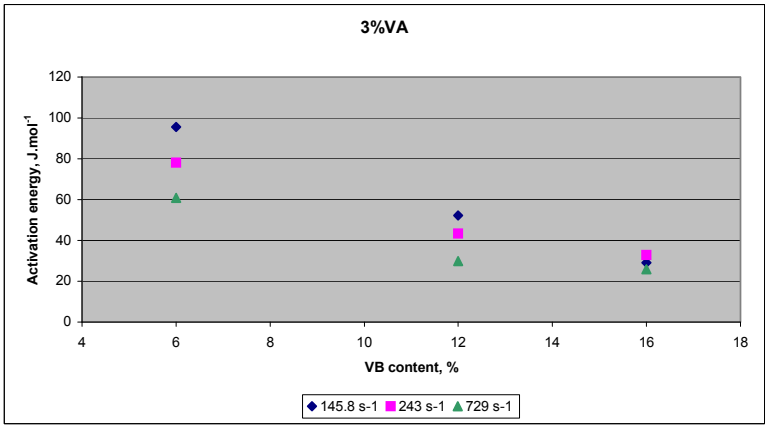

Figure 6. Activation energy changes for P_{22}, P_{52} and P_{62} samples

The variation of Ta_{Re} number with temperature and the VB content, respectively, is shown in Figure 7.

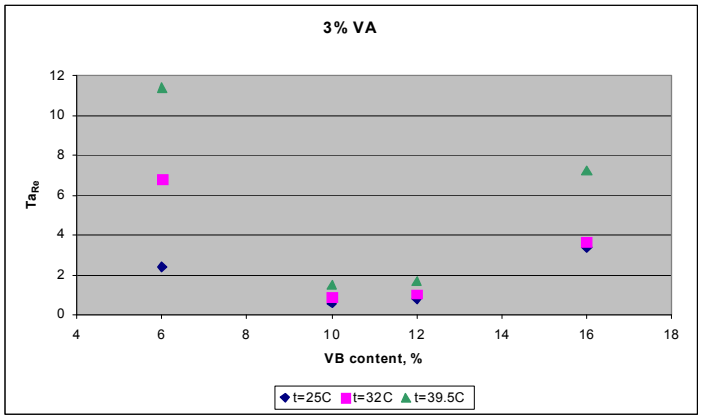

Figure 7. Ta_{Re} evolution for samples with 3% VA

CONCLUSIONS

The rheological behavior of solutions based on active-surface agents was studied, monitoring the influence of the nature and concentration of surfactants and of the temperature, respectively.

The rheological characterization was carried out in thermostatic conditions, using a rotational viscometer Rheotest-2 which correlates the shear stress value τ with the shear rate $\dot{\gamma}$. Specific rheological equations $\tau = K \cdot \dot{\gamma}^n$ were established.

P_{12}, P_{14} and P_{24} solutions could not be analysed using Rheotest-2 viscometer, as being too little viscous.

The temperature increase does not change the non-Newtonian nature of $\tau = f(\dot{\gamma})$ dependence, but leads to the increase of the shear stress value for samples with 5%VA. For the samples with 3%VA, the temperature increase leads to the decrease of exponent n and the increase of K.

The activation energy values decrease as the content of VB component and shear rate increase, which corresponds with the increase of Ta_{Re} number (according to the intensification of system turbulence).

For all temperatures there is a range of concentrations at which Ta_{Re} number has minimum values.

EXPERIMENTAL SECTION

Using the stalagmometer method (drop weight method) the surface tension has been determined of VA and VB aqueous solutions with different concentrations. From the dependence between the surface tension σ and

the concentration c natural logarithm the corresponding values of CMC were established.

Determinations were made using the viscometer Rheotest-2 with the system vat-drum S/S_1, in temperature range 25÷40°C.

The samples were analyzed immediately after preparation. Conservation of these solutions, at room temperature, for 2-3 months has not led to significant changes in rheological properties.

REFERENCES

1. T.S. Davies, A.M. Ketner, S.R. Raghavan, *J. Am. Chem. Soc.,* **2006**, *128,* 6669.
2. K. Hashizaki, N. Tamaki, H. Taguchi, Y. Saito, K. Tsuchiya, H. Sakai, M. Abe, *Chem. Pharm. Bull.*, **2008**, *56*(12), 1682.
3. R. Kumar, G.C. Kalur, L. Ziserman, D. Danino, S.R. Raghavan, *Langmuir*, **2007**, *23*, 12849.
4. J.R. Gladden, A. Belmonte, *Physical Review Letters*, **2007**, *98*, 224501.
5. M.C. Sostarecz, A. Belmonte, *Physics of Fluids*, **2004**, *16*(9), L67.
6. A. Bhardwaj, D. Richter, M. Chellamuthu, J.P. Rothstein, *Rheol. Acta*, **2007**, *46*, 861.
7. E. Miller, J.P. Rothstein, *J. Non-Newtonian Fluid Mech.*, **2007**, *143*, 22.
8. G. Schramm, "A Practical Approach to Rheology and Rheometry", Thermo Electron Karlsruhe, 2nd Edition, **2004**.
9. N. Borş, A. Tămaş, Z. Gropşian, *Chem. Bull. of "Politehnica" Univ. of Timişoara*, **2008**, *53*(67), 1-2, 16.

STUDIA UBB CHEMIA, LVI, 2, 2011 (p. 95 - 106)

A PRELIMINARY STUDY OF THE DYNAMIC BEHAVIOUR OF THERMAL CRACKING PROCESSES FOR IMPLEMENTING ADVANCED CONTROL AND OPTIMIZATION

ANDREEA SAVU[a], GHEORGHE LAZEA[a], PAUL-ŞERBAN AGACHI[b]

ABSTRACT. Nowadays industrial chemical processes must operate at maximum efficiency and one of the ways to save energy and still obtain high quality products is by using advanced process control.

The coking furnace is the heart of any thermal cracking installation and the coil outlet temperature influences directly the quality of the end products and the coke deposits on the walls. The major concern is to maintain a constant gas outlet temperature in order to decrease the deposits and implicitly maintain the tube metal temperature and the pressure, constant. Advanced control is a good alternative solution to obtain the desired product yield and still maintain the safety conditions, without changing the system's configuration or replacing the existent components with new ones.

A mathematical model of a thermal cracking coil was developed, based on free radical mechanism and some basic assumptions. In order to predict the coil's behaviour (temperature, product yields and pressure), a simulator for the dynamic process was used.

Keywords: *thermal cracking, coking plant, ethylene furnace, advanced control, optimization, real-time control systems.*

INTRODUCTION

Process models are usually used for the research of an operating strategy of a plant in an optimal mode, advanced process control systems (APC), for the training of operators and for a number of other studies (influences of the operating parameters and processing problems) that can be performed on the model in order to protect the real process from test disturbances. Additionally, a lot of control concepts are based on using a model of the process as part of the controller. This model based controllers' performance depend on the validity of the model. Several thermal cracking

[a] *Department of Automation, Technical University of Cluj-Napoca, 71-73 Dorobanţilor Street, 400609, Cluj-Napoca, România, Andreea.SAVU@aut.utcluj.ro, Gheorghe.Lazea@aut.utcluj.ro*

[b] *Department of Chemical Engineering and Oxide Materials Science, Babeş-Bolyai University Cluj-Napoca, 11 Arany János Street, 400028, Cluj-Napoca, România, sagachi@chem.ubbcluj.ro*

reactor models can be found in literature ([3], [5], [6], [10], [11] and others) and a full simulation of the reactor and the radiant box is provided by [7]. Some models for a delayed Coker are presented in the chemical engineering thesis of Albers [1].

According to Herink and Belohlav [4], the rigorous models are far more complex than models obtained using artificial neural networks, for example, and could be used for the design of pyrolysis furnaces, fundamental chemical engineering calculations and the prediction of the lighter feedstock cracking yields (ethane or naphtha).

It is not very difficult to implement a dynamic model described by differential equations, using specialized software, but to implement it using a real time control environment, such as Emerson's DeltaV Control Studio, it is a real challenge, because of the need to simplify its conditions and also obtain a valid model.

The purpose of this study is to design an optimal control system for the output variables of the simulated system. The starting point was the development of the dynamic model of an infinitesimal volume of pipe, Fig. 1, using the fundamental equilibrium equations: material balance, thermal balance and momentum balance. The method adopted for solving these equations is the Euler's Method for differential equations, even if efficiency loss may occur in comparison with results obtained applying other, more sophisticated methods, such as Runge-Kutta.

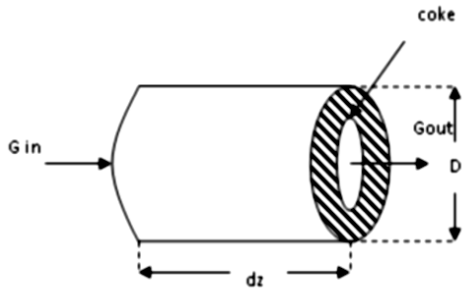

Figure 1. Differential element

The feed-forward control, the state estimators based control and the predictive model control (MPC) are all advanced control techniques that usually need a reliable model of a process. MPC is a method that uses the model of the process to calculate manipulated variable changes from the future predictions of the controlled variables, on the basis of a cost function as an objective which needs to be minimized.

THERMAL CRACKING FURNACES AND PROCESSES

The most frequently used thermal cracking furnaces in today's industry are the cracking furnace from the petrochemical field (cracking of naphtha, ethane, etc.) and the furnace from the coking plant.

The pyrolysis furnaces can be used for any type of raw material; the only implied condition being the boiling point that must be under 600^0 C. The furnace represents the centre of the cracking plant and the consumption of energy is also concentrated in this area. The desired products from this reaction are the light olefins, such as: ethylene, propylene and butadiene.

The furnace, described in this case, is similar to an ordinary fired heater but there are some differences concerning: the added dilution steam, the production of coke layers on the tubes, the testing of the effluent with a GC (gas chromatograph) and the effluent's routing to the TLE's (transfer line exchangers), for generating high pressure steam.

Ethylene is industrially obtained through thermal cracking of hydrocarbons. In order to obtain a larger amount of ethylene and decrease the energy and material loss, the process parameters must be held between certain limits, as follows [10]:

- Residence time inside the coil, between 0.08 and 0.25 [s] – as short as possible. In order to reduce the residence time, tubes' diameters are reduced; the fabrication materials are improved and the burners tend to be much more efficient.
- Dilution steam, measured as the ratio S/Hc (steam/hydrocarbon), between 0.3 and 0.6 – high quantity of steam. The dilution steam is introduced in the process to reduce the coke production and to decrease the gas pressure (minimize the undesired secondary reactions).
- Reaction pressure, between 175 and 240 kPa – as low as possible. Coil output pressure is indirectly controlled by the aspiration pressure of the gas compressor, placed downstream.
- Reaction temperature – at least 900^oC – as high as possible. The pyrolysis is an endothermic reaction and high temperature generates smaller hydrocarbons molecules. Lower temperature favors the production of coke and shortens the tubes' life.

CASE STUDY

The free radicals mechanism represents a universal accepted description of the hydrocarbons pyrolysis. Once the conversion and the olefin concentration increases, the secondary reactions become more frequent. A small segment of pipe, of infinitesimal volume is represented in Fig. 1.

According to the free radicals mechanism [8], the considered reactions are:

Initiation: $C_2H_6 \xrightarrow{k_1} CH_3\cdot + CH_3\cdot$ (1)

Propagation: $CH_3\cdot + C_2H_6 \xrightarrow{k_2} CH_4 + C_2H_5\cdot$ (2)

$C_2H_5\cdot \xrightarrow{k_3} C_2H_4 + H\cdot$ (3)

$C_2H_6 + H\cdot \xrightarrow{k_4} H_2 + C_2H_5\cdot$ (4)

Interruption: $H\cdot + C_2H_5\cdot \xrightarrow{k_5} C_2H_6$ (5)

$C_2H_5\cdot + C_2H_5\cdot \xrightarrow{k_6} C_4H_{10}$ (6)

$C_2H_5\cdot + CH_3\cdot \xrightarrow{k_7} C_3H_8$ (7)

$CH_3\cdot + CH_3\cdot \xrightarrow{k_8} C_2H_6$ (8)

$CH_3\cdot + H\cdot \xrightarrow{k_9} CH_4$ (9)

Dynamic model of the thermal cracking process

The mathematical description of a one-dimensional plug-flow reactor tube is presented, with the following assumptions: laminar flow regime, ideal gas behavior and inert steam used as diluent.

- Mass balance for component *j*:

$$dw_j/dt = -v\cdot\left(w_j - w_{j_0}\right)/dz\cdot\sum_i r_i \times S(i,j) \quad (10)$$

Where r_i is the i-th reaction rate and it evolves with temperature according to an Arrhenius equation:

$$r_i = A_i\cdot e^{-E_{i_j}/R\cdot T} \quad (11)$$

- Energy balance

$$dT_g/dt = v\cdot(T_g - T_{g\_0})/dz - \frac{[(T_g - T_W)\cdot A\cdot k_{T_g} + \sum_i r_i H_i + \varphi\cdot(T_W^4 - T_g^4)]}{\rho\cdot C_p} \quad (12)$$

$$dT_W/dt = A\cdot k_t\cdot\left(T_g - T_W\right)/\left(\rho\cdot C_p\right) \quad (13)$$

- Momentum balance:

$$dP/dt = d\rho/dt\cdot\frac{c_i^2}{(\rho^2\cdot g)}\cdot\left(\frac{2f}{D} - 1\right) \quad (14)$$

For the entire equation system (10), (12), (13) and (14), we have considered as outlet variables:

- w_j (j=1, 9) – components mass fraction for: ethane, methyl radical, methane, ethyl radical, ethylene, hydrogen radical, hydrogen, propane and butane
- Temperatures – T_g, T_W
- Density - ρ
- Pressure – P

The considered inlet variables are:

- Ethane concentration – $[C_2H_6]$;
- Fluid velocity inside the tube- v ($^{dz}/_{dt}$)

Implementation and simulation

The DeltaV system is a part of Plant Web architecture that uses predictive intelligence to improve plant performance. Besides traditional PID control, DeltaV advanced control can be configured to provide model predictive control, neural networks, fuzzy logic and different types of analysis. These digital control technologies can reduce variance in the process, reduce start-up time and improve the performance of processes.

DeltaV Control Studio has an extremely limited ability to solve systems of complex algebraic and differential equations. The idea is to simplify the model to the level it can be represented in Control Studio. Consequently, the simplest way to solve a differential equation is using Euler's integration method.

The differential equations need to be modified in order to be implemented using DeltaV. For a simple equation: $dx/dt = 1 - x$, with the initial conditions $x(0) = 0\ at\ t = 0$ and a sampling time Δt, Euler method can be implemented in Control Studio using the structure presented in Fig. 2 and the equation is modified as: $dx/dt = 1/\tau \cdot (u - x)$.

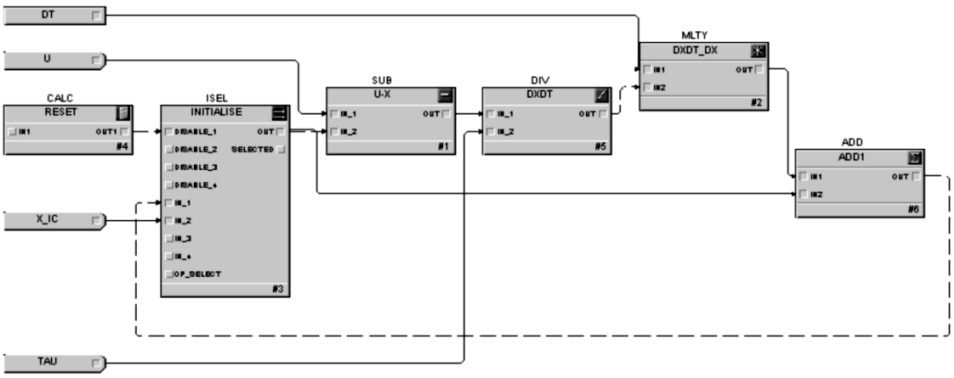

Figure 2. Euler's method DeltaV implementation, for a simple equation

If the equations are more complex, for example:

$$\begin{cases} dx_1/dt = 1/\tau \cdot (u_1 - x_1) - R \\ dx_2/dt = 1/\tau \cdot (u_2 - x_2) + R \end{cases} \quad (15)$$

where:

$$\begin{cases} R = k_f x_1 - k_r x_2 \\ x_3 = x_{3(0)} - x_1 - x_2 \end{cases} \quad (16)$$

and the initial conditions are:

$$\begin{cases} x_{1(0)} = x_1(t=0) = 0 \\ x_{2(0)} = x_2(t=0) = 0 \\ x_{3(0)} = x_3(t=0) = 1 \end{cases} \quad (17)$$

then the implementation has the structure presented in Fig. 3.

The equations are solved using simple arithmetic blocks: multiply, add, divide and subtract. We also needed to use a reset block to restart the integration process. The DT parameter is equal to the scanning rate of the module and has an implicit value of 10.

As a result, the structure used for implementing the *ethylene coil segment* mathematical model is extremely complex and it contains three interconnected derivation blocks. The result is a time and space description of all parameters, depending on the inlet mass flow variation.

In order to be implemented, the balance equations had to be modified as follows:

- Mass balance equation :

$$dw_j = -v \cdot (w_j - w_{j_0})/\mathrm{d}z \cdot \sum_i r_i \times S(i,j) \cdot dt + w_{j\_0} \quad (18)$$

- Energy balance equation:

$$dT_g = \left[v \cdot (T_g - T_{g\_0})/dz - \frac{[(T_g - T_w) \cdot A \cdot k_t + \sum_i r_i H_i + v \cdot (T_g^2 - T_g^2)]}{\rho \cdot C_p} \right] \cdot dt + T_{g\_0} \quad (19)$$

$$dT_w = A \cdot k_t \cdot (T_g - T_w)/(\rho \cdot C_p) \cdot dt + T_{w\_0} \quad (20)$$

- Momentum balance equation:

$$dP_x = G_3^2/(\rho \cdot g) \cdot dt \cdot (2f/D - 1) + dP_0 \quad (21)$$

and $$d\rho_x = \sigma_\rho \cdot dt + \rho_0 \quad (22)$$

where: $\sigma_\rho = \frac{\Delta P \cdot \rho^2 \cdot g \cdot D}{G_3^2 \cdot (2f - D)}$.

For the *entire coil*, the implementation was made using ode15s function from Matlab, solving nine material balance differential equations for: $C_2H_6, \dot{C}H_3, CH_4, \dot{C}_2H_5, C_2H_4, \dot{H}, H_2, C_4H_{10}, C_3H_8$ mass fractions and two energy balance differential equations for gas and wall temperature.

The result is a time and space variation of all parameters, an isobaric process which depends on the inlet mass flow variation and considering the inlet gas temperature as a disturbance.

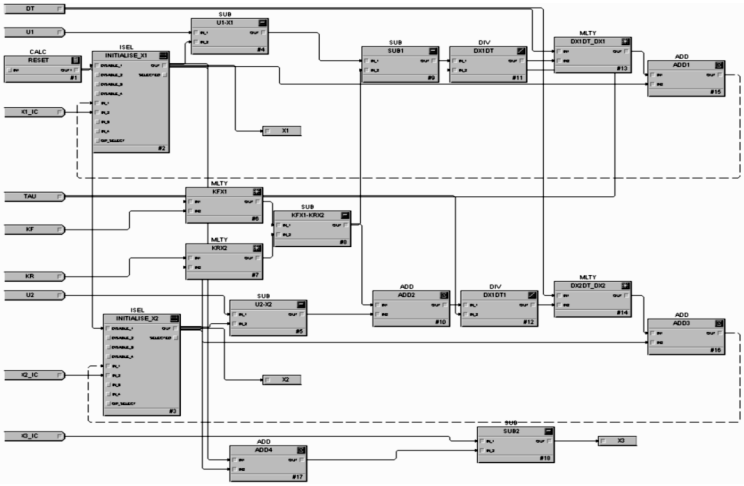

Figure 3. Euler's method DeltaV implementation, for complex equations

The inlet flow represents 97.2% ethane. The ethane concentration decreases in time, along with radicals and final products formation, Fig. 4. The radicals concentrations increase rapidly and afterwards they recombine in final products. In comparison with the other products, the concentration of ethylene is high.

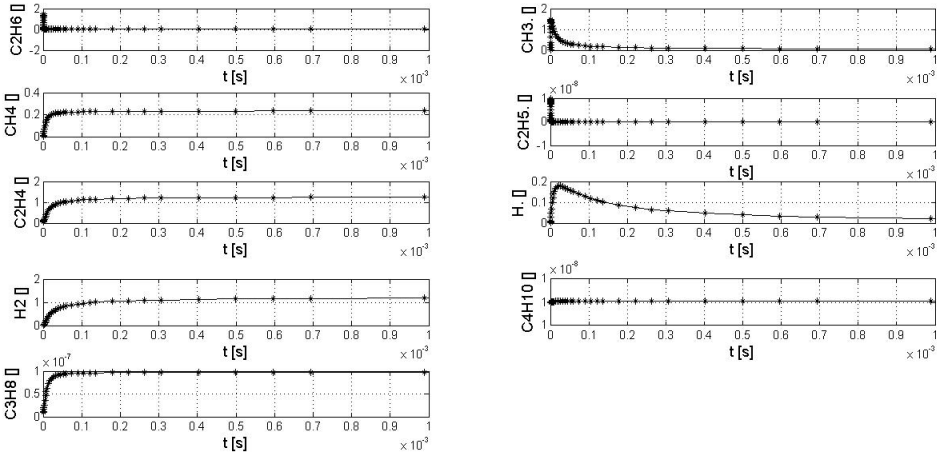

Figure 4. Evolution of products concentration

Due to the fact that the cracking reactions are endothermic, one can observe in Fig. 5, the decrease of the gas temperature. In time, the gas temperature stabilizes. The wall temperature remains constant in time (the change is insignificant).

A reliable dynamic model for this type of coil can be used for a future advanced control project, based on the following techniques: feed-forward control, state estimators based and predictive model controllers.

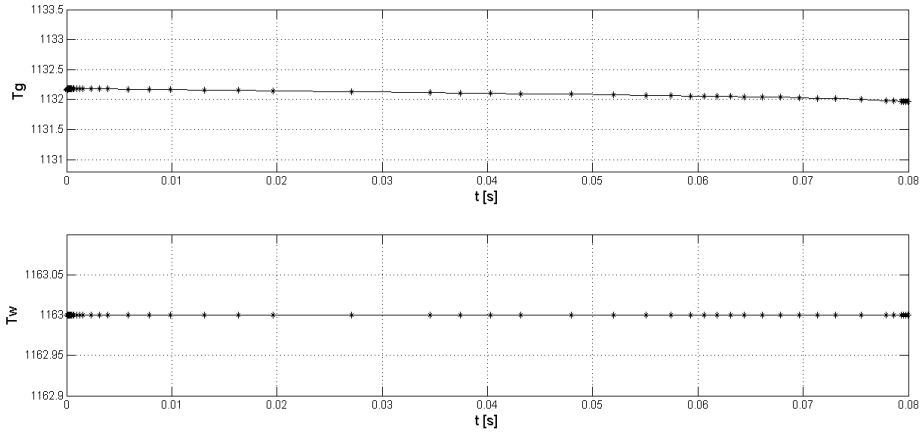

Figure 5. Gas and wall temperatures' evolution

CONTROL SYSTEM ANALYSIS

The operating objectives are to maintain the outlet temperature constant, operate within constraints, while minimizing the excess air and fuel consumption.

The overall control system structure is presented in Fig.6, where one can observe the communication between the optimization and advanced control layers. The MPC receives information from the field and controls the inlet flows and the combustion (air and fuel).

These rules could be applied also in the case of a coking plant when the actual temperature control point is at the heater outlet. The chemical reactions are endothermic and consequently the coke drum temperature (following the heater) will be lower. If the temperature is too low, the coke will be too soft and the other products' specifications will not be met. If the temperature is too high, the coke will be too hard and difficult to remove [1].

The development of a model for this type of furnace is a theme of present interest because of the petrochemical industry evolution and of the increased need of optimization. Studies on the optimization of such a plant were made by Riverol and Pilipovik [9] and Belohlav and Zamostny [2].

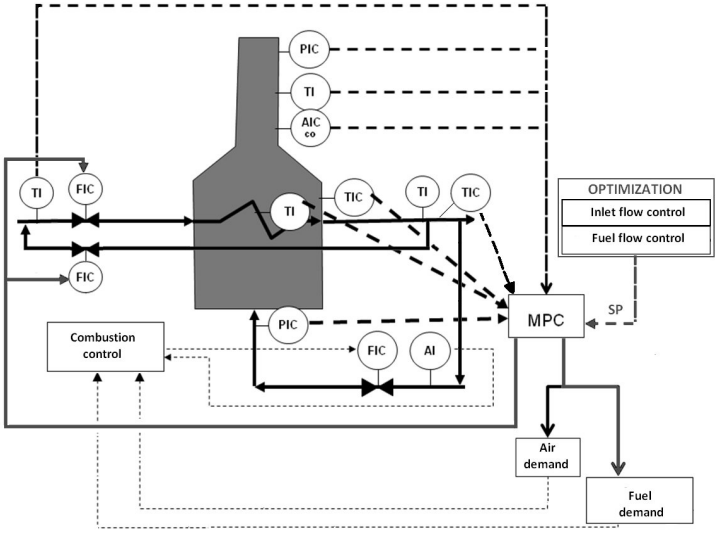

Figure 6. Control system structure

As mentioned earlier, this paper develops a dynamic regime study that can be followed by the implementation of an advanced process control system of the MPC design presented above.

ECONOMIC OPTIMIZATION

The cracking furnace is the heart of the installation and the frequent changes in feed, quality and prices, and the demand for its olefin products are influencing directly the production efficiency. Each reactant in the feed produces a certain distribution of products and, in order to satisfy the demand at the lowest cost, one needs to manipulate the amounts of each reactant, in an optimal way.

The DeltaV Model Predictive Control Professional (MPCPro) function block allows the control of large interactive processes (as large as 40 manipulated variables and 80 controlled variables), within the measurable operating constraints. The optimizer can be used to provide maximum profit or minimum production cost, with respect to the process constraints and the input limits. The MPCPro function block can replace traditional control systems that use feed-forward, decoupling networks and perform multivariable control. Process optimization is implemented using a linear program (LP) optimizer. The predictive control algorithm is based on Dynamic Matrix Control (DMC) technology, but with significant differences. These modifications lead to an improvement in the robustness of the controller, especially those concerning the utilization of the embedded LP optimization, range control and the penalties on manipulated variables moves and errors [12].

PredictPro was used to build an application that has 7 manipulated variables (MV's) and 10 controlled variables or constraints (CV's). The considered MV's are: the inlet feeds (four reactants), the recycle feeds (produced ethane and propane) and the added fuel (including the produced methane and fuel oil). The furnace capacity is limited and the downstream processing limitations have been considered, as well.

The MPCPro works in percentage values, so the ranges associated to each MV and CV need to be carefully chosen when the MPCPro gain matrix is initiated. In operation, in order to simulate nonlinearities the possibility to manipulate the gain matrix at every optimization scan has been considered by using the vectors GAIN_FACT and the module NON_LIN.

The prices for reactants and products are introduced by the operator or from another source and the associated costs and profit are calculated in specific modules (MV_PRC, CV_PRC and COSTS).

With this system the MV's and CV's can be either included or not, in the optimization problem according to different situations, for example: when the MV is no longer under automatic control (operator control) or base-load cases (fixed rates). Their status can be checked in the Optimizer screen, or by using the operator interface.

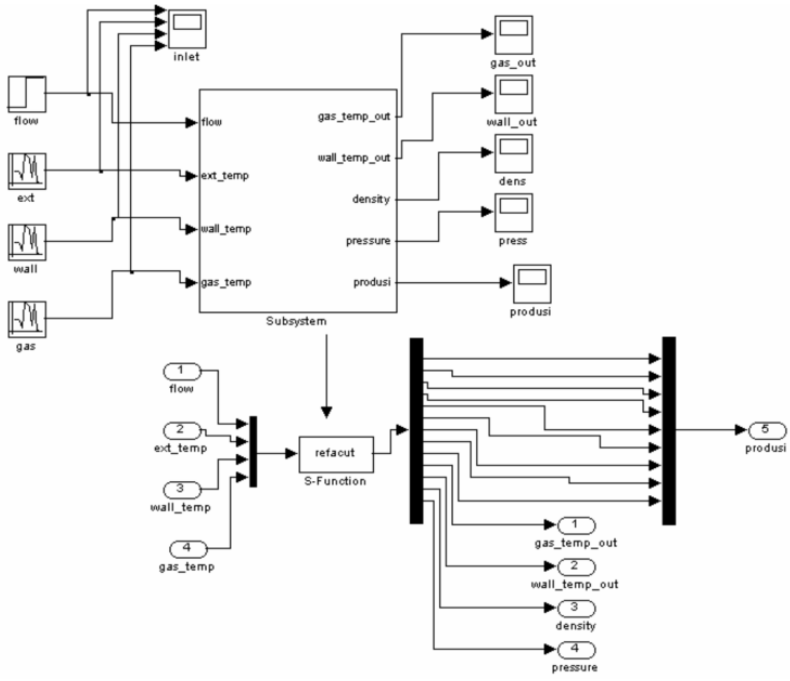

Figure 7. Coking process simulator

The main advantages emerged from the use of DeltaV PredictPro consist in the capability of running its applications on a stand-alone computer interfaced to other automation systems via an OPC communications link and of using up to five different optimization objectives, while increasing the flexibility of the system (different operating modes depending on external conditions).

CONCLUSIONS

This paper stands as the groundwork for the development of a simulator for the entire reactor, with large number of cracking tubes, useful for both monitoring and control of its outlet variables.

By using the simulator, Fig. 7, a steady state optimization built in a real-time control environment was tested, for different configurations, and additionally, a predictive model can be generated in order to build an MPC preliminary structure, for test purposes and operator training. The ethylene coil's developed model can be also the basis for building an equivalent model devoted to the implementation in the real time control environment.

NOMENCLATURE

w_j [kg/kg] – Mass fraction of component j
w_{j_0} [kg/kg] – Inlet mass fraction of ethane
z [m] – Length along coil
t [s] – Scanning rate
S (i, j) – Stoichiometric constant of component j, in reaction i
v [m/s] – Fluid velocity
r_i [kmol/m^3·s] – Reaction rate
$\overline{C_p}$ [kcal/kg.K] – Process gas specific heat
H_i [kcal/kmole] – Heat of reaction
A [m^2] – Transfer tube area
T_w [K] – Refractory wall temperature
T_{w_0} [K] – Inlet refractory temperature
T_g [K] – Flue gas temperature
T_{g_0} [K] – Inlet flue gas temperature
k_{tg} [W/m.K] – Gas thermal conductivity
k_t [W/m.K] – Tube thermal conductivity
σ [W/m^4 K^4] – Boltzmann coefficient referring to radiant energy
P [N / m^2] – Pressure
P_0 [N / m^2] – Inlet pressure value
ρ [kg/ m^3] – Process gas density
ρ_0 [kg/ m^3] – Ethane density

G_3 [kg/ s^2.m] – Dimensional constant
f – Friction factor
A_i [s^{-1}] – Frequency factor
E [kcal/mol] – Activation energy
g [m/s^2] – Gravitational acceleration
D [m] – inside tube diameter

ACKNOWLEDGMENTS

Paper written during the "PRODOC" program: "Development project for PhD studies, in advanced technologies" - (POSDRU 6/1.5/S/5).

REFERENCES

1. J. E. Albers, "Modeling of a delayed Coker", A Thesis in chemical engineering Submitted to the Graduate Faculty of Texas Tech University, **1996**.
2. Z. Belohlav, P. Zamostny, T. Herink, *Chemical Engineering and Processing,* **2003**, *42(6),* 461.
3. E. H. Edwin, J. G. Balchen, *Chemical Engineering Science,* **2001**, *56,* 989.
4. T. Hernik , Z. Belohlav, P. Zamostny, J. Doskocil, *Petroleum Chemistry,* **2006***, 46(4),* 237.
5. M. E. Masoumi, S. M. Sadrameli, J. Towfighi, A. Niaei, *Energy,* **2006***, 31,* 516.
6. A. Niaei**,** J. Towfighi, S. M. Sadrameli, R. Karimzadeh, *Applied Thermal Engineering,* **2004***, 24,* 2251.
7. R. M. Rao, M. P. Plehiers, G. F. Fromet, *Chemical Engineering Science,* **1988***, 43(6),* 1223.
8. S. Raseev, "Thermal and Catalytic Processes in Petroleum Refining", Marcel Dekker, New York, **2003**.
9. C. Riverol, M. V. Pilipovik, *Chemical Engineering Journal,* **2007***, 133(1-3),* 133.
10. C. M. Tham, "Pyrolysis furnace", URL: http://kolmetz.com/pdf/Pyrolysis-Furnace-Rev-1.pdf last viewed on 21st of September 2010.
11. K. M. Van Geem, R. Zajdlik, M.-F. Rayniers, G. B. Marin, *Chemical Engineering Journal,* **2007***, 134,* 3.
12. "DeltaV Books Online 9.3", *Fisher-Rosemount Systems, Inc.* **1994-2006***.*

STUDIA UBB CHEMIA, LVI, 2, 2011 (p. 107 - 113)

PRELIMINARY RESULTS ON THE ANALYSIS OF STEROIDS IN POULTRY SAMPLES BY DIRECT IMMERSION SOLID-PHASE MICROEXTRACTION AND GAS CHROMATOGRAPHY-MASS SPECTROMETRY

LĂCRIMIOARA ŞENILĂ[a], MIRELA MICLEAN[a], ERIKA LEVEI[a], CECILIA ROMAN[a], CORNELIA MAJDIK[b]

ABSTRACT. This paper reports a rapid method for analysis of steroid hormones in poultry serum samples. The target compounds were first extracted by direct immersion on solid-phase microextraction (SPEME) procedure, followed by on fiber derivatization with methyl-N-(trimethylsilyl) trifluoroacetamide (MSTFA) and, final, analysis by gas chromatography with mass spectrometry (GC-MS). The average correlation coefficient of the calibration curve of the steroid hormones was 0.9955. The LOD/(LOQ) values of the steroid hormones in poultry serum samples were in the range of 0.020-0.068/(0.060-0.204) μg L^{-1}. The concentrations of estrone and ß-estradiol in poultry serum were 2.08 μg L^{-1} and 3.61 μg L^{-1}, respectively.

Keywords: *Steroid hormones, SPME, GC-MS*

INTRODUCTION

In recent years, various adverse health effects of endocrine disrupting compounds have been reported [1]. Endocrine disruptor chemicals interfere with chemical from aquatic environment and induce feminization, decrease in fertility or hermaphroditism of aquatic organisms [2, 3]. Estrogens are called the female sex hormones. Steroids are a group of lipophilic, low-molecular weight, biologically active compounds that act as hormones. Various examinations regarding endocrine disrupting chemicals (EDCs) are being conducted across the world. In the environment the hormones are excreted by the humans and animals [4, 5].

[a] *INCDO-INOE 2000, Research Institute for Analytical Instrumentation, Donath 67, 400293, Cluj-Napoca, Romania; E-mail: icia@icia.ro, Tel: +40-264-420590; Fax: +40-264-420667*

[b] *"Babes-Bolyai" University, Faculty of Chemistry and Chemical Engineering, Arany Ianos 11, 400028, Cluj-Napoca, Romania, Tel: +40-264-593833; Fax: +40-264-590818*

Steroid sex hormones can be found in the livestock wastes such as sheep, cattle, pigs, poultry and other animals, as well as growth regulators in aquaculture [6, 7].

Recently, a number of methods have been reported for the determination of steroid hormones, such as: gas chromatography coupled with mass spectrometry (GC–MS), tandem mass spectrometry (GC–MS–MS), liquid chromatography coupled with mass spectrometry (LC–MS) and tandem mass spectrometry (LC–MS–MS) [8]. GC-MS is the most used techniques for steroid hormones analysis [9, 10]. Over the years, various analytical procedures have been developed for the efficient clean-up of biological matrices, such as liquid–liquid extraction (LLE), solid phase microextraction (SPME), solid–liquid extraction (SLE) and solid phase extraction (SPE). SPME is a simple and fast to use technique, solvent free and single step sample preparation, which is used frequently in the environmental, biological, pharmaceutical and another field analyses [11]. Because SPME uses small volumes of samples, is an ideal method for extraction of steroid hormones from serum samples, because SPE and LLE require large amounts of sample [12, 14].

Prior to GC analysis, due to the poor thermal stability and volatility of steroid hormones, a derivatization step is needed to produce more volatile compounds and to improve the chromatographic separation. The most commonly used derivatisation for steroids before GC–MS analysis is silylation [8, 9]. In general, N,O-Bis(trimethylsilyl)trifluoroacetamide (BSTFA) and methyl-N-(trimethylsilyl) trifluoroacetamide (MSTFA) are used as derivatizing agents [12, 13].

The purpose of this paper is to determine two natural steroid hormones from poultry samples using a sensitive and rapid technique. SPME is the technique employs for the extraction of estrone and ß-estradiol from poultry serum samples. Separation of the target compound from serum samples was realized by direct immersion in serum samples, with on-fiber silylation, followed by derivatizations with MSTFA and analysis by gas chromatographic with mass spectrometry. The proposed method was used for the first time for determination of EDCs from biological poultry samples and is a rapid, sensitive and accurate method.

RESULTS AND DISCUSSION

The aim of this work was to perform preliminary investigations regarding the analysis of steroids hormones in poultry serum samples. The structure of the target compounds analyzed from poultry serum samples are show in Figure 1.

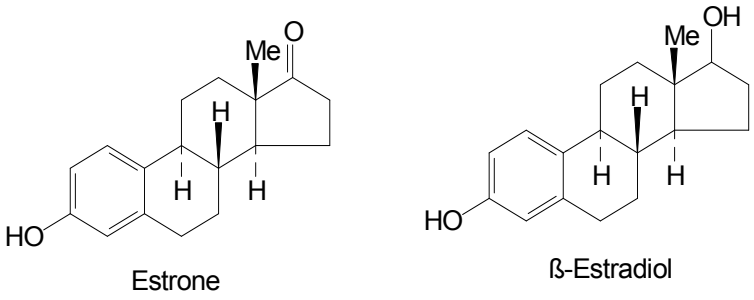

Figure 1. Structures of the steroid hormones

Direct immersion solid-phase microextraction with on fiber derivatization with MSTFA was applied to the poultry serum samples. MSTFA was selected as silylating agent because the products MSTFA silylates are more volatile than BSTFA. The general reaction of derivatization of steroid hormones with MSTFA is presented in Figure 2.

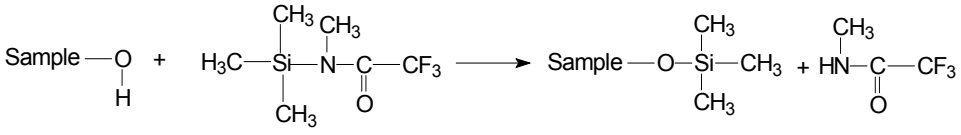

Figure 2. General reaction of steroid hormones derivatization with MSTFA

Estrone and ß-estradiol contained hydroxyl groups can be silylated by replaced labile hydrogens with TMSi groups and to prepare volatile and thermal stable estrogen derivatives for gas chromatography and mass spectrometry. For estrone contained mono-hydroxyl group, the mono-TMSi is formed, ß-estradiol contained bis-hydroxyl groups, the bis-TMSi is formed.

The steroid hormones standards analyzed in this study and their characteristics are given in Table 1.

Table 1. Characteristics of steroid hormones analyzed by GC-MS

Compounds	Molecular mass	Retention time (min.)	Quantitative ions (*m/z*)	Qualitative ions
Estrone	270	20.550	342	257, 218
ß-estradiol	272	21.368	416	129, 285,326

The ions monitored for estrone was *m*/*z* 342 and for ß-estradiol *m*/*z* 416.

The quantification was performed using standard addition method, as presented in the experimental section. The linearity of the calibration curves are presented in the Table 2.

Table 2. Recoveries, limit of detection (LOD) and limit of quantification (LOQ) for steroid hormones from serum poultry samples

Compounds	Correlation coefficient (R^2)	LOD (μg L^{-1})	LOQ (μg L^{-1})	RSD (%)	Recovery (%)
Estrone	0.996	0.068	0.204	12	95
ß-estradiol	0.995	0.020	0.060	13	90

Limits of detection (LOD) for steroid hormones were calculated as lowest concentration that can be determined with an acceptable level of repeatability and fidelity, by consecutive dilutions of spiked solution of serum and were calculated using the 3s criterion. The limits of quantification (LOQ) for steroid hormones were calculated to the three times of limits of detection.

The relative standard deviation (RSD) of the peaks area of steroid hormones derivatives in the chromatogram (calculated for 6 replicated of a spiked solution containing estrone and ß-estradiol) were 12 % for estrone and 13 % for ß-estradiol.

The recoveries of estrone and ß-estradiol from serum were evaluated by using a serum spiked solution before ether extraction followed by steps presented in experimental section.

The SIM chromatogram of the products ions of estrone in poultry serum sample is presented in Figure 3. The identification of steroid hormones was based on the standard mass spectra of the MS spectral library.

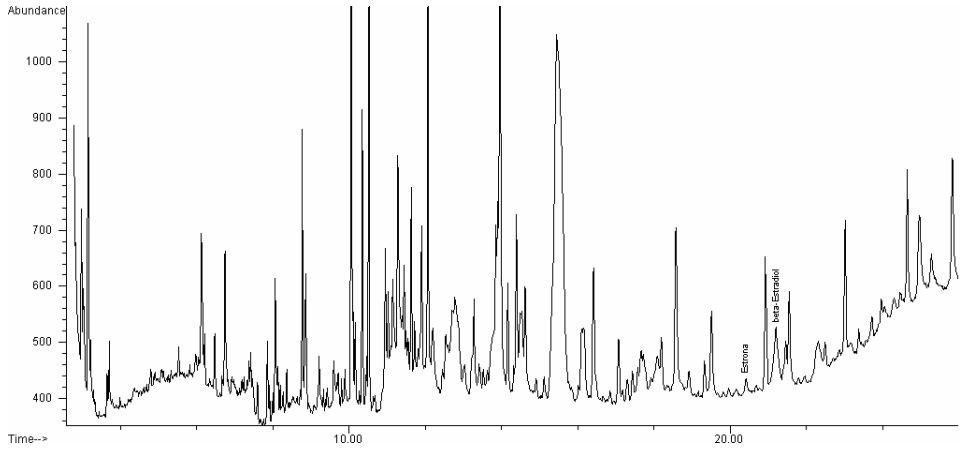

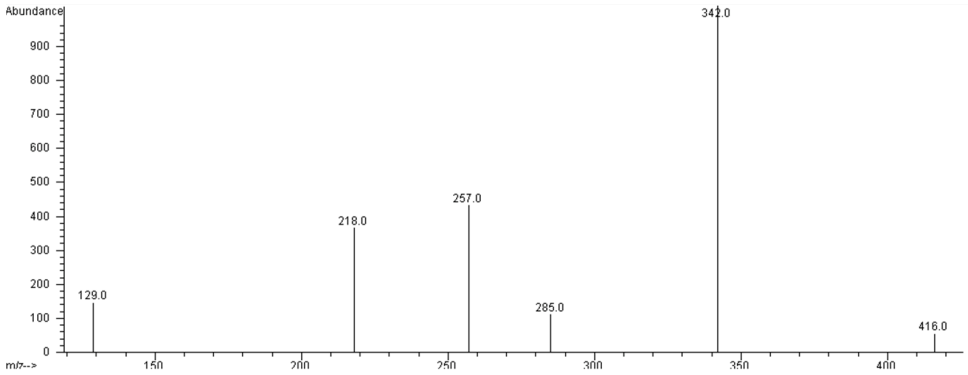

Figure 3. The SIM chromatogram of steroid hormones from poultry serum (and the ions for the quantitative and qualitative analysis of silylation derivatives of estrone)

The extraction time, derivatization time and temperature were selected according to other studies [8, 9].

Temperature is an important factor for SPME process because it controls the diffusion kinetics and the equilibrium between fiber and liquid phase. The obtained average concentrations of estrone and ß-estradiol in poultry serum were: 2.08 μg L^{-1} and 3.61 μg L^{-1}, respectively.

The concentration of estrone and ß-estradiol obtained from poultry serum samples were higher than those obtained by Yang et al. [8] from fish serum.

EXPERIMETAL PART

Chemicals and materials

Steroid hormones including estrone (99+ %) and ß-estradiol (98%) were obtained from Sigma–Aldrich. Methanol, diethyl ether, sodium chloride (NaCl, 99%) and hydrochloric acid (HCl, 37%) was supplied by Merck (Darmstadt, Germany). The derivatization agents MSTFA were also purchased from Sigma–Aldrich. All solvents used were of HPLC grade. Deionized water used in dilutions was obtained using a Milli-Q purification system (Millipore, Bedford, MA, USA).

The blood samples were collected from five farmed chickens. The SPME device consists of manual fiber holder supplied from Supelco Inc. (Bellefonte, PA, USA) with 85 μm polyacrylate (PA) fiber supplies by Supelco Inc. (Bellefonte, PA, USA). The fiber was conditioned before use in split mode in the inlet for 2 h at 300 °C according to Supelco's specifications.

For SPME process was used a heater unit and a magnetic stirrer for stirring samples during the process.

Sample preparation

Blood was taken from each poultry sample using heparinized syringe (10 mg mL^{-1} heparin in 0.9 % NaCl). Serum was obtained by separating from plasma by centrifugation for 10 min at 5,000 rpm.

Blood serum is a complex matrix, and contains of proteins, lipids and glucose. In this case, to remove inhibitors extraction, serum was pretreated before of immersing the SPME fiber directly into the serum [12]

An aliquot of 10 mL of the serum was extracted with 50 mL ether three times. The organic phases was combined and evaporated to dryness. The extract was dissolved in methanol and then was transferred to the vials for SPME, MSTFA derivatization and GC-MS analysis.

Stock standards solution of estrone and ß-estradiol (500 µg L^{-1}) were prepared in methanol and stored at -18°C. Working standard mix solutions were performed by dilutions in ultrapure water.

For steroid hormones quantification, the sample was splited into six even aliquots in separate volumetric flasks of the same volume. The first flask was diluted to volume with water. A standard containing the analytes was then added in order to obtain the following concentrations: 1, 10, 50, 75 and 100 µg L^{-1} and then diluted to volume with water. The areas for all calibration levels were measured and linear regression was performed using standard addition method.

Direct immersion SPME analysis

Estrogens were extracted from serum poultry sample by direct immersion of fiber in serum (9 ml serum samples). An amount of 0.9 g NaCl was added to serum to increase of the response of steroids hormones.

In order to control the temperature, sampler vials sealed with a septum were kept in a thermostatic water bath; a magnetic stirring bar was put in for agitation at 250 rpm. Extraction time was 120 min at 45°C. Before SPME, 100 g L^{-1} NaCl was added to sample to enhance the volatilization of the compound.

Derivatization procedure was performed by immersion of the fibre into a sampler vial containing 100 µl MSTFA to a sampler vial sealed with a septum, for 60 min at room temperature (approximately 25 °C).

Finally, the derivatized estrogens were desorbed by introducing the fiber directly into the GC injector.

GC-MS analysis

Analyses were performed using a gas chromatograph (Agilent Technologies, 6890N GC) coupled with mass spectrometer (Agilent Technologies, 5973N MSD) and capillary column of 30 m length×0.25 mm I.D.×0.25 µm HP-3 MS film thickness. The injection port was in splitless

mode. Samples were analyzed in SIM (selected ion monitoring) mode. The temperature program was as following: the initial oven temperature was set at 90 °C, held for 2 min, from 90 to 180 °C via a ramp of 30 °C/min, 180 to 240 °C at a ramp of 10°C/min and 240 to 270 °C at 3 C/min, 270 to 300 °C at 15 °C/min and maintained at 300 °C for 2 min.

CONCLUSIONS

In this paper, a GC-MS method has been successfully utilized for the analysis of the steroid hormones in poultry serum samples. The steroids were extracted from serum by solid phase microextraction and mass spectrometry. The target compounds were first extracted by SPME procedure, followed by derivatization with MSTFA and analysis by GC-MS.

The obtained results confirmed that SPME procedure is very sensitive, and compresses the extraction, concentration and introduction in one step. This method greatly reduces sample preparation time and increases sensitivity comparatively with other extraction methods.

ACKNOWLEDGEMENTS

This work was supported by the Bilateral Project Romanian-Hungarian No. 19/2008, CONTALIM (ANCS Program).

REFERENCES

1. S. Jungju, K. Hye-Young, C.C. Bong, H. Jongki, *Journal of Chromatography A*, **2005**, *1067*,303.
2. L.S. Shore, M. Shemesh, *Pure Appl. Chem.*, **2003**, *75*, 11–12, 1859.
3. M.L. Jugan, L. Oziol, M. Bimbot, V. Huteau, V. Tamisier-Karolak, J.P. Blondeau, V. Lévi, *Science of the Total Environment*, **2009**, *407*, 3579.
4. H. Noppe, B.L. Bizec, K. Verheyden, H.F.D. Brabander, *Analytica Chimica Acta*, **2008**, *611*, 1.
5. J. Beck, K.U. Totsche, I. Kögel-Knabner, *Chemosphere,* **2008**, *71,* 954.
6. R. Liu, J.L. Zhou, A. Wilding, *Journal of Chromatography A,* **2004***, 1022,* 179.
7. D. Arroyo, M.C. Ortiz, Sarabia, L.A., *Journal of Chromatography A*, **2007**, *1157,* 358.
8. L. Yang, T. Luan, C. Lan, *Journal of Chromatography A*, **2006**, *1104*, 23–32.
9. K.M. McNamara, D.T. Harwood, U. Simanainen, K.A. Walters, M. Jimenez, D.J. Handelsman, *Journal of Steroid Biochemistry & Molecular Biology*, **2010**, *121*, 611.

10. L. Yang, C. Lan, H. Liu, J. Dong, T. Luan, *Analytical and Bioanalytical Chemistry,* **2006**, *386*, 391-397.
11. F.M. Musteata, J. Pawliszyn, *Trends in Analytical Chemistry*, **2007,** *26* (1), 36.
12. D.P. Grover, Z.L. Zhang, J.W. Readman, J.L. Zhou, *Talanta*, **2009**, *78*, 1204.
13. A.N. Neale, B.I. Escher, A.I. Schäfer, *Science of the Total Environment*, **2009**, *407,* 1167.
14. H. Chang, K. Choo, B. Lee, S. Choi, *Journal of Hazardous Materials*, **2009**, *172*, 1.

STUDIA UBB CHEMIA, LVI, 2, 2011 (p. 115 - 124)

SEDIMENTATION OF CONCENTRATED SUSPENSIONS IN NON-NEWTONIAN FLUIDS

ADINA GHIRIŞAN[a], SIMION DRĂGAN[a]

ABSTRACT. The behavior of polydisperse concentrated solid suspensions (ε smaller than 0.95) of quartz sand in carboxymethylcellulose (CMC) aqueous solutions (with 0.5%, 1.0% and 1.5%, in weight) during the sedimentation process was investigated. The influence of solid size, solid concentration and rheological parameters of CMC disperse fluid with a non-Newtonian behavior on the settling kinetics has been theoretically accounted. The experimental hindered settling velocities determined graphically by Kynch method and those expressed by Richardson-Zaki equation are compared and analyzed.

Keywords: *particle settling velocity, particle size distribution, hindered settling velocity, Richardson-Zaki equation, rheological parameters.*

INTRODUCTION

The sedimentation of particles in non-Newtonian fluids is an essential problem in the case of suspensions storage for a long time, in many pharmaceutical products, paints, detergents, agro-chemicals, emulsions and foams being often desirable to keep the active component uniformly suspended. The stability of these systems can be quantitatively determined by the settling velocity of suspended particles.

The settling velocity of a single particle in a viscous fluid, under steady-state conditions, in a large vessel is easily estimated by balancing the weight of the particle with the buoyancy and drag forces, as Stokes' equation (1) shows:

$$w_s = \frac{g \cdot d^2 (\rho_s - \rho)}{18 \cdot \eta} \tag{1}$$

where: d is the average particle size (m), ρ_s – the solid density (kg/m^3), ρ - the disperse fluid density (kg/m^3), η - the fluid viscosity (Pa·s), g – the gravitational acceleration (m/s^2).

[a] *Universitatea Babeş-Bolyai, Facultatea de Chimie şi Inginerie Chimică, Str. Kogălniceanu Nr. 1, RO-400084 Cluj-Napoca,Romania, ghirisan@chem.ubbcluj.ro*

Experience with Newtonian fluids has shown that the hydrodynamics of systems consisting of single particles, drops or bubbles serves as a useful starting point for understanding the mechanism of the more complex multiparticle systems [1]. Determination of the settling velocity in polydisperse concentrated suspensions, which are far more common, named hindered settling velocity, is a difficult problem due to the complexity of the particle-particle and particle-fluid interactions [2, 3].

The expression proposed by Richardson-Zaki for Newtonian fluids, equation (2), applied at values of terminal Reynolds number Re_t up to about 2 [4], is the most popular empirical equation used in modeling and numerical simulation of hindered settling velocities [5-8]:

$$w(c) = w_S\left(1 - C_v\right)^z = w_S \cdot \varepsilon^z \tag{2}$$

where: *w(c)* is the hindered settling velocity (m/s), w_S - the Stokes' velocity (m/s), which graphically represents the extrapolation of the velocity to the voidage equal 1, related to a single particle terminal settling, C_v - the solid volume concentration (m^3/m^3), ε - the voidage or void fraction (-) and z – the sedimentation exponent (-).

Parameter z was found to be a function of the flow regime, expressed by the terminal Reynolds number Re_t, equation (3), and the particle to column diameter ratio d/D (Table 1) [4, 9]. Smaller vessel dimensions lead to a reduction of the settling velocity, more pronounced as the particle diameter, d, becomes comparable to the vessel diameter, D.

Table 1. Values of the parameter z as recommended by Richardson-Zaki.

$Re_t < 0.2$	$z = 4.65 + 19.59(d/D)$
$0.2 < Re_t < 1$	$z = 4.35 + 17.5(d/D)\,\mathrm{Re}_t^{-0.03}$
$1 < Re_t < 200$	$z = 4.65 + 18(d/D)\,\mathrm{Re}_t^{-0.1}$
$200 < Re_t < 500$	$z = 4.45\,\mathrm{Re}_t^{-0.1}$
$Re_t > 500$	$z = 2.39$

The terminal Reynolds number corrected for power-law liquids has the expression [1]:

$$\mathrm{Re}_t = \frac{\rho \cdot {w_S}^{2-n} \cdot d^n}{k} \tag{3}$$

where: w_S is the Stokes' velocity corrected for the sedimentation in non-Newtonian fluids (m/s), d - the average particle size (m), ρ - the disperse fluid density (kg/m^3), k – the fluid consistency coefficient (Pa·s^n), n – the flow behavior index (-).

In creeping regime (Re_t < 2), the settling velocity of a spherical particle in non-Newtonian fluids following power-law can be estimated by equation (4) [1]:

$$w_s = \frac{g \cdot d^{n+1}(\rho_s - \rho)^{1/n}}{18 \cdot k \cdot X(n)} \tag{4}$$

where: ρ_S is the disperse fluid density (kg/m^3), $X(n)$ - the deviation factor, a function of flow index n [1, 10].

For Re_t > 2, the parameter z is a function of Archimedes number and (d/D) ratio, and is given by equation (5) [1]:

$$\frac{4{,}8 - z}{z - 2{,}4} = 0.0365 Ar^{0{,}57}\left[1 - 2{,}4(d/D)^{0{,}27}\right] \tag{5}$$

where for power-law liquids, the Archimedes number, Ar, is defined by equation (6):

$$Ar = \xi \,\mathrm{Re}^{2/(2-n)} = \frac{4}{3} g d^{(2+n)/(2-n)} \left(\rho_s - \rho\right) \rho^{n/(2-n)} k^{2/(n-2)} \tag{6}$$

It is obvious that the settling velocity shows in the case of non-Newtonian fluid a stronger dependence on particle diameter and density difference than in a Newtonian fluid.

The sedimentation theory by Kynch was used as graphical approach in our study in order to find the settling velocity of quartz sand suspension over time, keeping in mind, that in this method the wall effects are neglected and uniform particle shape and size are assumed [11]. The Kynch method involves constructing tangents to the settling curves, and the slope of each of these tangents is the velocity at that time.

The aim of the present study was to compare the theoretical settling velocities predicted by Richardson-Zaki equation corrected for non-Newtonian fluids with those experimentally determined by Kynch method, in the case of sedimentation of quartz sand in carboxymethylcellulose (CMC) solutions with different concentrations. The influence of particle size determined by particle size distribution (PSD), quartz sand concentration and rheological parameters of disperse fluid (CMC) on theoretical settling velocities are accounted and analyzed.

RESULTS AND DISCUSSION

Rheological characterization of CMC solutions

The flow curves of carboxymethylcellulose (CMC) solutions, based on the dependence of the shear stresses on the shear rates, shown in Figure 1, and the diagram of apparent viscosities versus shear rates, shown in Figure 2, indicate a typical shear-thinning or pseudoplastic behavior [12, 13].

The decrease of apparent viscosity (η_{app}) with shear rate ($\dot{\gamma}$) follows an Ostwald power-law model, described by equation (7):

$$\eta_{app} = k\dot{\gamma}^{n-1} \tag{7}$$

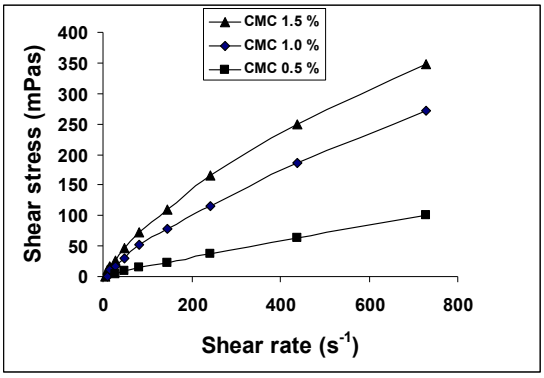

Figure 1. Flow curves of CMC solutions.

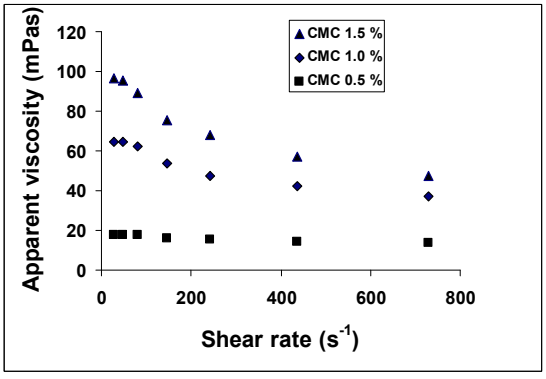

Figure 2. Apparent viscosity vs. shear rate.

The interpretation of experimental data leads to the average value of consistency coefficient *k* and the flow behavior index *n* shown in Table 2.

Table 2. Values of *k* and *n* at different concentration of CMC.

CMC concentration (%)	*k* (mPa·s)	*n*
1.5	287.82	0.7846
1.0	115.69	0.8471
0.5	26.705	0.9050

Sedimentation study

Experimental settling velocities

Typical settling curves of quarz sand (d < 200 μm) suspensions (C_v ranging from 0.088 to 0.265) in 0.5% CMC solution are shown in Figure 3.

The incipient settling velocities are determined from the slope of linear portion of each settling curve. Results clearly show that the settling velocity decreases with the increase of solid particle concentration.

Similar interpretation are done for the sedimentation of quarz sand suspensions in 1.0% and 1.5% CMC solutions.

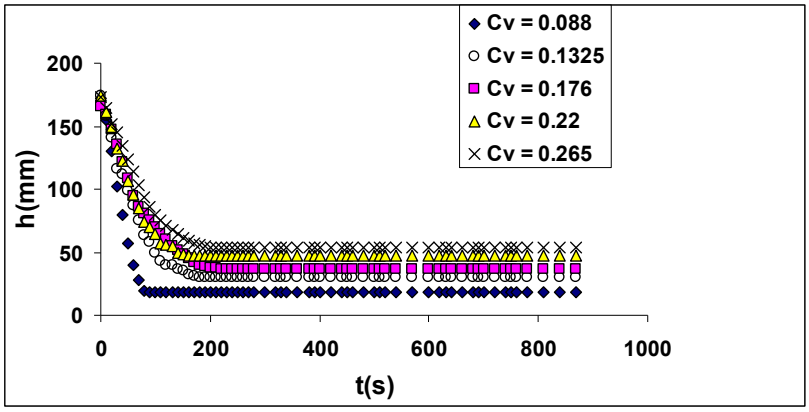

Figure 3. Sedimentation curves of quartz sand in 0.5% CMC solution.

Theoretical settling velocities

The theoretical Stokes' velocities are calculated by equation (4) with the obtained values of rheological parameters *k* and *n* and the average particle size considered one of the follows (Table 3) [13]:

a. d_{mode} - the equivalent diameter corresponding to the top (maximum) of the differential particle size distribution (PSD) curve (Figure 4);

b. d_{50} - the average equivalent diameter considering the cumulative PSD curve at T% = R% = 50% (Figure 4);

c. d_m - the average weighted diameter of particles by equation (8):

$$d_m = \frac{d_{m1}p_1 + d_{m2}p_2 + ... + d_{mn}p_n}{p_1 + p_2 + ... + p_n} = \frac{\sum_{i=1}^{n} d_{mi}p_i}{100} \quad (8)$$

where: d_{mi} is the arithmetic mean of two consecutive mesh sieve of sieve shaker used in PSD analyze, and p_i – the percentage of each retained fraction.

The theoretical hindered settling velocities are estimated by Richardson-Zaki equation, all terminal Reynolds numbers verified by equation (3) being lower than 2.

No significant influence of *d/D* ratio was observed because the solid particles are much smaller (*d* < 200 μm) than the cylinder diameter (*D* = 28 mm), and so the wall effect can be ignored.

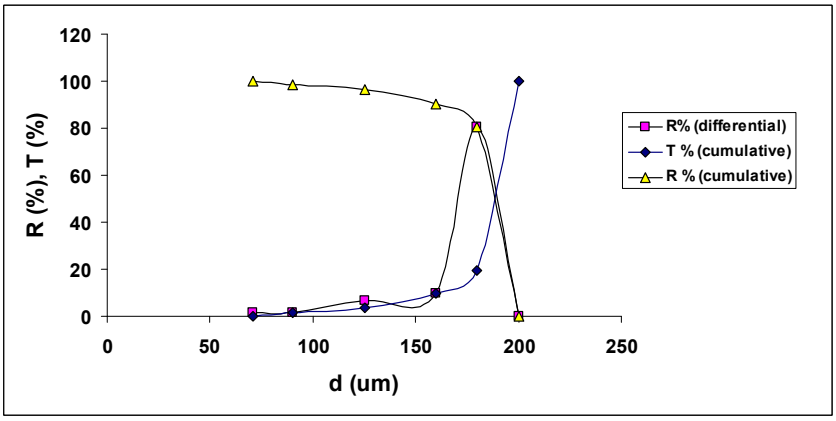

Figure 4. Particle size distribution (PSD) curves.

Table 3. Average particle size.

Particle fraction	d_{mode} (μm)	d_{50} (μm)	d_m (μm)
< 200 (μm)	180	190	180

Experimental settling velocities and corresponding Richardson-Zaki predictions as function of voidage in tested CMC solutions are shown in Figure 5 (a, b, c).

It is obvious that there are considerable differences between theoretical settling velocities estimated by Richardson-Zaki equation, w_t, and experimental values graphically determined by Kynch method, w_{exp}. In all analyzed cases, the theoretical velocities are larger than those experimentally determined.

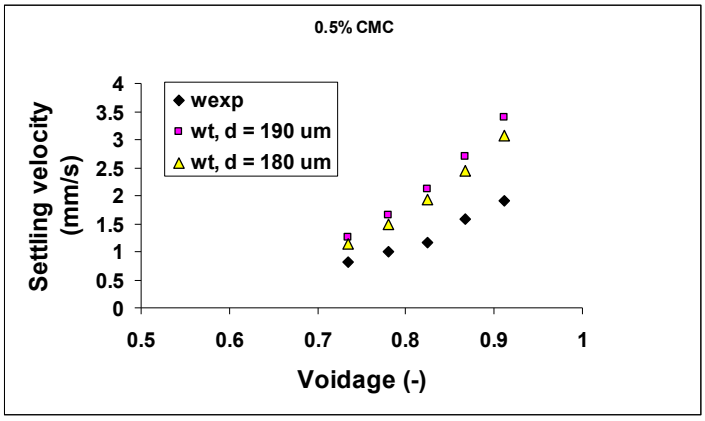

a.

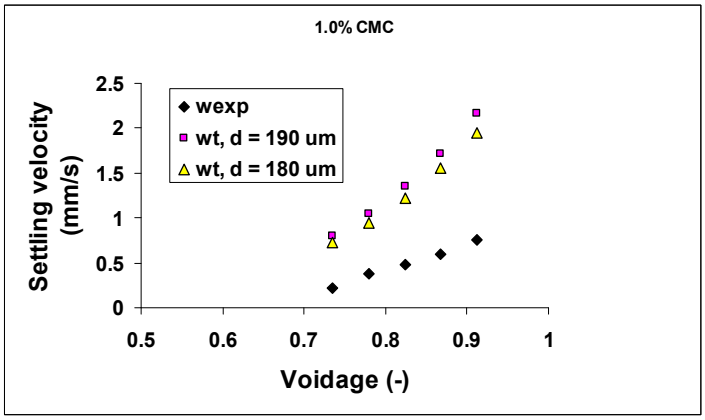

b.

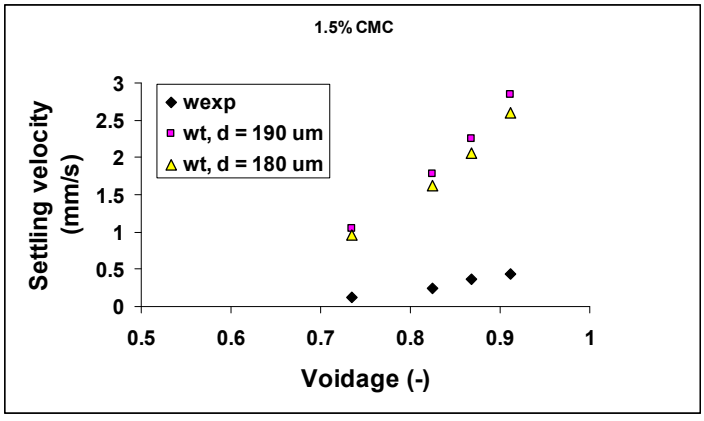

c.

Figure 5. Experimental and theoretical settling velocities vs. voidage.

For the 180 μm average particle size, the ratio w_t/w_{exp} is about 1.5 - 1.6, in the case of sedimentation in 0.5% CMC solution, 2.5 – 3.3 in 1.0% and 6.0 – 7.5 in 1.5% CMC solution. This means that the difference between theoretical and experimental velocities decreases with the decrease of CMC concentration.

In the same time the difference between theoretical and experimental velocities is influenced by the solid concentration. Generally, the difference decreases slowly with the increase of quartz sand concentration in the same CMC solution.

In order to determine the values of sedimentation exponent *z*, the experimental settling velocity w_{exp} and voidage are plotted on log-log coordinates, as a linearized Richardson-Zaki equation (Figure 6).

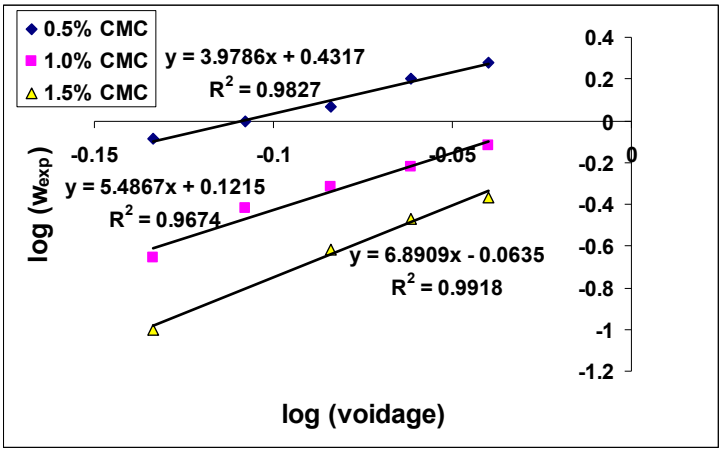

Figure 6. Log-log plot of experimental settling velocity and voidage.

The obtained values of *z* parameter are shown in Table 4.

Table 4. Values of sedimentation exponent.

0.5% CMC	1.0% CMC	1.5% CMC
$z \cong 4.0$	$z \cong 5.5$	$z \cong 6.9$

The obtained value of sedimentation exponent *z* is lower than Richardson-Zaki value (z=4.65) in solution of 0.5% CMC, and larger than Richardson-Zaki value in 1.0% and 1.5% CMC solutions, showing an increase with the increase of CMC concentration. Excepting the sedimentation exponent *z* obtained in 1.5% CMC solution, the other two values are comparable with those founded in literature [14, 15].

It is possible that the hindered settling effect of quartz sand sedimentation in CMC solutions with non-Newtonian behavior, especially in 1.0% and 1.5% concentration, to be greater than could be estimated by theoretical relations. Other secondary effects (e.g. adsorption of CMC on quartz sand) which can induce a higher friction between particles are not excluded.

CONCLUSIONS

The Stokes' velocities and the theoretical velocities estimated by Richardson-Zaki equation (z=4.65) were calculated, using experimental values of rheological parameters n and k for each CMC solution and the average particle size of quartz sand.

The obtained values were compared with experimental values determined by Kynch method. Generally, the theoretical velocities values predicted by Richardson-Zaki expression were larger than those experimentally obtained, the difference between theoretical and experimental velocities decreasing with the decrease of CMC concentration and with the increase of solid concentration.

The sedimentation exponent z determined by experimental data was different from the Richardson-Zaki value (z=4.65), comparable with the value founded in literature in CMC solution of 0.5% and 1.0%. It is possible that the hindered settling effect in non-Newtonian fluids to be greater than could be estimated by theoretical relations.

For the important practical cases of concentrated solid suspensions in non-Newtonian fluid it is indicated to evaluate the settling velocities by experimental measurements.

EXPERIMENTAL SECTION

Rheological measurements of CMC solutions of different concentration (0.5%, 1.0% and 1.5%, in weight) have been carried out at room temperature 20 ± 1^0C, using the rheometer Rheotest-2, and the system S/S1. Three replicates were performed for each new solution. The fluid rheological characteristics are shown in Table 2.

Experimental settling velocities were determined by the sedimentation curves considering the Kynch method. Experimental runs were carried out in cylinders with internal diameter of 28 mm and 300 mm tall.

The quartz sand particles ($d < 200\mu m$) were sieved in order to determine the average particle size using a sieve shaker with sieve mesh of 200, 180, 160, 125, 90 and 71 μm.

Different suspensions were made by mixing quartz sand with CMC solutions (0.5%, 1.0% and 1.5%, in weight). Prior each settling experiment, the blends were strongly mixed by shaking, directly in the cylinder were the tests are done, in order to obtain a well dispersed initial state. After mixing, the cylinder was allowed to stand, and the height of quartz sand was noted at regular intervals until no further sedimentation occurs. The boundary between the settling suspension and the supernatant phase were determined visually for each sample, as a function of time in order to establish the sedimentation curves. Each experiment was performed in triplicates.

REFERENCES

1. R.P. Chhabra, J.F. Richardson, "Non-Newtonian Flow in Process Industries. Fundamentals and Engineering Applications", Butterworth-Heinemann, Linacre House, Jordan Hill, Oxford OX2 8DP, **1999**.
2. S. Berres, R. Buerger, E. M. Tory, *Chem. Eng. Journal*, **2005**, *111*, 105.
3. P. Krishnamoorthy, *International J. Sediment Research*, **2010**, *25*(2), 119.
4. J.F. Richardson, W.N. Zaki, *Trans. Inst. Chem. Engrs.*, **1954**, *32*, 35.
5. Bo-Xue, Yan Sun, *Chem. Eng. Science*, **2003**, *58*, 1531.
6. A. Hazzab, A. Terfous, A. Ghenaim, *Powder Technology*, **2008**, *184*, 105.
7. D. K. Basson, S. Berres, R. Buerger, *Applied Math. Modelling*, **2009**, *33*, 1815.
8. V. Goia, A.L. Ghirişan, V. M. Cristea, *Studia UBB Chemia*, **2009**, *54*(1), 93.
9. R. Di Felice, R. Kehlenbeck, *Chem. Eng. Technol.*, **2000**, *23*, 1123.
10. A. Tripathi, R.P. Chhabra, *AIChEJ*, **1995**, *42*, 728.
11. C.J. Geankoplis, "Transport Processes and Unit Operations", Ed. Prentice Hall, Englewood Cliffs, New Jersey, **1993**.
12. T.G. Mezger, "The Rheology Handbook", 2nd revised edition, Vincentz Network GmbH &Co. KG, Hannover, **2006**.
13. A.L. Ghirişan, "Separarea fizico-chimică a sistemelor eterogene solid-lichid", Ed. Casa Cărții de Ştiință, Cluj-Napoca, **2005**.
14. L.C. van Rijn, *J. Hydraul. Eng.*, **1984**, *110*, 1613.
15. K.J. Scott, W.G.B. Mandersloot, *Powder Technol.*, **1979**, *24*, 99.

STUDIA UBB CHEMIA, LVI, 2, 2011 (p. 125 - 132)

OBTAINING PYRAZINE-2,3-DICARBOXYLIC ACID THROUGH ELECTROCHEMICAL OXIDATION OF QUINOXALINE ON NICKEL ELECTRODE

POPA IULIANA[a], ŢĂRANU BOGDAN[a], ŢĂRANU IOAN[a], DRAGOŞ ANA[a], MARIUS DOBRESCU[a]

ABSTRACT. The purpose of this paper is to investigate the pyrazine-2,3-dicarboxylic acid (PDCA) synthesis process by quinoxaline chemical oxidation on nickel electrode with electrochemically regenerated potassium permanganate ($KMnO_4$). The investigation of electrode reaction was carried out through cyclic voltammetry and an efficient electrolyser for PDCA synthesis was used. Anodic regeneration of Mn^{7+} on the nickel electrode is possible. This process is favoured by KOH, Mn^{7+} (Mn^{6+} implicitly) and quinoxaline concentrations as well as by temperature increase. Current and substance efficiencies of 80% and 85%, respectively, were achieved.

Keywords: *quinoxaline, pyrazine-2,3-dicarboxylic acid, potassium permanganate, cyclic voltammetry, electrolysis, nickel electrode.*

INTRODUCTION

Medical statistics show that tuberculosis is once again on the verge of becoming a threat. This is why any method for synthesizing drugs known to have antituberculosis effects must be carefully evaluated and investigated [1].

In this context pyrazine synthesis in the most advantageous conditions is of the outmost importance. The raw stock for the production of pyrazinamide is dipotassium-pyrazine-2,3-dicarboxylic acid (K_2PDCA), which can be synthesized through chemical oxidation of quinoxaline (Q) [2-4] with potassium permanganate in alkaline medium [5-7]:

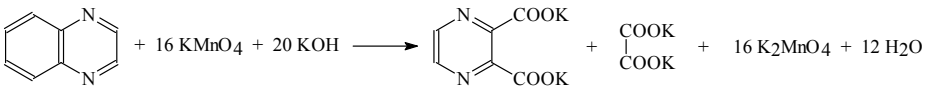

[a] *National Institute of Research-Development for Electrochemistry and Condensed Matter Timişoara, Romania 300569, Dr. A.P Podeanu, 144, Pho: 0256-222.119, Fax: 0256-201.382, e-mail: iuliana.popa@incemc.ro*

The chemical oxidation involves a very high consumption of potassium permanganate, Q: $KMnO_4$ = 1:16M (kg/kg) [8, 9]. By contrast, the original electrochemical process for PDCA synthesis proposed by us ensures considerable higher efficiencies. This paper focuses on how these efficiencies can be obtained using the perforated nickel plate electrode.

The chemical reaction taking place in the electrochemical process is similar to that of the classical chemical process, but potassium permanganate is continuously regenerated by electro-oxidation of potassium manganate generated during the process. This leads to appreciable decrease of potassium permanganate consumption, the ratio of reactants being higher: Q: $KMnO_4$ = 1 – 3: 1kg/kg.

Previous studies have shown that Mn^{7+} regeneration on platinum electrode is possible both in the absence [10] and presence of quinoxaline [11]. The price of an electrolyser equipped with such an electrode is very high and finding a cheaper material for manufacturing of the anode, while maintaining the platinum performance, constitutes a strong issue for the process at hand.

This paper shows the results obtained through cyclic voltammetry in the study of the Mn^{6+}/Mn^{7+} couple behaviour on nickel electrode as well as the manufacturing of the laboratory electrolyser made with perforated nickel plate electrode for PDCA synthesis using electrochemically regenerated potassium permanganate as chemical reagent.

RESULTS AND DISCUSSION

The Mn^{7+}/Mn^{6+} redox couple behaviour in alkaline medium was studied through cyclic voltammetry. The curves obtained using the nickel anode in 4M KOH solution in the presence of manganese ions at various concentrations, are shown in figure 1.

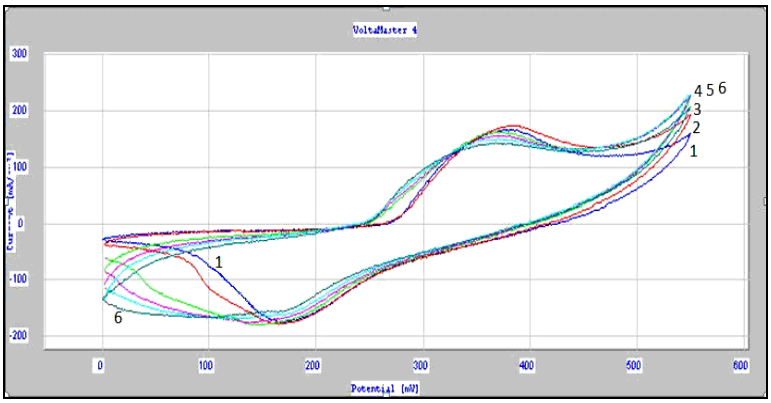

Figure 1. Cyclic voltammograms at different concentration (M) of Mn^{6+}: 0(1); $0.4 \cdot 10^{-3}$(2); $2 \cdot 10^{-3}$(3); $4 \cdot 10^{-3}$(4); $8 \cdot 10^{-3}$(5); $16 \cdot 10^{-3}$(6); [KOH] = 4M; 25ºC; v = 100 mV/s.

Cycle 1 (blue) – generated in the absence of Mn^{6+} ions – shows an anodic peak at ~ 0.38V and a cathodic peak at ~ 0.16V. The presence of the two peaks was attributed to the process:

$$2NiO(OH) + 2H_2O + 2e^- \leftrightarrow 2Ni(OH)_2 + 2OH^-$$

When metallic Ni is sunk in a NaOH solution, it gets covered with a $Ni(OH)_2$ monomolecular layer. During anodic polarization, the Ni^{2+} thus formed is converted in Ni^{3+} (NiOOH). The process is reversible and during cathodic polarization $Ni(OH)_2$ is obtained once again.

Increasing Mn^{6+} concentration (cycles 2-6) leads to a depolarization of the oxygen release and at the same time there is an observed decrease and slight displacement of the anodic peak towards more negative potentials. Another tendency towards more negative potentials is observed at the cathodic peak, starting at 0.16V. Besides this cathodic peak – present due to a reduction in Ni^{3+} – at the 0.100V potential a wave appears and increases. At an increase in Mn^{6+} ion concentration, the wave shifts significantly towards more negative potentials and the current intensity increases. The wave seems to appear as a result of the reduction in Mn^{7+} ions formed during the anodic process.

It's possible that Mn^{6+} oxidation on the nickel electrode takes place at the same time with oxygen release. During the process the color of the electrolyte solution turns from green to violet, due to $KMnO_4$ formation.

An increase in temperature from 20 to 45ºC determines the increase of the peak currents. The plots of anodic peak currents as functions of temperature and supporting electrolyte concentration for 4.10^{-3}M K_2MnO_4 are shown in figure 2.

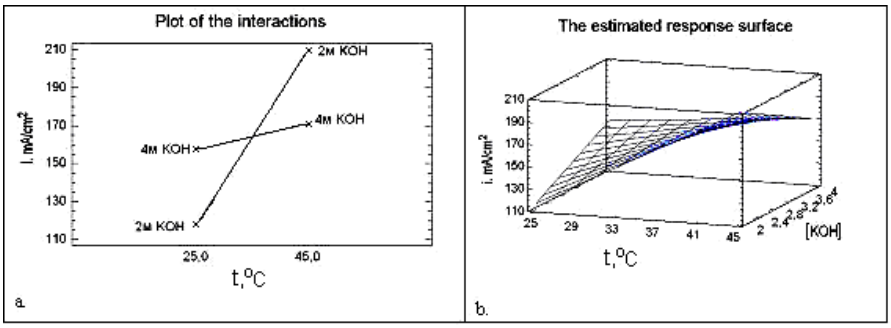

Figure 2. Anodic current density variation with temperature and supporting electrolyte concentration for 4.10^{-3}M K_2MnO_4.

The regression equation is:

$$i = -138 + 8.6 \cdot t + 69.375\,[KOH] - 1.975 \cdot t\,[KOH]$$

The cyclic voltammograms corresponding to different quinoxaline concentrations, obtained at 45°C in 2M KOH solution with $6 \cdot 10^{-2}$M $KMnO_4$, are shown in figure 3. Cycle 1, obtained in the absence of Q, the peak pair due to the $Ni^{2+} + e^- \leftrightarrow Ni^{3+}$ balance can be observed. The presence of quinoxaline in the electrolyte solution leads to a shift in the anodic peak towards more negative potentials - of up to ~ 0.30V. The intensity of this peak increases slowly with the Q concentration. The peak potential moves slowly towards more positive values as the Q concentration increases. Two peaks appear on the cathodic branch. The cathodic peak present at 0.15V – it's associated with Ni^{3+} reduction – increases with the Q concentration and moves towards more negative potentials. Next to this peak another cathodic peak can be observed, present at a potential of 0.07V. This peak also increases with Q concentration and also tents towards more negative potentials. The peak appears in the same area where Mn^{7+} ions reduction takes place.

It seems that Q oxidation can be achieved through mediated oxidation in two ways: first, using electrochemically regenerated Ni^{3+} and second, using electrochemically regenerated Mn^{7+}. The later takes place simultaneously with oxygen generation.

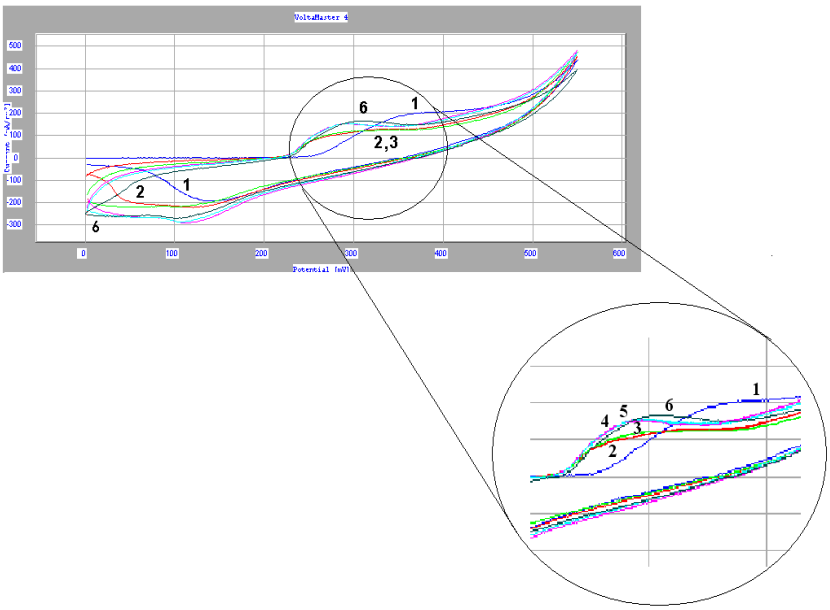

Figure 3. Cyclic voltammograms obtained for different [Q]: 0(1); $0.4 \cdot 10^{-3}$(2); $2 \cdot 10^{-3}$(3) ; $4 \cdot 10^{-3}$(4) ; $8 \cdot 10^{-3}$(5) and $16 \cdot 10^{-3}$(6) M ; t = 45°C; 2M KOH solution, [$KMnO_4$] = $6 \cdot 10^{-2}$M, *v* = 100 mV/s.

Cyclic voltammetry studies performed at 25°C and 45°C respectively, in KOH solution containing Mn^{6+} ions, on the nickel electrode show that:

- there are several processes taking place on nickel electrode:

$$2NiO(OH) + 2H_2O + 2e^- \leftrightarrow 2Ni(OH)_2 + 2OH^-$$
$$Mn^{7+} + e^- \leftrightarrow Mn^{6+}$$

- the addition of Q in the electrolyte solution leads to a shift in the anodic peak towards negative potentials of up to ~ 0.30V. The cathodic peaks don't change when temperature is increased.

- the increase in KOH concentration, temperature, Mn^{6+} and Q concentrations favours the anodic regeneration process of Mn^{7+}.

The experimental results obtained on the nickel plate anode syntheses are shown in table 1, where: Q_{el} *– electricity quantity;* U_{med} *– cell tension;* m_{Qi} *– initial quantity of quinoxaline;* m_{Qf} *– final quantity of quinoxaline; Conv. – conversion of quinoxaline* and m_{K2PDCA} *–* K_2*PDCA quantity.*

Table 1. The experimental results for the PDCA synthesis on the nickel electrode with electrochemically regenerated $KMnO_4$.

I [A]	*i* [A/m^2]	Q_{el} [C]	U_{med} [V]	*T* [°C]	m_{Qi} [g]	m_{Qf} [g]	*Conv* [%]	m_{K2PDCA} [g]	η_s [%]	η_c [%]	*C. En.* KWh/Kg
1.8	3.5	20000	3.5	45	2	0.3	85	2.5	66.6	79.10	7.78
1.8	3.5	40000	3.5	45	2	0	100	3.2	85.2	50.62	12.15
0.9	1.7	30000	2.1	45	2	0	100	2.8	74.6	59.06	6.25
2.7	5.3	40000	3.8	45	2	0	100	2.5	66.6	39.55	16.89

- KOH concentration – 23 %
- quinoxaline concentration – 1,4 – 2,8 %
- Mn^{7+} concentration – 1,4 %.

The best results for the current yield η_c are achieved at a current density of 3.5 A/dm^2. Lower current densities lead to a higher current efficiency and a lower cell tension U_{med} – thus to a desirable lower specific energy consumption *C.En.* = 6.25 KWh/Kg. On the other hand there is a high increase in reaction time and thus a decrease in electrolyser productivity. At higher current densities (5.3 A/dm^2) the substance η_s and current efficiencies are acceptable, but energy consumption increases significantly. However, in this case, the electrolyser productivity is higher.

CONCLUSIONS

From our studies (we did not identify any similar data in the scientific literature) the regeneration of Mn^{7+} takes place on the nickel electrode even at low current densities. The presence of the final product, pyrazine-2,3-dicarboxylic acid, was confirmed through quantitative methods.

Current efficiencies of ~ 80% have been achieved at ~ 85% conversions and substance efficiencies of ~ 85% have been achieved at 100% conversions and a current efficiency of ~ 50%. Nickel constitutes a very good material for manufacturing the anode of a $KMnO_4$ regeneration electrolyser used for quinoxaline oxidation.

EXPERIMENTAL SECTION

Electrochemical cell - Cyclic voltammetry method

For the cyclic voltammetry studies we used a glass electrolysis cell (figure 4) equipped with a heating/cooling jacket and with three electrodes: the working electrode made from a nickel wire (0,008 cm^2), the platinum counter electrode (1 cm^2) and the SCE reference electrode. A PGZ 301 Dynamic-EIS Voltammetry potentiostat with VoltaMaster 4 software manufactured by Radiometer Copenhagen was also used in these studies. All electrochemical potentials mentioned in this paper are related to the SCE electrode unless otherwise specified.

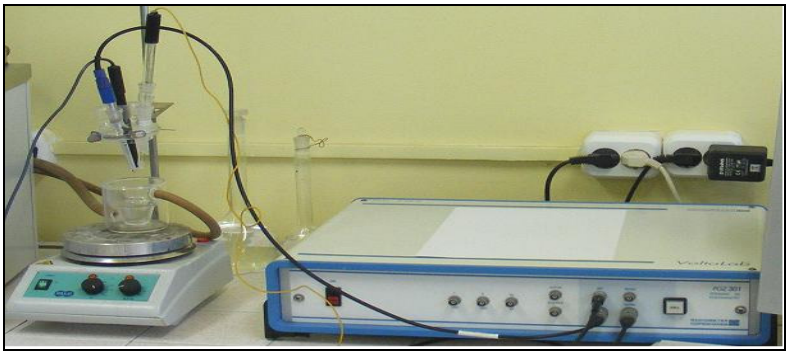

Figure 4. Electrochemical installation.

Electrolyte solution: 2 - 4M KOH (electrolyte support), K_2MnO_4 $0.4 \cdot 10^{-3}$ - $16 \cdot 10^{-3}$ M; $KMnO_4$ $2 \cdot 10^{-2}$ - $6 \cdot 10^{-2}$ M, quinoxaline $1.18 \cdot 10^{-2}$ – $3.62 \cdot 10^{-2}$ M. We used two temperatures: 25 and 45°C. The quinoxaline was from Merck, $KMnO_4$ from Riedel-de Haen and KOH, from Lach-Ner.

The method for synthesizing potassium manganate is as follows: an alkaline aqueous solution of 8N KOH containing 10g of potassium permanganate was heated at a temperature of 120°C. After the color changed from violet (Mn^{7+}) to intense green (Mn^{6+}) the supersaturated solution of Mn^{6+} was obtained. K_2MnO_4 crystals were filtered from this solution on a *S4* frit, washed with $CHCl_3$, dried and weighed, and then directly dissolved in 8N KOH solutions (25 ml measuring flask) and used in cyclic voltammetry tests.

Conductometric titration and UV-VIS Spectroscopy analysis methods were used for the quantitative determination of K_2PDCA [12], while repeated extractions with ethylic ether and evaporation to dryness followed by UV-VIS Spectroscopy were used for the quantitative determination of unreacted quinoxaline.

Laboratory electrolyser

The perforated plate electrolyser had a volume of ~ 100 ml. The perforated plate cathode and anode are shown in figures 5. The nickel anode underwent nitric acid pickling before each synthesis and between two syntheses it was washed with a mixture of sulphuric and oxalic acids.

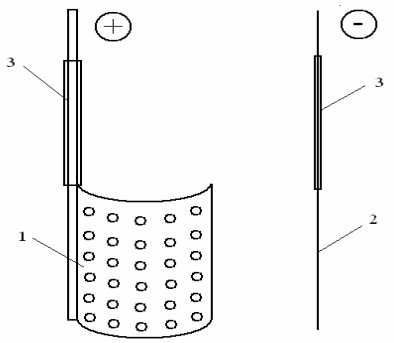

Figure 5. Components of the electrolyser used for the preliminary results of $KMnO_4$ regeneration. 1 - anode; 2 – cathode; 3 – insulating tube.

The general characteristics of the electrolyser and the working conditions are the following:

- Anodic surface, cm^2 S_A = 0.51
- Cathodic surface, cm^2 S_C = 0.034
- Sa/Sc – ratio - 15
- Electrolyte volume, ml – 90
- Current density, mA/cm^2 – 1.7 – 5.3
- Working temperature, ^oC – 45
- Total volume of the electrolyser, ml – 150
- anodic material – nickel perforated plate
- cathodic material – stainless steel

ACKNOWLEDGMENTS

The financial support within the Project 2CEx 06-11.57/2006 is gratefully acknowledged.

REFERENCES

1. W. Wang, J.W. Lown, *Journal of Medicinal Chem*istry, **1992**, *35*(15), 2890-2896.
2. G. Reuben, G. Jones, K.C. McLaughlin, *Organic Syntheses*, **1963***, 4*, 824.
3. D. Arndt, "Manganese Compounds as Oxidizing Agents in Organic Chemistry", Open Court Publishing Co.: La Salle, IL, **1981**, 254.
4. J. March, "Advanced Organic Chemistry – Reactions, Mechanisms and Structure", 3rd Edition, *Wiley*, **1984**, 1048-1100.
5. C.A. Obafemi, W. Pfleiderer*, Helvetica Chimica Acta*, **1994**, *72,* 1549-1556.
6. H. Lund, *Journal of The Electrochemical Society*, **2002**, *149*(4), S21- S33.
7. S.A. Kotharkar, D.B. Shinde, *Journal of The Iranian Chemical Society*, **2006**, *3*(3)*,* 267-271.
8. C.A. Obafemi, W. Pfleiderer, *Helvetica Chimica Acta,* **2004**, *77*(6)*,* 1549-1556.
9. G. Reuben, G. Jones, K.C. McLaughlin, *Organic Syntheses,* **1950**, *30*, 86.
10. I. Popa, A. Dragos, I. Taranu, M. Stefanuţ, C. Vaszilcsin, D. Buzatu, *Scientific Bulletin of UPT, Series of Chemistry and Environmental Engineering*, **2007**, *52*(66)*,* 1-2*,* 99-103.
11. A. Dragoş, I. Popa, I. Taranu, *New Trends and Strategies in the Chemistry of Advanced Materials with Relevance in Biological Systems, Technique and Environmental Protection,* Timişoara, 8 - 9 November **2007**, 28.
12. Țăranu B., Vlaia V., Stefănuț M., Vlătănescu N., Dobrescu M., Popa I., Analysis Methods in Obtaining Pyrazine-2,3-Dicarboxylic Acid Through Electrochemical Oxidation of Quinoxaline, *Environmental Engineering and Management Journal, "Gheorghe Asachi" Technical University of Iasi*, Romania, **2010**, *9*(8), 1115-1120.

STUDIA UBB CHEMIA, LVI, 2, 2011 (p. 133 - 140)

EFFECT OF DIFFERENT SUBSTRATE TEMPERATURE ON GROWTH OF NANO CRYSTALLINE DIAMOND BY HFCVD TECHNINQUE

HASTI ATEFI[a], MAHMOOD GHORANNEVISS[a*], ZAHRA KHALAJ[a], MIRCEA V. DIUDEA[b]

ABSTRACT. In this paper, we investigated the effects of different substrate temperature and nitrogen etching gas on synthesis of Nano Crystalline Diamonds (NCDs). We prepared all samples by Hot Filament Chemical Vapor Deposition (HFCVD) system. Silicon wafers (100) were used as substrates for all experiments. All samples were coated by Au at 50 nm thickness, as catalyst layers, by sputtering system. To remove the native oxide on silicon, all the samples were cleaned in ultrasonic bath by acetone, ethanol and de-ionized water, respectively. Substrate temperature was controlled by thermocouple in contact with substrate holder, between 550°C and 650°C. The samples were examined by X-Ray diffraction spectroscopy at room temperature. The changes of surface morphology of the diamond Nano crystals were clearly viewed by the Scanning Electron Microscopy SEM. The results show nanocrystalline diamond films and diamond nano crystals grown on substrate under various temperatures with different crystalline structures.

Keywords: *Etching, Hot filament CVD, Nanocrystalline diamond films, SEM.*

INTRODUCTION

Due to the unique properties such as high thermal conductivity, chemical stability, and high field failure diamond nano crystals are used in various fields including mechanical, electrical, semiconductor parts, optical application, etc [1-11]. Since 1950, many researcher groups have investigated the growth of diamond by various Chemical Vapor Deposition CVD techniques in view of finding particular ways to obtain diamond for different applications by low pressure, low temperature methods instead of those methods using high

* *Author for correspondence: Prof. Mahmood Ghoranneviss, Tel: +98 21 44869624 Fax: +98 21 44869626, Email: Ghoranneviss@gmail.com*

[a] *Plasma Physics Research Center, Science and Research Branch, Islamic Azad University, Tehran, Iran, P.O.BOX:14665-678*

[b] *Faculty of Chemistry and Chemical Engineering, Babes-Bolyai University, Cluj, Romania*

pressure, high temperature [12 -25,38]. Compared to the other CVD technique, the Hot Filament Chemical Vapor Deposition HFCVD process presents several advantages, such as the possibility of deposition of thick layers on large areas (over 1000cm^2), the possibility of coating various types of substrate surface, high film uniformity, easy to operate, relatively cheap, etc [29,7].

Since 1990, studies were shifted from poly-crystal to nano-crystal diamond [34]. In these studies, different parameters have been varied: type of gas, gas pressure, gas concentration, substrate preparation, surface roughness, filament's temperature, on seed size and crystal growth rate, etc [7, 28-33]. Some studies reported measurements of the experimental parameters in the growth of Nano Crystalline Diamonds NCD [11, 25-26]. According to D.C. Barbosa's group [11], one of the most important parameters in growing NCD films is the substrate temperature (in the range 550˚C to 850˚C). In 2008, C. J. Tang et al. added N_2 and O_2 in the mixture of CH_4 and H_2 at MPCVD method; they could grow large-grained polycrystalline and nanocrystalline diamond [34]. They used N_2 as the main gas in the reaction chamber to promote the secondary nucleation rate. Similarly, Sobia Allah et al. have grown NCDs films by HFCVD in $Ar/N_2/CH_4$ gas mixtures; they found that N_2 concentration in the flow added to plasma has a great influence on the grain size of the nano diamonds, as measured by X-Ray Diffraction XRD. In this case the diamond peaks became narrower [32].

In this work, we investigate the growth of diamond nano-crystals on silicon substrate using HFCVD method and the effect of different temperatures on surface morphology and the formation of diamond crystals. The nitrogen was used in the pretreatment of the substrates for the first nucleation. Scanning electron microscopy SEM, X-ray diffraction XRD and Dektak profilometer were used for analyzing the samples.

RESULTS AND DISCUSSION

A. Methods for Substrate pre-treatment

Several methods for coating, including sputtering, evaporation, ion implantation and plasma-assisted chemical vapor deposition (CVD) can be used. Substrate coating adhesion can be enhanced by carrying out several pre-treatments of the substrate. Owing to growing diamond for better quality, we used some pretreatments before the main growing process.

In this study all samples were prepared by a sputtering system, previously described in ref [35]. Figure 2 shows the thickness of the gold catalyst layer, deposited on the substrates for 8 minutes (Dektak profilometer 3, version 2.13). The substrate temperature reached 550°C when the nitrogen was introduced into the system. This made gold islands on the surface; clearly, the nitrogen etching-treatment changed the morphology of the surface by creating nucleation sites thus increasing the diamond deposition.

B. Morphology Study

The surface morphology of the nanocrystalline diamond films was observed by SEM analysis (model XL30, Philips Company, Holland) as shown in Figure 3. In a first sample (Figure 3, a), the cauliflower nano crystalline diamond, grown at 550 °C substrate temperature, is evidenced. When the substrate temperature increased to 600 °C, the particle size decreased and a higher distribution of NCD could be observed (Figure 3, b). At 650°C, the grain size the particles became low and one can see a low density of NCD, which dispersed over the substrate surface (Figure 3,c). Thus, by increasing the temperature from 550°C to 650°C the crystal quality lowers. This indicates that nano crystalline diamond is suitably formed in a lower-temperature process.

C. X-Ray Diffraction XRD analysis

In XRD, the main peak is observed at 2θ=41.68°, 2θ=41.81° and 2θ=41.67°, which indicates the diffraction of (101) diamond for samples (a), (b) and (c), respectively. The results indicate a decrease in the quality of NCD by increasing the temperature up to 650°C and suggested that the film has a strong (101) preferential texture. The full-width-half-maximum (B) of these peaks was used to calculate the grain size from the well-known Sherrer's formula [7].

$$L(hkl) = \frac{K\lambda}{B\,\mathrm{Cos}\theta\ hkl}$$

Here K=0.9, λ=1.54A˚and θ is the Bragg angel.

The grain size decreases from 43.1nm to the 35.9nm with the substrate temperature increasing. Similar results have been reported by Barbosa‘s group. They suggested that the increase in defect density is induced by temperature raising [11]. Next, the patterns show the peaks with 2θ=42.72° and 42.90° which indicate the diffraction of (102) diamond structure. Figure 4 shows the XRD patterns for NCD grown on substrates at different temperatures.

CONCLUSION

In this paper, we investigated the effects of variation of the substrate temperature on the synthesis of nano crystalline diamond NCD. For enhancing the diamond nucleation, we used gold as a catalyst nano layer and nitrogen as an etching gas. We prepared all samples by a hot filament chemical vapor deposition system. The results show that the optimum conditions are placed at the minimum temperature (550 °C) in this experiment. The XRD, SEM and DEKTAK profilometer were the equipments used for analyzing the results in this experiment.

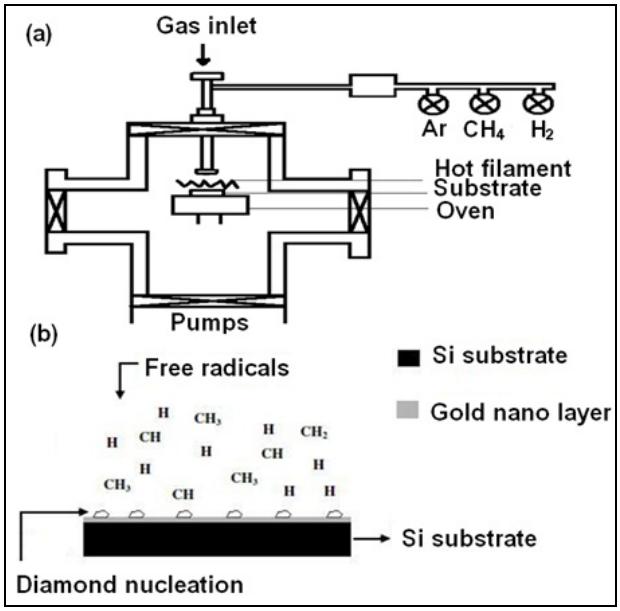

Figure 1. Generalized schematic HFCVD system (a) and the growth process in a diamond CVD reactor (b).

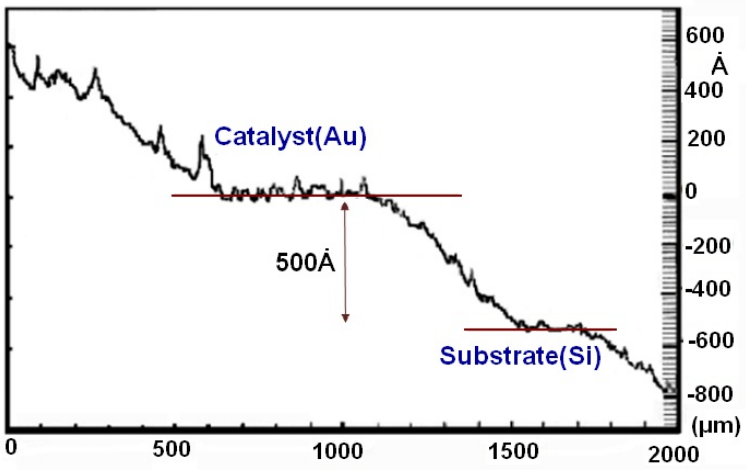

Figure 2. The gold layer thickness, on silicon substrates, equals 50nm.

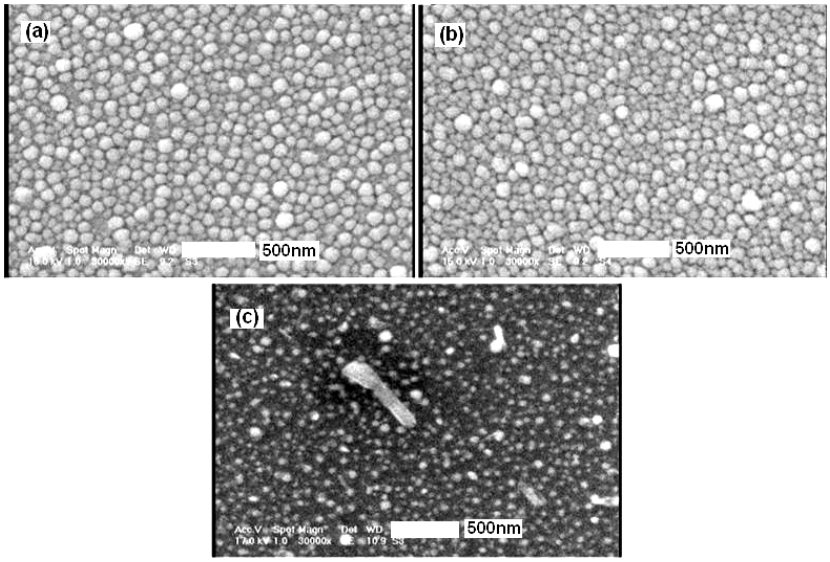

Fig. 3. SEM images of nanocrystalline diamond NCD grown at different substrate temperature (a): 550°C, (b):600°C, (c):650°C.

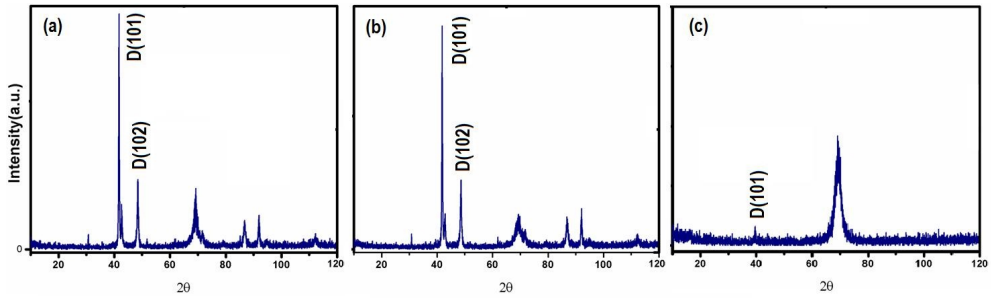

Fig. 4. X-Ray diffraction of nano crystalline diamond grown at different substrate temperature (a):550°C; (b):600°C; (c):650°C.

EXPERIMENTAL SECTION

A. HFCVD System

We prepared all samples in a Hot Filament Chemical Vapor Deposition HFCVD system. It consists of a reaction chamber, two rotary and diffusion pumps, an oven, water cooled vessel, a gas mixture, and a movable filament holder. The filament consists of a flat tungsten wire of 0.5mm in diameter for activating the source gas. The scheme of this system and therein reaction is shown in Figure 1.

B. Growth Process

Silicon wafers [p-typed Si (100)] was used as the substrates for all experiments. For pre-treating the samples and reducing the surface containments, we cleaned them, in an ultrasonic bath, by acetone, ethanol and de-ionized DI water for 15 min, respectively. The substrates were loaded to the CVD reaction chamber after pre-treatment. The distance between the substrate and filament was kept around 2cm. Before deposition process, to enhance diamond nucleation density and to improve the crystalline quality, argon Ar gas, was introduced into the system at a pressure of 8 Torr, and a flow ratio of 80 Sccm, for 45 minutes. Then N_2 gas was added to the reaction chamber. By using N_2 as etching gas, a suitable surface roughness was made [35]. In this step, the pressure, flow ratio, substrate temperature and etching time were: 15 Torr, 80 Sccm, 550 °C, and 45min respectively. For the deposition process, the chamber was evacuated down to 8.5×10^{-5} Torr. All the parameters were fixed during the deposition process except the substrate temperature, of which variation was controlled by a thermocouple in contact with the substrate holder, between 550°C and 650°C. The total flow rate of CH_4 /H_2 was fixed at 220 Sccm (concentrations Vol. 5.5% CH_4/ H_2). The overall pressure was 25 Torr while the deposition time was 80 min for each experiment.

Recall that the mechanism of deposition process was reported in many articles. In the growth process on silicon based materials by HFCVD, SiH_4 undergoes a catalytic decomposition into SiH_x or Si_2H_x (x = 1, 2, 3) radical species by the hot filament [36]. The radicals thus resulted can either deposit on substrates or further react with other gas phase species to produce precursor radicals for film deposition. These radicals were found to play an important role in producing high quality amorphous hydrogenated and polycrystalline silicon thin films [36]. Therefore, the nature of the precursor radicals has a great influence on the structure of the as-deposited films [36]. Recent studies performed by Matsumura et al. [37] on the radicals desorbed from a tungsten hotwire, by using threshold ionization mass spectrometry, evidenced various precursor radicals and their effect on the growth process. They shown that the H radical is one of the key radicals and it is used to determine the structure and characteristics of the as-grown diamond films. It was found that the crystalline fraction increased with the increasing dilution ratio (H_2/SiH_4), and amorphous and crystalline silicon were etched rapidly by the H radical [36, 37].

In this paper, the quality of diamond crystals was examined by X-Ray diffraction spectroscopy at room temperature. The surface morphology of the samples was investigated by the scanning electron microscopy SEM. The thickness of the catalyst layer was examined by Dektak profilometer.

ACKNOWLEDGMENTS

The authors acknowledge to Iran National Science Foundation (INSF) for supporting this project.

REFERENCES

[1] C. Popov, G. Favaro, W.Kulisch, J.P.Reithmaier, *Diamond and Related Material*, **2009**, *18*, 151.

[2] C. Popov, W. Kulisch, S. Bliznakou, G. Ceccone, D. Gilliland, L. Sirghi, F. Rossi, *Diamond and Related Material*, **2008**, *17*, 1229.

[3] ShanShan Wang, Guohuo Chen, Fenglin Yang, *Thin Solid Films*, **2009**, *317*, 3559**.**

[4] C.K. Lee, *Applied Surface Science*, **2008**, *254*, 4111.

[5] C.S. Abreu, M. Amaral, F.J. Oliveira, J.R. Gomes, R.F. Silva, *Diamond and Related Material*, **2009**, *18*, 271.

[6] Waqar Ahmed, Htet Sein, Mark Jackson, Riccardo Polini, *Tribologycal International*, **2004**, *37*, 957.

[7] A. Amorim, P.A. P. Nascente, V.J. Trava-Airoldi, E.J. Corat, A.R. Alves, J.R. Moro, *Vacuum*, **2009**, *83*, 1054.

[8] Z.L. Wang, C. Lu, J.J. Li, C.Z.Gu, *Diamond and Related Material*, **2009**, *18*, 132.

[9] N. Kohmura, K. Sudoh, K. Sato, K.K. Hiraku, K. Miake, G. Friedbacher, *Diamond and Related Material*, **2005**, *14*, 283.

[10] C. Pietzka, A. Denisenko, A. Romanyuk, P.J. Schafer, L.A. Kibler, J.Scharpf, E. Kohn, *Diamond and Related Material*, **2010**, 19, 213.

[11] D.C. Barbosa, F.A. Almeida, R.F. Silva, N.G.Ferreia, V.J. Trava-Airoldi, E.J. Corat, *Diamond and Related Material*, **2009**, *18*, 1283.

[12] Qiu-ping Wei, Z.M. Yu, Michael N.R. Ashfold, J. Ye, L. Ma, *Applied Surface Science,* **2010**, *256*, 4357.

[13] B.J. Jones, S. Wright, R.C. Barklie, J.Tyas, J. Franks, A.J. Reynolds, *Diamond and Related Material*, **2008**, *17*, 1629.

[14] K. Subramanian, W. P. Kang, J.L. Davidson, W.H. Hofmeister, *Diamond and Related Material*, **2005**, 14, 404.

[15] M. Akbarzadeh Pasha, A. Shafiekhani, M.A. Vesaghi, *Applied Surface Science*, **2009**, *256*, 1365.

[16] Lianh Guo, Guohua Chen, *Diamond and Related Material*, **2007**, *16*, 1530.

[17] A.H. Mahan, P.A. Parilla, K.M. Jones, A.C. Dillon, *Chemical Physics Letters*, **2003**, *413*, 88.

[18] Min-Sheng You, Franklin Chau-Nan Hong, Yeau-Ren Jeng, Shih-Ming Huang, *Diamond and Related Material*, **2009**, *18*, 155.

[19] W.L. Wang, R.Q.Zhang, K.L. Liao, Y.W. Sun, B.B. Wang, *Diamond and Related Material*, **2000**, *9*, 1660.

[20] M. Kadlečikova, M. Vojs, J.Breza.M.Veselý, Z. Fragla, M. Michalka, J. Matějková, A.Vojačková, T. Daniš, M. Marton, *Microelectrons Journal*, **2007**, *38*, 20.

[21] Yu.A. Mankelevich, P.W. May, *Diamond and Related Material*, **2008**, *17*, 1021.

[22] Yong K. Cho, Woo S. Jang, Sehoon Yoo, Sang G. Kim, Sung W. Kim, *Surface Coating Technology*, **2008**, *202*, 5390.

[23] A.K. Dua, M. Roy, J. Nuwad, V.C. George, S.N. Sawant, *Applied Surface Science*, **2004**, *229*, 254.
[24] S. Gastélum, E. Cruz-Zaragoza, A. Favalli, R. Meléndrez, V. Chernov, M. Barboza-Flores, *Diamond and Related Material*, **2008**, *17*, 1283.
[25] Shumin Yang, Zhoutong He, Qintao Li, Dezhang Zhu, Jinlong Gong, *Diamond and Related Material*, **2008**, *17*, 2075.
[26] Qiu-ping Weia, Z.M. Yua, Michael N.R. Ashfoldb, J. Yea, L. Mac, *Applied Surface Science*, **2010**, *256*, 4357.
[27] Daniel Franta, Lenka Zaíčková, Monika Karásková, Ondřej Jašek, David Nečes, Petr Klapetek, Miroslav Valtr, *Diamond and Related Material*, **2008**, *17*, 1278.
[28] Samuele Porro, Gregory De Temmerman, Steve Lisgo,Philips John, Isaela Villapando, Jerry W. Zimmer, Bob Johnson, John I.B. Wilson, *Diamond and Related Material*, **2009**, *18*, 740.
[29] Sobia Allah Rakha, Zhou Xintai, Dezhang Zhu, Yu Guojun, *Current Applied Physics*, **2010**, *10*, 171.
[30] M. Amaral, A.J.S. Fernandes, M. Vila, F.J. Oliveria, R.F. Silva, *Diamond and Related Material*, **2006**, *15*, 1822.
[31] Z.L.Wang, C. Lu, J.J. Li, C.Z. Gu, *Applied Surface Science*, **2009**, *255*, 9522.
[32] Yongqing Fu, Bibo Yan, Nee Lam Loh, *Surface Coating Technology*, **2000**, *130*, 173.
[33]. H.Li, Hak-Joo Lee, Jong-Keuk Park, Young-Joon Baik, Gyu Weon HwangJeung-hyun Jeong, Wook-Seong, *Diamond and Related Material*, **2009**, *18*, 1369.
[34]. C.J. Tang, A.J.Neves, S. Pereira, A.J.S. Fernandes, J. Grácio, M.C. Carmo, *Diamond and Related Material*, **2008**, *17*, 72.
[35]. Z. Khalaj, M. Ghoranneviss, S. Nasirilaheghi, Z. Ghorannevis, R. Hatakeyama, *Chinese Journal Chemical Physics*, **2010**, *23*, 689.
[36] GUO Xiao-Song, BAO Zhong, ZHANG Shan-Shan, XIE Er-Qing. *Chinese Physics Letters*, **2011**, *28*. 2.
[37] Matsumura H., Material Research Society Symposium Proceeding, **1999**, 55I7, 67.
[38] Z. Khalaj, S.Z. Taheri, S.N. Laheghi, P.A. Eslami, *Iranian Physics Journal,* **2009**, 3-1,19.

STUDIA UBB CHEMIA, LVI, 2, 2011 (p. 141 - 148)

EFFECT OF CATALYST LAYER THICKNESS ON GROWTH OF CVD DIAMOND

FATEMEH SHAHSAVARI[a, b], MAHMOOD GHORANNEVISS[a, †], ZAHRA KHALAJ[a], MIRCEA V. DIUDEA[c]

ABSTRACT. Tungsten Nanocrystalline Diamond (NCD) films were grown on silicon substrates by Hot Filament Chemical Vapor Deposition (HFCVD) method using three different catalyst layer thicknesses. At first, the silicon substrates are ultrasonically cleaned in acetone; ethanol and demonized water for 15 minutes in each step to remove organic contaminants, then gold layers were deposited on silicon substrate by DC magnetron sputtering. Nitrogen gas 80 Sccm was introduced into HFCVD chamber for 40 minutes and the growing process were done in a mixture of CH_4/H_2 for 75 minutes. Crystal structure investigations were carried out by X-ray diffraction (XRD) measurements for deposited films. The XRD spectra of the NCD films demonstrated different diffraction peaks for different catalyst layer thicknesses that confirmed the presence of crystalline diamond. Morphology of the diamond films were investigated by scanning electron microscopy. The thickness of the gold nanolayer of each substrate was measured by DEKTAK surface profile measuring system.

Keywords: *Nanocrystalline diamond films, Catalyst, Hot filament CVD, Etching*.

INTRODUCTION

Synthesis of diamond films by chemical vapor deposition (CVD) have been extensively studied during the last decades because of their unique properties and potential applications in mechanics, optics and electronics [1-7]. Diamond films could be produced by various chemical vapor deposition (CVD) methods, including microwave plasma [8-12], hot filament [13-17], arc plasma jet system [18-20] and magnetically enhanced radio frequency assisted plasma [21-22] methods. Among these methods, hot filament chemical vapor deposition (HFCVD) has been one of the most common methods for synthesis of diamond films.

† *E-mail address: Ghoranneviss@gmail.com*
[a] *Plasma Physics Research Center, Science and Research Branch, Islamic Azad University, Tehran, Iran. P.O. Box:14665/678*
[b] *Eghbal Techno-Center, Yazd Scientific and Technology Park, Yazd, Iran*
[c] *Faculty of Chemistry and Chemical Engineering, Babes-Bolyai University, Cluj, Romania*

During the HFCVD system, various gas species formed on and near the filament which their transport to substrate play an important role in growing of diamond film [17]. Therefore the parameters, such as the gas pressure [16-17, 23], the temperature of filament and substrate [24-28], the composition of the source gas [13, 16, 29-30] play an important role in CVD diamond growth. Another important part in growing of CVD diamond deposition is nucleation. Various nucleation processes were used such as bias enhanced nucleation (BEN) [24, 31-33], seeding the substrates by scratching with diamond powder, and ultrasonic agitation of substrate with diamond powder [16, 34-36]. It can also be done by etching gas [37]. In the present work, nitrogen used as etching gas to provide suitable nucleation sites for growing nano diamonds.

Using catalyst nano layer, is a useful method to reduce the time from over than four hours to about one hour in HFCVD systems [16], so we used catalyst nano layer to reduce time into around one hour. To study the effect of different catalyst layer and find the best catalyst thickness layer on the growth of NCD films, different catalyst nano layer's thickness were deposited on the substrates. The XRD spectra of the NCD films demonstrate different diffraction peaks for different catalyst thicknesses layer which confirm the presence of crystalline diamond. Scanning electron microscopy (SEM) shows the various morphologies of the films.

RESULTS AND DISCUSSION

1. Catalyst Layer Thickness Measurements

The thickness of the catalyst nano layer varied within the range of 21.6-62nm. The Fig. 1 shows the thickness measurement of the catalyst nano layer for the three samples by Dektak3 profilometer. Fig.1 (a) shows the 21.6 nm thickness for the first sample. Fig. 1(b) and Fig. 1(c) corresponded to second and third sample with thickness of 49 and 62.4 nm for catalyst layer, respectively. These three samples were named A, B and C, respectively.

2. Morphology study

Fig. 2 shows the SEM morphology of the NCD films deposited at different layer thicknesses of the catalyst. The morphology of the samples are similar, as shown in the Fig. 2, revealing diamond films with cauli-flower like structure.

A wide dispersion of NCD structures were observed in sample A with a lowest thickness layer (Fig.2a). By increasing the catalyst thickness layer to 49nm in sample B, the film morphology became denser and smoother and the whole surface is covered by diamond film (see Fig. 2b). In the sample C with the highest catalyst thickness layer, the crystal size increased

around 200nm (see Fig. 2c). In Fig. 2c there is also changes in nucleation density and the films became less dense. For comparing the grain size of samples B and C was shown in the inset of Fig. 2. The smallest grain size with around a couple of tens nanometers corresponded to sample B. The second nucleation made bigger particles in sample C.

3. X-ray diffraction

XRD patterns of the diamond films deposited for different catalyst layer thicknesses were shown in Fig. 3. For diamond films in sample A, XRD patterns exhibit four peaks from (1 1 1), (104), (110), and (311) crystal planes of diamond. By increasing the layer thickness in sample B, five different crystalline structure of(101), (1 0 2), (104), (108) and (311) was observed, in which the best quality of the diamond peaks refer to the structure with (101) crystallinity. For sample C, the diamond peaks with (111) and (106) crystal planes were only observed. To investigate more, the XRD results were summarized in Table 1. Crystalline structures of (104) and (311) existed in both sample A and B, which they had a higher relative intensity and FWHM in sample B. Regarding to Sherrer's formula, sample B had a better quality and smaller grain size. There was the same crystalline structure of (111) for sample A and C which had the same amount of FWHM and different relative intensities. In XRD spectra of sample C, a sharper peak at 16.3˚ and 33.13˚ corresponded to non-diamond structures. The results show that, by increasing the thickness of the catalyst layer, from 49nm to 62nm, we can see some extra structures. It can be concluded that catalyst thickness layer directly changed the quality, grain size and even crystalline structure of deposited diamond films. XRD studies confirmed previous observation in SEM images that the smallest grain size was corresponding to sample B, which has also the best quality of diamond films. In all samples, the peak at 2theta≈69.2˚ corresponded to Si, the substrate.

CONCLUSIONS

In this study, the effect of different thicknesses layer of the Au catalyst was investigated in HFCVD system. Different thicknesses of nano catalyst layers within the range of 21-62nm, has different effects on CVD diamond growth. XRD characterizations presented changes in diffraction peaks of crystalline diamond within changing the catalyst thickness layer. Optimized catalyst layer thickness found in sample B with the sharpest peak and small FWHM which indicates the higher quality of CVD diamonds. In sample C with the highest catalyst layer thickness, the quality of diamond films decreased and other non diamond structures appeared.

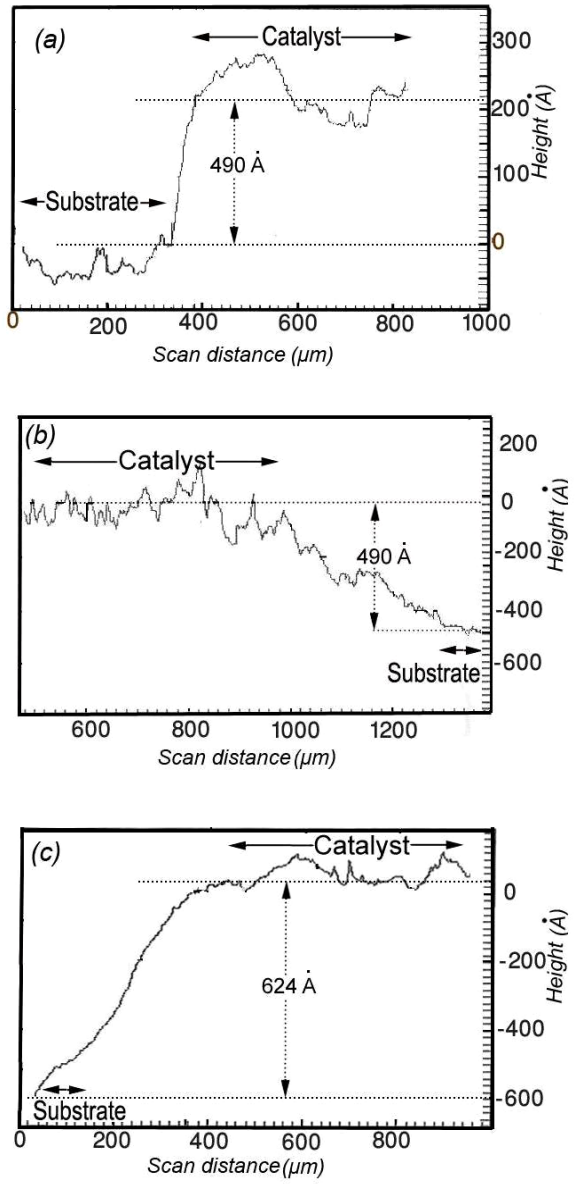

Fig. 1. DEKTAK profilometer results show:
a) sample A with 21.6nm, b) Sample B with 49nm, and
c) sample C with 62.4 nm, for thickness layer.

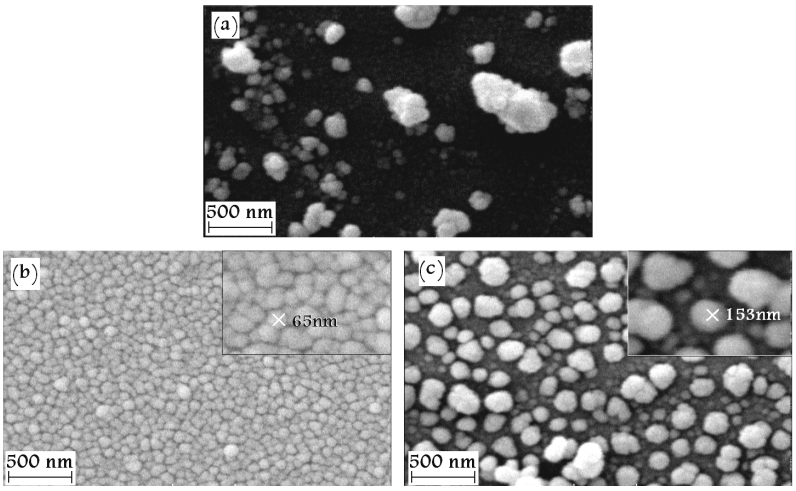

Fig. 2. SEM morphologies of the nanocrystalline diamond deposited in various thicknesses of catalyst layers: (a) sample A, (b) sample B, and (c) sample C. The inset shows the Increasing of the grain size in 200nm scale by increasing the thickness of the nano catalyst layer from sample B to C.

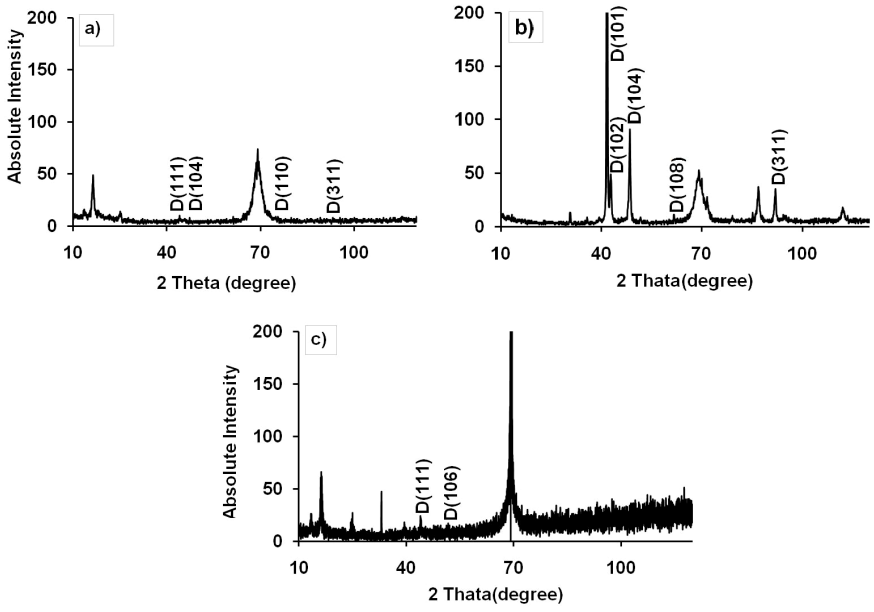

Fig. 3. X-ray diffraction spectra of the diamond films for (a) sample A, (b) sample B, (c) sample C.

Table 1. Results of the XRD studies of the diamond films grown at different catalyst layer thicknesses

Sample	Catalyst layer thickness	Orientation of plane	Pos. [°2Th.]	Height [cts]	FWHM [°2Th.]	Rel. Int. [%]
A	21.6 (nm)	[111]	44.02	2.89	0.315	6.98
		[104]	47.28	2.72	0.236	6.58
		[110]	75.55	2.15	0.315	5.19
		[311]	92.48	1.15	0.197	2.78
B	49 (nm)	[101]	41.68	279.04	0.275	100
		[102]	42.88	38.67	0.315	13.86
		[104]	48.55	84.73	0.275	30.36
		[108]	61.69	6.66	0.197	2.39
		[311]	92.02	28.74	0.275	10.3
C	62.4 (nm)	[111]	44.07	10.76	0.315	0.06
		[106]	53.40	2.28	0.236	0.01

EXPERIMENTAL SECTION

A hot filament CVD system was used for deposition of nanocrystalline diamond in which the tungsten filament was 1.1mm in diameter and about 1.5 cm in length. P-type silicon wafers with [100] orientation were used as the substrates. The substrates were ultrasonically cleaned in acetone, ethanol and deionized water for 15 minutes in each step to remove organic contaminants.

After pretreatment of Si substrates, to deposit different catalyst layers of gold [38], they were loaded in a DC magnetron sputtering system at 1.3 Pa (10^{-2} Torr) in Ar with Au target. The thickness of the gold nano layer of each substrate was measured by DEKTAK3 surface profile measuring system. Then the substrates put into the stainless steel subholder below the hot filament wires. The distance between filament and substrates was 1.5 cm. The chamber was pumped down to the base pressure of 1.3 Pa with a rotary pump and after that reached to 2×10^{-2} Pa (1.5×10^{-4} Torr) with diffusion pump.

In the first step, argon gas with flow ratio of 208 sccm was introduced into the chamber for etching the substrates with total pressure of 4 KPa (30 Torr) for 45 minutes. In the second step, nitrogen was introduced into the chamber as an etching gas with flow rate of 80 sccm. At this time, the filament was reached to about 1600°C. The working pressure was kept in 667 Pa (5 Torr) and duration of time was 40 minutes. In the last step, for growing the nanocrystalline diamond, a mixture of precursor gases of methane and hydrogen were introduced into the chamber. Methane and hydrogen were introduced to the reaction chamber with a total flow rate of 150 sccm to keep the CH4/H2 ratio at 10%. The working pressure in this step was 4 KPa

and nanocrystalline diamond was grown after only 75 minutes. During each step, the substrate temperature was controlled by the thermocouple and was kept on 600°C.

The deposited films were characterized by scanning electron microcopy (SEM, XL30), X-ray diffraction spectroscopy (Cu Kα, λ=0.1541 nm), and DEKTAK3 version 2.13 at room temperature.

REFERENCES

1. R.F. Davis, "Diamond Films and Coatings", Noyes publication, New Jersey, **1992**.
2. K.E. Spear, J.P. Dismukes, "Synthetic Diamond: Emerging CVD Science and Technology", John Wiley, New York, **1993**.
3. R.L.C. Wu, A.K. Rai, A. Garscadden, P. Lee, H.D. Desai,K. Miyoshi, *Journal of Applied Physics*, **1992**, *72*, 110.
4. C. Zuikeer, A.R. Krauss, D.M. Guren, X. Pan, J.C. Li, R. Csencsits, A. Erdemir, C. Bindal, G. Fenske, *Thin Solid Films*, **1995**, *270*, 154.
5. J. Lee, B. Hong, R. Messier, R.W. Collins, *Applied Physics Letters*, **1996**, *69*, 1716.
6. K. Kobashi, "Diamond Films: Chemical Vapor Deposition for Oriented and Heteroepitaxial Growth", first edn. Elsevier Science, Oxford, **2005**.
7. O.A. Shenderova, D.M. Gruen. "Ultrananocrystalline Diamond - Synthesis, Properties, and Applications", William Andrew Publishing, New York, **2006**.
8. N. Jiang, K. Sugimoto, K. Eguchi, T. Inaoka, Y. Shintani, H. Makita, A. Hatta, A. Hiraki, *Journal of Crystal Growth*, **2001**, *222*, 591.
9. L.C. Chen, T.Y. Wang, J.R. Yang, K.H. Chen, D.M. Bhusari, Y.K. Chang, H.H. Hsieh, W.F. Pong, *Diamond and Related Materials*, **2000**, *9*, 877.
10. H. Yoshikawa, C. Morel, Y. Koga, *Diamond and Related Materials*, **2001**, *10*, 1588.
11. A. Stacey, I. Aharonovich, S. Prawer, J.E. Butler, *Diamond and Related Materials*, **2009**, *18*, 51.
12. T. Tachibana, Y. Ando, A. Watanabe, Y. Nishibayashi, K. Kobashi, T. Hirao, K. Oura, *Diamond and Related Materials*, **2001**, *10*, 1569.
13. L. Chow, D. Zhou, A. Hussain, S. Kleckley, K. Zollinger, A. Schulte, H. Wang, *Thin Solid Films*, **2000**, *368*, 193.
14. A. Heiman, I. Gouzman, S.H. Christiansen, H.P. Strunk, A. Hoffman, *Diamond and Related Materials*, **2000**, *9*, 866.
15. S. Rakha, Z. Xintai, D. Zhu, Y. Guojun, *Current Applied Physics*, **2010**, *10*, 171.
16. M. Pandey, R. D'Cunha, A.K. Tyagi, *Journal of Alloys and Compounds*, **2002**, *333*, 260.
17. Sh. Yang, Zh. He, Q. Li, D. Zhu, J. Gong, *Diamond and Related Materials*, **2008**, *17*, 2075.
18. W.Tang, C.Zhu, W.Yao, Q.Wang, C.Li, F.Lu, *Thin Solid Films*, **2003**, *429*, 63.
19. T.B. Huang, W.Z. Tang, F.X. Lu, N. Ali, J. Gracio, *Thin Solid Films*, **2003**, *429*, 108.

20. J.A. Smith, K.N. Rosser, H. Yagi, M.I. Wallace, P.W. May, M.N.R. Ashfold, *Diamond and Related Materials*, **2001**, *10*, 370.
21. S.S. Proffitt, S.J. Probert, M.D. Whitfield, J.S. Foord, R.B. Jackman, *Diamond and Related Materials,* **1999**, *8*, 768.
22. M.P. Pai, D.V. Musale and S.T. Kshirsagar, *Diamond and Related Materials*, **1998**, *7*, 1526.
23. K. Fabisiak, A. Banaszak, M. Kaczmarski, M. Kozanecki, *Optical Materials*, **2006**, *28*, 106.
24. M.M. Larijani, A. Navinrooz, F. Le Normand, *Thin Solid Films*, **2006**, *501*, 206 .
25. S.A. Rakha, Sh. Yang, Zh. He, I. Ahmed, D. Zhu, J. Gong, *Current Applied Physics*, **2009**, *9*, 698.
26. Q.P. Wei, Z.M. Yu, L. Ma, D.F. Yin, J.Ye, *Applied Surface Science*, **2009**, *5*, 1322.
27. N.A. Braga, C.A.A. Cairo, E.C. Almeida, M.R. Baldan, N.G. Ferreira, *Diamond and Related Materials*, **2009**, *18*, 1065.
28. D.C. Barbosa, F.A. Almeida, R.F. Silva, N.G. Ferreira, V.J. Trava-Airoldi, E.J. Corat, *Diamond and Related Materials*, **2009**, *18*, 1283.
29. L.C. Chen, T.Y. Wang, J.R. Yang, K.H. Chen, D.M. Bhusari, Y.K. Chang, H.H. Hsieh, W.F. Pong, *Diamond and Related Materials*, **2000**, *9*, 877.
30. V.Baranauskas, H.J. Ceragioli, A.C. Peterlevitz, S.F. Durrant, *Thin Solid Films*, **2001**, *398-399*, 250.
31. N. Jiang, K. Sugimoto, K. Eguchi, T. Inaoka, Y. Shintani, H. Makita, A. Hatta, A. Hiraki, *Journal of Crystal Growth*, **2001**, *222*, 591.
32. J.T. Huang, W.Y. Yeh, J. Hwang, H. Chang, *Thin Solid Films*, **1998**, *315*, 35.
33. G.H. Song, C. Sun, B. Wang, A.Y. Wang, R.F. Huang, L.S. Wen, *Material Letters*, **2001**, *48*, 8.
34. J.G. Buijnsters, L. Vázquez, J.J. ter Meulen, *Diamond and Related Materials*, **2009**, *18*, 1239.
35. K. Fabisiak, W. Masierak, E. Staryga, M. Kozanecki, *Optical Materials*, **2008**, *30*, 763.
36. Tien-Syh Yang, Jir-Yon Lai, Chia-Liang Cheng, Ming-Show Wong, *Diamond and Related Materials*, **2001**, *10*, 2161.
37. Z. Khalaj, M. Ghoranneviss, S. Nasirilaheghi, Z. Ghorannevis, R. Hatakeyama, *Chinese Journal of Chemical Physic*s, **2010**, *23*, 689.
38. Chih-Kuang Kao, Jhih-Kun Yan, Li Chang, Shih-Yin Cho, Hou-Gaung Chen, *Diamond and Related Materials*, **2004**, *13*, 585.

STUDIA UBB CHEMIA, LVI, 2, 2011 (p. 149 - 154)

DETERMINATION OF RATE COEFFICIENTS AND DIFFUSION COEFFICIENTS OF BUTANOL USING RF-GC METHODOLOGIES

KHALISANNI KHALID[*], RASHID ATTA KHAN[*], SHARIFUDDIN MOHD. ZAIN[*]

ABSTRACT. Reversed-flow gas chromatography, which is a sub-technique of inverse gas chromatography, is an experimental arrangement simulating a simple model for the action of liquid pollutants in laboratory scale. By using a commercial gas chromatograph and an appropriate mathematical analysis, kinetic parameters such as rate coefficients, k_c and diffusion coefficients, D of analyzed liquid were calculated. These physicochemical properties of the liquid experimented will contribute to the references for future research in the area of environment, food, agriculture as well as physical sciences.

Keywords: *Chromatography, Diffusion Coefficient, Evaporation, Pollutant, Rate Coefficient*

INTRODUCTION

Evaporation is a vital ecological fate for compounds introduced into both freshwater and marine environments by accidental spills, industrial effluents, or introduced directly into the air from industrial unit processes such as bioreactors and cooling towers. Atmosphere contains many gases that homogeneously distributed such as, carbon monoxide, nitrogen oxides, sulphur oxides, petroleum hydrocarbons and pesticides. These pollutants attack solids; including historical buildings and monuments that are finally malformed to permanently damaged products. Gases also pollute seawater, transferred from the atmosphere to the water surface and then dissolved into the liquid phase. The transfer rate of pollutants from the air onto the sea surface depends on rate coefficients and diffusion coefficients in the gas phase [1].

The first idea on reversed-flow gas chromatography (RF-GC) differential aspect was that of Phillips and co-researchers[2], who stopped the flow of the carrier gas for a short time period repeatedly, producing each time extra narrow peaks. By this method, he measured the differential rate of a catalytic

[*] *Department of Chemistry, Faculty of Science, University of Malaya, 50603 Kuala Lumpur, Malaysia, typhloids@gmail.com*

reaction-taking place on the stationary phase in a gas chromatographic column. The method permitted a direct determination of reaction rates, not only for small conversions to products, or for reaction times around zero, but in the whole range of conversions covering an extended period of time [3].

The aim of the research was to determine the rate coefficients and diffusion coefficients of butanol under study assisted by RF-GC techniques.

RESULTS AND DISCUSSION

The results obtained from the preliminary experiments were evaluated for physicochemical quantities of butanol.

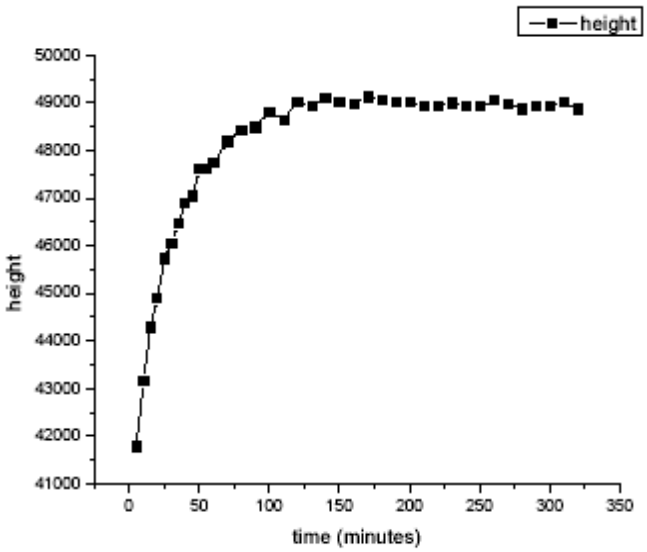

Figure 1. The rise of the sample peak height with time for the diffusion of butanol vapor into nitrogen (V=cm^3 s-^{1}), 313.15K and 1 atm.

In Figure 1, the height, h of the sample peaks as a function of the time t_0, when the flow reversal was made, is plotted on a semilogarithmatic scale [4]. It shows the steep rise and then the leveling off with time of the sample peak height. As an example using equation,

$$\ln(h_\infty - h) = \ln h_\infty - [2(k_c L + D)/L^2]t_0 \qquad \textbf{Equation 1}$$

$$\ln[h(L/2t_0^{1/2} + k_c t_0^{1/2})] = \ln[4k_c c_0/v(D/\pi)^{1/2}] - (L^2/4D)(1/t_0) \qquad \textbf{Equation 2}$$

which derived from Katsanos [5] to analyze the experimental findings, the data on Figure 1 are treated as follows. Iterated some points, which correspond to small times, the rest of the experimental points are plotted according to Equation 1, as shown in Figure 2.

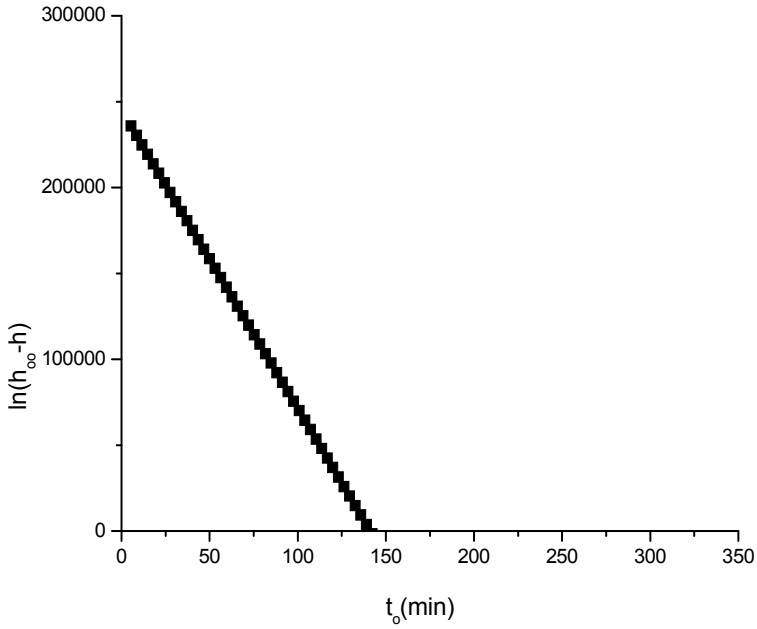

Figure 2. Diffusion of butanol vapor into nitrogen (V=1cm^3 s^{-1}), at 313.15K and 1atm.

As infinity value h_∞ was taken the mean of the values found in the time interval, which differed little from one another. From the slope of this plot, which is equal to - $2(k_cL+D)/L^2$, according to Equation 1, using the theoretically calculated value of 0.1020 cm^2 s^{-1}, and the actual value of L (28.5cm), a value of 208.68 cm s^{-1} for k_c, is calculated.

This approximate value is now used to plot all but the few point closed to h_∞ according to Equation 2 as shown in Figure 3.

From the slope of this latter plot, a value of 0.1020 cm^2 s^{-1} for *D* is found. If this is combined with the slope of the previous plot (Figure 2), a second value for k_c= 208.68 cm s^{-1} is calculated and further used to replot the data according to Equation 2. The new value for *D* found coincides with the previous one (0.1020 cm^2 s^{-1}), and thus the iteration procedure must be stopped.

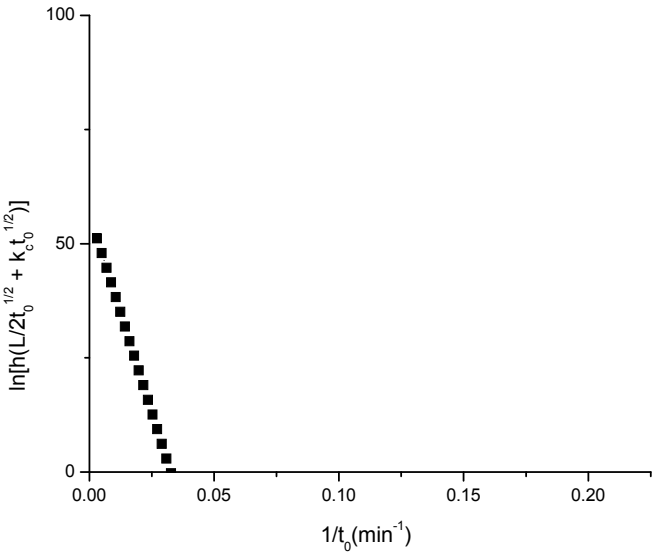

Figure 3. Data from evaporation of butanol into nitrogen (V=1cm^3 s^{-1}), at 313.15K and 1atm.

Table 1. Rate Coefficients for Evaporation of Pure Liquid and Diffusion Coefficients of Vapors Into Nitrogen at 1atm

			D, cm^2 s^{-1}		
Liquid	T, K	k_c, cm s^{-1}	This work	Theoretical	Deviation (%)
Butanol	313.15	208.68±0.08	0.1020±0.0005	0.1020	0.01
	323.15	218.75±0.04	0.1079±0.0015	0.1078	0.13
	333.15	229.80±0.12	0.1137±0.0004	0.1137	0.04
	343.15	241.65±0.05	0.1197±0.0002	0.1197	0
	353.15	254.39±0.10	0.1259±0.0001	0.1259	0
	363.15	268.08±0.07	0.1322±0.0008	0.1322	0.04
	373.15	283.57±0.02	0.1386±0.0002	0.1387	0.07

Table 1 summarizes the results obtained with the pure liquid studied. In the same table, the diffusion coefficients determined here are compared with those calculated theoretically. As one can see from the Table 1, the *D* values determined in this work are very close to the theoretical ones. The deviation given in the last column is the accuracy of the experimental values from those calculated theoretically [6]:

$$\text{Deviation (\%)} = 100[(D_{found}-D_{theory})/D_{found}]$$

With no exception, this accuracy is better than 0.5% in all cases and indicated that investigation of liquid pollutants using reversed-flow gas chromatography (RF-GC) is of great significance in environmental science. However, the comparison of experimental and literature values is impossible because the experimental temperatures, column length, gas flow rate and pressure are varies [7].

Evaporation of chemicals from water bodies to the atmosphere can be an important environmental pathway for certain pollutant liquids. The transfer rate of pollutants from the air onto the sea surface depends on rate coefficients and diffusion coefficients in the gas phase. The chemical interaction involves measurement of the rate of liquid loss into a gas stream flowing horizontally across the liquid surface. In the majority of these techniques relative evaporation rates, which cannot be related to the physical properties of the evaporating species, as well as evaporation halftimes are measured. Thus, this relative new technique of reversed-flow gas chromatography (RF-GC) is suitable to study various physicochemical measurements, such as of rate coefficients and diffusion coefficients for the evaporation of pure liquid.

CONCLUSIONS

The uniqueness of the method is its accuracy and simplicity. The presented style of reversed-flow gas chromatography can be used to simultaneously determine correct absolute evaporation rates and vapours diffusivities of pure liquids.

EXPERIMENTAL SECTION

In this type of chromatography, the column is unfilled with any material and sampling process is carried out by reversing of the carrier gas from time to time producing sample peaks. Selected liquid pollutants of 99.99% purity (MERCK) will be used as solute, while carrier gas was nitrogen of 99.99% purity. After the injection of 1 cm^3 s^{-1} of liquid pollutant at atmospheric pressure and selected temperature, a continuous concentration–time curve is record passing through a maximum and then declining with time. By means of a six-port valve, the carrier gas flow direction is reversed for 5 s, which is a shorter time period than the gas hold-up time in both column sections *l* and *l'*, and then the gas is again turned to its original direction. This procedure creates extra chromatographic peaks (sample peaks) superimposed on the continuous elution curve. This is repeated many times during the experiment lasting a few hours. The height, *h* of the sample

peaks from the continuous signal, taken as baseline, to their maximum is plotted as ln (h_∞-h) versus time, giving a *diffusion band*, whose shape and slope both depend on vessel *L* which is empty, as well as on the geometric characteristics of the vessel and the temperature. In all experiments, the pressure drop along *l* + *l'* will negligible, while the carrier gas flow-rate will keep constant (1.0 cm^3 s^{-1}).

ACKNOWLEDGMENTS

The author is indebted to University Malaya, who supported the research project and Ministry of Science and Technology Malaysia (MOSTI) for the scholarship. Last but not least, special thanks to the staff from Department of Chemistry, University of Malaya for their technical supported

REFERENCES

1. S.G. Robert, *Addiction*, **2004**, *99*, 686.
2. C.S.G. Phillips, A.J. Hart-Davis, R.G.L. Saul, J. Wormald, *Journal Gas Chromatography*, **1967**, *5*, 424.
3. N.A. Katsanos, *Journal Chromatography A*, **2002**, *969***,** 3.
4. G. Karaiskakis, P. Agathonos, A. Niotis, N.A. Katsanos, *Journal Chromatography A,* **1986**, *364*, 79.
5. N.A. Katsanos, A.R. Khan, G. Dimitrios, K. George, *Journal Chromatography A,* **2001**, *934,* 31.
6. G. Karaiskakis, D. Gavril, *Journal Chromatography A,* **2004**, *1037*, 147.
7. G. Dimitrios, A.K. Rashid, G. Karaiskakis, *AIChE*, **2006**, *52*, 2381.

STUDIA UBB CHEMIA, LVI, 2, 2011 (p. 155 - 166)

BIOCATALYTIC PREPARATION OF ENANTIOPURE 2-AMINO-3-(5-ARYL-FURAN-2-YL)PROPANOIC ACIDS

LAURA ANCUȚA POP*

ABSTRACT. The synthesis of both enantiomers of 2-amino-3-(5-aryl-furan-2-yl)propanoic acids acids is presented by two kinetic resolution processes: the enantiomer selective Acylase I mediated hydrolysis of *N*-acetylated amino acids and the enantiomer selective baker's yeast catalysed ester hydrolysis of the double protected amino acids.

Keywords: *Kinetic resolution, Acylase I, baker's yeast, enantioselectivity, amino acids*

INTRODUCTION

Unnatural amino acids are useful building blocks for the asymmetric synthesis of several anticancer and antiviral compounds[1].They can increase the activity, stability, bioavailability and binding specificity of the peptides and proteins in which they are inserted[2]. Some of them are already important drugs in the treatment of Parkinson's disease, arthritis and high blood pressure. Due to their nature, they can also be used as templates for asymmetric catalysis[3].

While fermentation is widely used for the production of natural α-amino acids, for the synthesis of unnatural α-amino acids several chemical[1-2,4] or chemoenzymatic[5] methods were developed. The chemical asymmetric syntheses are generally multistep procedures requiring special reagents, tedious purification steps and in most of the cases the global yields are low. Several synthetic enzymatic procedures involving aminomutases[6], ammonia lyases[7], transaminases[8] or hydrolases as biocatalysts were developed for the efficient preparative scale synthesis of both L- and D-unnatural amino acids.

Hydrolases are one of the most important biocatalysts for the kinetic resolution of various heterocyclic racemic substrates, including secondary alcohols[9], ethane-1,2-diols[10], α-cyanohydrins[11] and β-hydroxy acids[12].

On one hand, Acylase I (Aminoacylase I, *N*-acyl- L-amino acid amidohydrolase, E.C. 3.5.1.14) as a readily available inexpensive enzyme with relaxed substrate specificity is widely used for the synthesis of L-amino

* *Universitatea Babeş-Bolyai, Facultatea de Chimie şi Inginerie Chimică, Str. Kogălniceanu, Nr. 1, RO-400084 Cluj-Napoca, Romania, lisprava@chem.ubbcluj.ro*

acids[13]. It is also preferred for the industrial preparation of enatiopure L-amino acid by the kinetic resolution of corresponding racemic *N*-acyl derivatives[14].

On the other hand, due to its low cost and broad substrate acceptability, baker's yeast is an useful catalysts for organic synthesis. Since it is a non-pathogenic microorganism, is simple to grow at any scale, is accessible in stable dried form and it can be bought from a local store, baker's yeast was widely used for the regio-, chemo- and stereoselective reduction of various kind of carbonylic compounds[15]. Enantiomerically enriched heteroaryl ethanols[16] or non chiral heteroayl methanols[17] were synthesized with high yields by cellular reduction. Baker's yeast reduction of hydroxymethyl ketones and acetoxymethyl ketones proved to be useful for production of both opposite enantiomeric forms of 1,2-diols with 100% theoretical yield[18]. The kinetic resolution of racemic phenothiazine-based aldehyde sulfoxides by baker's yeast mediated enantioselective reduction was also reported[19].

Beside the reductive capacity, the hydrolytic ability of the baker's yeast cells is also known. Some reports already presented the baker's yeast mediated stereoselective hydrolysis of the ester moiety of natural *N*-acetyl amino acid esters[20].

Herein we describe the synthesis of both optically pure enantiomers of various 2-amino-3-(5-aryl-furan-2-yl)propanoic acids by enzymatic kinetic resolution of the racemic substrates using as biocatalyst two enzymes acting on different functional groups: Acylase I and esterases from baker's yeast.

RESULTS AND DISCUSSION

1. Chemical synthesis

The racemic amino acids and their derivatives (*N*-acetyl amino acids and *N*-acetyl amino esters) were synthesized by a known procedure starting from their corresponding aldehydes[21] (Scheme 1).

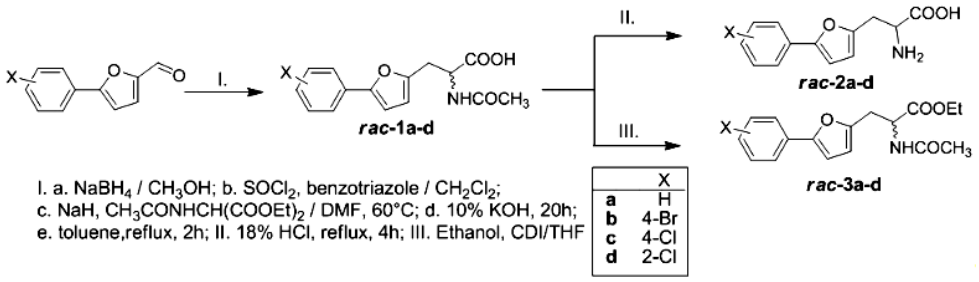

Scheme 1

2. Enzyme catalysed synthesis

For the synthesis of enantiopure **L**-alanines two distinct enzymatic kinetic resolution methods were tested.

In the first method, the racemic *N*-acetyl alanines were hydrolyzed in presence of Acylase I at a pH 7-8 obtaining the optically enriched L-2-amino-(5-aryl-furan-2-yl)propanoic acids **L-2a-d** and their *N*-acetylated counterparts, D-2-acetamido-3-((5-aryl-furan-2-yl) propanoic acids **D-1a-d** (Scheme 2).

In the second method, exploiting the stereoselective esterase activity of the baker's yeast cells, the racemic ethyl 2-acetamido-3-(5-phenyl-furan-2-yl)propanoates (*rac*-**3a-d**) were transformed into D-ethyl-2-acetamido-3-(5-phenyl-furan-2-yl)propanoates **D-3a-d** and L-2-acetamido-3-((5-phenyl-furan-2-yl) propanoic acids **L-1a-d** (Scheme 2).

The obtained D-2-acetamido-3-((5-aryl-furan-2-yl) propanoic acids **D-1a-d** and D-ethyl-2-acetamido-3-(5-phenyl-furan-2-yl)propanoates **D-3a-d** can be further hydrolyzed into the corresponding D-alanines in accordance with the known procedure which states that *N*-acetyl amino acid esters can be deprotected by the sequential hydrolysis of the ester in weak basic medium followed by the acidolysis of the amidic bond (Scheme 2).

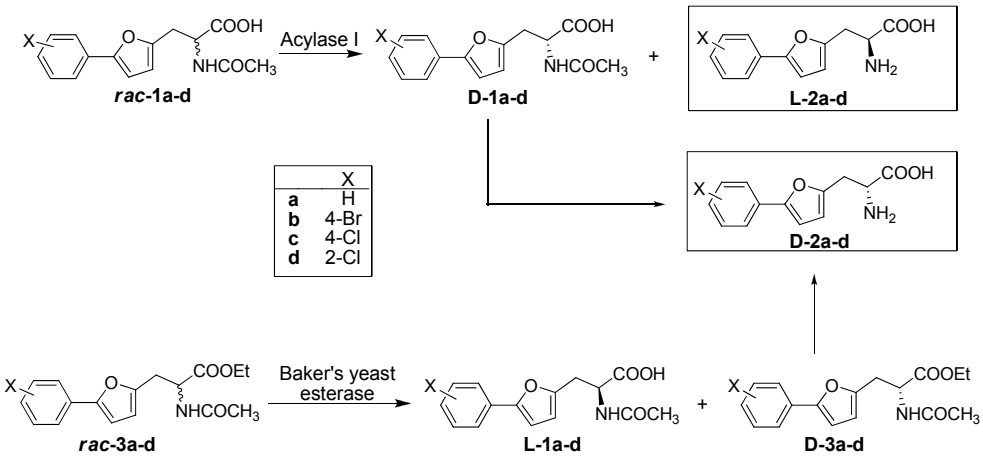

Scheme 2

In order to find the optimal conditions (high reaction rates and high stereoselectivity) first the analytical scale experiments were performed. The optimal Aminoacylase I catalyzed transformation occurred in water, pH 7-8 in presence of $CoCl_2 \times 6H_2O$ as additive. The reactions were stopped after 24 h, at approx. 50% conversion. Best result for the baker's yeast mediated enantiomer selective hydrolysis were found when reactions were performed without additives in presence of non fermenting water suspended cells.

Stopping the reaction by extracting the products with dichloromethane at approx. 50% conversion, highly enatiomerically enriched products (ee 99%) were formed. With these results in our hands, the preparative scale experiments were performed. All the dilutions, substrate-biocatalysts *ratio* and reaction conditions were the same with those found as optimal for the analytical scale reactions and no significant differences for yield and enantiomeric excesses of the products were observed, compared to those found for the analytical scale biotransformations. The enantiomeric excess, optical rotation and yields for each individual enantiomer is presented in Table 1.

Table 1. Enantiomeric excess, optically rotatory power and yield of each compound from the preparative scale experiments

Compound	ee%	$[\alpha]_D$	Yield (%)
L-1a	99	-25.8[a]	46.3
L-1b	99	-12.9[a]	49.1
L-1c	99	-21.8[a]	44.2
L-1d	99	-20.8[a]	40.3
L-2a	99	+28.2[b]	38.5
L-2b	99	+10.8[b]	45.2
L-2c	99	+17.8[b]	42.8
L-2d	99	+16.7[b]	44.5
D-3a	99	+17.2[c]	40.5
D-3b	99	+19.9[c]	45.3
D-3c	99	+18.3[c]	43.4
D-3d	98	+15.5[c]	44.9

[a-] in MeOH; [b] in CH_3COOH; [c] in $CHCl_3$,

CONCLUSIONS

The present work describes the usability of the enzymatic kinetic resolution process for obtaining both highly enantiomerically enriched 2-amino-3-((5-aryl-furan-2-yl)propanoic acids using two kind of biocatalysts (Acylase I from *Aspergillus meleus* and esterases from baker's yeast) showing the same enantio-preference. Besides the high stereoselectivity, both procedures provide good yields for the pure isolated products.

EXPERIMENTAL SECTION

1. Analytical methods

The ^{1}H- and ^{13}C-NMR spectra were recorded on a Bruker Advance spectrometer operating at 300 and 75 MHz, respectively at 25 °C in DMSO-d_6 or $CDCl_3$. Electron impact mass spectra (EI-MS) were taken on a LCQ advantage

by ThermoFisher spectrometer operating at 1950-2050V, the samples were dissolved in MeOH/H_2O=50/50 (v/v), or MeOH/CH_3CN=50/50.

High Performance Liquid Chromatography (HPLC) analyses were conducted with a HP 1200 instrument using an Astec Chirobiotic-Tag column (4.6×250 mm) and a mixture of methanol and TEAA buffer, pH 4.1 (80:20, v/v) as eluent for enantiomeric separation of *rac*-**1,2 a-d** and a Chiralpak IA column (4.6×250 mm) and a mixture of hexane and 2-propanol (90:10, v/v) as eluent for enantiomeric separation of *rac*-**3a,c,d**, and a Chiralpak IC column (4.6x250mm) and a mixture of *n*-hexane: 2-propanol (90:10, v/v) as eluent for enantiomeric separation of *rac*-**3b** at 1 mL/min flow rate in all cases. For all chiral compounds, high resolution enantiomeric separation was performed. Retention times for **L-** and **D-1-3a-d** are presented in Table 2.

Thin Layer Chromatography (TLC) was carried out using Merck Kieselgel 60F_{254} sheets. Spots were visualized by treatment with 5% ethanolic phosphomolybdic acid solution and heating. Preparative chromatographic separations were performed using column chromatography on Merck Kieselgel 60 (63-200 μm). Melting points were determined by hot plate method and are uncorrected. Optical rotations were determined on a Perkin-Elmer 201 polarimeter and $[\alpha]_D^{20}$ values are given in units of 10^{-1} deg cm^2 g^{-1}.

Table 2. Retention times of the enantiomers of *rac*-**1-3a-d**.

				R_t (min.)			
L-1a	**D-1a**	**L-1b**	**D-1b**	**L-1c**	**D-1c**	**L-1d**	**D-1d**
10.9	3.2	13.6	3.3	12.7	3.2	12.9	3.7
L-2a	**D-2a**	**L-2b**	**D-2b**	**L-2c**	**D-2c**	**L-2d**	**D-2d**
9.0	13.9	9.7	16.2	9.2	15.4	10.2	15.4
L-3a	**D-3a**	**L-3b**	**D-3b**	**L-3c**	**D-3c**	**L-3d**	**D-3d**
13.0	9.6	10.4	9.3	15.8	10.1	10.8	8.5

2. Reagents and solvents

All inorganic reagents and solvents were products of Aldrich or Fluka. All solvents were purified and dried by standard methods as required. Acylase I was purchased from Fluka and baker's yeast Budafok Ltd, Hungary was purchased from a local store.

3. Chemical synthesis of racemic alanines and their derivatives

3.1. Synthesis of rac-2-acetamido-3-((5-aryl-furan-2-yl)propanoic acids rac-1a-d. The racemic 2-acetamido-3-aryl-propanoic acids *rac*-**1a-d** were synthesized from the corresponding 5-phenylfuran-2-carbaldehydes prepared using a known procedure[21]. Aldehydes were transformed in chloromethylene derivatives *via* the corresponding alcohols. Further the coupling of the halogenated compounds with diethyl-2-acetamido-malonate afforded the diethyl-

2-acetamido-2-((aryl-furan-2-yl)-methyl)malonates which generate the diethyl esters by mild basic hydrolysis. These compounds were further decarboxylated in boiling toluene into the corresponding 2-acetamido-3-(arylfuran-2-yl)propanoic acids *rac*-**1a-d**.

3.1.1. rac-2-Acetamido-3-(5-phenylfuran-2yl)propanoic acid (rac-1a) Yield 47%, m.p. 197 °C; ^{1}H-NMR (300 MHz, DMSO-d_6): δ = 1.83 (3H, s); 3.03 (1H, dd, *J*=8.47Hz, *J*=15.25Hz); 3.12(1H, dd, *J*=5.08Hz, *J*=15.25Hz); 4.52 (1H, ddd, *J*=5.27Hz, *J*=8.28Hz, *J*=8.1Hz), 6.26 (1H, d, *J*=3.3Hz), 6.81 (1H, d, *J*=3.3Hz); 7.24(2H, dd, *J*=7.65Hz, *J*=7.35Hz); 7.39(1H, dd, *J*=7.35Hz, *J*=7.65Hz); 7.26(2H, d, *J*=7.35Hz); 8.31(1H, d, *J*=8.1Hz); ^{13}C-NMR (75 MHz, DMSO-d_6): 22.40; 29.90; 51.13; 106.56; 109.46; 123.14; 127.13; 128.82; 130.48, 151,48; 151.98; 169.33; 172.62; ESI^{+}-MS: m/z: 296.0890 [M+Na^{+}].

3.1.2. rac-2-Acetamido-3-(5-(4-bromophenyl)furan-2-yl)propanoic acid (rac-1b) Yield 54%, m.p. 194°C; ^{1}H-NMR: (300 MHz, DMSO-d_6): δ = 1.83 (3H, s); 2.69 (1H, dd, *J*=8.57Hz, *J*=15.30Hz); 2.78 (1H, dd, *J*=5.08Hz, *J*=15.30Hz); 4.51 (1H, ddd, *J*=5.27Hz, *J*=8.28Hz, *J*=8.1Hz); 6.27 (1H, d, *J*=3.3Hz); 6.88 (1H, d, *J*=3.3Hz); 7.58-7.95 (4H, m); 8.29(1H, d, *J*=8.1Hz); 12.84(1H, s); ^{13}C-NMR (75 MHz, DMSO-d_6): 22,37; 29.87; 51.03; 107.49; 109,66; 119.90; 125.08; 129.63; 131.74; 150.88; 151.99; 169.28; 172.57; ESI^{-}-MS: m/z (abundance): 350.0027 (100%); 352.0017 (98.13%) [M-H^{-}].

3.1.3. rac-2-Acetamido-3-(5-(4-chlorophenyl) furan-2-yl)propanoic acid (rac-1c). Yield 43%, m.p.196°C; ^{1}H-NMR: (300 MHz, DMSO-d_6): δ = 1.82 (3H, s); 3.02 (1H, dd, *J*=8.57Hz, *J*=15.30Hz); 3.11(1H, dd, *J*=8.57Hz, *J*=15.30Hz); 4.48 (1H, ddd, *J*=5.27Hz, *J*=8.28Hz, *J*=8.1Hz); 6.27 (1H,d, *J*=3.2Hz); 6.87 (1H,d, *J*=3.2Hz); 7.46 (2H,d, *J*=8.47Hz); 7.66 (2H,d, *J*=8.47Hz); 8.31 (1H,d, *J*=7.72Hz); ^{13}C-NMR (75 MHz, DMSO- d_6): 22.39; 29.88; 51.09; 107.42; 109.66; 124.83; 128.88; 129.33; 131.41; 150.87; 151.97; 169.34; 172.59; ESI^{+}-MS: m/z (abundance): 330.0506 (100%); 332.0494 (34.51%) [M+Na^{+}].

3.1.4. rac-2-Acetamido-3-(5-(2-chlorophenyl) furan-2-yl)propanoic acid (rac-1d). Yield 36%, m.p. 130°C; ^{1}H-NMR: (300 MHz, DMSO-d_6): δ = 1.82 (3H, s); 3.04 (1H, dd, *J*=8.47Hz, *J*=15.25Hz); 3.15 (1H, dd, *J*=4.99Hz, *J*=15.25Hz); 4.51 (1H, ddd, *J*=5.27Hz, *J*=8.28Hz, *J*=8.1Hz), 6.32 (1H, d, *J*=3.3Hz); 7.01 (1H, d, *J*=3.3Hz); 7.26 (1H, dd, *J*=7.53Hz, *J*=1.2Hz); 7.38 (1H, dd, *J*=7.53Hz, *J*=8.1Hz); 7.43 (1H, d, *J*=7.91Hz); 7.81 (1H, d, *J*=7.91Hz); 8.23 (1H, d, J=7.91Hz); ^{13}C-NMR (75 MHz, DMSO-d_6): 22.49; 30.00; 51.38; 109.45; 112.00; 127.54; 128.44; 128.53; 128.73; 130.71; 148.05; 152.30; 169.25; 172.80; ESI^{+}-MS: m/z (abundance): 330.0515 (100%); 332.0501 (35.72%) [M+Na^{+}].

3.2. Synthesis of rac-2-amino-3-((5-aryl-furan-2-yl)propanoic acids (rac-2a-d). *rac*-2-acetamido-3-aryl-propanoic acid *rac*-**1a-d** (1 g) was suspended in half concentrated HCl (10 mL) and the mixtures was refluxed for 4 h. After that the solvent was removed *in vacuo*. The crude product was washed with diethylether and dried yielding the pure product.

3.2.1. rac-2-Amino-3-(5-phenylfuran-2-yl)propanoic acid (rac-2a). Yield 61%, m.p.= 170°C. ^{1}H-NMR: (300 MHz, DMSO-d_6): δ = 3.24 (2H, dd, *J*=5.7Hz, *J*=7.5Hz); 4.14 (1H, t, *J*=5.4Hz); 6.46 (1H,d, *J*=2.7Hz); 6.89 (1H, d, *J*=2.7Hz); 7.52-7.92(5H, m); 8.55(3H, s, NH_3^+); ^{13}C-NMR (75 MHz, DMSO-d_6): *δ* = 28.5; 50.9; 106.6; 111.0; 123.7; 127.9; 128.6; 130.3; 153.5; 153.4; 170.14; HRMS ESI$^+$: m/z: 232.1087 [M+H$^+$].

3.2.2. rac-2-Amino-3-(5-(4-bromophenyl)furan-2-yl)propanoic acid (rac-2b). Yield 68%, m.p.=175°C. ^{1}H-NMR: (300 MHz, DMSO-d_6): δ = 3.22 (2H,dd, *J*=5.7Hz, *J*=7.5Hz); 4.14 (1H, t, *J*=5.4Hz); 6.46 (1H,d, *J*=3Hz); 6.87 (1H,d, *J*=3Hz); 7.72 (2H, d, *J*=8.4Hz); 7.89 (2H,d, *J*=8.4Hz); 8.45 (3H, s, NH_3^+); ^{13}C-NMR (75 MHz, DMSO-d_6): *δ* = 28.5; 50.8; 107.4; 111.2; 120.0; 125.2; 129.4; 131.7; 149.0; 151.5; 169.9; HRMS ESI$^+$: m/z (abundance): 310.0183 (100%); 312.0176 (99.12%) [M+H$^+$].

3.2.3. rac-2-Amino-3-(5-(4-chlorophenyl)furan-2-yl)propanoic acid (rac-2c). Yield 60%, m.p.=180°C. ^{1}H-NMR: (300 MHz, DMSO-d_6): δ = 3.23 (2H,dd, *J*=5.7Hz, *J*=7.5Hz); 4.13(1H, t, *J*=5.4Hz); 6.65(1H,d, *J*=3Hz); 6.95 (1H,d, *J*=3Hz); 7.58 (2H,d, *J*=8.7Hz); 7.97 (2H,d, *J*=8.7Hz); 8.54 (3H, s, NH_3^+); ^{13}C-NMR (75 MHz, DMSO-d_6): *δ* = 28.4; 50.8; 108.3; 111.2; 125.0; 128.8; 129.8; 135,0; 152.5; 154.7; 170.1; HSMS ESI$^-$: m/z (abundance): 282.0521 (100%), 284.508 (35.66%) [M+OH$^-$].

3.2.4. rac-2-Amino-3-(5-(2-chlorophenyl)furan-yl)propanoic acid (rac-2d). Yield 65%, m.p.=210°C. ^{1}H-NMR: (300 MHz, DMSO-d_6): δ = 3.35 (2H,dd, *J*=5.7Hz, *J*=7.5Hz); 4.20 (1H, t, *J*=5.4Hz); 6.46 (1H,d, *J*=2.7Hz); 7.04 (1H,d, *J*=3Hz); 7.29-7.84 (4H,m); 8.72(3H, s, NH_3^+); ^{13}C-NMR (75 MHz, DMSO-d_6): 28.60; 51.01; 111.23; 112.07; 127.55; 127.94; 128.38; 128.65; 128.73; 130.72; 148.89; 149.07; 170.01; HRMS ESI$^+$: m/z (abundance): 266.0579 (100%); 268.0549 (33.02%) [M+H$^+$]; HRMS ESI$^-$: m/z (abundance):264.0438(100%); 266.0415(34.41%) [M-H$^-$]

3.3. Synthesis of racemic ethyl 2-acetamido-3-(5-aryl-furan-2-yl) propanoates rac-3a-d. Into a solution of *N*,*N'*-carbonyldiimidazole (90 mg, 0.55 mmol) and *rac*-2-acetamido-3-((5-phenyl-furan-2-yl)propanoic acid *rac*-**1a-d** (0.5 mmol) in anhydrous THF (2.5 mL), ethanol (45 mg, 56 µL, 0.75 mmol) was added in one portion at room temperature. After the reaction was completed (checked by TLC), the solvent was distilled off *in vacuo* and the crude product was purified by column chromatography on silica gel using as eluent dichloromethane:acetone (90:10, v/v).

3.3.1. rac-ethyl 2-acetamido-3-(5-phenylfuran-2-yl)propanoate (rac-3a). Yield 24.58%. ^{1}H-NMR: (300 MHz, $CDCl_3$): δ = 1.17 (3H, t, *J*=8.4Hz); 1.92 (3H, s); 3.15 (1H, dd, *J*=4.8Hz, *J*=2.63Hz); 3.17(1H, dd, *J*=3.01Hz, *J*=4.8Hz); 4.15 (2H, q, J=8.4Hz); 4.76 (1H, dd, *J*=5.4Hz, *J*=6.15Hz,); 6.05 (1H, d, *J*=2.4Hz); 6.43 (1H, dd, *J*=2.4Hz); 7.16 (2H, dd, *J*=7.8Hz, *J*=7.8Hz); 7.28 (2H, dd, *J*=7.8Hz, *J*=6.9Hz); 7.45(1H, d, *J*=7.8Hz); 7.50 (1H, s). ^{13}C-NMR (75 MHz,

$CDCl_3$): 14.30; 23.34; 30.92; 51.65; 61.93; 105.88; 110.27; 123.59; 127.38; 128.83; 130.86; 150.16; 153.65; 169.88; 171.43; ESI^+-MS: m/z: 324.1194 [$M+Na^+$]; 365.1459 [$M+CH_3CN+Na^+$].

3.3.2. rac-ethyl 2-acetamido-3-(5-(4-bromophenyl) furan-2-yl)propanoate (rac-3b). Yield 22%. ^{1}H-NMR: (300 MHz, $CDCl_3$): δ = 1.24 (3H, t, *J*=7.05Hz); 2.05 (3H, s); 3.23 (1H, dd, *J*=2.4Hz, *J*=4.8Hz); 3.51(1H, dd, *J*=3Hz, *J*=4.8Hz); 4.18 (2H, q, J=7.1Hz), 4.83 (1H, ddd, *J*=5.4Hz, *J*=7.5Hz, *J*=5.4Hz); 6.14 (1H, d, *J*=3Hz); 6.52 (1H, d, *J*=3Hz); 7.40 (2H, d, *J*=8.7Hz); 7.46(2H,d, *J*=8.7Hz); 7.85 (1H, s); ^{13}C-NMR (75 MHz, $CDCl_3$): 14.28; 23.30; 30.93; 51.55; 61.92; 106.48; 110.37; 121.05; 125.06; 129.75; 131.94; 150.61; 152.54; 169.80; 171.39; ESI^+-MS: m/z (abundance): 443.0590 (100%); 445.0573 (99.95%) [$M+CH_3CN+Na^+$]; 402.0319 (57.38%); 404.0296 (58.22%) [$M+Na^+$].

3.3.3. rac-ethyl 2-acetamido-3-(5-(4-chlorophenyl) furan-2-yl)propanoate (rac-3c). Yield 20%. ^{1}H-NMR: (300 MHz, $CDCl_3$): δ = 1.23 (3H, t, *J*=7.05Hz); 2.00 (3H, s); 3.23 (1H, dd, *J*=2.4Hz, *J*=4.8Hz); 3.24 (1H, dd, *J*=3Hz, *J*=4.8Hz) ; 4.18 (2H, q, *J*=7.1Hz); 4.82(1H,ddd, *J*=5.27Hz, *J*=5.53Hz, *J*=7.5Hz); 6.14 (1H,d, *J*=2.4Hz); 6.51 (1H,d, *J*=2.4Hz); 7.30 (2H,d, *J*=8.4Hz); 7.47 (2H,d, *J*=8.4Hz); 8.00 (1H,s); ^{13}C-NMR (75 MHz, $CDCl_3$): 14.27; 23.28; 30.89; 51.59; 61.93; 106.36; 110.35; 121.97; 124.78; 129.08; 132.96; 150.51; 152.54; 169.94; 171.39; ESI^+-MS: m/z (abundance): 358.0831 (100%); 360.0807 (34.95%) [$M+Na^+$]; 399.1097 (100%); 401.1077 (35.57%) [$M+CH_3CN+Na^+$].

3.3.4. rac-ethyl 2-acetamido-3-(5-(2-chlorophenyl) furan-2-yl)propanoate (rac-3d). Yield 79.96%. ^{1}H-NMR: (300 MHz, $CDCl_3$): δ = 1.24 (3H, t, *J*=6.15Hz); 2.02 (3H, s); 3.26 (1H,dd, *J*=2.4Hz, *J*=4.8Hz); 3.28(1H, dd, *J*=3Hz, *J*=4.8Hz); 4.00 (2H, q, *J*=6.2Hz); 4.18 (1H, ddd, *J*=5.27Hz, *J*=7.5Hz, *J*=5.53Hz); 5.29 (1H, d, *J*=3Hz); 6.20 (1H, d, *J*=3Hz); 7.17 (1H, d, *J*=7.8Hz); 7.29(2H, dd, *J*=7.8Hz, *J*=8.1Hz); 7.4(1H, d, *J*=8.1Hz); 8.09(1H, s); ^{13}C-NMR (75 MHz, $CDCl_3$): 14.27; 23.31; 30.84; 51.58; 61.97; 110.37; 111.83; 126.99; 127.71; 128.10; 129.19; 130.03; 130.88; 149.97; 150.31; 170.01; 171.38; ESI^+-MS: m/z (abundance): 358.0818 (100%); 360.0795 (32.5%) [$M+Na^+$].

4. Enzymatic analytical scale reactions

4.1. Enzymatic kinetic resolution of racemic 2-acetamido-3-(5-aryl-furan-2-yl)propanoic acids (rac-1a-d) by Acylase I mediated hydrolysis. *rac*-2-Acetamido-3-((5-aryl-furan-2-yl)propanoic acid (*rac*-**1a-d**) (0.5 mmol) was suspended in water (5mL). By adjusting the pH to 7.5- 8 with LiOH solution (1.25 M), the suspension merged into solution. Acylase I (2.5 units, 6 mg) and $CoCl_2 \times 6H_2O$ (2.5 mg, 0.02 mmol) were added and the reaction mixture was stirred at 37 °C, while by additions of LiOH solution (1.25 M), the pH of the solution was permanently kept between 7 and 8. After the completion of L-2-acetamido-3-arylfuryl-propanoic acid (**L-1a-d**) hydrolysis (approx. 24 h, checked by HPLC) the pH was adjusted to 1.5 with 5% HCl solution. The untransformed enantiopure D-2-acetamido-3-arylfuryl-propanoic acid (**D-1a-d**)

was filtered off and washed with ultrapure water (3×1 mL). The filtrate was heated with active charcoal (10 mg) to 50 °C for 1 min., cooled to room temperature, filtered, and the solvent was evaporated *in vacuo* to obtain the amino acid hydrochloride. The latest was dissolved in the minimal amount of water and the pH was adjusted to 6.5 to obtain **L-2a-d.**

4.2. Enzymatic kinetic resolution of racemic ethyl 2-acetamido-3-(5-aryl-furan-2-yl)propanoates (rac-3a-d) by baker's yeast esterase mediated hydrolysis. Baker's yeast (5g) was suspended in 50 ml water. After 1h, the *rac*-ethyl 2-acetamido-3-(5-phenyl-furan-2-yl)propanoates (*rac*-**3a-d**) (0.2 mmol) in 0.5 mL ethanol was added under stirring and left at room temperature for 48 h. The reaction mixture was centrifuged at 5000 rpm for 20 minutes. The supernatant was extracted with CH_2Cl_2 (3×30mL) and the organic layer was dried over Na_2SO_4, filtered and evaporated *in vacuo* affording the D-ethyl 2-acetamido-3-(5-phenyl-furan-2-yl)propanoates. The aqueous layer was concentrated in *vacuo*. The remained water trace from pure **L-1a-d** was eliminated in under high vacuum (freze drying).

4.3. Chemical hydrolysis of D-acetamido-3-(5-aryl-furan-2-yl)propanoic acids (D-1a-d) and ethyl-D-2-acetamido-3-(5-aryl-furan-2-yl)propa-noates (D-3a-d). D-2-acetamido-3-(5-aryl-furan-2-yl)propanoic acid **D-1a-d** (0.5 mmol) was suspended in half concentrated HCl (5 mL) and the mixture was refluxed for 4 h, cooled to room temperature, obtaining the product as a white precipitate, which was filtered, dried and finally washed with diethyl ether. The precipitate was resuspended in water, the pH was adjusted to 6.5, stirred for 30 min, filtered and dried at room temperature yielding the pure enantiomerically enriched **D-2a-d**.

The ethyl D-2-acetamido-3-(5-aryl-furan-2-yl)propanoates **D-3a-d** (1 mmol) was suspended into a vigorously stirred solution of sodium carbonate (0.053 g, 5 mmol) in water (8 mL) and the mixture was gently heated to reflux. After 2 h of heating, the solution was cooled to 5 °C and extracted with dichloromethane (3×10 mL). The aqueous layer was then acidified carefully with concentrated HCl solution. The deposited precipitate was filtered off and washed several times with cold water. The isolated D-2-acetamido-3-(5-aryl-furan-2-yl)propanoic acids **D-2a-d** were further hydrolyzed as described above.

ACKNOWLEDGMENTS

Laura Ancuța Pop wishes to thank for the financial support provided from programs co-financed by The SECTORAL OPERATIONAL PROGRAMME HUMAN RESOURCES DEVELOPMENT, Contract **POSDRU 6/1.5/S/3** – „Doctoral studies: through science towards society". Sincere thanks to Prof. Florin Dan Irimie and all the members of the Biochemistry and Biochemical Engineering Department of the Faculty of Chemistry and Chemical Engineering, Cluj Napoca, for all their help, support and guidance during this work.

REFERENCES

[1] (a) G. Beck, *Synlett,* **2002**, 837; (b) M. J O'Donnell, *Aldrichimca Acta,* **2001**, *34*, 3; (c) C. Cativiela, M.D. Dıaz-de-Villegas, *Tetrahedron: Asymmetry,* **2000,** *11*, 645; (d) C. Cativiela, M.D. Dıaz-de-Villegas, *Tetrahedron: Asymmetry,* **1998**, *9*, 3517; (e) S. Hannesian, G. McNughton-Smith, H.-G.Lombart, W.D. Lubell, *Tetrahedron,* **1997**, *53*, 12789; (f) F.J. Sardina, H. Rapoport, *Chemical Rev*iews, **1996**, *96*, 1825; (g) D. Seebach, A.R. Sting, M. Hoffmann, *Angewandte Chemie International Edition,* **1996**, *35*, 2708; (h) L. Hegedus, *Accounts of Chemical Res*earch, **1995**, *28,* 299; (i) R.O. Duthaler, *Tetrahedron,* **1994**, *50*, 1539; (j) Y. Ofune, *Accounts of Chemical Research,* **1992**, *25,* 360.

[2] (a) L. Wang, P.G. Schultz, *Chemical Communications*, **2002**, 1; (b) A.E. Pojitkov, E.N. Efremenko, S.D. Varfolomeev, *Journal of Molecular Catalysis B: Enzymatic,* **2000**, *10*, 47; (c) R.M. Liskamp, *Angewandte Chemie International Edition,* **1994**, *33*, 305; (d) J. Gante, *Angewandte Chemie International Edition,* **1994**, *33*, 1699; (e) A. Giannis, T. Kolter, *Angewandte Chemie International Edition*, **1993,** *32*, 1244.

[3] (a) R.M. Williams, "Synthesis of Optically Active α-Amino Acids", Pergamon Press, Oxford, **1989**; (b) T. Wirth, *Angewandte Chemie International Edition,* **1997**, *36,* 225; (c) J.A. Ma, *Angewandte Chemie International Edition,* **2003**, *42,* 4290.

[4] (a) A. Boto, R. Hernandez, A. Montoya, E. Suarez, *Tetrahedron Letters,* **2002**, *43*, 8269; (b) W. Wang, J. Wang, H. Li, *Tetrahedron Letters*, **2004**, *45*, 7243.

[5] (a) J. Altenbuchner, M. Siemann-Herzberg, C. Syldatk, *Current Opinion in Biotechnology*, **2001**, *12*, 559; (b) J.D. Stewart, *Currrent Opinion in Chemical Biology*, **2001**, *5*, 120; (c) P.P. Taylor, D.P. Pantaleone, R.F. Senkpeil, I.G. Fotheringham, *Trends in Biotechnology*, **1998**, *16*, 412; (d) A.S. Bommarius, M. Schwarm, K. Drauz, *Journal of Molecular Catalysis B: Enzymatic,* **1998**, *5*, 1; (e) C.H. Kao, H.H. Lo, S.K. Hsu, W.H. Hsu, *Journal of Biotechnology,* **2008**, *134*, 231; (f) S.K. Hsu, H.H. Lo, W.D. Lin, I.C. Chen, C.H. Kao, W.H. Hsu, *Process Biochemistry,* **2007**, *42*, 856.

[6] (a) W. Szymanski, B. Wu, B. Weiner, S. de Wildeman, B.L. Feringa, D.B. Janssen, *Journal of Organic Chemistry,* **2009**, *74*, 9152; (b) B. Wu, W. Szymanski, P. Wietzes, de S. Wildeman, G.J. Poelarends, B.L. Feringa, D.B. Janssen, *ChemBioChem,* **2009**, *10*, 338; (c) D. Krug, R. Muller, *ChemBioChem,* **2009**, *10*, 741; (d) B.M. Cox, J.B. Bilsborrow, K.B. Walker, *Journal of Organic Chemistry,* **2009**, *24*, 6953.

[7] (a) G.B. Dcunha, V. Satyanarayan, P. Madhusudanan Nair, *Enzyme and Microbial Technology,* **1994**, *16,* 318; (b) S. Takac, B. Akay, T.H. Ozdamar, *Enzyme and Microbial Technology,* **1995**, *17,* 445; (c) C. Paizs, A. Katona, J. Rétey, *Chemistry-A European Journal,* **2006**, *12*, 2739; (d) A. Gloge, J. Zon, A. Kovari, L. Poppe, J. Retey, *Chemistry- A European Journal,* **2000**, *6*, 3386; (e) C. Paizs, A. Katona, J. Rétey, *European Journal of Organic Chemistry,* **2006**, 1113; (f) A. Katona, M.I. Toşa, C. Paizs, J. Rétey, *Chemistry and Biodiversity* **2006**, *3*, 502; (g) C. Paizs, M.I. Toşa, L.C. Bencze J. Brem, F.D. Irimie, J. Rétey, *Heterocycles,* **2011**, *82*, 1217.

[8] (a) T. Li, A.B. Kootstra, I.G. Fotheringham, *Organic Process Research & Development,* **2002**, *6*, 533; (b) P.P. Taylor, D.P. Pantaleone, R.F. Senkpeil, I.G. Fotheringham, *Trends in Biotechnology,* **1998**, *16*, 412; (c) S.T. Chen, M.J. Tseng, T. Kao, B. Sookkheo, T. Surat, U.S. Patent, **2000**, 6.146.859; (d) H.H. Lo, S.K. Hsu, W.D. Lin, N.L. Chan, W.H. Hsu, *Biotechnology Progr*ess, **2005**, *21*, 411; (e) M. Senuma, K. Nakamichi, K. Nabe, S. Nishimoto, T. Tosa, *Applied Biochemistry and Biotechnology,* **1989**, *22*, 141; (f) B.K. Cho, J.H. Seo, T.W. Kang, B.G. Kim, *Biotechnology and Bioengineering,* **2003**, *83*, 226.

[9] (a) J. Brem, M.I. Tosa, C. Paizs, A. Munceanu, D. Matkovic-Calogovic, F.D. Irimie, *Tetrahedron: Asymmetry,* **2010**, *21*, 1993; (b) L.C. Bencze, C. Paizs, M.I. Tosa, M. Trif, F.D. Irimie, *Tetrahedron: Asymmetry,* **2010**, *21,* 1999; (c) M.I. Tosa, S. Pilbák, P. Moldovan, C. Paizs, G. Szatzker, G. Szakács, L. Novák, F.D. Irimie, L. Poppe, *Tetrahedron: Asymmetry,* **2008**, *19*, 1844; (d) C. Paizs, M.I. Toşa, V. Bódai, G. Szakács, I. Kmecz, B. Simándi, C. Majdik, L. Novák, F.D Irimie, L. Poppe, *Tetrahedron: Asymmetry,* **2003**, *14*, 1943.

[10] L.C. Bencze, C. Paizs, M.I. Toşa, F.D. Irimie, *Tetrahedron: Asymmetry,* **2011**, *22*, 675.

[11] (a) L.C. Bencze, C. Paizs, M.I. Tosa, E. Vass, F.D. Irimie, *Tetrahedron: Asymmetry,* **2010**, *21*, 443; (b) C. Paizs, P. Tähtinen, M.I. Toşa, C. Majdik, F.D. Irimie, L.T. Kanerva, *Tetrahedron,* **2004**, *60*, 10533; (c) C. Paizs, P. Tähtinen, K. Lundell, L. Poppe, F.D. Irimie, L.T. Kanerva, *Tetrahedron: Asymmetry,* **2003***, 14*, 1895; (d) C. Paizs, M.I. Toşa, C. Majdik, P. Tähtinen, F.D. Irimie, L.T. Kanerva, *Tetrahedron: Asymmetry,* **2003**, *14*, 619.

[12] (a) J. Brem, M.I. Tosa, C. Paizs, E.I. Vass, F.D. Irimie, *Tetrahedron: Asymmetry,* **2010**, *21*, 365; (b) J. Brem, C. Paizs, M.I. Tosa, E. Vass, F.D. Irimie, *Tetrahedron: Asymmetry*, **2009**, *20*, 489.

[13] H.K. Chenault, J. Dahmer, G. Whitesides, *Journal of the American Chemical Society*, **1989**, *111*, 6354.

[14] (a) A.S. Bommarius, K. Drauz, H. Klenk, C. Wandrey, *Annals of the New York Academy of Science,* **1992**, *672,* 126; (b) T. Sato, T. Tosa, *Bioprocess Technology,* **1993**, *16*, 3; (c) P.V. Podea, M.I. Toşa, C. Paizs, F.D. Irimie, *Tetrahedron: Asymmetry,* **2008,** *19*, 1959.

[15] (a) R. Csuk, B.I. Glanzer, *Chemical Rev*iews, **1991**, *91*, 49; (b) S. Servi, *Synthesis* **1990**, 1.

[16] (a) M.I. Toşa, P.V. Podea, C. Paizs, F.D. Irimie, *Tetrahedron: Asymmetry,* **2008**, *19*, 2068; (b) C. Paizs, M.I. Toşa, C. Majdik, P.V. Moldovan, L. Novák, P. Kolonits, A. Marcovici, F.D. Irimie, L. Poppe, *Tetrahedron: Asymmetry,* **2003**, *14*, 1491; (c) E. Busto, V. Gotor-Fernandez, V. Gotor, *Tetrahedron: Asymmetry,* **2006**, *17*, 1007.

[17] (a) M.I. Toşa, C. Paizs, C. Majdik, P. Moldovan, L. Novák, P. Kolonits, É. Szabó, L. Poppe, F.D. Irimie, *Journal of Molecular Catalysis B: Enzymatic,* **2002**, *17*, 241.

[18] (a) C. Paizs, M.I. Toşa, C. Majdik, V. Bodai, L. Novák, F.D. Irimie, L. Poppe, *Journal of the Chemical Sociaty, Perkin Transactions 1,* **2002**, *21,* 2000; (b) L.C. Bencze, C. Paizs, M.I. Toşa, F.D. Irimie, *Tetrahedron: Asymmetry,* **2010**, *21,* 356; (c) P.V. Podea, C. Paizs, M.I. Tosa, F.D. Irimie, *Tetrahedron: Asymmetry,* **2008**, *19*, 1959.

[19] M.I. Toşa, C. Paizs, C. Majdik, L. Novák, P. Kolonits, F. Irimie, L. Poppe, *Tetrahedron: Asymmetry,* **2002**, *13*, 211.
[20] (a) B.I. Glanzer, K. Faber, H. Griengl, *Tetrahedron Letters,* **1986**, *27*, 4293; (b) B.I. Glazer, K. Faber, H. Griengl, *Tetrahedron,* **1987**, *43*, 771.
[21] P.V. Podea, M.I. Toşa, C. Paizs, F.D.Irimie, *Tetrahedron: Asymmetry,* **2008**, *19*, 500.

STUDIA UBB CHEMIA, LVI, 2, 2011 (p. 167 - 178)

GRAPHITE ELECTRODE ELECTROACTIVATED BY POTENTIOSTATIC MULTI-SEQUENCE TECHNIQUES FOR HYDROGEN PEROXIDE ELECTROSYNTHESIS

CODRUȚA AURELIA VLAIC[a], SORIN-AUREL DORNEANU[a,*], PETRU ILEA[a]

ABSTRACT. Studies concerning the hydrogen peroxide electrosynthesis carried out by cyclic hydrodynamic voltammetry (CHV), revealed that graphite anodisation followed by a sequence of surface partial reduction has a positive effect upon the HPE efficiency. In order to improve the promising results obtained by CHV a set of original multi-sequences techniques for repetitive potentiostatic graphite electroactivation for HPE efficiency improvement was designed. The new electroactivation protocols were tested in hydrodynamic controlled conditions using a Pt-graphite wall-jet ring disk electrode. The potentiostatic measurements using different shapes of the applied signal allowed us to identify the possible processes involved in the electroactivation and production sequences. Experimental optimisation of the original potentiostatic electroactivation technique of the graphite cathode was carried out leading to a decrease of the electrical energy consumption.

Keywords: *hydrogen peroxide electrosynthesis, graphite electroactivation, wall-jet ring disk electrode, multi-sequence technique*

INTRODUCTION

The use of hydrogen peroxide, a “green” reagent, is continuously increasing in many technological processes (bleaching, wastewater treatment etc.) [1]. The exceptional ability of this compound to reduce or eliminate pollution makes it safe for the environment because it is transformed into noncontaminant products such as water and oxygen [2].

Hydrogen peroxide electrosynthesis (HPE) by partial reduction of oxygen (PRO) has received much attention over recent decades [3 – 6]. HPE allows to electrogenerate on site this valuable chemical using only water, atmospheric oxygen and electricity.

[a] *”Babes-Bolyai” University, Faculty of Chemistry and Chemical Engineering, 11 Arany Janos Street, RO-400028 Cluj-Napoca, Romania*

[*] *corresponding author: e-mail: dorneanu@chem.ubbcluj.ro*

Modified and unmodified carbonaceous materials are widely used for HPE, a special attention being paid to graphite [7 - 11] due to increased HPE efficiency on this material. The reactivity of carbon electrodes is essentially influenced by the material microstructure, the cleanliness of the electrode surface as well as by the type and the number of the functional groups existing on the electrode surface. All these parameters depend considerably on the type of the used carbon material and the applied pretreatments. The presence of native functional groups such as carboxyl, phenolic hydroxyl, quinine-type carbonyl on the carbon surface explains the special ability of carbon materials to reduce oxygen to hydrogen peroxide since they are involved in the reduction mechanism [12]. A major drawback for HPE on carbon electrodes is the slow kinetics of the reaction. An increased number of functional groups or active centres can be related to an enhancement of the electrocatalytic effect for these electrode materials.

Consequently, different pretreatment procedures, including electrochemical ones, were investigated and numerous studies attempted to establish the effect of carbon electrodes pretreatment upon oxygen reduction reaction [12-16]. The electrochemical pretreatments involve the application of relatively large negative or positive potentials to the working electrode. The amplitude and duration of the applied potentials varied largely, many researchers recommending the use of potential cycling or alternating current wave forms [12, 17-21]. These studies generally concluded that the performance of carbon electrodes can be improved by electrochemical pretreatment which introduces new functional groups on the electrode surface or modifies the nature of the native active centres [12], increasing the number of the oxygen functional groups [17] especially of quinoid type functional groups [15, 19].

Unfortunately, the simple oxidized carbon electrodes catalyze the total oxygen reduction or the subsequent reduction of hydrogen peroxide, affecting the HPE process efficiency [15]. To overcome these impediments, in the present paper, we describe a set of original multi-sequences techniques used for graphite electroactivation with the aim of enhancing the HPE efficiency.

RESULTS AND DISCUSSION

1. Preliminary studies by cyclic hydrodynamic voltammetry

Paliteiro et al. [15] point out that after anodisation the graphite electrodes become more active for the complete reduction of oxygen, without an increase in HPE efficiency. Contrarily to this observation, during our preliminary studies [16] concerning the graphite electroactivation by cyclic hydrodynamic voltammetry (CHV) on ring-disk electrode, we noticed an interesting phenomenon: when the graphite electrode was polarised to relatively large negative potential

values after a preliminary oxidation at positive potential values, an enhancement in the current detected on the ring electrode (I_r) could be registered. An example, including 4 successive voltammograms (without polishing the electrode surface between measurements) and also I_r (that indicates the H_2O_2 electrosynthetized on the disk), is presented in Figure 1.

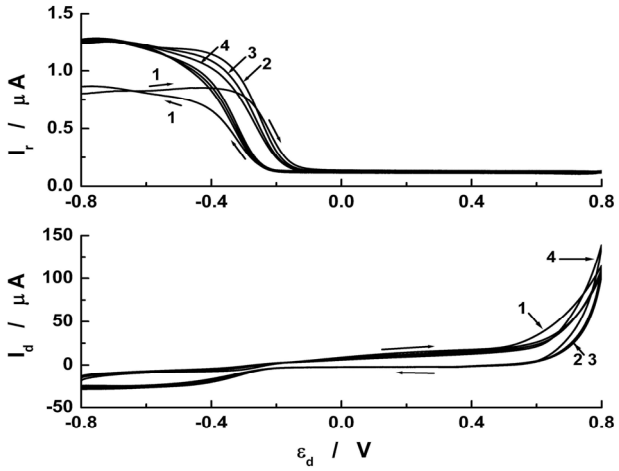

Figure 1. The correlation between the disk applied potential (ε_d) and the currents recorded by CHV on disk (I_d) and ring (I_r) for 4 consecutives cycles between -0.8 V and +0.8 V. The numbers on the figures represent the cycle number. Experimental conditions: v = 10 mV/s; volumetric flow rate (V_f = 1.42 mL/min

As one can see, at disk potentials higher than +0.6 V, the corresponding recorded current on the disk electrode (I_d) greatly increased due to the oxygen evolution and the intense oxidation of the graphite surface. For the cathodic scans, I_r clearly increases after the first cycle (corresponding to a fresh, unmodified graphite surface). In spite of HEP enhancement, this kind of electroactivation implied high energy consumption because of the large currents involved. This enhancement in HPE could be explained by the fact that during the oxidation new active centres are generated on the graphite surface. Unfortunately, these freshly generated active centres are not able to catalyse HPE because, more probably, they are in an oxidised form. Contrarily, after a short time polarisation of the oxidised electrode at more negative potential values (near the value corresponding to the total oxygen reduction), we observed that H_2O_2 production increased. We supposed that the process taking place at these negative potentials (that we called partial reduction) transforms the newly generated oxidised active centres in partially reduced ones, more suitable for the HPE process.

In order to better understand the previous described behaviour and to improve the electrocatalytic properties of graphite for HPE, we carried out similar tests concerning the graphite electroactivation using CHV between several values of oxidation (+0.5, +0.8, +1.1 and +1.35 V) and partial reduction (-0.4, -0.8 and -1.1 V) potentials. Based strictly on comparative observations of I_r and I_d values, we conclude that the best results concerning the HPE efficiency increase were obtained when the graphite electrode was subjected to oxidation potential values between +0.5 V and +0.8 V and the partial reduction that followed the anodisation took place at -0.8 V. Another important finding was that the partial reduction potential value has a great importance and this sequence represents a key factor for the HPE efficiency increase. Accordingly, enhancements of HPE process could not be observed when the partial reduction potential was considerably different from -0.8 V. We explain this phenomenon by the fact that, at more positive values, the applied potentials were not negative enough for a proper electroreduction of the active centres. Contrarily, the active centres generated during anodisation were totally reduced or destroyed at potential values more negative than -0.8 V. Even though this manner of graphite electroactivation shows a promising HPE enhancement effect, unfortunately, it is time consuming and, consequently, inefficient for larger scale applications. Another approach using an original multi-step technique is further described.

2. Potentiostatic electroactivation using rectangular multi-step signal

The new proposed multi-impulse potentiostatic technique consists in a rapid switch between the potential values corresponding to the graphite electroactivation and HPE. Concretely, a programmed rectangular multi-step signal (RMSS), consisting of three specific potential values, was applied on the disk electrode. These values correspond to three processes: anodisation (1), partial reduction (2) and actual HPE (3), also named production sequence (PS). The anodisation sequence (AS) and the partial reduction sequence (PRS) were provided for the graphite electroactivation while the third one was used to evaluate the effect of this electroactivation on the HPE process efficiency.

During the AS a positive potential was applied to the disk electrode for a short time period with the purpose to generate active centres on the graphite surface in their oxidized form. To partially reduce the newly generated active centres, a negative potential value was applied during the PRS, for a similar period. Finally, a less negative potential value was applied in the PS for a longer period of time and the HPE efficiency was evaluated based on I_r evolution. The partially reduced active centres presented a poor stability and for this reason I_r decreased over a rather short period of time (≈ 10 seconds). Taking this into account we considered that the electroactivation process needs to be periodically repeated, including all the potential sequences

described above. We performed this type of experiments and as an example, in Figure 2 we present the results obtained using a RMSS for five consecutive cycles, at three different oxidation potential values.

Comparing the presented I_r values with those obtained in a steady-state potentiostatic HPE experiment (I_r around 1.1 μA), it can be noticed a great increase of H_2O_2 production immediately after each electroactivation phase. Unfortunately, the recorded I_d values attain very high values during the AS and PRS. As a consequence, even if the HPE is enhanced in the PS, this increase becomes insignificant because of the huge energy consumption during the electroactivation sequences.

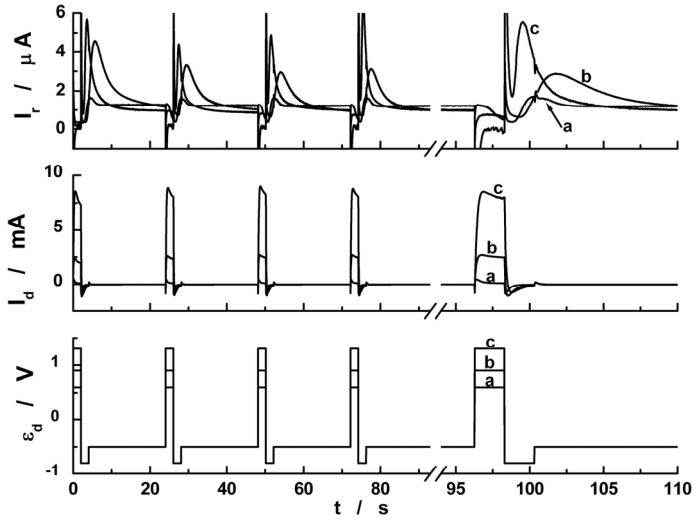

Figure 2. The influence of the disk applied potential (ε_d) on the currents recorded on disk (I_d) and ring (I_r) for different values of the oxidation potential: a) +0.6 V; b) +0.9 V; c) +1.3 V. Experimental conditions: volumetric flow rate (V_f) = 1.42 mL/min.; $t_{AS} = t_{PRS}$ = 2 s; t_{PS} = 20 s; ε_{PRS} = -0.8 V; ε_{PS} = -0.5 V

In the attempt to enhance the HEP process and to reduce the energy consumption, we perform several measurements using the RMSS in different experimental conditions: potentials ranged between +0.5 and +2.0 V for anodisation, -0.4 and -1.0 V for partial reduction and -0.6 and -0.1 V for peroxide PS and steps duration from 0.5 to 10 s for activation and from 20 to 200 s for PS.

Unfortunately, the very high currents recorded during the activation steps allowed us to make only relative comparisons between the effects of the different sets of experimental conditions, without a real possibility to

evaluate the current efficiency (CE) or the specific energy consumption (SEC). Consequently, we appreciate that the best results were obtained for potentials of +1.1 V for anodisation, -0.8 V for partial reduction and -0.5 V for the PS, respectively. Concerning the steps duration, the best results were achieved at 2 s for AS and PRS and at 20 s for the PS.

The measurements based on the RMSS also confirmed that the PRS is essential in the graphite electroactivation process because the enhancement of HPE efficiency was not observed when this step was skipped. Based on previous observed phenomena, in Table 1 we summarize the possible processes which we consider that can explain the large currents recorded on the disk in the electroactivation steps and also, the HEP improvement.

Table 1. Possible processes involved in the sequences of graphite electroactivation and peroxide production and their effect on HEP efficiency

Sequence	Processes	Eq.	PEUH[a]
AS	graphite → C_{ox}* + n[b] e^-	(1)	+
	4 HO^- → O_2 + 2 H_2O + 4 e^-	(2)	+
	$C_{DL, PS}$ → $C_{DL, AS}$ + n e^-	(3)	-
	C_{red}* → C_{ox}* + n e^-	(4)	-
	HO_2^- + HO^- → O_2 + H_2O + 2 e^-	(5)	-
PRS	C_{ox}* + n e^- → C_{red}*	(6)	+
	$C_{DL, AS}$ + n e^- → $C_{DL, PRS}$	(7)	-
	C_{red}* + n e^- → graphite	(8)	-
	O_2 + 2 H_2O + 4 e^- → 4 HO^-	(9)	-
	HO_2^- + H_2O + 2 e^- → 3 HO^-	(10)	-
	H_2O + 2 e^-→ H_2 + 2 HO^-	(11)	-
PS	O_2 + H_2O + 2 e^- → HO_2^- + HO^-	(12)	+
	C_{red}* + O_2 + H_2O → HO_2^- + HO^- + C_{ox}*	(13)	+
	$C_{DL, PRS}$ → $C_{DL, PS}$ + n e^-	(14)	-

[a] The process effect upon HPE efficiency: (+) positive; (-) negative
[b] n represents an indefinite number of electrons

First of all, due to the rectangular shape of the polarisation signal, the extremely large values of I_d at the beginning of each step can be attributed to the charging and discharging processes of the electrical double layer for each sequence: anodisation ($C_{DL, AS}$) partial reduction ($C_{DL, PRS)}$ and production ($C_{DL, PS}$), symbolised by the equations 3, 7 and 14.

A great amount from the recorded current during AS can be associated with the graphite anodisation, requesting important amount of energy to generate the active centres in their oxidized form (**C_{ox}***), this being an important and mandatory process for the graphite electroactivation (Eq. 1) and favourable

to our goal. Moreover, at higher positive potential values, the oxygen evolution reaction (Eq. 2) had a significant contribution to the large current observed. This process can increase the oxygen availability near and on the graphite surface, counterbalancing the low oxygen solubility in electrolyte and inducing a positive effect upon HPE. In parallel to the favourable processes, during the AS, the partially reduced active centres ($\mathbf{C_{red}^*}$) could be oxidized (Eq. 4), loosing their electrocatalytic ability and also increasing the current consumption. Finally, the oxidation of generated hydrogen peroxide (Eq. 5) decreased HPE efficiency.

During PRS, we consider that the most favourable process for HPE enhancement consists in the partial reduction (Eq. 6) of the active centres generated upon anodisation ($\mathbf{C_{ox}^*}$), these partially reduced active centres being able to catalyse the H_2O_2 synthesis (Eq.12). The side processes that took place during PRS were: the total reduction of the partially reduced active centres (Eq. 8), the total reduction of oxygen (Eq. 9), the subsequent oxidation of generated hydrogen peroxide (Eq. 10) and hydrogen evolution at excessive negative potential values (Eq. 11).

In the PS, carried out at less negative potentials than during PRS, the most important processes are the HPE (Eq. 12) and the peroxide synthesis (Eq. 13) catalysed by the partially reduced active centres generated is the previous sequences (AS and PRS), both processes having a positive effect upon HPE improvement. The latter process, described in Eq. 13, seems to be a pure chemical one, fact proved by several experiments carried out at disk potential around -0.25 V, when we record a significant I_r even if I_d is almost zero. Both processes described in Eq. 12 and 13 use the initial dissolved oxygen as well as the supplementary O_2 generated during AS (Eq. 2), the last one inducing a significant increase in peroxide production.

Based on the above described experimental results and processes from Table 1, we conclude that, comparing to the unmodified carbonaceous materials, the electroactivated graphite using RMSS is more efficient for HPE. Moreover, the described *in-situ* electroactivation technique can be conducted continuously, without periodical external electrode treatment such as mechanical, thermal or chemical modification, reducing the maintenance time and the required costs. Unfortunately, the great amount of electric energy employed in the electroactivation sequences cause a modest improvement of HPE. As a consequence, we decided to modify the shape of the disk applied signal in order to reduce the global energy consumption.

3. Potentiostatic electroactivation using multi-sequence signal of sweeps and plateaus

As resulting from the previous results, the extremely large values for I_d recorded when a cyclic RMSS was used have two main reasons: (i) the charging and discharging of the double layer and (ii) the undesired redox

processes of some active centres and the products obtained in the previous sequence. It is worth to mention that these products (like H_2O_2 and O_2) can be adsorbed on the electrode surface and remain in the proximity of the electrode, further decreasing HPE efficiency. In order to reduce the mentioned disadvantages, we decided to change the shape of the applied signal, replacing the step potential changes between the desired potential values with linear sweeps, obtaining a new multi-sequence signal of sweeps and plateaus (MSSSP). It consists in a PS carried out at a constant potential value, followed by three sweeps used to reach the extreme potential values for anodisation, partial reduction and, finally, to return to the PS specific value. We replaced the RMSS with MSSSP considering that the current due to the charging and discharging of the double layer capacitance will be significantly decreased and the interest products could be transported further from the interface, diminishing their undesirable transformation. Moreover, this shape of the applied signal can better exploit the C_{red}*, diminishing their oxidation current during the AS.

A first set of measurements using MSSSP was carried out using ramps with low scan rates (10 mV/s) and, comparing to the experiments based on RMSS, the newly obtained results revealed a small decrease of the I_d during the electroactivation sequences and, also, an increase of HPE efficiency. Based on these promising results, we started a first optimisation study concerning the potential values for AS and PRS. In order to validate the results obtained by CHV, a PS of 20 s was added before each AS, at the potential value equal to the extreme potential value for PRS. The optimisation criterion was represented by the amount of electrogenerated peroxide during the 4th PRS normalised in respect to the value calculated for the first PRS, corresponding to the unmodified graphite. The relative amounts of H_2O_2 were calculated for several sets of extreme potential values for oxidation and partial reduction, all being presented in Table 2.

Table 2. The relative amount of electrogenerated peroxide during the 4th PRS for different values of extreme potentials for anodisation and partial reduction

Partial reduction minimum potential (V)	Anodisation maximum potential (V)			
	+0.5	+0.8	+1.1	+1.35
-0.4	0.59	0.66	1.19	0.92
-0.5	0.74	0.89	1.32	1.20
-0.6	0.85	0.88	1.31	1.12

As one can see, the optimal extreme values found were +1.1 V for the anodic process and -0.8 V for the partial reduction of the active centres. At low scan rates, the electroactivation process takes a relatively long time that causes very large electric energy consumption and for this reason we started a new set of optimisation experiments concerning the scan rates, values of 50, 100 and 200 mV/s were investigated. In order to increase the

relevance of the findings, the duration of the experiments was extended up to 30 cycles/experiment, being comparable to long industrial approach. As an example, Figure 3 presents the results of the experiment where the best enhanced of HPE efficiency was observed when a scan rate of 100 mV/s was used for reaching the electroactivation potential values.

The experiments carried out at high scan rate revealed that the I_d values diminished, but remained still too large for an efficient and economical HPE process. As an example, from the data presented in Fig. 3, the amount of electrical charge used for electroactivation was around 100 times larger than that employed for HPE.

All the experiments described above allowed us to conclude that the new potentiostatic technique for graphite electroactivation, implying anodisation followed by partial reduction, has a positive effect for HPE, increasing the amount of H_2O_2 obtained during the production sequences. This electrical energy consumption was maximal for the RMSS experiments. In the case of MSSSP the energy consumption decreased when low scan rates were used, but the minimal value was obtained during the measurements using MSSSP with high scan rates.

Several other optimisation studies were carried out concerning the PS potential and duration and also the combination of different scan rates for the electroactivation sequences, all of them confirming the optimal values of -0.5 V for the PS potential and of 100 mV/s for the scan rate.

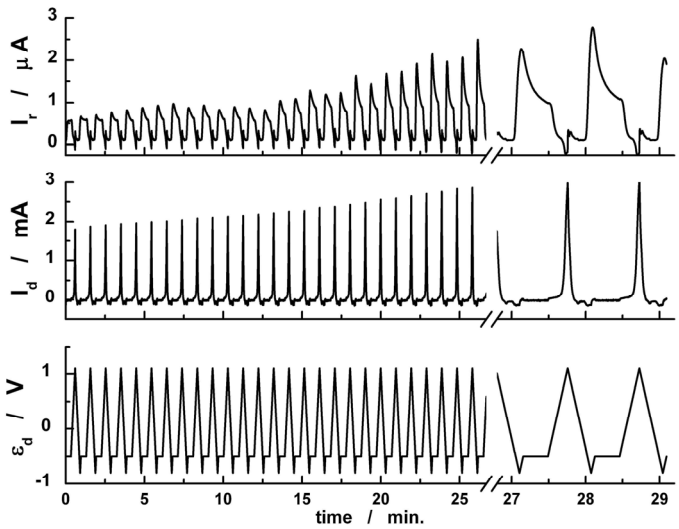

Figure 3. The correlation between the disk applied potential (ε_d) and the currents recorded on disk (I_d) and ring (I_r) for 30 cycles at high scan rate (100 mV/s) between the electro-activation and production sequences. Experimental conditions: volumetric flow rate (V_f) = 1.42 mL/min.; t_{PS} = 20 s; $\varepsilon_{AS, MAX}$ = +1.1 V;$\varepsilon_{PRS, MIN}$ = -0.8 V; ε_{PS} = -0.5 V

CONCLUSIONS

In order to increase the HPE efficiency on a graphite electrode, we developed a new electroactivation protocol consisting in the initial surface oxidation followed by a partial reduction. In this way, new active centres are generated on the graphite surface, but their stability is limited, requiring repeated electroactivation.

Consequently, a multi-sequence technique was proposed and tested in potentiostatic conditions. Based on the potentiostatic experiments, we conclude that, using this manner of graphite pretreatment, an enhancement in peroxide production could be obtained, the partial reduction of the newly generated active centres playing a key role in the process. The potentiostatic measurements allowed us to identify the possible processes involved in the electroactivation and production sequences. Because high current values were recorded on the disk electrode during electroactivation the multi-sequence electroactivation technique was applied using different signal shapes.

The energy consumption decreased for MSSSP signal carried out at low scan rates and the minimal value was obtained for the measurements using MSSSP with high scan rates.

EXPERIMENTAL SECTION

$K_4[Fe(CN)_6]$ and NaOH (purchased from Merck) were of analytical grade and were used as received. 1 M NaOH aqueous solution was used as supporting electrolyte for establishing the hydrodynamic condition and HPE investigation, respectively. All solutions were prepared with double distilled water (Double D Still, JENCONS, England).

The electrochemical measurements performed at room temperature (25 ± 1 ^{o}C) were carried out in controlled hydrodynamic conditions, using a wall-jet ring-disk electrode (WJRDE). The working electrode was a disk (∅= 2.5 mm) of spectral graphite (Ringsdorff-Werke GmbH, Germany) and the ring electrode (I.D. = 3 mm, O.D. = 3.4 mm) was made of Pt. The counter electrode was a Pt wire. An Ag/AgCl/1 M KCl system was used as reference electrode (RE) and *all potential values presented are referred to this electrode*. A peristaltic pump (Reglo Analog, Ismatec, Switzerland), a wall-jet type cell (WJC) [22] and a fully computer controlled home-made bipotentiostat were also used. Applications elaborated using Labview software were exploited to control the experimental parameters and for data acquisition and treatment. Before each set of experiments, the WJRDE surface was polished on waterproof emery paper of 800 and 1200 grit (Struers, Denmark) and, subsequently, it was intensively washed with double distilled water.

Within measurements of hydrodynamic voltammetry with linear scan of the flow rate [23], the distance between the injector and disk electrode was fixed at 1 mm in order to achieve a planar parallel flow hydrodynamic

regime in the WJC. The collecting efficiency (N) was evaluated using a 10 mM $K_4[Fe(CN)_6]$ solution in 1 M NaOH as supporting electrolyte and a value of 0.11 was obtained. N represents the ratio between the absolute values of the currents recorded on the ring and on the disk electrode. The current recorded on the disk electrode is due to $K_4[Fe(CN)_6]$ oxidation process, while the current on the ring is recorded when a fraction of $K_3[Fe(CN)_6]$ generated during the oxidation process on the disk is reduced to $K_4[Fe(CN)_6]$. For HPE experiments, an air saturated ($[O_2]$ ~ 8 ppm) aqueous solution of the supporting electrolyte, was pumped in the WJC at a volume flow rate of 1.42 mL/min. To evaluate the amount of hydrogen peroxide generated on the disk, the ring electrode was polarised at a constant potential value of +0.5 V, corresponding to the mass transport controlled domain for the H_2O_2 oxidation and an optimal signal to background ratio. Significant oxidation currents are usually recorded in strong alkaline media for Pt electrodes even at relatively low positive potential values (> +0.5 V) [24]. For this reason, we applied an oxidative pretreatment on the ring electrode in order to minimize the background recorded currents. This pretreatment consisted in oxidizing the ring at +0.8 V for 10 seconds and, afterwards, the applied potential was maintained at +0.5 V until a stable current value of +0.4 μA was recorded. Consequently, this background value was subtracted from all recorded ring currents.

ACKNOWLEDGMENTS

The authors wish to thank for the financial support provided from programs co-financed by The SECTORAL OPERATIONAL PROGRAMME HUMAN RESOURCES DEVELOPMENT, Contract POSDRU 6/1.5/S/3 – „Doctoral studies: through science towards society".

REFERENCES

1. E. Lobyntseva, T. Kallio, N. Alexeyeva, K. Tammeveski, K. Kontturi, *Electrochim Acta,* **2007***, 52*, 7262.
2. E. Brillas, F. Alcaide, P.L. Cabot, *Electrochim Acta,* **2002**, *48*, 331.
3. J.M. Campos-Martin, G. Blanco-Brieva, J.L.G. Fierro, *Angew Chem Int Edit,* **2006**, *45*, 6962.
4. K. Tammeveski, K. Kontturi, R.J. Nichols, R.J. Potter, D.J. Schiffrin, *J Electroanal Chem,* **2001**, *515*, 101.
5. G. Zhang, F. Yang, *Electrochim Acta*, **2007**, *52*, 6595.
6. T. Wilson, J. Zhang, C.C. Oloman, D.D.M. Wayner, *Int J Electrochem Sc,* **2006**, *1*, 99.
7. K. Kinoshita, "Electrochemical Oxygen Technology", *Willey J. Sons*, NY, **1992**, 19–66.
8. Xu W., Zhou X., Liu C., W. Xing, Lu T., *Electrochem Commun,* **2007**, *9*, 1002.

9. M.H.M.T. Assumpção, R.F.B. De Souza, D.C. Rascio, J.C.M. Silva, M.L. Calegaro, I. Gaubeur, T.R.L.C. Paixão, P. Hammer, M.R.V. Lanza, M.C. Santos, *Carbon,* **2011**, *49*, 2842.
10. R. Berenguer, J.P. Marco-Lozar, C. Quijada, D. Cazorla-Amorós, E. Morallón, *Carbon,* **2009**, *47*, 1018.
11. P. Ilea, S. Dorneanu, I.C. Popescu, *J Appl Electrochem,* **2000**, *30*, 187.
12. R.C. Engstrom, V.A. Strasser, *Anal Chem,* **1984**, *56*, 136.
13. A.L. Beilby, T.A. Sasaki, H.M. Stern, *Anal Chem,* **1995**, *67*, 976.
14. R.C. Engstrom, *Anal Chem*, **1982**, *54*, 2310.
15. C. Paliteiro, A. Hamnet, J.B. Goodenough, *J Electroanal Chem,* **1987**, *233*, 147.
16. C. Vlaic, S.A. Dorneanu, P. Ilea, *Studia UBB Chemia,* **2009***, LIV*, 135.
17. T. Nagaoka, T. Yoshino, *Anal Chem,* **1986**, *58*, 1037.
18. T. Nagaoka, T. Sakai, K. Ogura, T. Yoshino, *Anal Chem*, **1986**, *58*, 1953.
19. M.S. Hossain, D. Tryk, E. Yeager, *Electrochim Acta,* **1989,** *34*, 1733.
20. M.L. Bowers, *Anal Chim Acta,* **1991**, *243*, 43.
21. H.P. Dai, K.K. Shiu, *J Electroanal Chem,* **1996**, *419*, 7.
22. R. Appelqvist, G. Marko-Varga, L. Gorton, A. Torstensson, G. Johansson, *Anal Chim Acta,* **1985**, *169*, 237.
23. S.A. Dorneanu, V. Coman, I.C. Popescu, P. Fabry, *Sensor Actuat B-Chem,* **2005**, *105*, 521.
24. A.J. Bard, M. Stratman, "Encyclopedia of Electrochemistry", *Wiley-VCH*, **2007**, *5*, 39-43.

STUDIA UBB CHEMIA, LVI, 2, 2011 (p. 179 - 188)

PRECUSOR CHEMISTRY FOR THE ACETYLACETONATE-BASED CHEMICAL SOLUTION DEPOSITION OF EPITAXIAL CERIA THIN FILMS

TANIA RISTOIU[a], LELIA CIONTEA[a], TRAIAN PETRISOR JR.[a], MIHAI GABOR[a], TRAIAN PETRISOR[a]

ABSTRACT. Cerium acetylacetonate (beta-diketonate) $Ce(C_5H_7O_2)_3xH_2O$ has been used in the preparation of the precursor solution for the deposition of epitaxial ceria thin films. Propionic acid easily dissolves the cerium acetylacetonate resulting in a stable coating solution. The precursor chemistry of the as-prepared coating solution, resulted powder and thin films has been investigated by infrared spectroscopy, mass spectrometry coupled with thermal analysis and X-ray diffraction. The analysis suggests the complex nature of the coating solution due to the formation of a cerium acetylacetonate-propionate mixed ligand complex. The CeO_2 thin films deposited by spin coating on single crystalline (100)MgO substrates starting from this solution exhibit a high degree of epitaxy with a [h00]‖[h00] epitaxial relationship between the substrate and the film.

Keywords: *cerium acetylacetonate, chemical solution deposition (CSD), ceria epitaxial thin films, DTA-TG-MS*

INTRODUCTION

Cerium oxide thin films have a large range of applications in electronics, optics, catalysis, wear resistance, corrosion protection and superconductivity [1]. Pure and doped cerium oxide thin films have been widely investigated as buffer layer for $YBa_2Cu_3O_{7-x}$ (YBCO) superconducting coated conductors manufacturing. This interest is explained by the smaller lattice mismatch and the similar thermal expansion coefficient of CeO_2 both with YBCO and the Ni based flexible metallic substrate [2]. Lately, doped ceria is being extensively studied as a potential solid electrolyte for fuel cells [3]. Many deposition techniques have been used for the preparation of CeO_2 thin films, including both physical [4] and chemical methods [5]. Among the latter, the sol-gel

[a] *Technical University of Cluj–Napoca, 28, Memorandumului Str., RO-400114, Cluj-Napoca, Romania, tristoiu@phys.utcluj.ro*

processing route is particularly attractive for the scaling-up of oxide thin films fabrication, since the liquid precursor can easily be applied on a substrate by dipping, spinning or spraying [6,7] and heat treated at lower temperatures.

Metal β-diketonates have become adequate precursors for metal oxides thin films, due to their high volatility, low decomposition temperature, ease of use, commercial availability and relatively low cost. The metal acetylacetonates show a very low solubility in simple alcohols (methanol, ethanol, propanol, butanol) and other organic solvents like toluene, hexane, acetylacetone, but dissolve in propionic acid up to high concentrations. Several attempts have been made to bring into solution the metal acetylacetonates by using carboxylic acids (eg. acetic acid, propionic acid), resulting in a stable coating solution for the deposition of thin films [6].

In this work we report on the fabrication and characterization of cerium oxide thin films on single crystalline (100) MgO substrates starting only from cerium acetylacetonate (2,4-pentadionate) and propionic acid, hereafter denoted in the text by $Ce(acac)_3$ and HPr, respectively. Due to the fact that the quality of the thin films strongly depends on the chemistry of the precursor solution, on the thermal treatment, the reactions that take place during the decomposition of the precursor, a special attention has been given to the precursor chemistry.

RESULTS AND DISCUSSION

a. Precursor chemistry

FTIR studies

The FTIR spectra of the precursor solution and the precursor film are given in Figure 1.

From these spectra, information regarding the vibrational modes of the different functional groups present in the precursor have been extracted and compared with the spectra corresponding to pure $Ce(acac)_3$ and HPr, as presented in Table 1. The assignment of the most relevant bands is in good agreement with literature data [8-10].

The vibrational modes corresponding to HPr have been identified in the precursor solution, the most significant being located at 1711, 1466, 1236 cm^{-1} and attributed to C=O stretching, CH_3 asymmetric bending and C-O stretching, respectively. This is in good agreement with the presence of the HPr excess. It is to be noticed the absence of the vibrational modes corresponding to free propionic acid in the precursor film, as a result of the evaporation of the HPr excess.

New vibrational modes at 1540 (solution) and 1538 (film) cm^{-1} are assigned to the ν_{as}(COO) mode in the deprotonated and coordinated propionate ligand. Concomitantly, the ν(C=O) mode of acetylacetonate ligand

found in $Ce(acac)_3$ at 1600 cm^{-1} it is shifted to the above values probably due to a modification of the coordination behaviour.

The coordination of propionate ligand to cerium is also supported by the positiv shift of the ν(C-O) mode of HPr (1240-1236 cm^{-1}) to 1417 cm^{-1} in the precursor film. According to K. Nakamoto [10], the difference between the two COO frequencies $\Delta\nu = \nu_a - \nu_s$ is indicative for the coordination of the carboxylate ligand to the metal ion. In our case, $\Delta\nu$ = 125 cm^{-1} (precursor solution) and $\Delta\nu$ = 128 cm^{-1} (precursor film) lay close to the corresponding value of $\Delta\nu$ = 145 cm^{-1} calculated for the sodium propionate. These data suggest a bridging coordination of propionate ligand to the cerium ion.

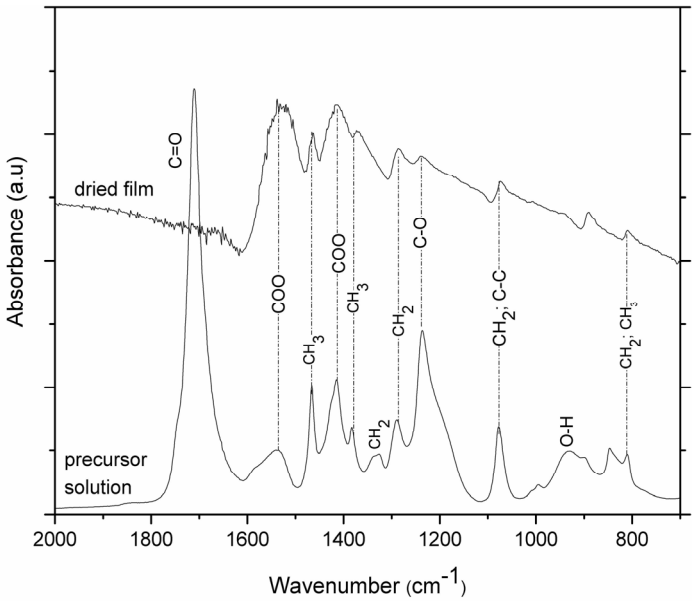

Figure 1. FTIR spectra of the precursor solution and dried film.

Table 1. Spectral assignment of the main IR peaks

HPr	$Ce(acac)_3$	Precursor solution	Precursor film	Assignment
1716		1711		ν(C=O)
	1600			ν(C⋯O)
		1540	1538	ν_{as}(COO)+ ν(C⋯O)
	1530			ν_{as}(C=C)
1467		1466	1464	$\delta_{as}(CH_3)$
1416		1415	1417	δ(C-O-H)+ ν_s(COO)
1384	1395	1383		$\delta_s(CH_3)$
1325		1326		$\nu_s(CH_2)$

HPr	$Ce(acac)_3$	Precursor solution	Precursor film	Assignment
1291		1289	1286	δ_s (CH_2)
	1260			v_s C=C
1240		1236		v C-O
1080	1020	1078	1074	ρ CH_3 v C-C
933		930		π O-H
	920			v C-CH_3
848		847		v C-C
811		810	810	γ CH_2

TG-DTA studies

The TG-DTA studies have been performed in dynamic argon atmosphere which actually is poor in oxygen, but not inert, so that the oxidative processes are not completely hindered and the evolved gases can be identified more easily.

Figure 2 comparatively presents the TG-DTA curves both for cerium acetylacetonate and the precursor powder. The difference between the two curves is clearly seen, suggesting the formation of a new precursor compound. The total weight loss has the value 56.3% for the precursor powder attained around 700°C and sticks to the same value up to 800°C.

The X-ray diffraction pattern of the resulted powder, Figure 3, evidences the presence of CeO_2 only. This enables the calculation of the molecular weight of the estimated precursor of 394 a.m.u., which, in a simplified way, might be attributed to a complex, where two of the acetylacetonate ligands have been replaced by two propionates ligands, $Ce(acac)(Pr)_2x0.5\ H_2O$, in agreement with the IR spectra.

From Figure 2 it is observed that all the transformations are associated with a mass loss. This suggests that there is no structural change independent of mass change in the precursor. All the DTA peaks give additional support to the TG results. The precursor is stable up to 80°C. The thermal decomposition of the precursor takes place in three steps:

I. 80 - 275°C, in which the weight loss $\Delta m = 6.5\%$ is accompanied by an endothermal peak at 232°C.

II. 275 - 500°C, in which the main weight loss takes place, $\Delta m = 48.9\%$ and, simultaneously, two endothermal peaks at 306°C and 372°C, and one exothermal peak at 430°C. The prominent large exothermal peak is also associated with complex competitional oxidation processes, due both to the burning of the organic moieties and to the oxidation of Ce^{3+} to Ce^{4+}, in agreement with the overall reaction:

$$Ce(C_5H_7O_2)(C_3H_5O_2)_2\,x0.5H_2O + 26.5[O] \rightarrow CeO_2 + 11CO_2 + 9H_2O$$

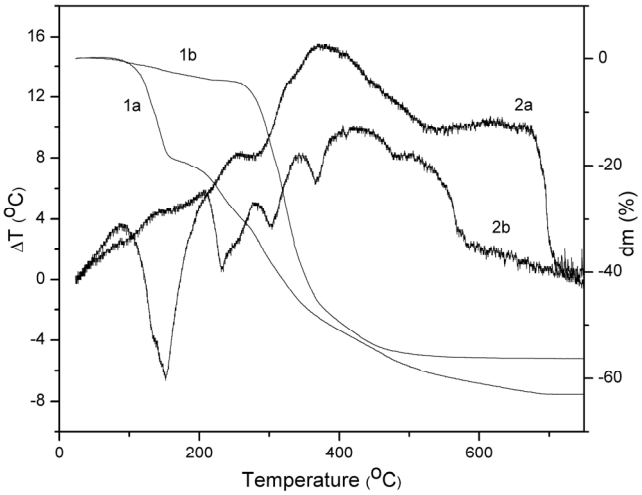

Figure 2. TG(1) and DTA(2) analyses for the (a) $Ce(acac)_3$ and (b) $Ce(acac)_3$+HPr

III. 500 - 800°C, in which the weight loss reaches the value of Δm = 56.3%, the final product being stable from 700°C.

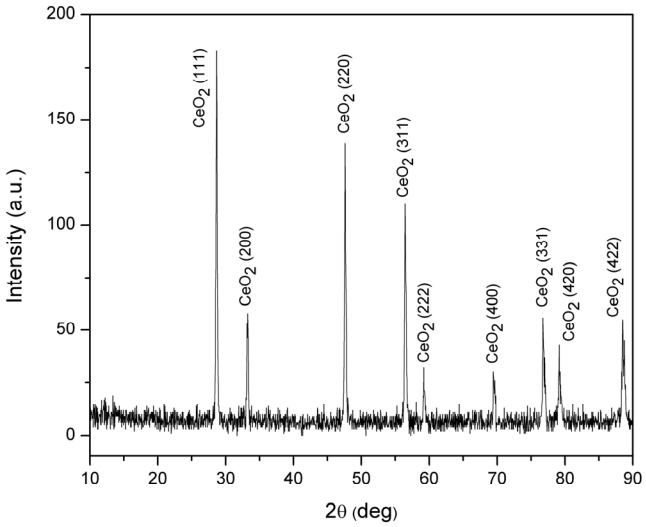

Figure 3. X-Ray diffraction pattern of the thermal treated ceria powder

Since the thermogravimetric-differential thermal analyses TG-DTA do not give information about the qualitative aspects of the evolved gases during the thermal decomposition, simultaneous mass spectra of the gaseous reaction products have been performed.

MS studies

In Figure 4 three significant mass spectra of the gases evolved during the TG-DTA analyses are presented comparatively. The first spectrum recorded at room temperature (25^{o}C) represents the argon enriched atmosphere, m/z = 40, for the simple ionized argon atoms and m/z = 20 for the double ionized argon atoms, mentioned above, in which the analyses have been carried out. The mass spectrum registered at 289^{o}C, at the beginning of the second thermal decomposition stage, is characterized by the appearance of the m/z = 42, 43, 45, 57 peaks, as well as by the significant increase of the m/z = 44, 22 peaks. At 331^{o}C the greatest number of fragments has been registered in the mass spectrum. Additional broader and more intense peaks appear at m/z = 85-86, 53-58, 41-46. It is worthwhile mentioning that they are maintained during the entire TG-DTA second stage, but with a smaller intensity.

Due to the fact that the low mass fragments appear in the mass spectra of numerous molecules, it is difficult to attribute them to a certain parent molecular ion. Furthermore, some of the fragments appear at the same m/z with the background. The heavy fragments registered in the range of the mass spectrometer derive from long chain molecules, some of them might belong to the initial compounds, e.g. m/z = 42, 85 from $Ce(acac)_3$, m/z=45, 57, 55, 56 from HPr, while others can be associated to new molecules, e.g. m/z =57, 86 from 3-pentanone, m/z = 43, 86 from 2-pentanone, m/z = 43, 58, 42 from acetone, m/z = 43, 85 from acetylacetone or m/z = 55, 72, 26, 45 from 2-propenoic acid. It is difficult to ascertain their generation, from either the initial ligands or from the complex thermal decomposition products. At the same time, the variety of the m/z fragments might be attributed to complex attachment mechanism among spatially separated ligands that coordinate the cerium ion as chelating or bidentate bridging, suggested for similar acetylacetonates [9].

In Figure 5 the TG analysis has been superposed onto the temperature dependent evolution of the most frequent fragments in the mass spectra of the precursor at m/z = 43 (CH_3CO^+), 45 ($COOH^+$) and, for CO_2 emission, m/z = 44 (COO^+). The correlation between TG-MS is remarkable, demonstrating a short response time (1s) of the RGA and the accuracy of the method. Nevertheless, the presence of a larger amount of gases prolongues the MS signal even after the end of the emission, leading to a broad band of overlapped effects at 430^{o}C. It is evident that the main weight loss is due to the simultaneous evolution of m/z = 43, 44, 45 fragments. The significant growth of the m/z = 44 fragment indicates the evolvement of CO_2 during the combustion of the organic moieties.

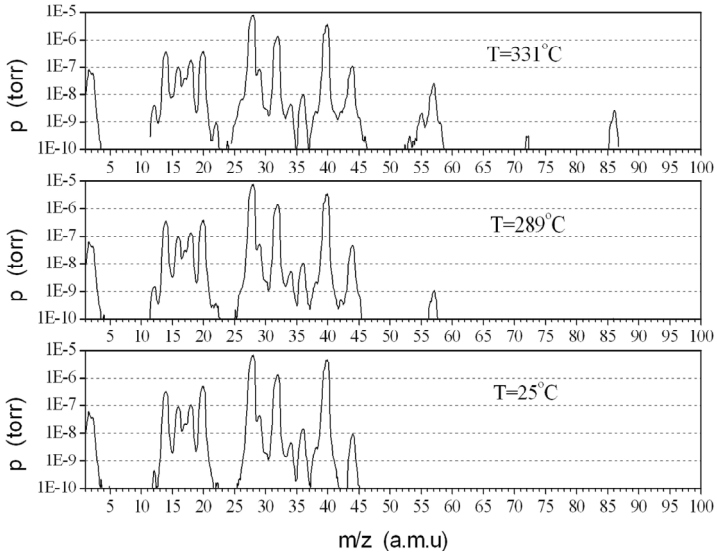

Figure 4. The mass spectra of the evolved gasses at different temperatures

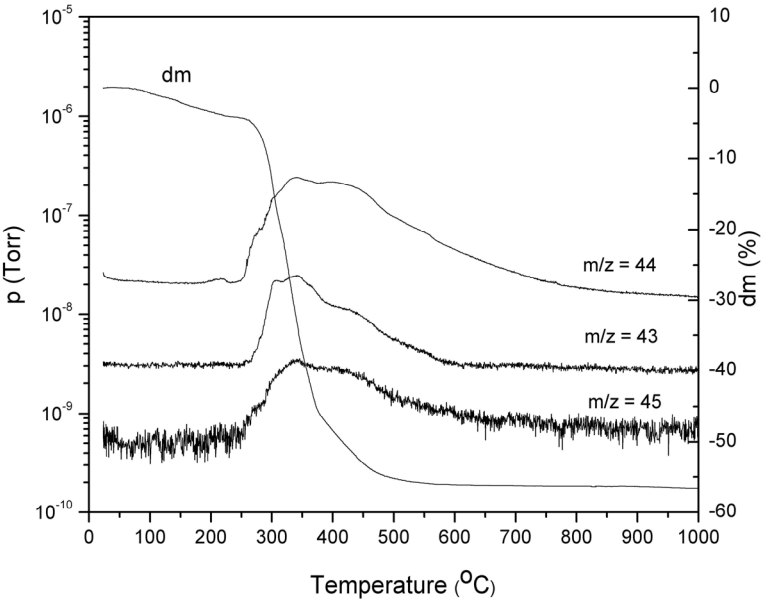

Figure 5. Correlated TG-MS analyses for the dried solution

b. Film analysis

Figure 6 shows the θ-2θ scans for the CeO_2 films on (100) MgO monocrystaline substrates heat treated at 1000°C for 15 minutes in Ar+12%H_2 atmosphere and subsequently quenched to room temperature. As it can bee seen from the figure, apart for the (200) CeO_2 peak, no other CeO_2 reflections are detected. This demonstrates that the CeO_2 films are epitaxially grown with a [h00]||[h00] epitaxial relationship between the substrate and the film.

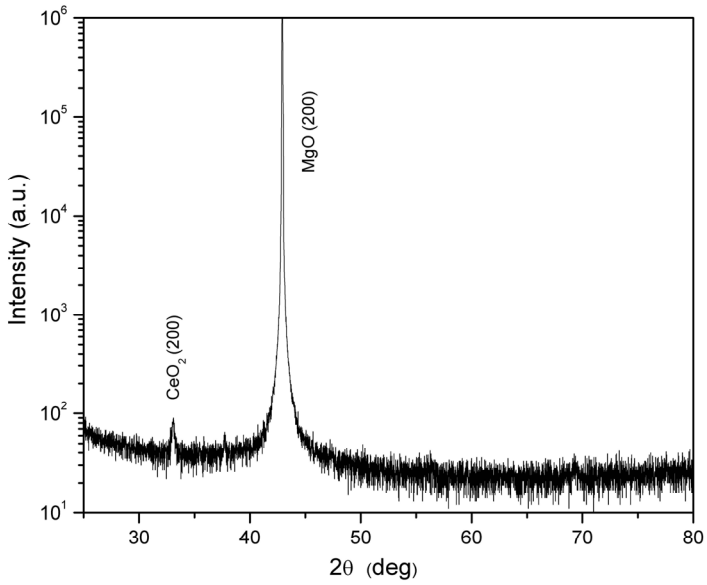

Figure 6. The XRD pattern of the (100) MgO/CeO_2 structures heat treated at 1000°C for 15 min.

CONCLUSIONS

Epitaxial 50 nm ceria thin films have been successfully prepared by CSD using only acetylacetonate and propionic acid as reactants, as revealed by X-ray diffraction. Additional informations regarding the thermal decomposition of the precursor coating solution have been obtained from the precursor chemistry studies. By comparing the FTIR spectra and the TG-DTA of the $Ce(acac)_3$ and ceria coating solution results that the ceria precursor is most probable a mixed acetylacetonate-propionate complex. This is also sustained by the high m/z fragments corresponding to the evolvement of 2-, 3-pentanone. In order to understand the chelating process in the coating solution formation

and the complex thermal decomposition processes, higher mass fragments (e.g. cluster) should be considered in the MS analyses. These as obtained epitaxial ceria thin films are promising as buffer layers in the coated conductor architecture and their further structural and morphological characterization is under progress.

EXPERIMENTAL SECTION

The cerium acetylacetonate, $Ce(C_5H_7O_2)_3xH_2O$ and the propionic acid, CH_3CH_2COOH with a purity of 99% used in this work were purchased from Alfa Aesar. The coating solution was prepared by mixing 3 mmol of $Ce(acac)_3xH_2O$ in 5 ml of propionic acid (excess) under stirring to form a clear yellow solution. The as-obtained solution was heated at 75^{o}C resulting in a change of colour to redish-brown. Further, the precursor solution was evaporated to dry powder on an oil bath.

The precursor thin films were deposited by spinning on 10x10 mm^2 substrates at 4000 rpm for 60 s. Prior to the deposition, the single crystalline (100) MgO substrates were ultrasonically cleaned with isopropanol. The deposition was performed under special cleaning conditions and controlled humidity to hinder the formation of the most common spinning defects (comets and striations) and nonuniform solvent evaporation.

The precursor films were thermally treated in Ar+12%H_2 atmosphere, under different temperature (900-1100^{o}C) and time (15-45 min.) conditions and quenched to room temperature. Before the heat treatment the samples were purged for about 10 minutes at room temperature in Ar+8%H_2. The thickness of the films produced under these conditions was typically 50 nm, as resulted from Scherrer equation.

The termogravimetric-differential thermal analyses (TG-DTA) were performed on the precursor powder, at a rate of 10ºC/min from ambient temperature to 900^{o}C in a dynamic atmosphere of argon (20 ml/min), in the temperature range 20-900^{o}C using an upgraded computer controlled equipment. The specimens (approximately 0.5 g) were weighed in an α-Al_2O_3 crucible.

The TG-DTA has been hyphenated with a quadrupole mass spectrometer QMS 200 atmospheric sampling system, residual gas analyzer (RGA-Stanford Research System) [12, 13], through a 120 cm long stainless steel capillary of an internal diameter of 0.075 mm. The capillary was heated at about 100^{o}C to prevent the condensation of water and other gaseous products. The acceleration voltage of the ionization was fixed at a potential of 70 eV. Two types of temperature dependent mass spectra were performed, by either registering the selected fragments supposed to be evolved, or the continuous registration between 1-100 a.m.u (in argon dynamic atmosphere).

The precursor was characterized in both solution and film by FT-IR spectroscopy. FT-IR spectra were performed on a Bruker Equinox 55 FT-IR spectrophotometer to identify the IR active functional groups of the precursor molecule. Spectra were collected with 2 cm^{-1} spectral resolution and 30 scans.

The structural characterization of the thermal analyses resulted powder and of the thin films was performed by X–ray diffraction analysis (θ-2θ) using a Bruker D8 Discover equipment with Cu Kα radiation. The diffractometer is equipped with a graphite monochromator on the diffracted beam to suppress the K_β component and parasitic scattering.

ACKNOWLEDGMENTS

The solution preparation was supported by the National University Research Council–Executive Agency for Higher Education and Research Funding (CNCSIS-UEFISCSU), project number PNII-IDEI nr. 4/2010, code 106/2010.

REFERENCES

1. M.S. Bhuiyan, M. Paranthaman, K.Salama, *Supercond. Sci. Tecnol.,* **2006**, *19*, R1.
2. A. Goyal, R. Feenstra, M. Paranthman, J.R. Thompson, B.Y. Kang, C. Cantoni, D.F. Lee, F.A. List, P.M. Martin, E. Lara-Curzio, C. Stevens, D.M. Kroeger, M. Kowalewski, E.D. Specht, T. Aytug, S. Sathyamurty, R.K. Williams, R.E. Ericson, *Physica C*, **2002**, *382*, 251.
3. R. Chockalingam, V.R.W. Amarakoon, H. Giesche, *J. Eur. Ceram. Soc*, **2008**, *28*, 959.
4. V. Boffa, T. Petrisor, S. Ceresara, L. Ciontea, F. Fabbri, P. Scardi, *Physica C*, **1999**, *312*, 202.
5. Y. Akin, E. Celik, W. Sigmund, Y. S. Hascicek, IEEE Trans. *Appl. Supercond*, **2003**, *13*, 2563.
6. K. Knoth, B. Schlobach, R. Hunne, L. Schultz, B. Holzapfel, *Physica C*, **2005**, *979*, 426–431.
7. L. Ciontea, T. Ristoiu, R.C. Suciu, T. Petrişor Jr, T. Petrişor, *AIP Conference Proceeding*, **2007**, *899*, 620.
8. H. Provendier, C. Petit, J.L. Schmitt, A. Kiennemann, C. Chaumont, *Journal of Materials Science,* **1999**, *34*, 4121.
9. G.B. Deacon, R. J. Phillips, *Coordination Chemistry Reviews,* **1980**, *33*, 227.
10. K. Nakamoto, *Infrared and Raman Spectra of Inorganic and Coordination Compounds*, Part B, J.Wiley&Sons, Inc., **2009**.
11. K. Knoth, R. Huehne, S. Oswald, L. Schultz, B. Holzapfel, *Acta Materialia*, **2007**, *55*, 517.
12. G.A.M Hussein, H.M. Ismail, *Powder Tech*, **1995**, *84*, 185.
13. T. Arii, A. Kishi. M. Ogawa, Y. Sawada, *Anal. Sci*., **2001**,*17*, 875.

STUDIA UBB CHEMIA, LVI, 2, 2011 (p. 189 - 194)

DEGRADATION KINETICS OF ANTHOCYANINS FROM CRUDE ETHANOLIC EXTRACT FROM SOUR CHERRIES

BIANCA MOLDOVAN[a], LUMINIȚA DAVID[a], ROXANA DONCA[a], CRISTIAN CHIŞBORA[b]

ABSTRACT. Storage stability of anthocyanins in ethanolic extract from dried sour cherry (*Prunus cerasus L.*) fruits was studied. Total anthocyanins content was determined using the pH differential method. Results indicate that the storage degradation of anthocyanins followed first-order reaction kinetics.

Keywords**:** *sour cherry extract, anthocyanins, degradation kinetics*

INTRODUCTION

Anthocyanins are a group of naturally occuring phenolic compound, which have an important role in the color quality of many flowers, fruits, vegetables and related products derived from them. Thus, measurement of anthocyanin content and investigation of their degradation is very useful for the food industry.

The anthocyanins are glycosides of anthocyanidines. Up to now, more than 540 anthocyanins and 23 anthocyanidins were reported [1] of which only six are the most common in vascular plants (Figure 1).

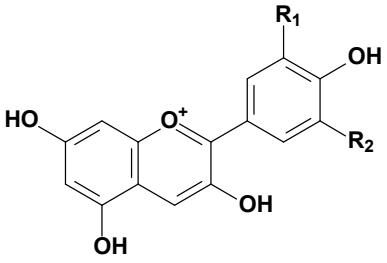

R_1	R_2	Anthocyanidine
H	H	Pelargonidin
OH	H	Cyanidin
OH	OH	Delphinidin
OCH_3	H	Peonidin
OCH_3	OH	Petunidin
OCH_3	OCH_3	Malvidin

Figure 1. The six more commun anthocyanidins structure

[a] *„Babeş-Bolyai" University, Faculty of Chemistry and Chemical Engineering,, 11 Arany Janos Str., 400028, Cluj-Napoca, Romania, muntean@chem.ubbcluj.ro*
[b] *National College „Emil Racoviță", 11, Mihail Kogălniceanu Str., 400084, Cluj-Napoca, Romania*

The most commonly found in nature are the glycoside derivatives of the three non-methylated anthocyanidins: cyanidin, delphinidin and pelargonidin.

The isolation and determination of anthocyanin content have been investigated by many authors [2-5]. The anthocyanin content of sour cherries varies largely with genotype. The most abundant anthocyanins found in the fruits of *Prunus cerasu*s are the glucoside forms of cyanidin (Cy) and peonidin (Pn) [6]: Cy-3-glucoside, Cy-3-glucosylrutinoside, Cy-3-sophoroside, Cy-3-rutinoside, Cy-3-xylosylrutinoside, Pn-3-glucoside, Pn-3-rutinoside, Cy-3-gentobioside.

Anthocyanins, like other polyphenolic compounds found in fruits, are known for their antioxidant activity. This plays a vital role in the prevention of cancer, diabetes, cardiovascular and neuronal illnesses [7]. There are several studies focused on the effect of anthocyanins in cancer treatments [8] and also on their antiinflammatory and plateled inhibitory effects [9]. Anthocyanins content in fruits and vegetables is also reported as responsible for their antimicrobial properties [10].

Anthocyanins are very unstable and susceptible to degradation [11]. Their stability is affected by storage and processing conditions, including pH, temperature, light, solvent, oxygen.

Substantial quantitative and qualitative information can be obtained from the spectral characteristics of anthocyanins. Anthocyanin pigments undergo reversible structure transformation as a function of pH, which can be measured using optical spectroscopy. The colored flavilium cation form predominates at pH = 1, while, at pH = 4.5 the colorless hemiketal form is the most stable (Scheme 1).

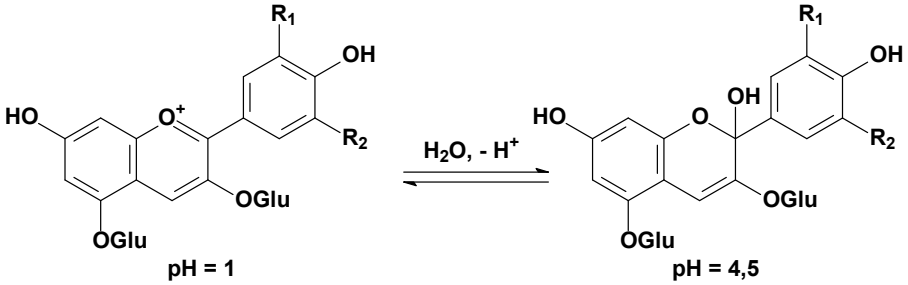

Scheme 1. Structural forms of anthocyanins at different pH values

The pH differential method is a rapid and easy procedure to determine the total anthocyanins content from various sources [12]. The method is based on the reaction depicted in Scheme 1 and permits an accurate measurement even in the presence of other interfering compounds.

The aim of this study was to determine the degradation kinetic parameters of sour cherry fruits anthocyanins in ethanolic extract during storage at room temperature (25^{o}C).

RESULTS AND DISCUSSION

The experiments were carried out on refrigerated sour cherry fruits (commercially available) which were allow to stay at room temperature until complete drying occurred.

Total anthocyanin content was determined using the pH-differential method [12], using two buffer systems: potassium chloride buffer (0.025 M, pH = 1.0) and sodium acetate buffer (0.04 M; pH = 4.5). The extract was mixed with the corresponding buffer and the absorbance of the samples was measured at 525 nm ($\lambda_{VIS\ max}$; see Figure 1) and 700 nm (for haze correction).

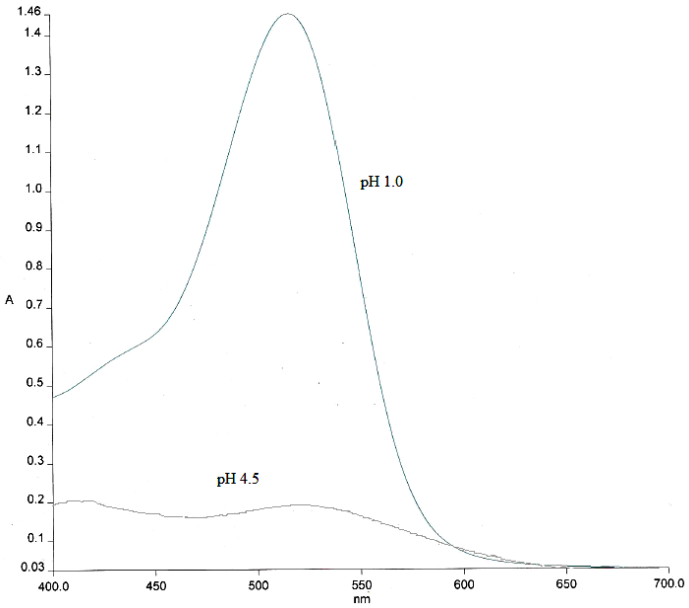

Figure 1. UV-VIS spectra of anthocyanins in buffer solutions at pH = 1 and pH = 4.5

The following equation was used to calculate the total anthocyanins as cyanidin-3-glucoside equivalents [12]:

$$TA = \frac{A \cdot M \cdot F \cdot 1000}{\varepsilon \cdot l} \tag{1}$$

where:

TA = total anthocyanins content (mg/l)

A = absorbance, calculated as;

$$A = (A_{pH\ 1.0} - A_{pH\ 4.5})_{525\ nm} - (A_{pH\ 1.0} - A_{pH\ 4.5})_{700\ nm} \quad (2)$$

M = molecular weight
F = dilution factor
l = pathlenght (cm)
ε = molar extinction coefficient
1000 = conversion factor from gram to miligram
All measurements were done in triplicate (n = 3).

The anthocyanin content during storage at 25^0C was plotted as a function of time (Figure 2). The linear dependence of ln [A] = f(t) demonstrates that the degradation process of monomeric anthocyanins follows first order reaction kinetics, results which are in agreement with those from the previous studies, reporting a first order reaction model for the degradation of these flavonoidic compounds from various sources [13,14].

The kinetic parameters were calculated using the following equations:

$$\ln[TA] = \ln[TA_0] - kt \quad (3)$$

$$t_{1/2} = \frac{0.693}{k} \quad (4)$$

where:

[TA] = total anthocyanin content (mg/l) at time t
$[TA_0]$ = initial total anthocyanin content (mg/l)
k = reaction rate constant (h^{-1})
t = reaction time (h)
$t_{1/2}$ = half-life (h)

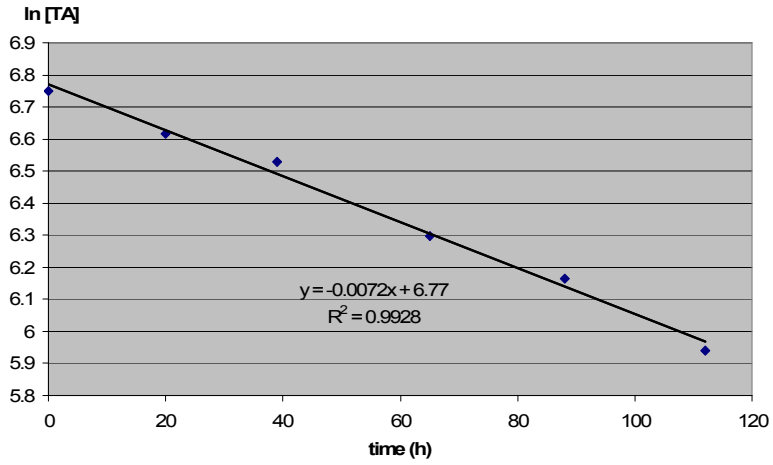

Figure 2. Degradation of anthocyanins in sour cherries ethanolic extract during storage at 25^0C

The determined value for the kinetic rate constant was $7.2 \cdot 10^{-3}$ h^{-1} and the half-life value was $t_{1/2}$ = 96.25 h. First order reaction kinetics for the degradation process of anthocyanins in sour cherry concentrates with a 38 days value for $t_{1/2}$ at 20^0C was reported [15]. In comparison, the alcoholic extract of anthocyanins from sour cherries is significantly less stable ($t_{1/2}$ = 4 days).

CONCLUSIONS

The total anthocyanin content in the ethanolic extract of sour cherries was determined (850.97 mg/kg dried fruits, in agreement with literature data [6]) and the degradation process of these compounds during storage at 25^0C was investigated. The degradation followed first order reaction model and the kinetic parameters values (k and $t_{1/2}$) were determined.

The extract is less stable than the concentrate juices obtained from sour cherry fruits.

EXPERIMENTAL SECTION

The dried sour cherry fruits were crushed in a mortar. 2 g of fruits were transferred to an Erlenmeyer flask, 50 ml of 96% ethanol and 0.1 ml of concentrated HCl were added and the mixture was stirred for 1 h at room temperature and then filtered. The filtrate was quantitatively transferred to a 100 ml volumetric flask and made up to 100 ml with 96% ethanol. The extract was kept away from light in a thermostated water bath, preheated to 25^0C, well capped to avoid evaporation. At regular time intervals, samples were taken and analysis was conducted immediatly.

5 ml of ethanolic extract were transferred to a 10 ml volumetric flask and made up to 10 ml with corresponding buffer (potassium chloride buffer, 0.025 M, pH = 1 and sodium acetate buffer, 0.4 M, pH = 4.5) and allowed to equilibrate for 15 minutes.

The absorbance of each solution was then measured at 525 ($\lambda_{VIS\ max}$) and 700 nm (for haze correction), using a Perkin Elmer Lambda 35 UV-VIS double beam spectrophotometer.

Pigment content was calculated as equivalents of cyanidin-3-glucoside (MW = 442.9 g/mol, ε = 26900 l/mol/cm) [12]. Visible spectra of samples were recorded by scanning the absorbance between 400 and 700 nm. Quartz cuvettes of 1 cm pathlength were used, absorbance readings were made against distilled water as a blanck. All the measurements were carried out at room temperature (~22^0C).

REFERENCES

1. J.M. Kong, L.S. Chia, N.K. Goh, T.F. Chia, R. Brouillard, *Phytochemistry*, **2003**, *64*(5), 923
2. B. Mozetic, P. Trebse, *Acta Chimica Slovenica*, **2004**, *51*, 151
3. A. Chaovanalikit, R.E. Wrolstad, *Journal of Food Science*, **2004**, *29*(1), 101
4. A. Chaovanalikit, R.E. Wrolstad, *Journal of Food Science*, **2004**, *29*(1), 107
5. G. Urbanyi, K. Horti, *Acta Alimentaria*, **1992**, *21*, 307
6. V. Šimunić, S. Kovač, D. Gašo-Sokač, W. Pfannhauser, M. Murkovic, *European Food Research & Technology*, **2005**, *220*, 575
7. I. Konczak, W. Zhang, *Journal of Biomedicine & Biotechnol*ogy, **2004**, *5*, 239
8. S.U. Lule, W. Xia, *Food Reviews International*, **2005**, *21*(4), 367
9. T. Maier, A. Schieber, D.R. Kammerer, R. Carle, Food Chemistry, **2009**, *112*, 551
10. A.D. Duman, M. Ozgen, K.S. Dayisoylu, N. Erbil, C. Durgac, Molecules, 2009, *14*, 1808
11. M.M. Giusti, R.E. Wrolstad, *Biochemical Engineering Journal*, **2003**, *14*(3), 217
12. M.M. Giusti, R.E. Wrolstad, „Current Protocols in Food Analytical Chemistry”, Wiley, New York, **2001**, F.1.2.1-F1.2.13
13. G.A. Garzon, R.E. Wrolstad, *Journal of Food Science*, **2002**, *67*(5), 1288
14. A. Kirca, M. Özkan, B. Cemeroğlu, *Food Chemistry*, **2007**, *101*, 212
15. B. Cemeroğlu, S. Velioğlu, S Işik, *Journal of Food Science,* **1994**, *59(6)*, 1216

STUDIA UBB CHEMIA, LVI, 2, 2011 (p. 195 - 204)

SIMULTANEOUS DETERMINATION OF TWO ANTIOXIDANTS IN COSMETC PRODUCTS BY GAS CHROMATOGRAPHY

ANCA MARIA JUNCAN[a], CRISTINA ELENA HORGA[b], TEODOR HODISAN[a]

ABSTRACT. A gas chromatographic method for the simultaneous determination of two antioxidants in o/w („oil in water") cosmetic formulations was developed by using GC with FID detection. A simple extraction procedure of the sample was required. The sample treatment proposed consists of dissolving the oil-rich products sample (Anti-Wrinkle Eye Contour Cream, Intensive Moisturizing Day Lift Cream and Replenishing Night Lift Cream) by sonication with organic solvent, centrifugation and filtration of the supernatant. The analytes were separated on a fused silica capillary column coated with DB-5 (5% diphenyl-95% dimethylpolysiloxane) and good separation was obtained for analysed antioxidants. The analysis was carried out in commercial samples, and satisfactory results were obtained for the recovery of this compounds.

Keywords: *cosmetic product, antioxidants, GC-FID.*

INTRODUCTION

Antioxidants have great popularity as primary ingredients in cosmetics [1]. Latest generation of cosmetic treatments developed against wrinkles, rely on antioxidant properties of some ingredients [2]. Products containing substances with antiradical activity were created mainly to satisfy expectations of treatment and prevention of photo-aging [3]. There are considerable data to suggest the benefits of such ingredients in cosmetics [4].

Antioxidant preservatives are able to inhibit reactions promoted by oxygen, thus avoiding the oxidation and rancidity of commonly used fats, oils, waxes, surfactants, perfumes, etc.. In cosmetics they are usually reducing agents and free radical scavangers [5]. Antioxidants can be naturally occuring compounds, or synthetic molecules based on phenolic structures with varying degrees of hydroxylation and side-chain substitutions [6]. Natural antioxidants

[a] *"Babeş-Bolyai"University, Faculty of Chemistry and Chemical Engineering, Arany Janos Str. 11, 400028, Cluj-Napoca, Romania*
[b] *Institute of Public Health, Louis Pasteur Str. 6, 400349, Cluj-Napoca, Romania*

are mainly represented in cosmetic products by tocopherols [7], which is the primary active form of vitamin E. The vitamin E isomers are usually eserified to acetates for use in commercial vitamins and topical formulations because the esters are far more stable [8].

Some of the synthetic antioxidants used in cosmetic formulas, such as butylated hydroxyanisole (BHA) and butylated carcinogenic [9, 10] so that extensive use of such raw materials in cosmetics may represent a potential health risk [11]. Long term and hydroxytoluene (BHT) are widespread studies indicate that the use of synthetic antioxidants in cosmetic products cand result in potential health risks associated with their intake [12].

3-tert-butyl-4-hydroxy anisole (BHA) is one of the widely used synthetic antioxidant in cosmetic preparations. This substance is generally recognized as safe for use in products, when the total content of antioxidants is not over 0,02% of fat or oil content, including essential (volatile) content of the product.

Determination of antioxidant compound from cosmetics is often difficult due to the matrix complexity, therefore great attention must be devoted to developing suitable extraction procedures and reliable evaluation of the mean recovery values. The procedure used to extract antioxidants from cosmetics depends on the nature of the formulaton (emulsion, cream, shampoos, etc.) and also on the characteristic of the analytical techniques employed for determination of active substances [5].

Various analytical tehniques have been developed to determine antioxidants in cosmetics, pharmaceutical preparations and drugs. The methods include high - performance chromatography (HPLC) [11, 13, 14, 15, 16, 17, 18, 19, 20], gas chromatography (GC) [12, 21, 22], capillary elecrophoresis (CE) [23] and micellar electrokinetic chromatography (MEKC) [24, 25].

Cosmetic formulations contain very often mixtures of antioxidant preservatives belonging to different chemical classes and characterized by different functional groups. Therefore, multicomponent analysis methods are required. In this sense, chromatographic techniques are those most commonly used to determine antioxidants and preservatives in cosmetic products. Gas chromatography (GC) with flame ionization detector (FID), electron capture detector (ECD) or mass spectrometry (MS) are widely used for the detection and determination of this compounds in cosmetics. Liquid chromatography (LC) is also one of the most commonly used technique to separate and determine antioxidant preservatives, in particular both ion-pair and reversed-phase LC with UV/VIS detection [5].

The official methods approved by the different legislations are not enough to carry out the necessary analytical control of cosmetics [5]. That is why, it is necessary to establish new efficient analysis methods, for monitoring the use of this controversal antioxidants in a adequate mode, and for the determination, and for the admissibility limit control of antioxidants permitted, and used in the cosmetic industry [26].

In view of functional group similarities between tocopherols and the synthetic antioxidants, it was decided to investigate the same approach to the latter group of antioxidants. The objective of this study was the simultaneous identification and determination of 3-tert-butyl-4-hydroxy anisole (BHA) and tocopherol acetate (α-TA) in cosmetic formulas by gas chromatography with FID detection.

In the present study, there is applied a method based on simple extraction procedure with organic solvent of the studied antioxidants in anti-aging cosmetic preparations prior to analysis by reversed-phase gas chromatography with FID detection. The application of this procedures to the assay of commercial products is presented.

RESULTS AND DISCUSSION

Good separation of standards was obtained for GC analysis with retention characteristics of $t_{R,BHA}$=8.073 and $t_{R,\alpha\text{-}TA}$=23.301. The choosen chromatographic conditions allowed a good separation of the two compounds taken into account. On the basis of conducted experiments methods for the simultaneous determination of BHA and α-TA in cosmetic formulas by GC-FID was established.

Confirmation of peak identity for the natural antioxidant α-TA was obtained by the GC determination in cosmetic samples. The retention parameters of compound from cosmetic formulation are listed in Table 1. The synthetic antioxidant BHA and the natural antioxidant α-TA, respectively, could be eluted with acceptable peak shape by method developed.

Table 1. t_R values of BHA and α-TA in the analized samples

Sample	t_R Value (min.)	
	BHA	**α-TA**
Anti-Wrinkle Eye Contour Cream	8.053	23.281
Intensive Moisturizing Day Lift Cream	8.057	23.284
Replenishing Night Lift Cream	8.055	23.280

Stock solutions were prepared by dissolving the appropiate amounts of the standard antioxidants in ethanol. A set of working solutions was prepared by dilluting aliquots of the stock solution to give concentrations ranging from 10 to 1000 mg/L for the two studied compounds.

The standard solutions of the two antioxidants were injected, to determine the individual retention times of the synthetic and natural antioxidants. Figure 2 shows the chromatogram of a standard solution of the two antioxidants studied for the gas chromatographic method at the concentration of 50 mg/L BHA and 500 mg/L α-TA respectively:

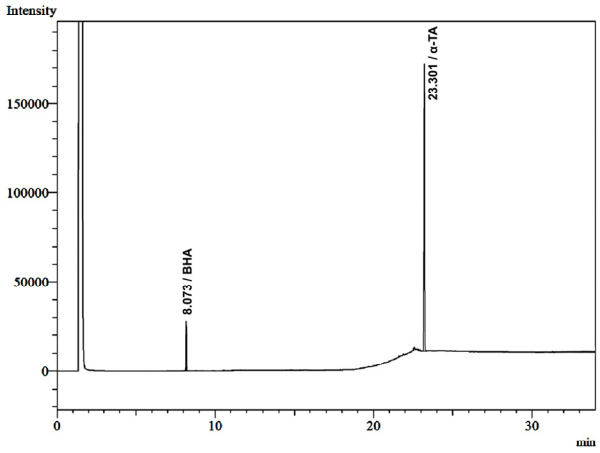

Figure 1. Chromatogram of a BHA and α-TA Standard

The calibration graphs for BHA and α-TA were constructed over the covered range of concentration, as indicated in the experimental part and are presented in Figure 2a for BHA and Figure 2b for α-TA respectively:

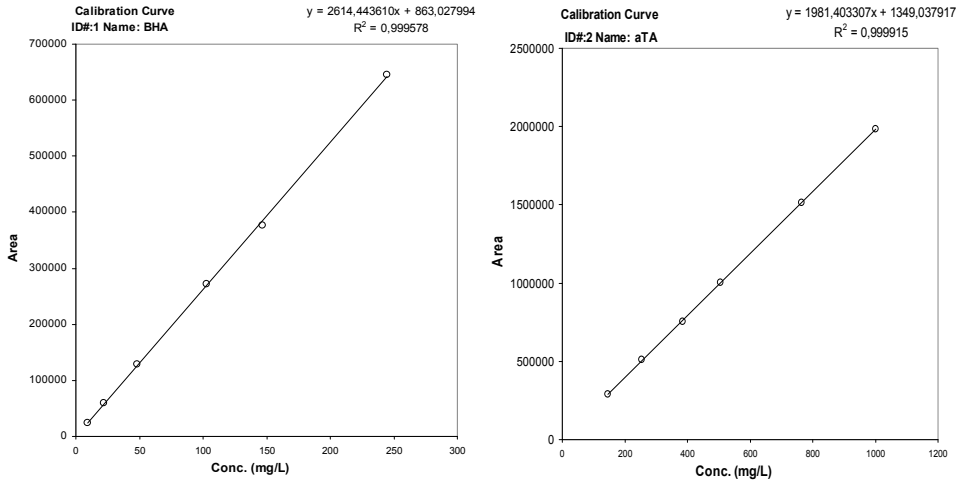

a b

Figure 2. Calibration curves for standards.

Calibration curves were constructed in order to study method liniarity. The linearity obtained was satisfactory and present a correlation coefficient of 0.999578 for BHA and 0.999915 for α-TA for the proposed GC method.

The detection limit (LOD) and quantitation (LOQ) expressed as signal/noise = 3 and signal/noise =10, were determined based on standard deviation through responses and the slope of regression equation of a curve constructed concentration levels of 10,25, 50, 100, 150 and 250 mg/L for BHA, and 150, 250, 375, 500, 750 and 1000 mg/mL for α-TA, respectively. The LOD value obtained for BHA was 0,131 and 0,383 for α-TA, respectively. There was calculated a LOQ of 0,396 for BHA and 1,160 for α-TA.

Three anti-aging cream samples- Anti-Wrinkle Eye Contour Cream, Intensive Moisturizing Day Lift Cream and Replenishing Night Lift Cream were prepared in the laboratory by adding 0,05% BHA and 0,5% α-TA (w/w). The recovery, defined as (found concentration/spiked concentration) × 100%, was calculated for each cream sample. The concentrations of the synthetic antioxidant BHA and the natural antioxidant α-TA, respectively, determined from the cosmetic samples are listed in Table 2. Complete triplicate analysis was performed on all cream samples to allow the calculation of average deviations as a measurement of chromatographic reproductibility.

Table 2. Concentration values of synthetic and natural antioxidants in the three anti-aging cream samples

Cream	Concentration (g/100g)±SD (n=3)		Recovery (%)	
	BHA	**α-TA**	**BHA**	**α-TA**
Anti-Wrinkle Eye Contour	0,0447±0,003	0,4241±0,002	**89,4**	**84,8**
Intensive Moisturizing Day Lift	0,0468±0,002	0,4414±0,003	**93,6**	**88,3**
Replenishing Night Lift	0,0470±0,001	0,4159±0,004	**94,0**	**83,2**

Commercial samples of three anti-aging creams (Anti-Wrinkle Eye Contour Cream, Intensive Moisturizing Day Lift Cream and Replenishing Night Lift Cream) that contained combinations of these two antioxidants were analysed and the target compounds were identified by comparing the retention times of the observed peaks with those obtained from the standard solutions.

The GC chromatogram of Anti-Wrinkle Eye Contour Cream, Intensive Moisturizing Day Lift Cream and Replenishing Night Lift Cream are presented in Figure 3a, Figure 3b and Figure 3c, respectively.

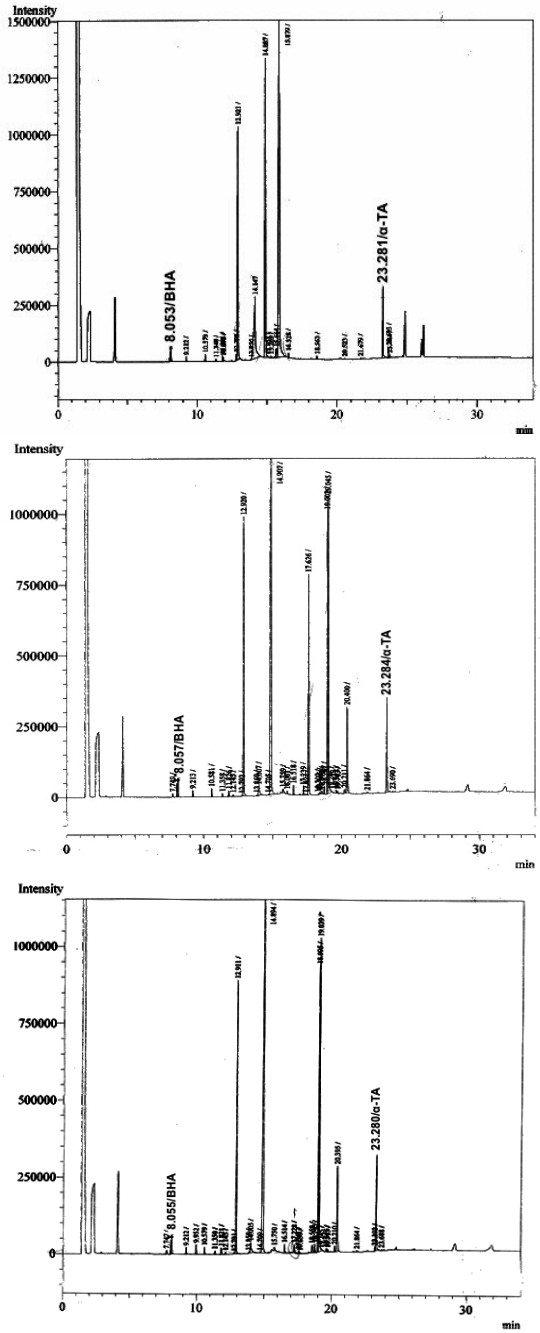

Figure 3. Chromatograms of the samples: a-Anti-Wrinkle Eye Contour Cream, b-Intensive Moisturizing Day Lift Cream, c-Replenishing Night Lift Cream

The concentrations of the synthetic antioxidant BHA and the natural antioxidant α-TA respectively determined from the cosmetic samples are listed in Table 3:

Table 3. Concentration values of synthetic and natural antioxidants in the commercial anti-aging cream samples

Cream	Concentartion (g/100g) (n=3)		Claimed Concentartion (g/100g)	
	BHA	α-TA	BHA	α-TA
Anti-Wrinkle Eye Contour	0,0413±0,002	0,4391±0,002	0,05	0,5
Intensive Moisturizing Day Lift	0,0438±0,002	0,4663±0,003	0,05	0,5
Replenishing Night Lift	0,0406±0,002	0,4284±0,003	0,05	0,5

The developed method can be succesfully applied for the identification and determination of these antioxidants in cosmetic preparations. Good recovery of the natural antioxidant α-TA of 84,8% for a Anti-Wrinkle Eye Contour Cream 88,3% for a Intensive Moisturizing Day Lift Cream and 83,2% for a Replenishing Night Lift Cream by GC analysis were obtained. BHA could be eluted with acceptable peak shapes, and there were obtained satisfactory recoveries by the method: 89,4% for a Anti-Wrinkle Eye Contour Cream, 93,6% for a Intensive Moisturizing Day Lift Cream and 94% for a Replenishing Night Lift Cream. The quantities found for the cosmetic formulations were in conformity with the values claimed by the manufacturer.

CONCLUSIONS

Anti-aging products present a real interest, but there are few studies that can be found, regarding the analysis and monitoring methods of antioxidants in this category of products.

A GC-FID method following a simple and rapid extraction with ethanol was used for the determination of BHA and α-TA in three oil-rich cosmetic products (Anti-Wrinkle Eye Contour Cream, Intensive Moisturizing Day Lift Cream and a Replenishing Night Lift Cream).

Calibration curves of standard solution were linear in the range from 10 to 1000 mg/mL for the studied compounds. Good recoveries were obtained for the natural and synthetic antioxidants by the used gas chromatographic method.

This method allowed a simultaneous, simple, rapid and accurate determination and confirmation of BHA and α-TA in cosmetic products containing various ingredients. The described method presents good selectivity, adequate detection and quantitation limits and can be applied in the routine analysis for quality control of cosmetic preparations containg α-TA and BHA.

EXPERIMENTAL SECTION

Standards and reagents

All reagents used were of analytical grade and were used without further purification. Commercially available antioxidants used in the study are 3-tert-butyl-4-hydroxy anisole (JAN DEKKER, Nederland B.V.) and tocopheyl acetate (BASF SRL, Bucureşti, Romania). The molecules structures of the two investigated compounds are shown in Figure 4:

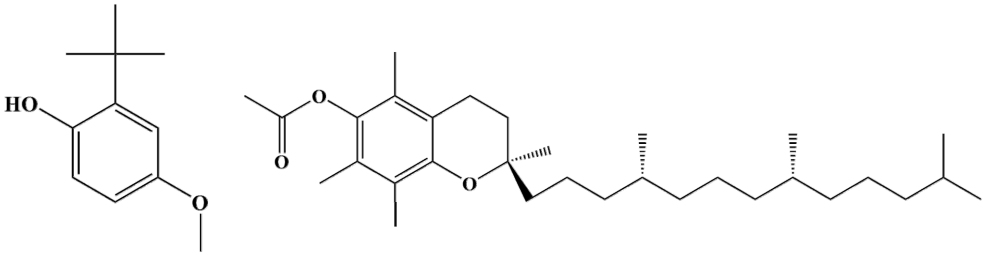

BHA **α-TA**

Figure 4. Structure of BHA and α-TA

Sample Preparation

Three oil-rich products (Anti-Wrinkle Eye Contour Cream, Intensive Moisturizing Day Lift Cream and Replenishing Night Lift Cream) were analyzed by dissolving 1.0 g of each o/w emulsions by sonication (HF-Freq. 35 kH, Transsonic T460, Elma GmbH&CO) with 10 mL of ethanol. After 5 min. centrifugation, the supernatant was filtered through a 0.45 µm filter (Chromafil PET-45/25, 0,45 µm, Macherey-Nagel GmbH&CO. KG.).

Calibration Standard Solutions

Stock solutions were prepared by dissolving the appropiate amounts of the standard antioxidants (0,0125 g BHA and 0,0500 g α-TA) in 10 mL ethanol, transfered to a 50 mL volumetric flask and brought to volume. A set of working solutions was prepared by dilluting aliquots of the stock solution to give concentrations ranging from 10 to 1000 mgL for the studied compounds.

Chromatographic Conditions

Chromatography was performed on a Shimadzu 2010 Model gas cromatograph equipped with a FID detector. Fused silica capillary column DB-5, 30m x 0,25 mm ID, coated with a 0,25 µm film of 5% diphenyl-95% dimethylpolysiloxane, was used. The owen temperature was held at 120ºC for five minutes, then increased at a rate of 10ºC/min to 310ºC and held for 10 minutes. Detector conditions were 320ºC, N_2-30 ml/min and H_2-40 ml/min flow-rate. The injection temperature was 350ºC. 1 µl aliquots of the standard and sample solutions were injected and analyzed under the operation conditions described above.

REFERENCES

1. M.P. Lupo, *Clinics in Dermatology*, **2001**, *19*, 470.
2. C. Rona, F. Vailati, E. Berardesca, *J. Cosmet. Dermatol.*, **2004**, *3*, 26.
3. E. Cadenas, L. Packer, „Handbook of Antioxidants", Marcel Dekker Inc., New York, **2002**, chapter 1.
4. M. Andreassi, L. Andreassi, *J. Cosmetic Dermatol.*, 2004, *2*, 153.
5. A. Salvador, A. Chisvert, „Analysis of Cosmetic Products", Elsevier, Amsterdam, **2007**, chapter 5.
6. L. Gagliardi, D. De Orsi, L. Manna, D. Tonelli, *J. Liq. Chrom. & Rel. Technol.*, **1997**, *20*, 11, 1798.
7. M. Gonzalez, E. Ballesteros, M. Gallego, M. Valcarcel, *Anal. Chim. Acta*, **1998**, *359*, 47.
8. E. Burke, *J. Cosm. Dermatol.*, **2004**, *3*, 149.
9. N. Ito, M. Hirose, S. Fukushima, Shirai T., M. Tatematsu, *Food Chem. Toxicol.*, **1986**, *24*, 10-11, 1071.
10. M. Hirose, Y. Takesada, H. Tanaka, S. Tamano, T. Kato, T. Shirai, *Carcinogenesis*, **1997**, *19*, 1, 207.
11. M.R. Lee, C.Y. Lin, Z.G. Li, T.F. Tsai, *J. Chromatogr. A.*, **2006**, *1120*, 244.
12. T.F. Tsai, M.R. Lee, *Chromatographia*, **2008**, *67*, 5-6, 425.
13. L. Gagliardi, D. De Orsi, L. Manna, D. Tonelli, *J. Liq. Chrom. & Rel. Technol.*, **1997**, *20*, 11, 1797.
14. S. Scalia, A. Renda, G. Ruberto, F. Bonina, E. Menegatti, *J. Pharm. Biomed. Analysis*, **1995**, *13*, 3, 273.
15. M.M. Almeida, J.M.P. Alves, D.C.S. Patto, C.R R.C. Lima, J.S. Quenca-Guillen, M.I.R.M. Santoro, E.R.M. Kedor-Hackmann, *Int. J. Cosmet. Sci.*, **2009**, *31*, 445.
16. E.R. Gaspar, M. Campos, *Int. J. Pharm.*, **2007**, *343*, 181.
17. T. Guaratini, M.D. Gianeti, M. Campos, *Int. J. Pharm.*, **2006**, *327*, 12.
18. P. Moreno, V. Salvado, *J. Chromatogr. A.*, **2000**, *870*, 207.

19. J.M. Irache, F.A. Vega, I. Ezpeleta, *Pharm. Acta Helv.*, **1992**, *67*, 5-6, 152.
20. R.C. Chiste, F. Yamashita, F.C. Gozzo, A.Z. Mercadante, *J. Chromatogr. A.*, **2011**, *1218*, 1, 57.
21. H.J. Jeong, M.H. Lee, K.W. Ro, C.W. Hur, J.W. Kim, *Int. J. Cosmet. Sci.*, **1999**, *21*, 41.
22. T.J. Yang, F.J. Tsai, C.Y. Chen, T.C. Yang, M.R. Lee, *Anal. Chim. Acta*., **2010**, *668*, 2, 188.
23. M. Urbanek, M. Pospisilova, M. Polasek, J. Sicha, *Chromatographia*, **2002**, *55*, 333.
24. M.C. Boyce, E.E. Spickett, *J. Liq. Chrom. & Rel. Technol.*, **2000**, *23*, 11, 1689.
25. Y. Guan, Q. Chu, L. Fu, J. Ye, *J. Chromatogr. A.*, **2005**, *1074*, 1, 201.
26. A. Juncan, T. Hodişan, C. E. Horga, N. Muntean, M. Mitan, *Rev. Soc. Rom. Chim. Cosmet.*, **2010**, *10*, 2, 8.